SANDIA REPORT

SAND87—2381 • UC—814
Unlimited Release
Printed March 1991

Yucca Mountain Site Characterization Project

Analysis of Component Surface/Downhole Ground Motions at Yucca Mountain for Underground Nuclear Explosions in Pahute Mesa

James S. Phillips

Prepared by
Sandia National Laboratories
Albuquerque, New Mexico 87185 and Livermore, California 94550
for the United States Department of Energy
under Contract DE-AC04-76DP00789

"Prepared by Yucca Mountain Site Characterization Project (YMSCP) participants as part of the Civilian Radioactive Waste Management Program (CRWM). The YMSCP is managed by the Yucca Mountain Project Office of the U.S. Department of Energy, Nevada Operations Office (DOE/NV). YMSCP work is sponsored by the Office of Geologic Repositories (OGR) of the DOE Office of Civilian Radioactive Waste Management (OCRWM)."

Issued by Sandia National Laboratories, operated for the United States Department of Energy by Sandia Corporation.

Available to DOE and DOE contractors from
Office of Scientific and Technical Information
PO Box 62
Oak Ridge, TN 37831

Prices available from (615) 576-8401, FTS 626-8401

Available to the public from
National Technical Information Service
US Department of Commerce
5285 Port Royal Rd
Springfield, VA 22161

NTIS price codes
Printed copy: A10
Microfiche copy: A01

SAND--87-2381

DE91 009820

SAND87-2381
Unlimited Release
March 1991

ANALYSIS OF COMPONENT SURFACE/DOWNHOLE GROUND MOTIONS AT YUCCA MOUNTAIN FOR UNDERGROUND NUCLEAR EXPLOSIONS IN PAHUTE MESA

James S. Phillips
Ground Motion and Seismic Division
Sandia National Laboratories
Albuquerque, NM 87185

ABSTRACT

Surface and downhole ground motion data have been recorded at Yucca Mountain stations. Peak amplitudes as well as pseudo-relative velocity response spectra (PSRVs) for these data are studied. Surface/downhole behavior of the ground motion is best described as an arithmetic average of the ratios of surface/downhole PSRVs at each station. For the most part, downhole motions are less than surface motions. The one exception to this is station W28, where an anomalous, high frequency signal is present in the horizontal components. Possible explanations are given for this behavior.

ACKNOWLEDGMENTS

J. G. Lee was responsible for data acquisition and J. D. Pearcey was responsible for data processing. J. W. Long assisted in the analysis.

FOREWORD

The Yucca Mountain Site Characterization Project (YMP), managed by the Nevada Operations Office of the U.S. Department of Energy, is examining the feasibility of siting a repository for commercial high level nuclear wastes at Yucca Mountain on and adjacent to the Nevada Test Site (NTS). This work, intended to extend our understanding of the ground motion at Yucca Mountain resulting from testing of nuclear weapons on the NTS, was funded jointly by the NNWSI project and the Military Applications Weapons Test Program. This report summarizes one aspect of the weapons test seismic investigation conducted in FY87.

CONTENTS

FIGURES

TABLES

PREFACE

The Weapons Test Seismic Investigations (WTSI) project has been working in support of the Yucca Mountain Site Characterization Project (YMP) since 1977. If a waste storage facility is located near the Nevada Test Site (NTS) it will be subjected to ground shaking generated by underground nuclear weapons tests. A knowledge of expected ground motion levels from these tests will enable the designers to provide for the necessary structural support in the designs of the various components of the repository. The primary mission of the WTSI project involves recording and analyzing ground motion data from these underground nuclear explosions (UNEs) and developing a method to predict the amplitude of ground motions generated at the repository site from future weapons tests.

The WTSI project has deployed a total of 29 seismic stations specifically for the YMP project. These seismic stations consist of triaxial accelerometers (i.e., accelerometers are mounted such that accelerations are measured in three mutually perpendicular directions), amplifiers, voltage controlled oscillators (VCO), multiplexers, and transmitters. All stations consist of surface accelerometers. Additionally, some of the stations have companion instrumentation installed below the ground surface (generally at depths greater than 100 m). Initially, these stations were located at several points around the NTS. After the Yucca Mountain site became the focus of the YMP project in 1980, the first WTSI seismic station at Yucca Mountain was installed. Since that time, the WTSI project has had a total of 11 stations in the Yucca Mountain area. At the present time, 5 stations are active and 4 of these stations consist of surface and downhole instrumentation.

The data acquisition process consists of selecting UNEs of interest to YMP, turning the seismic stations on by radio and recording the ground motion on analog tape. The analog tape is sent to Sandia National Laboratories in Albuquerque, NM, where it is digitized, processed and analyzed.

In general there is approximately 8 minutes of information recorded for each track at two to three amplifications (depending on the capabilities of the acquisition system fielded at a station). A total of 180 s of this information is digitized for study. About 60 s of this information is prior to ground motion arrival. This segment provides a sample of the system noise. The remainder of the digitized information is a combination ground motion and system noise. The entire 180 s is digitized at a sample rate of 500 points/second (from the sampling theorem, this sample rate provides adequate definition for frequencies less that 250 Hz). The digital data are displayed and compared with the paper playbacks of the analog tape. Any problems are identified and eliminated if possible. A calculation of the power density spectrum (PDS) is then made on the noise segment of the record and the signal-plus-noise segment. A typical comparison of the noise PDS and the signal PDS is shown in Figure P-1. Analysis of these two spectra is used to define the filter limits used in the filtering process. Finite Impulse Response filters are used to perform the filtering on these data. First, a low pass filter (frequency cutoff is usually about 30 Hz for this filter) is applied to the data. Next, the sample rate is decreased to 250 points/second (this preserves frequencies less than 125 Hz) and a high pass filter is applied to the data

(frequency cutoff is usually about 0.3 Hz). These filtered data are evaluated and the data are stored for future analysis.

UNEs are selected primarily on the basis of explosive yields. Yields of interest to the YMP project are between 80 and 150 kt. The lower yield limit was selected because ground motions generated by yields below this limit are of a very low amplitude and are of very little interest. The upper yield limit is mandated by the Threshold Test Ban Treaty of March 1976. The distance between the underground explosions of interest and Yucca Mountain varies from about 35 km to 50 km. There are about five UNEs conducted annually that are of interest to the YMP project.

As stated above, the primary objective of this effort is to provide a method to predict ground motions from future underground weapons tests at the repository site. This requires not only the development of a prediction model, but a selection of the appropriate future UNE for use in design. The selection of the future UNE has been made on the basis of real estate availability studies and off-site damage criteria (see SAND80-1020/1 listed in Table P-1 for further information). This design basis event is defined as a 700 kt explosion in the Buckboard Area of NTS. The distance between this future UNE and Yucca Mountain is about 22.5 km (this is the distance from the closest point in the Buckboard Area suitable for testing and Yucca Mountain). The prediction model could be developed by either theoretical studies or empirical studies. Both approaches have limitations. Because of the complex nature of the geology, the three-dimensional nature of the problem and limitations of current finite element or finite difference computer codes, quantitative results from theoretical studies would be subject to large uncertainties. The empirical approach uses past observations to predict future occurrences. The major limitation in this approach stems from the fact that the future event of interest to YMP falls outside of the realm of the existing data base. Even with this limitation, the empirical approach will have smaller uncertainties associated with the quantitative results than those from a theoretical study.

Because the UNE-generated ground motion data recorded at Yucca Mountain is from explosions of limited yield and distance variations, which do not encompass the design basis UNE, it is important to include ground motion data of larger yields and smaller distances in the analysis effort. Ground motion generated by UNEs has been of interest since the beginning of underground weapons testing. Ground motion data from UNEs, with yields up to 1400 kt, at both close-in locations (at distances within a few burial depths of the explosion) and at seismic distances (measured in terms of tens of burial depths from the explosion) have been recorded and studied. Many of these data were used to develop prediction models for the amplitude of ground motion and to study the transmission characteristics of the NTS area. These studies were conducted prior to the YMP project and are not directly applicable to the project. However, the data from some of these older UNEs exist on tape and have been analyzed in the context of the YMP project.

The resulting UNE ground motion data base assembled by the WTSI project for the YMP project consists of ground motion data from a total of 61 UNEs. Of this number, 38 have been recorded at Yucca Mountain seismic stations. These UNEs have explosive yields between 80 and 150 kt (the current treaty upper limit) and are located in the Yucca Flats and Pahute Mesa testing areas of the

NTS. These areas are roughly 35 to 50 km away from Yucca Mountain. The remainder of the UNEs that make up the data base consist of earlier events with yields ranging up to 1400 kt and recording stations located at various points on the NTS at distances of 1 km and greater.

In addition to the primary objective discussed above, the WTSI project is analyzing the UNE ground motion data to understand another important issue. This is the relationship of the transmission of seismic waves and the geologic structure between the testing areas of NTS and Yucca Mountain.

Table P-1 lists the analysis reports that the WTSI project has prepared for the YMP project. At this point in time, these reports may be categorized in three basic groups (as shown in the table). These are:
1) Quality Assurance related; 2) Prediction of surface ground motions; and 3) Prediction of downhole ground motions. (The subject of the transmission of seismic waves is discussed in both group 2 and 3 reports.) This report fits in the third category. It addresses the subject of the prediction of downhole ground motions. Past reports on this subject, primarily SAND80-0174 and SAND82-1647 (Table P-1), dealt with vector ground motions recorded at various locations around the NTS. This report deals with component ground motions recorded specifically at Yucca Mountain from UNEs in the Pahute Mesa Testing area of the NTS.

Table P-1. Reports Generated by WTSI for YMP

SAND79-1002	Prediction of Ground Motion from Nuclear Weapons Tests at NTS, Vortman, L. J., Group 2
SAND80-1020/1	Prediction of Ground Motion from Underground Nuclear Weapons Tests as it Relates to Siting of a Nuclear Waste Storage Facility at NTS and Compatibility with the Weapons Test Program, Vortman, L. J., Group 2
SAND81-0784	A Field Comparison of the Kistler 303 and Q-FLEX 1100 and 1200 Accelerometers, Vortman, L. J., Group 1
SAND81-2214	Ground Motion from Earthquakes and Underground Nuclear Weapons Tests: A Comparison as it Relates to Siting a Nuclear Waste Storage Facility at NTS, Vortman, L. J., Group 2
SAND82-0174	Effects of Repository Depth on Ground Motion - The Pahute Mesa Data, Vortman, L. J., and Long, J. W., Group 3
SAND82-1647	Effect of Repository Depth on Ground Motion - The Yucca Flats Data, Vortman, L. J., and Long, J. W., Group 3
SAND82-2478	Prediction of Downhole Waveforms, Long, J. W., Sabisch, K. A., Stearns, S. D., and Vortman, L. J., Group 3
SAND83-1553	Stresses and Strains at Yucca Mountain from Underground Nuclear Explosions, Vortman, L. J., Group 2
SAND83-2625	Proceedings of the Conference on DOE Ground Motion and Seismic Programs On, Around and Beyond NTS, Vortman, L. J., Ed., Groups 2 and 3
SAND85-1605	Ground Motion at Yucca Mountain from Pahute Mesa Underground Nuclear Explosions, Vortman, L. J., Group 2
SAND86-2201	Verification of Ground Motion Data Processing Codes, Phillips, J. S., Group 1

Figure P-1. Comparison of Noise PDS and Signal PDS of a Raw Digitized Record

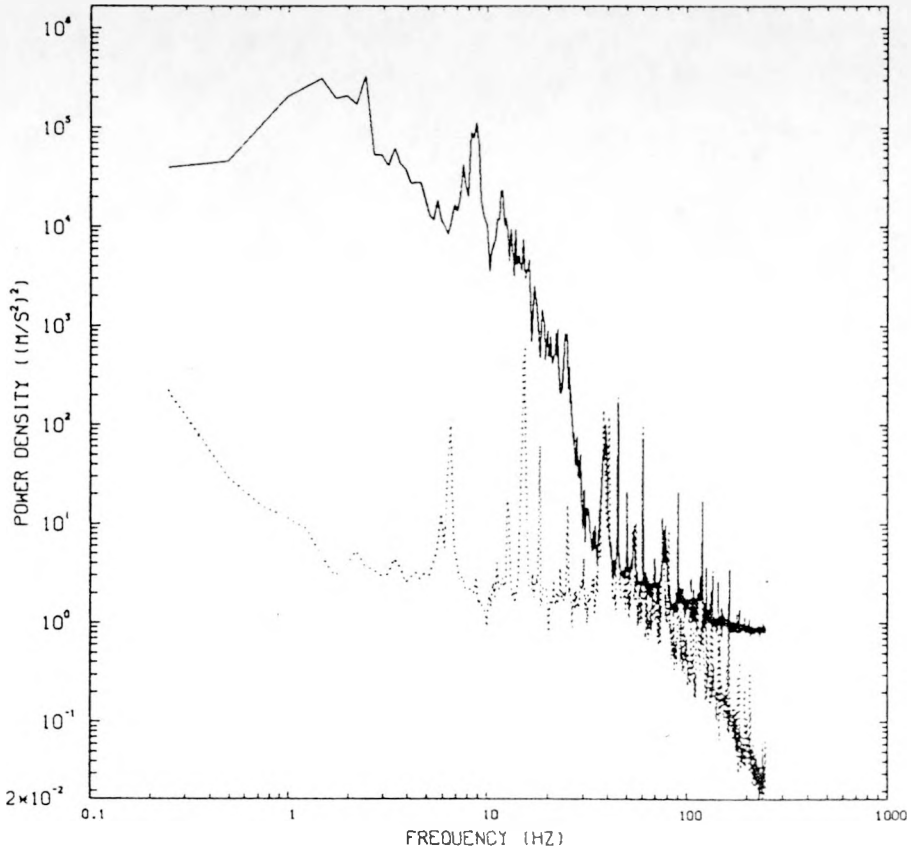

817.00	DEL:0200	NOISE START : -60.0000
TRACK 10	MIN:-.5901	NOISE END : -0.6080
14. KHZ	MAX: .5404	SIGNAL START : 0.0000
12-15-89	AZM: 197.	SIGNAL END : 88.0640
14:14:25	RNG: .	BLOCK SIZE : 2048
	VSN:	FREQUENCY INTERVAL : 0.24414

SOLID LINE-DATA
DOTTED LINE-BACKGROUND NOISE

1.0 INTRODUCTION

One of the primary goals of the Yucca Mountain Site Characterization Project (YMP) is the understanding and quantification of the seismic risk at the Yucca Mountain Site. This understanding must include the behavior of seismic signals as they propagate along the ground surface as well as the behavior of these signals at depth. The seismic risk at this site consists of both natural and man-made events. The major man-made seismic events of interest to the YMP project are the underground nuclear explosions (UNEs) conducted at the Nevada Test Site (NTS). The comparative behavior of the surface/downhole ground motions observed at Yucca Mountain from a data set of recent UNEs is the subject of this report.

UNEs are conducted primarily in two areas of the NTS: Yucca Flats and Pahute Mesa. The UNEs used in this study were all conducted in the Pahute Mesa area. The events included in this data set are listed in Table 1.0-1. Approximate location of the various events and the general Yucca Mountain area are shown in Figure 1.0-1.

The data discussed in this report were recorded at the currently active Yucca Mountain stations which have companion surface/downhole instrumentation. These stations are W25, W28, W29 and W30. Three of the downhole stations (W25, W28 and W30) are installed at depths comparable to the depth of the repository horizon. These stations will provide ground motion data which will support the design of the underground facilities of the repository. The fourth downhole station (W29) is fairly shallow in order to provide ground motion data to support the design of the surface facilities. The station locations are listed in Table 1.0-2 and shown with respect to the potential repository in Figure 1.0-2.

Ground motion from a total of eleven Pahute Mesa events have been recorded at these surface/downhole stations. Station W28 is the closest of the group at an average distance of 42 km away from the testing area. The downhole instrumentation at this station is located at a depth of 368 m. Data from a total of six events have been recorded at this station. At approximately 45 km from Pahute Mesa, Station W25 has recorded data from nine events. Downhole instrumentation at Station W25 is at a depth of 358 m. Station W29, at approximately 47 km from the testing area, has recorded data from a total of six events. The downhole instrumentation at W29 is located at a depth of 82 m. Located approximately 50 km from Pahute Mesa, Station W30 has recorded data from a total of nine events. W30 has the downhole instrumentation installed at a depth of 352 m.

The three stations with deep downhole instrumentation are shown on the estimated geologic profile (Ortiz et. al., 1985) in Figure 1.0-3. The downhole stations of W25 and W30 are in the geologic material denoted as TSw2 (described below). Published boring logs of the instrumentation holes identify the surface material at W28 and W30 as TCw, and UO at W25. (Ortiz et. al., 1985). The downhole canister at station W28 is in a material identified as TSw1. The descriptions of these materials are given below:

> TCw - "Moderately to densely welded, devitrified ashflow tuff of the Tiva Canyon Member of the Paintbrush Tuff."

UO - "Alluvium; colluvium; nonwelded, vitric ashflow tuff of he Tiva Canyon Member of the Paintbrush Tuff; any other tuff units that stratigraphically overlie the welded, devitrified Tiva Canyon Member."

TSw1- "Moderately to densely welded, devitrified ashflows of the Topopah Spring Member of the Paintbrush Tuff that contain more than approximately 10%, by volume, lithophysal cavities."

TSw2- "Moderately to densely welded, devitrified ashflows of he Topopah Spring Member of the Paintbrush Tuff that contain less than approximately 10%, by volume, lithophysal cavities." (Potential repository host rock)

Station W29 is located in the general area of the proposed surface facilities. The downhole instrumentation is installed at the alluvium/tuff interface. The stratigraphy at this station is not as well defined as at the deeper holes. For the purposes of this report, the description of the geologic material for both the surface and downhole instrumentation of W29 will be assumed as UO.

Section 2 contains the analyses performed in this study. Conclusions and recommendations are given in Section 3. Appendices A and B contain many of the plots discussed in the text. Appendix C contains a discussion of pseudo-relative velocity response spectrum. Appendix D contains "typical" surface/downhole acceleration time histories from all four Yucca Mountain stations for the Serena event.

Table 1.0-1 Database Used for This Study

Event	Area	Date	Stations W12/30	W25	W28	W29
Cabra	20	3/26/83	x			
Chancellor	19	9/ 1/83	x	x		
Kappeli	20	7/27/84	x	x		
Egmont	20	12/ 9/84		x		
Tierra	19	12/15/84		a	x	
Towanda	19	5/25/85	x	x		x
Salut	20	6/12/85	x	x	x	x
Serena	20	7/25/85	x	x	x	x
Goldstone	20	12/28/85	x	x	x	x
Jefferson	20	4/22/86	x	x	x	x
Labquark	19	9/30/86	x	x	x	x

a. Surface data at this station is questionable

Table 1.0-2 Location of Active Surface/Downhole Stations

Station	Coordinates (Central NV Grid) (m)	Depth (m)	Hole
W12/30	N229,420;E170,231	352	USW GU-3
W25	N234,848;E170,993	358	USW G-1
W28	N237,386;E170,841	368	USW G-2
W29	N232,285;E174,365	82	UE-25 RF4

Figure 1.0-1. Locations of the UNEs Used in This Study With Respect to the General Yucca Mountain Repository Area

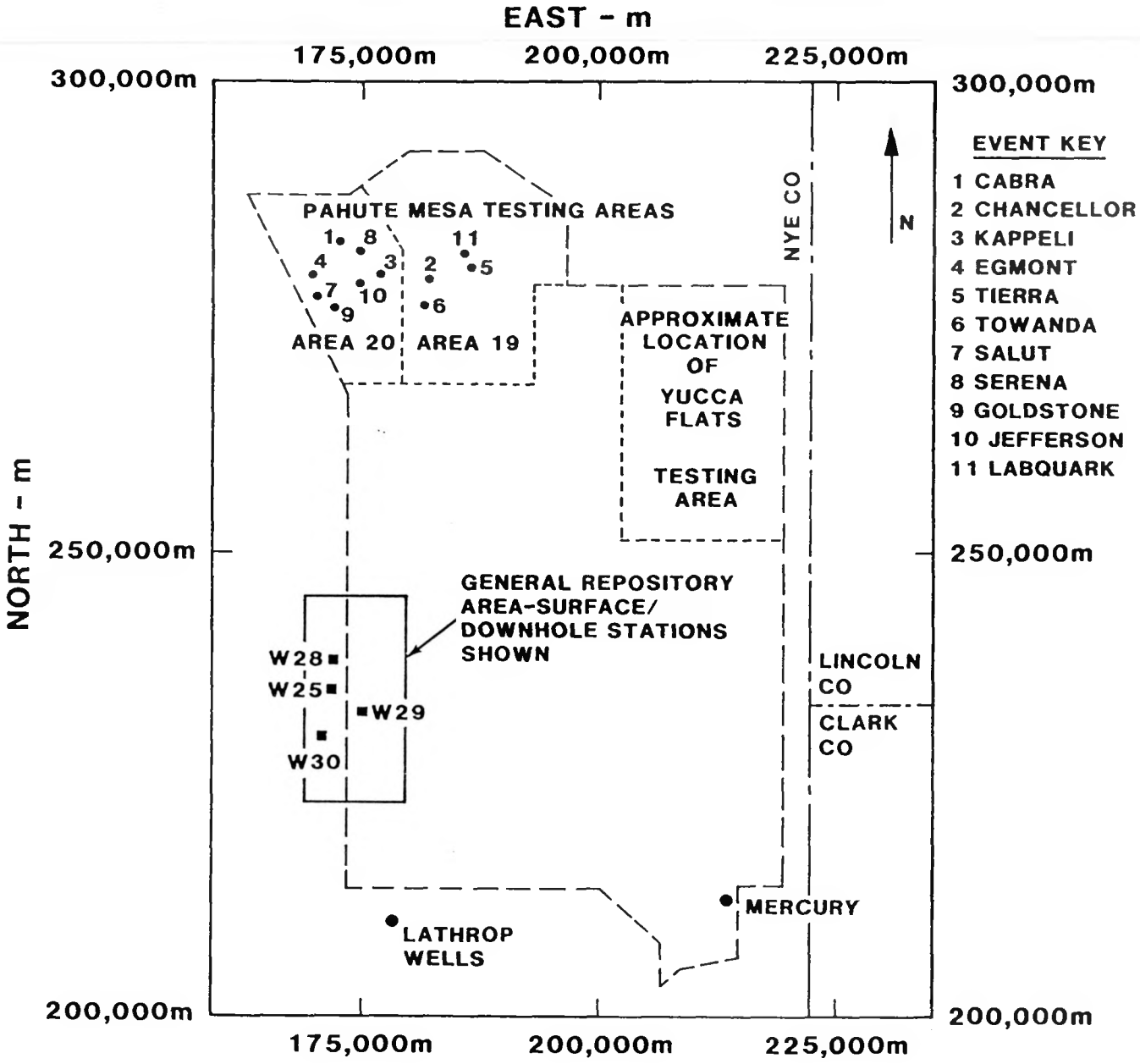

NOTE: COORDINATES SHOWN ARE CENTRAL NEVADA GRID

Figure 1.0-2. Locations of the Active Surface/Downhole Stations With Respect to the Potential Yucca Mountain Repository

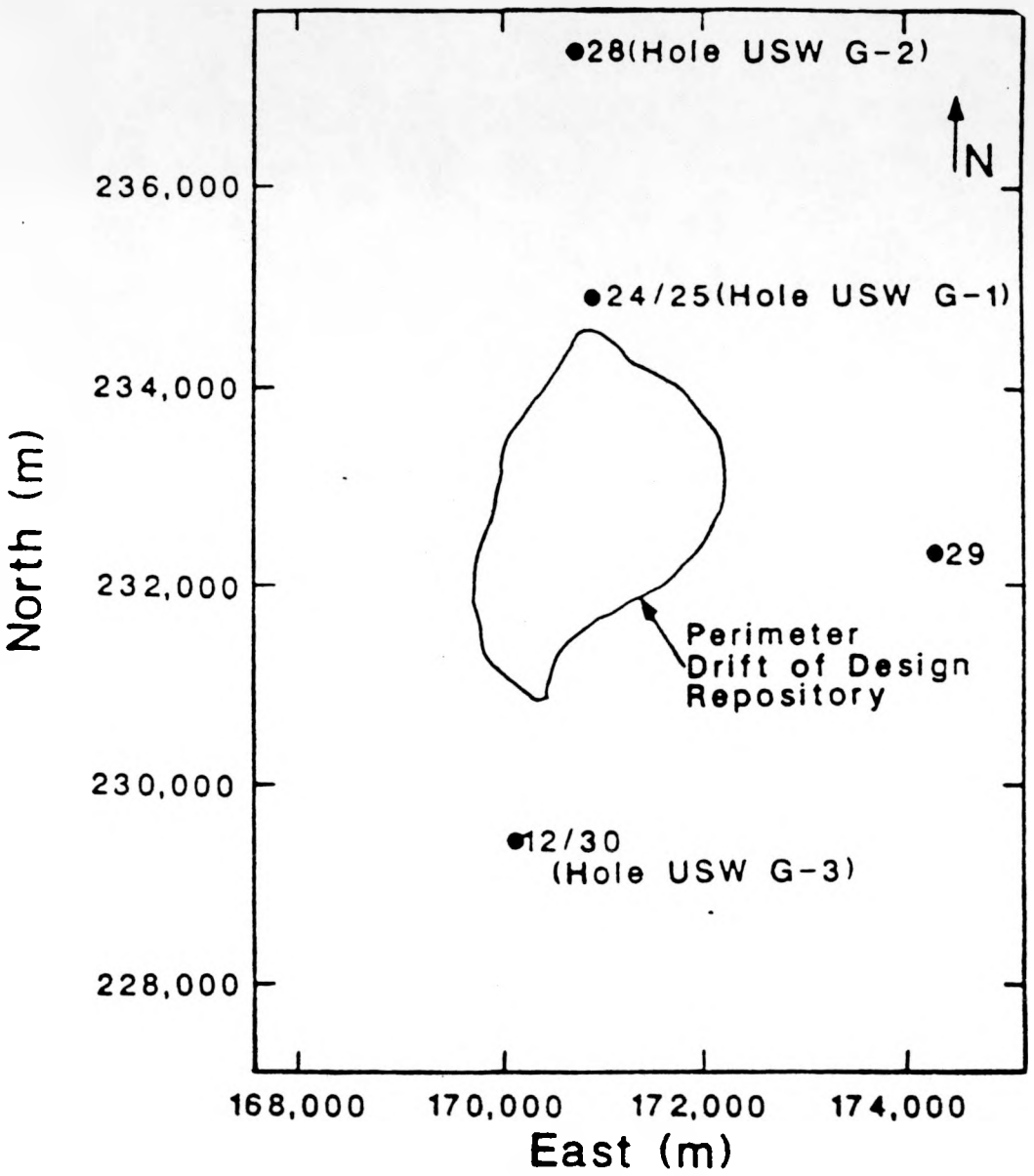

NOTE: COORDINATES SHOWN ARE CENTRAL NEVADA GRID

Figure 1.0-3. Estimated Profile From USW G-2 (Sta. W28) to USW GU-3 (Sta. 30). Approximate Locations of Downhole Canisters Shown as Circles (Ortiz et. al., 1985)

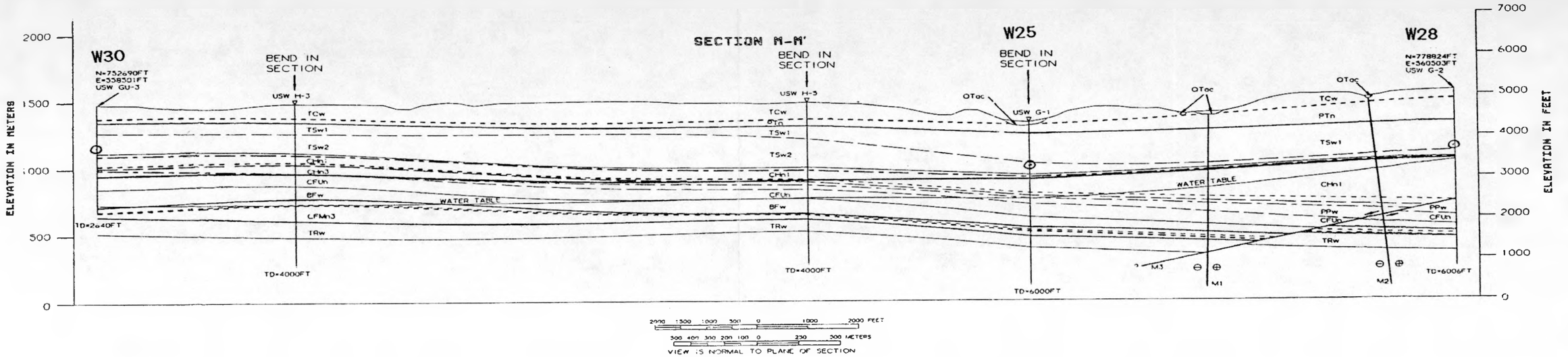

2.0 ANALYSES

2.1 Background

To study the behavior of ground motions with depth, it is useful to review the nature of observed ground motion phenomena. Ground motion at the source-to-station distances included in this data set may be thought of as consisting of two general components. These components are body waves and surface waves. Examples of "typical" body and surface waves observed at Yucca Mountain stations illustrated in Figure 2.1-1. [1] The time histories shown in this figure are the radial acceleration, velocity and displacement from Tierra (a low yield <150 kt event) at the W28 surface station. Also shown in this figure are the power density spectra (PDS) and pseudo relative velocity response (PSRV) spectra[2] calculated for these components.[3] The first arrivals are the body waves. The initial body waves travel at the compressional wave speed of the material and generally produce the largest magnitude accelerations. Other types of body waves arrive after this initial arrival; in most cases, these waves are of lower acceleration amplitude although they may produce the peak velocity amplitude. In general, UNE-induced body wave motions at NTS usually have frequencies between 1 and 20 Hz (Fig. 2.1-1).[4] The amplitude of these motions generally decrease rapidly with depth. The other major component of the ground motion is the surface wave. This motion usually is responsible for the peak displacement observed and may or may not cause the peak velocity. The frequency of this motion is relatively low, usually less than 1 Hz for the UNE motions observed at NTS (Fig. 2.1-1). The amplitude of the surface wave component generally decreases with depth, although at a slower rate than body waves. The theoretical change in amplitude with increasing depth of the surface or Rayleigh wave in an idealized medium is shown in Figure 2.1-2. Note that the vertical and horizontal surface wave components behave differently with increasing depth. For normalized depths (depth of observation divided by wavelength of the surface wave) less than about 0.18 and Poisson ratios 0.33 or less (typical for geologic materials), the amplitude of the vertical component of the surface wave at depth is greater than the amplitude observed at the ground

---

1. Additional "typical" surface/downhole acceleration time histories for each of the 4 Yucca Mountain stations are shown in Appendix D. These time histories are from event Serena.

2. The PSRV is the response of an elastic, single degree of freedom system to a given transient input as a function of the system natural frequency. This is used extensively in seismic design of structures. See Appendix C for more detail on PSRVs.

3. Note, the spectra shown on this figure were calculated from two segments of the acceleration time history. The body wave component was determined from the time history between 0 and 20 s. The surface wave component was determined from the waveform between 20 and 90 s. The amplitude of the spectra shown in this figure have been normalized. This comparison shows that both PDS and PSRV spectra provide the same picture of which frequencies dominate the ground motions. PSRV is more practical for generating predictions for design. The PDS is more useful in modeling applications. The objective of this study is to quantify surface/downhole behavior at Yucca Mountain for the purpose of generating predictions for UNE motions. A broader use of these data is to develop geologic models for stations, as well as travel paths. This broader analysis will be the subject of follow on studies. These analyses will include the use of the spectral ratios to study local station geologic structure.

4. In general, ground motions generated by large yield explosions (>500 kt) have somewhat lower frequency body wave motions than do the lower yield (<150 kt) events.

surface (i.e., the ratio of amplitude at depth to amplitude at surface is greater than 1).

The quantification of surface/downhole (S/D) behavior of UNE ground motion at Yucca Mountain has been the subject of an ongoing analysis effort (Vortman and Long, 1982a, 1982b; and Long et. al., 1983). A brief summary of this work is included here to provide some background and some additional understanding to the current analysis. Vortman and Long (1982a, 1982b) studied the behavior of the three-dimensional peak vector motions various locations around the NTS. The quantities evaluated were ratios of peak surface motion to peak downhole motion, ratios of S/D pseudo relative velocity response spectra and ratios of S/D time histories. This peak motion ratio was calculated for the single maximum peak as well as an average of the maximum 25 peaks in the waveform. These ratios were plotted as a function of depth. An average of the PSRV ratios was taken over the range of frequencies observed and plotted as a function of depth. The time history ratios were used to observe the qualitative behavior of the S/D motions. The major observations from these earlier studies were:

- There was a large variability in the observed ratios, i.e., calculated linear regression equations had low coefficients of determination ($r^2 < 0.6$) indicating poor fits.
- Local station geology played a major role in the observed variability in the behavior at depth.
- The behavior of S/D ratios appeared to be independent of yield in the data analyzed.
- The reduction in amplitude of surface wave motions with depth was minor when compared with the amplitude reduction observed in the body wave motions.

These analyses were done prior to the collection of a fairly large body of S/D data at Yucca Mountain itself and therefore included data from several other station pairs at NTS.

Long et. al. (1983) determined a method to calculate a downhole time history given the surface time history. A least-squares linear prediction method using an optimum finite impulse response filter was used. The method required the determination of the average optimum filter for a number of events recorded at a surface station. This optimum filter was then applied to a surface time history to predict a downhole time history. This method shows promise. However, at the time an insufficient number of events had been recorded at Yucca Mountain for full evaluation.

Following these earlier studies, a requirement for the quantification of the S/D behavior for ground motion component (i.e., vertical, radial and transverse ground motions) behavior specifically at Yucca Mountain emerged (URS/Blume, 1985). The current report addresses this requirement.

This current study was begun by analyzing the ratios of S/D peak motions in the same manner as done by Vortman and Long (1982a, 1982b). Figures 2.1-3 through 2.1-11 show the S/D ratios calculated for the peak component ground

motions plotted versus depth. The ratios and the linear regression equations calculated for the data as plotted are given in Tables 2.1-1 through 2.1-9.[5] The major observation from these tables and figures is the large amount of data scatter and the small values for r^2. (Note that $r^2 = 1$ is a perfect linear correlation and $r^2 = 0$ is no linear correlation.) This scatter is most obvious for stations W25, W28 and W30. These stations are at approximately the same depth (350-368 m) and yet there is a large amount of scatter (as much as a factor of 30 for transverse acceleration - 0.3 at W28 to 9.0 at W25). Predictions generated through the use of these regressions would have very large uncertainties resulting in low confidence.

Based on the scatter of the data noted above and the observation that local station geology is playing a major role in the variability of the S/D ratios (Vortman and Long, 1982a, 1982b), the decision was made to analyze the S/D behavior on an individual station basis rather than the regional basis. In addition, ratios of maximum amplitudes provide an indication of the S/D behavior of a single component. This can produce a misleading result because different components of ground motion (body and surface waves) have different S/D behavior. To further complicate the matter, the absolute maximum amplitudes observed in the waveforms may be the result of any one of these ground motion components. By calculating the ratio of the absolute maximum peak, regardless of the source, the S/D behavior is likely to be obscured by data scatter. Hence, the ratios of S/D PSRV versus frequency were chosen for analysis in the remainder of this study. This quantity has several advantages. First, it provides multiple S/D ratios (i.e., one for each ground motion component represented in the time history) for a particular S/D pair. This will produce a more accurate representation of S/D phenomena because the coefficients are determined for the same ground motion component in the surface and downhole records. Second, the PSRV has the advantage of being an accepted tool for seismic design and is understood by practicing engineers. Thus, when surface ground motion is expressed in terms of a PSRV, the downhole ground motion can be determined by applying the S/D ratio versus frequency to the surface PSRV. Finally, the pertinent ground motion parameters required for structural design can be obtained more efficiently from the PSRV than from a time history.

The PSRVs are calculated from a filtered acceleration time history. In general, these time histories are filtered such that the frequencies less than 0.3 Hz and more than 30 Hz are eliminated from the accelerations. The filters are chosen for each record on every UNE on the basis of a PDS calculated for the noise (approximately 60s prior to arrival) and the PDS calculated for the noise-plus-signal (approximately 120 s). For the majority of the records, the frequency band of the data is from 0.3 to 30 Hz. The acceleration time history is read into the PSRV program that calculates the pseudo velocity response at 48 discrete frequencies between 0.3 and 30 Hz. The results are then plotted in log pseudo velocity versus log frequency space. The PSRVs were calculated with 5% damping. (Plots are usually presented on tripartite graph paper where pseudo acceleration and displacement may also be

---

5. Stations W27 and W24 were included in this initial study. The downhole instrumentation at Station W24 was installed in the same hole as W25, but at a greater depth. W27 was in the same general area as W29. Data from only one event was recorded at both W27 surface and downhole stations and data from two events were recorded at W24. Because of the limited data available from the stations, it was decided not to include them in the subsequent analyses.

determined.) The PSRV data used in this study were manipulated in the following manner. Surface and downhole PSRVs were normalized to the largest value of the two and plotted on the same figure in semi-log space (normalized magnitude vs. log of frequency - referred to as the Relative Normalized PSRV). This provides a convenient way to study the similarity in the shapes and the relative importance of the magnitudes of the surface and downhole PSRVs. Then, the ratio of the S/D PSRV was calculated at each of the 48 frequencies. These ratios were also plotted in semi-log (ratio vs. log frequency) space. Finally, for each component at each station an average ratio was calculated using all data from all events recorded at the station. A separate average and standard deviation was calculated for each of the 48 frequencies. The average ratio and the plus and minus one standard deviations were plotted versus log frequency.

Table 2.1-1 Ratios (Top/Bottom) for 1-Peak Vertical Component Acceleration for Pahute Mesa Events

Event	Plot Symbol	Stations and Depths (ft) W27 (115.)	W29 (271.)	W12(30) (1155.)	W25 (1175.)	W28 (1230.)	W24 (1850.)
CHANCELLOR	○	b	b	1.58	3.55	b	b
CABRA	△	b	b	1.41	b	b	3.68
KAPPELI	◇	1.21	b	1.97	5.15	a	b
SALUT	▽	b	1.62	1.81	4.21	3.16	b
SERENA	□	b	2.13	1.64	4.09	2.37	b
EGMONT	○	a	b	a	3.41	a	b
GIBNE	+	b	b	b	b	b	3.32
TIERRA	×	a	b	a	3.84	2.41	b
TOWANDA	●	b	1.36	1.49	2.85	a	b
NUMBER OF EVENTS		1	3	6	7	3	2
STATION AVERAGE		1.21	1.7	1.65	3.87	2.64	3.5

Fitting equation is $R = 1.383e^{-0.000535\,d}$ $r^2 = 0.341$

where

a = data inadequate

b = station not installed at time of event

R = ratio (top/bottom)

e = Napierian base

d = depth (m)

r^2 = Co-efficient of determination

Table 2.1-2 Ratios (Top/Bottom) for 1-Peak Vertical Component Velocity for Pahute Mesa Events

Event	Plot Symbol	Stations and Depths (ft) W27 (115.)	W29 (271.)	W12(30) (1155.)	W25 (1175.)	W28 (1230.)	W24 (1850.)
CHANCELLOR	○	b	b	1.05	1.47	b	b
CABRA	△	b	b	0.97	b	b	1.32
KAPPELI	◇	1.12	b	1.5	2.74	a	b
SALUT	▽	b	1.15	1.06	1.31	2.06	b
SERENA	□	b	1.09	1.01	1.74	1.33	b
EGMONT	○	a	b	a	1.4	a	b
GIBNE	+	b	b	b	b	b	1.78
TIERRA	×	a	b	a	0.98	1.21	b
TOWANDA	●	b	1.13	0.99	1.1	a	b
NUMBER OF EVENTS		1	3	6	7	3	2
STATION AVERAGE		1.12	1.12	1.1	1.53	1.53	1.55

Fitting equation is $R = 1.061e^{-0.000208\,d}$ $r^2 \leq 0.315$

where

a = data inadequate

b = station not installed at time of event

R = ratio (top/bottom)

e = Napierian base

d = depth (m)

r^2 = Co-efficient of determination

Table 2.1-3 Ratios (Top/Bottom) for 1-Peak Vertical Component Displacement for Pahute Mesa Events

Event	Plot Symbol	Stations and Depths (ft) W27 (115.)	W29 (271.)	W12(30) (1155.)	W25 (1175.)	W28 (1230.)	W24 (1850.)
CHANCELLOR	○	b	b	1.02	1.1	b	b
CABRA	△	b	b	0.97	b	b	1.17
KAPPELI	◇	0.99	b	1	1.11	a	b
SALUT	▽	b	1.05	0.98	1.08	1.08	b
SERENA	□	b	1.04	1.02	1.13	1.09	b
EGMONT	○	a	b	a	1.13	a	b
GIBNE	+	b	b	b	b	b	1.14
TIERRA	×	a	b	a	0.85	1.04	b
TOWANDA	●	b	1.02	0.98	1.08	a	b
NUMBER OF EVENTS		1	3	6	7	3	2
STATION AVERAGE		0.99	1.03	0.99	1.07	1.07	1.16

Fitting equation is $R = 0.985e^{-0.000057\,d}$ $r^2 = 0.312$

where

a = data inadequate

b = station not installed at time of event

R = ratio (top/bottom)

e = Napierian base

d = depth (m)

r^2 = Co-efficient of determination

Table 2.1-4 Ratios (Top/Bottom) for 1-Peak Radial Component Acceleration for Pahute Mesa Events

Event	Plot Symbol	Stations and Depths (ft) W27 (115.)	W29 (271.)	W12(30) (1155.)	W25 (1175.)	W28 (1230.)	W24 (1850.)
CHANCELLOR	○	b	b	1.03	2.7	b	b
CABRA	△	b	b	1.24	b	b	2.74
KAPPELI	◇	1.36	b	1.06	4.45	a	b
SALUT	▽	b	2.09	1.7	3.67	1.04	b
SERENA	□	b	2.23	1.34	3.31	0.66	b
EGMONT	○	a	b	a	4.49	a	b
GIBNE	+	b	b	b	b	b	9.58
TIERRA	×	a	b	a	4.83	0.6	b
TOWANDA	●	b	1.23	1.49	3.94	a	b
NUMBER OF EVENTS		1	3	6	7	3	2
STATION AVERAGE	▶	1.36	1.85	1.31	3.91	0.77	6.16

Fitting equation is $R = 1.221e^{-0.000503\,d}$ $r^2 \leq 0.112$

where

a = data inadequate

b = station not installed at time of event

R = ratio (top/bottom)

e = Napierian base

d = depth (m)

r^2 = Co-efficient of determination

Table 2.1-5 Ratios (Top/Bottom) for 1-Peak Radial Component Velocity for Pahute Mesa Events

Event	Plot Symbol	Stations and Depths (ft) W27 (115.)	W29 (271.)	W12(30) (1155.)	W25 (1175.)	W28 (1230.)	W24 (1850.)
CHANCELLOR	○	b	b	1.42	2.22	b	b
CABRA	△	b	b	1.77	b	b	2.07
KAPPELI	◇	1.04	b	1.66	2.25	a	b
SALUT	▽	b	1.22	1.59	3.3	2.89	b
SERENA	□	b	1.16	1.39	2.65	2.23	b
EGMONI	○	a	b	a	3.05	a	b
GIBNE	+	b	b	b	b	b	1.77
TIERRA	×	a	b	a	2.56	2.07	b
TOWANDA	●	b	1.12	1.83	2.32	a	b
NUMBER OF EVENTS		1	3	6	7	3	2
STATION AVERAGE	▶	1.04	1.17	1.61	2.62	2.4	1.92

Fitting equation is $R = 1.140e^{-0.000475\,d}$ $r^2 \leq 0.453$

where

a = data inadequate

b = station not installed at time of event

R = ratio (top/bottom)

e = Napierian base

d = depth (m)

r^2 = Co-efficient of determination

Table 2.1-6 Ratios (Top/Bottom) for 1-Peak Radial Component Displacement for Pahute Mesa Events

Event	Plot Symbol	Stations and Depths (ft) W27 (115.)	W29 (271.)	W12(30) (1155.)	W25 (1175.)	W28 (1230.)	W24 (1850.)
CHANCELLOR	○	b	b	1.42	1.55	b	b
CABRA	△	b	b	1.61	b	b	1.68
KAPPELI	◇	0.85	b	1.64	2.63	a	b
SALUT	▽	b	1.22	1.66	1.72	2.14	b
SERENA	□	b	1.09	1.15	2.98	1.93	b
EGMONT	◯	a	b	a	2.32	a	b
GIBNE	+	b	b	b	b	b	0.95
TIERRA	×	a	b	a	2.78	1.5	b
TOWANDA	●	b	1.1	1.81	2.45	a	b
NUMBER OF EVENTS		1	3	6	7	3	2
STATION AVERAGE	▶	0.85	1.14	1.55	2.35	1.86	1.31

Fitting equation is $R = 1.155e^{-0.000343\,d}$ $r^2 \leq 0.264$

where

a = data inadequate

b = station not installed at time of event

R = ratio (top/bottom)

e = Napierian base

d = depth (m)

r^2 = Co-efficient of determination

Table 2.1-7 Ratios (Top/Bottom) for 1-Peak Transverse Component Acceleration for Pahute Mesa Events

Event	Plot Symbol	Stations and Depths (ft) W27 (115.)	W29 (271.)	W12(30) (1155.)	W25 (1175.)	W28 (1230.)	W24 (1850.)
CHANCELLOR	○	b	b	3.37	8.22	b	b
CABRA	△	b	b	1.99	b	b	7.85
KAPPELI	◇	1.68	b	2.11	5.34	a	b
SALUT	▽	b	1.44	1.97	4.79	1.11	b
SERENA	□	b	1.47	2.34	9.01	0.61	b
EGMONT	○	a	b	a	7.58	a	b
GIBNE	+	b	b	b	b	b	2.72
TIERRA	×	a	b	a	7.82	0.3	b
TOWANDA	●	b	1.37	2.2	4.16	a	b
NUMBER OF EVENTS		1	3	6	7	3	2
STATION AVERAGE		1.68	1.43	2.33	6.7	0.67	5.29

Fitting equation is $R = 1.300e^{-0.000697\ d}$ $r^2 = 0.147$

where

a = data inadequate

b = station not installed at time of event

R = ratio (top/bottom)

e = Napierian base

d = depth (m)

r^2 = Co-efficient of determination

Table 2.1-8 Ratios (Top/Bottom) for 1-Peak Transverse Component Velocity for Pahute Mesa Events

Event	Plot Symbol	Stations and Depths (ft) W27 (115.)	W29 (271.)	W12(30) (1155.)	W25 (1175.)	W28 (1230.)	W24 (1850.)
CHANCELLOR	○	b	b	1.79	3.28	b	b
CABRA	△	b	b	1.08	b	b	2.11
KAPPELI	◇	1.07	b	1.21	1.44	a	b
SALUT	▽	b	1.15	2.1	2.18	2.47	b
SERENA	□	b	1.13	1.27	1.66	2.12	b
EGMONT	○	a	b	a	1.88	a	b
GIBNE	+	b	b	b	b	b	2.5
TIERRA	×	a	b	a	1.56	1.3	b
TOWANDA	●	b	1.15	1.7	1.48	a	b
NUMBER OF EVENTS		1	3	6	7	3	2
STATION AVERAGE		1.07	1.14	1.53	1.93	1.96	2.3

Fitting equation is $R = 1.017e^{-0.000465\,d}$ $r^2 \doteq 0.829$

where

a = data inadequate

b = station not installed at time of event

R = ratio (top/bottom)

e = Napierian base

d = depth (m)

r^2 = Co-efficient of determination

Table 2.1-9 Ratios (Top/Bottom) for 1-Peak Transverse Component Displacement for Pahute Mesa Events

Event	Plot Symbol	Stations and Depths (ft) W27 (115.)	W29 (271.)	W12(30) (1155.)	W25 (1175.)	W28 (1230.)	W24 (1850.)
CHANCELLOR	○	b	b	1.33	1.43	b	b
CABRA	△	b	b	1.09	b	b	1.89
KAPPELI	◇	1.06	b	1.21	1.05	a	b
SALUT	▽	b	1.05	1.86	1.64	1.94	b
SERENA	□	b	1.04	1.17	1.17	1.51	b
EGMONT	○	a	b	a	1.51	a	b
GIBNE	+	b	b	b	b	b	2.58
TIERRA	×	a	b	a	1.05	1.42	b
TOWANDA	●	b	1.09	1.46	1.38	a	b
NUMBER OF EVENTS		1	3	6	7	3	2
STATION AVERAGE		1.06	1.06	1.35	1.32	1.62	2.24

Fitting equation is $R = 0.906e^{-0.000392\,d}$ $r^2 = 0.782$

where

a = data inadequate

b = station not installed at time of event

R = ratio (top/bottom)

e = Napierian base

d = depth (m)

r^2 = Co-efficient of determination

Figure 2.1-1 Typical Ground Motions and Their Frequency Content

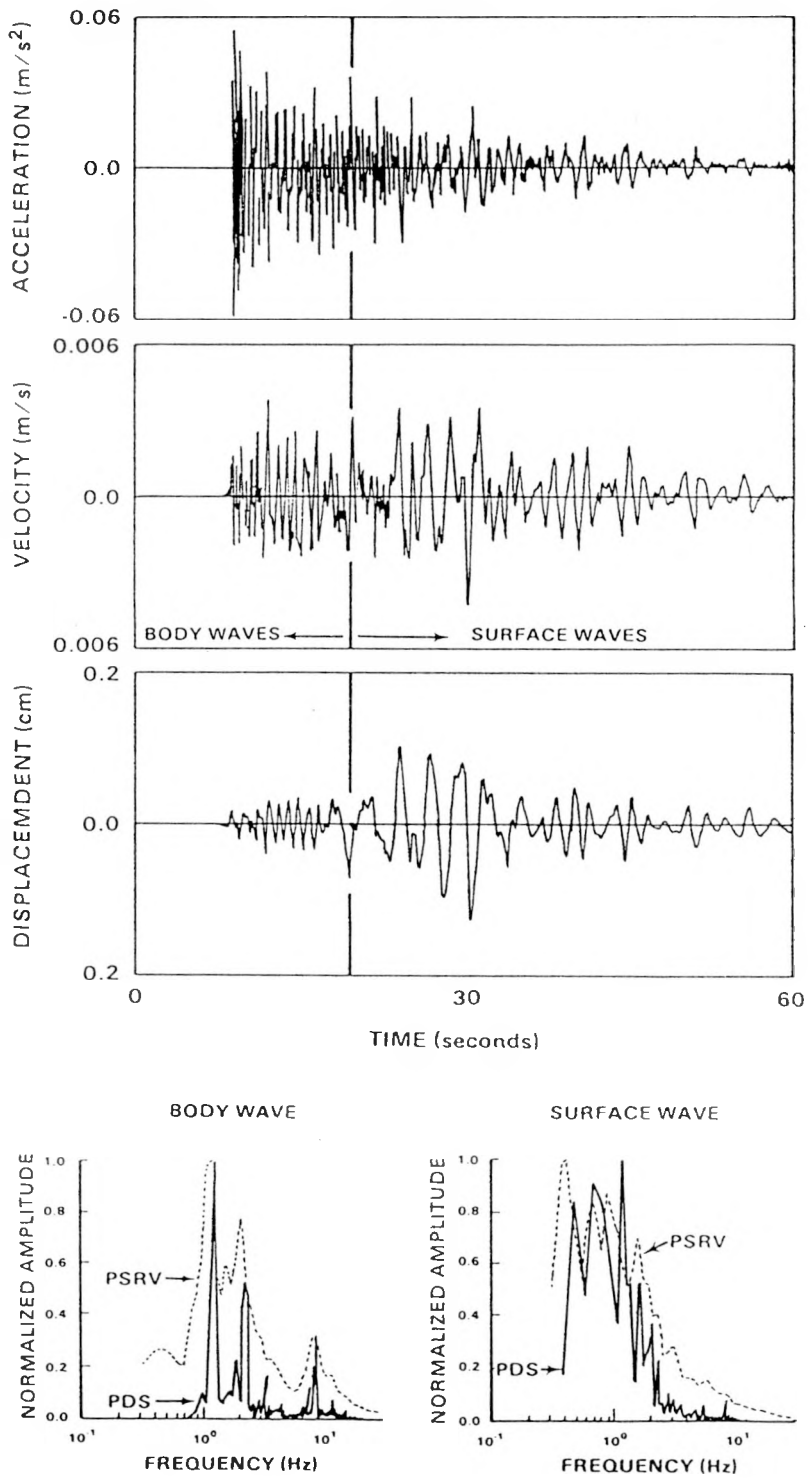

Figure 2.1-2. Theoretical Surface/downhole behavior of Rayleigh Waves as a Function of Normalized Depth and Poisson's Ratio(ν) (Richart et. al., 1970)

NOTE: Approximate Z/LR ratios for data used in this study are 0.1 or less.

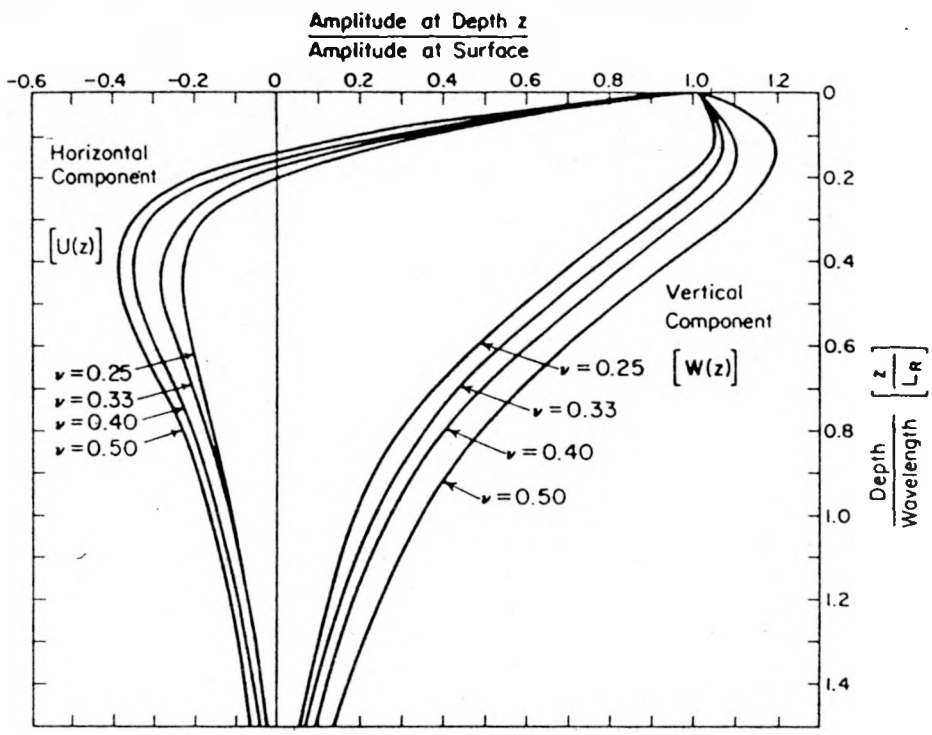

Figure 2.1-3. Ratios (Top/Bottom) for 1-Peak Vertical Component Acceleration for Pahute Mesa Events Plotted vs. Station Depth

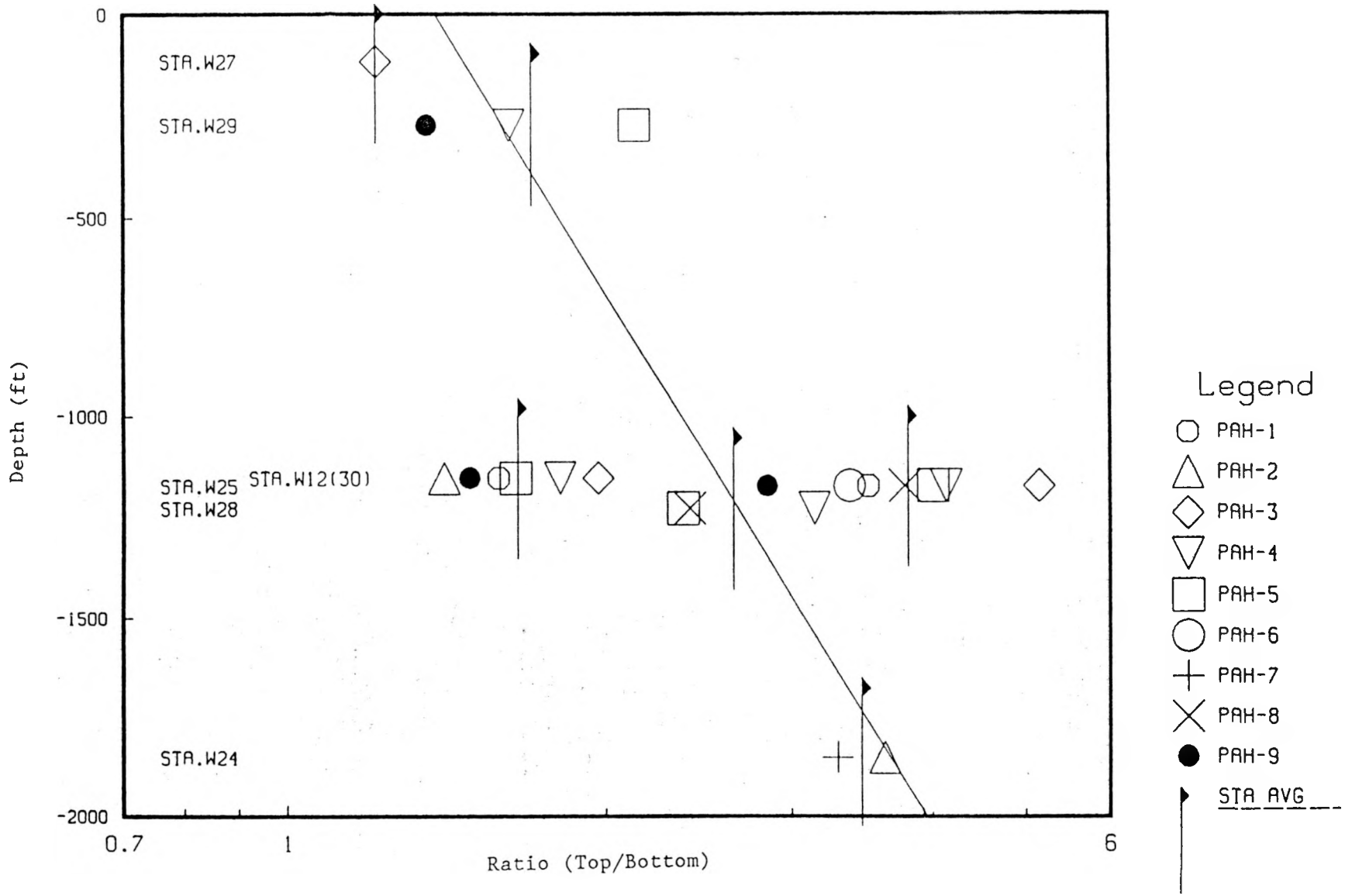

Figure 2.1-4. Ratios (Top/Bottom) for 1-Peak Vertical Component Velocity for Pahute Mesa Events Plotted vs. Station Depth

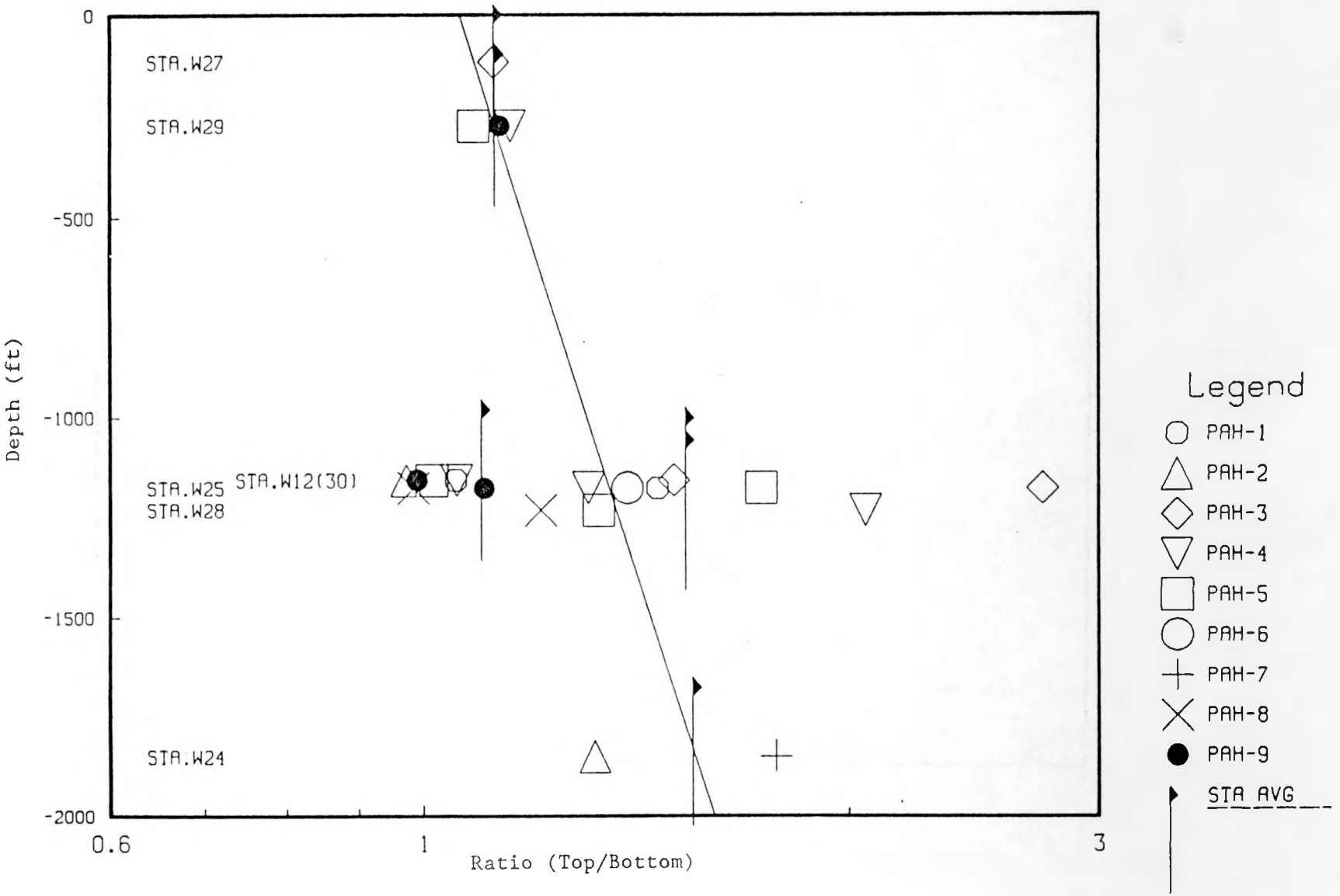

Figure 2.1-5. Ratios (Top/Bottom) for 1-Peak Vertical Component Displacement for Pahute Mesa Events Plotted vs. Station Depth

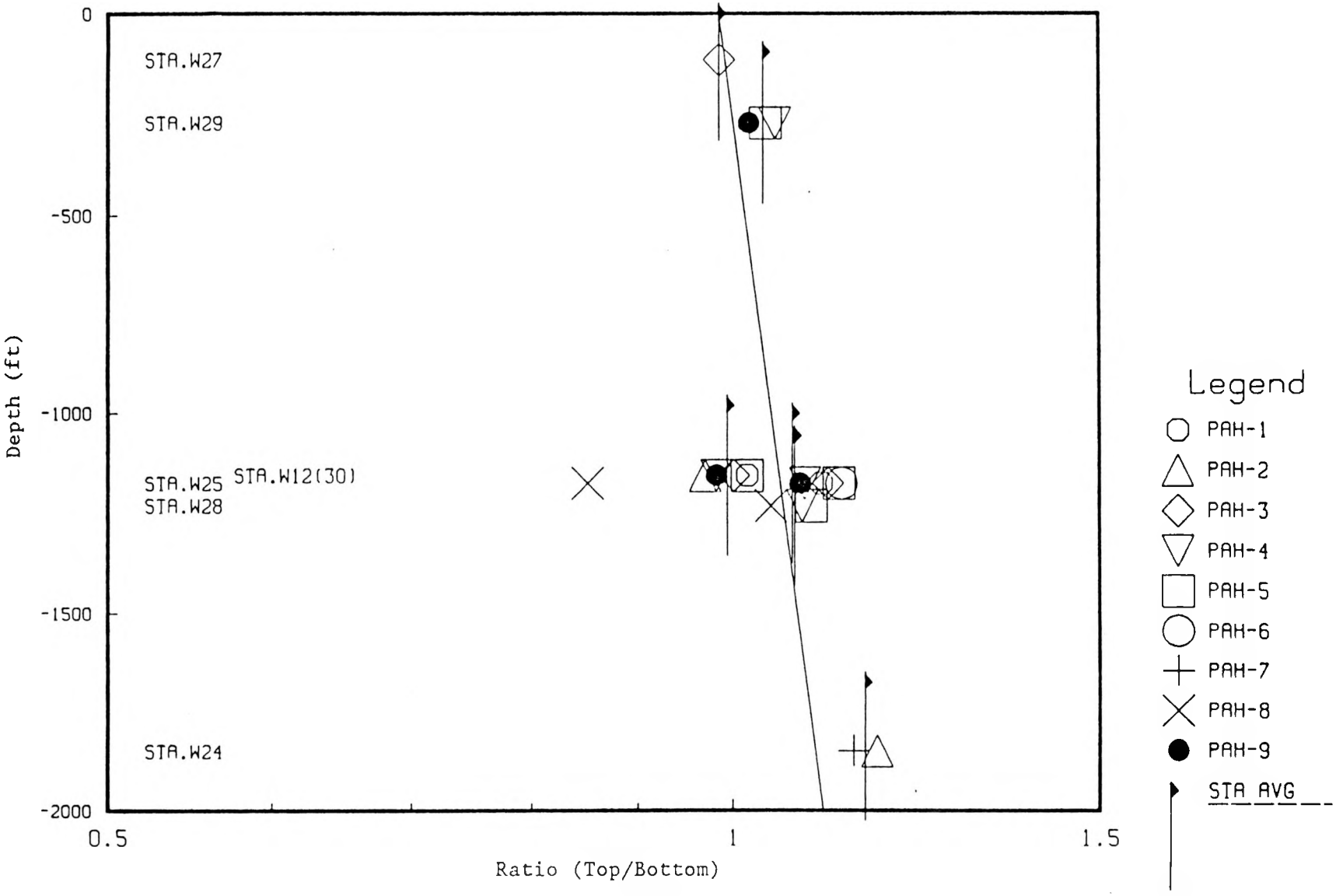

Figure 2.1-6. Ratios (Top/Bottom) for 1-Peak Radial Component Acceleration for Pahute Mesa Events Plotted vs. Station Depth

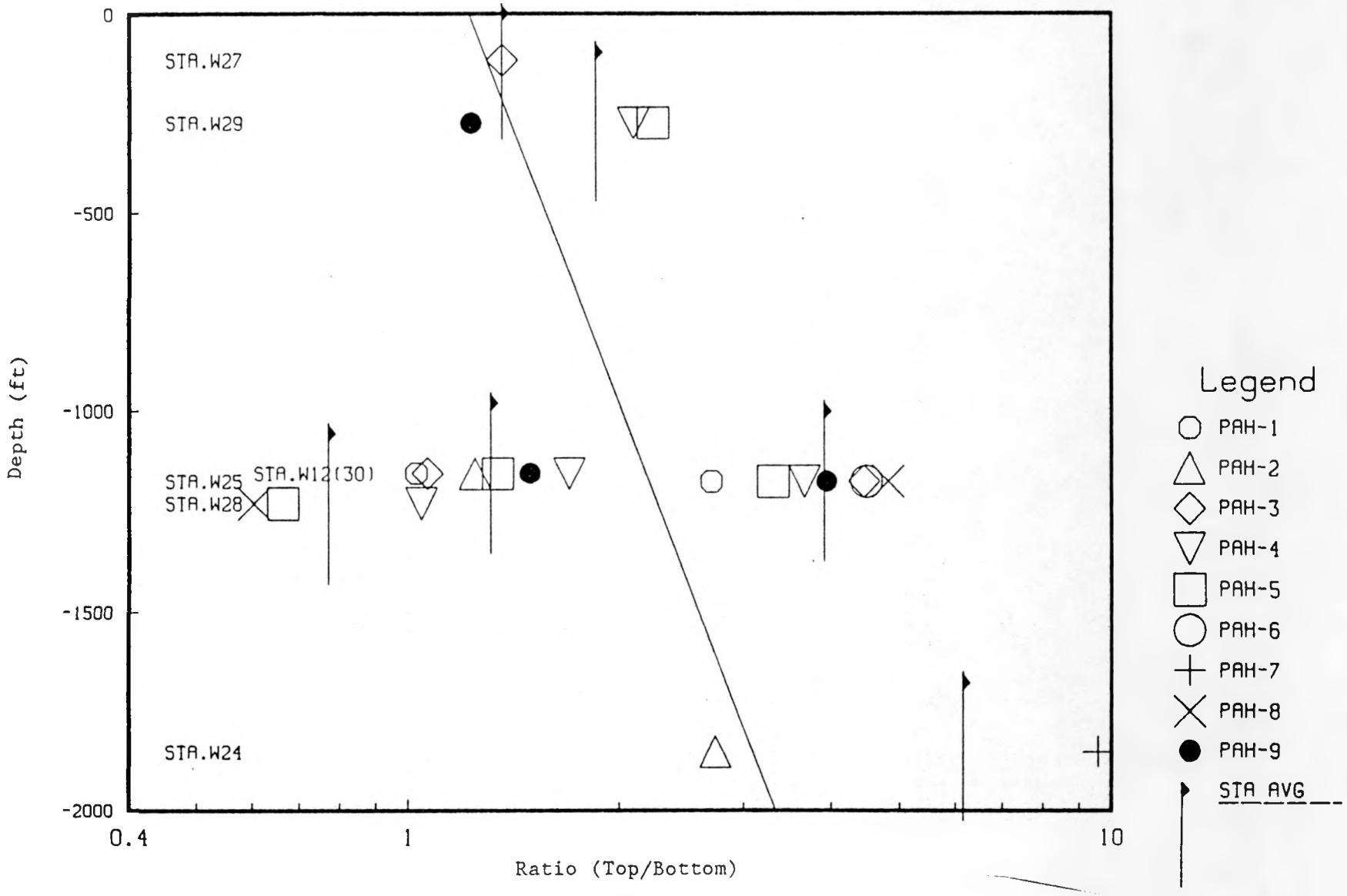

Figure 2.1-7. Ratios (Top/Bottom) for 1-Peak Radial Component Velocity for Pahute Mesa Events Plotted vs. Station Depth

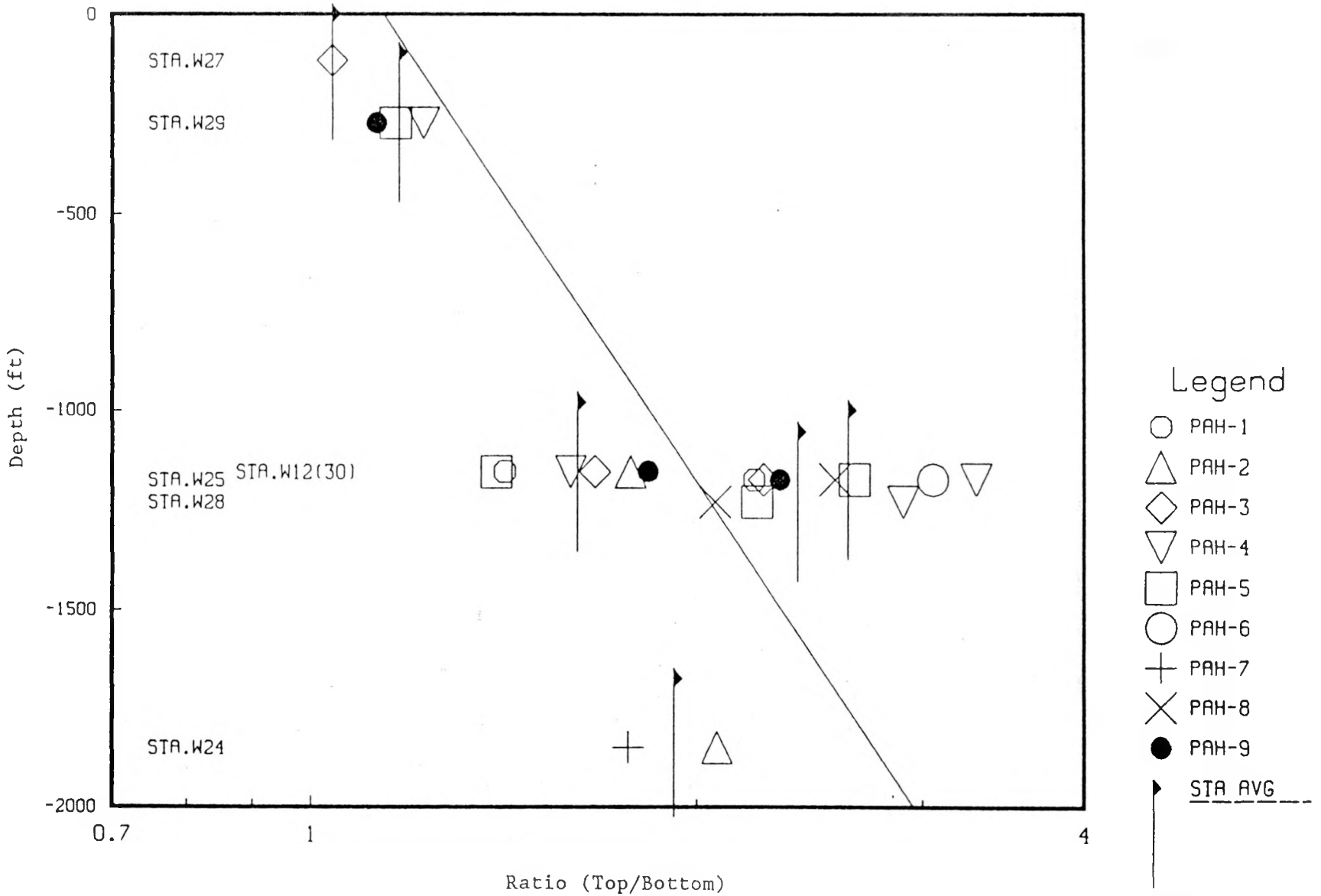

Figure 2.1-8. Ratios (Top/Bottom) for 1-Peak Radial Component Displacement for Pahute Mesa Events Plotted vs. Station Depth

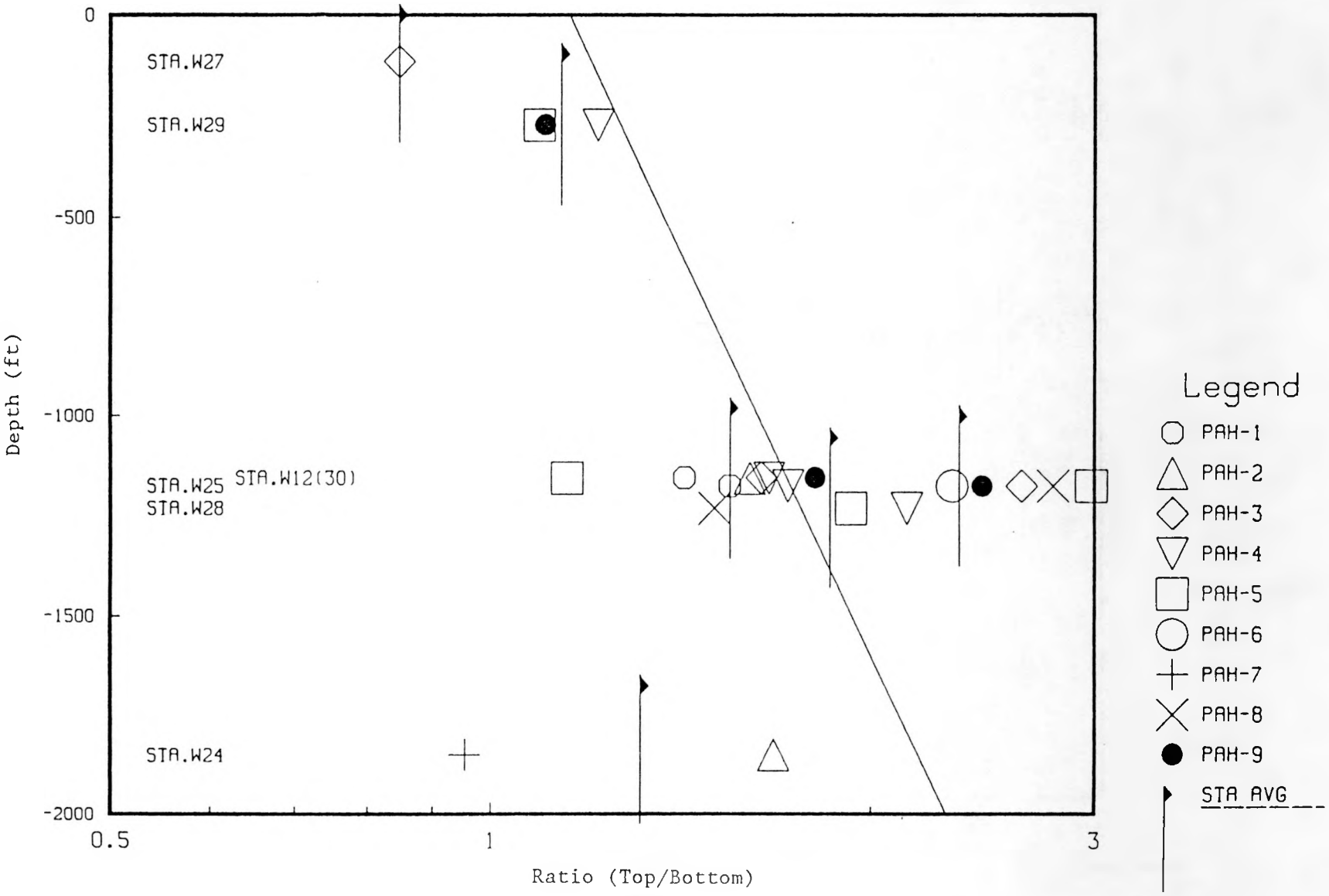

Figure 2.1-9. Ratios (Top/Bottom) for 1-Peak Transverse Component Acceleration for Pahute Mesa Events Plotted vs. Station Depth

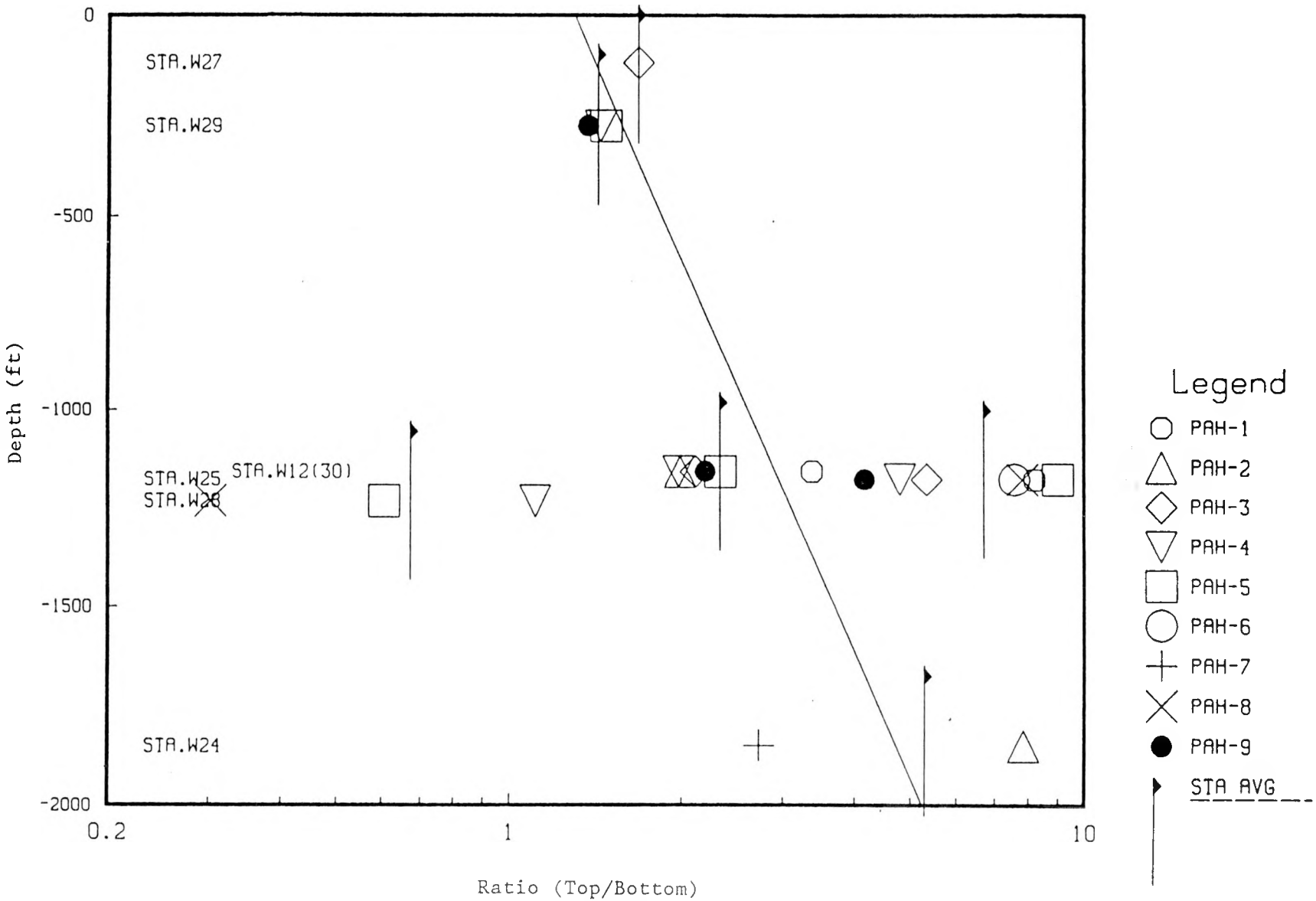

Figure 2.1-10. Ratios (Top/Bottom) for 1-Peak Transverse Component Velocity for Pahute Mesa Events Plotted vs. Station Depth

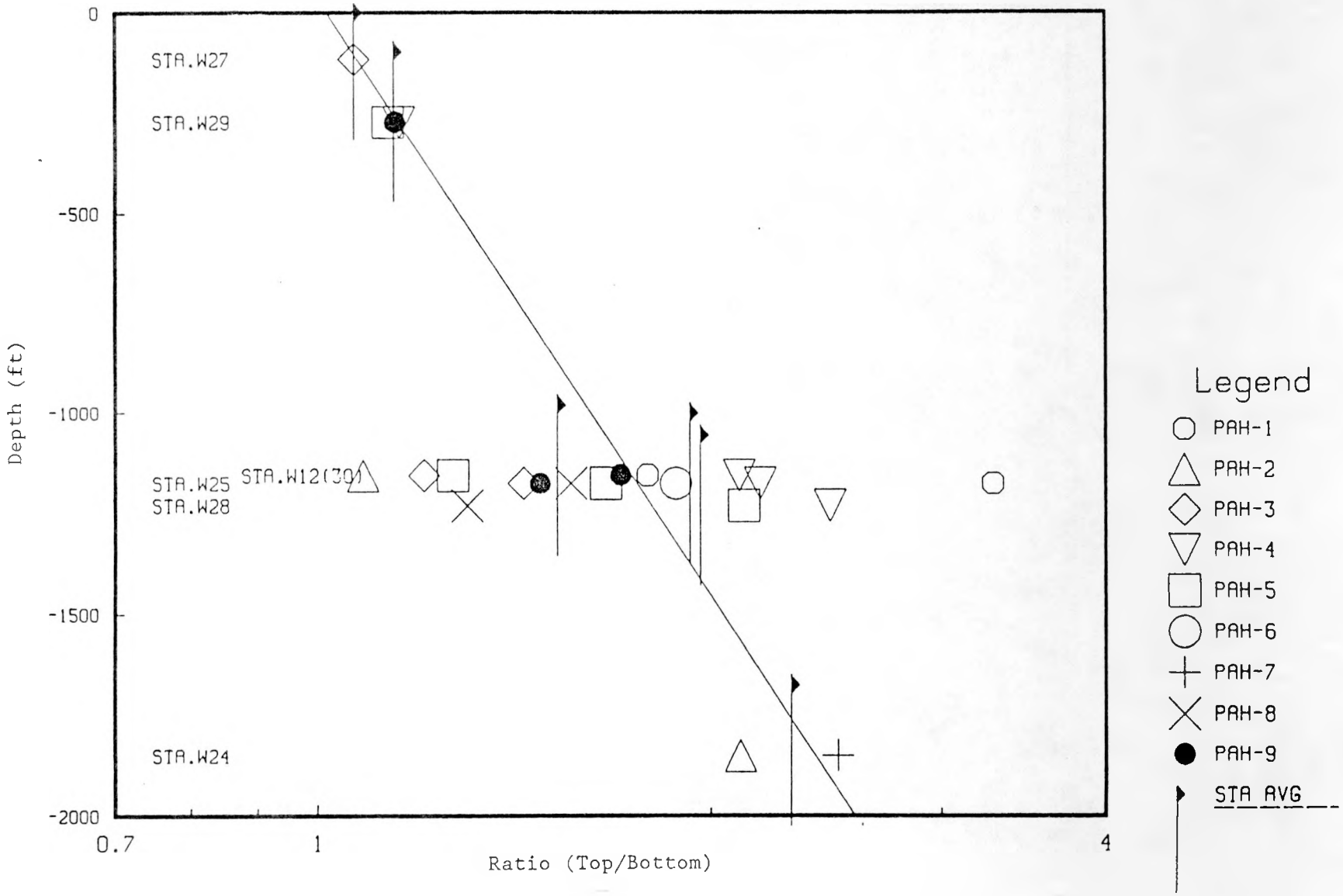

Figure 2.1-11. Ratios (Top/Bottom) for 1-Peak Transverse Component Displacement for Pahute Mesa Events Plotted vs. Station Depth

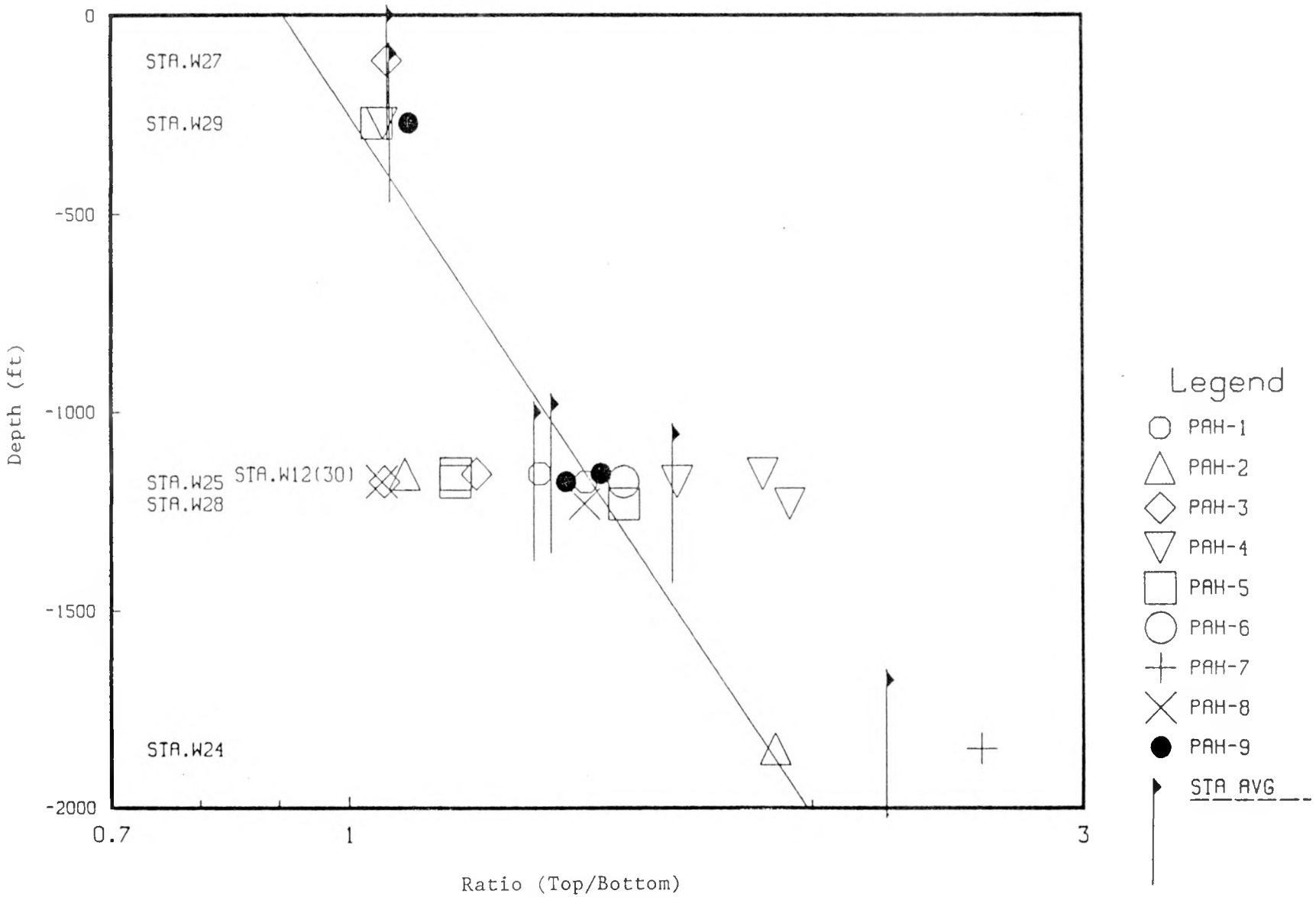

2.2 Presentation of Data and Observations

The PSRVs presented in this report were calculated from data that have been filtered. As a matter of convenience, the data presented is plotted from 0.1 to 100 Hz. The observations and conclusions only apply between 0.3 and 30 Hz.

The relative normalized PSRVs and ratios of S/D PSRVs are shown in Figures A.1 through A.90 in Appendix A. A review of these figures leads to the general observations listed below:

- The amplitude of downhole motions is generally less than the amplitude of the surface motions.
- The frequency content of a S/D pair is similar. Frequency content varies from component to component and station to station.
- The amplitude reduction of the higher frequency body wave motions is greater than the amplitude reduction observed in the surface wave motions.
- S/D ratios for vertical surface wave motions are approximately 1. Radial and transverse surface wave S/D ratios are greater than those calculated for the vertical component, but the S/D ratio is still generally less than 2.5 (an amplitude reduction factor of 0.4). This behavior agrees with the theoretical curves shown in Figure 2.1-2, (e.g., Event Labquark, station W25, Figures A.1, A.10 and A.19 -- the ratio of the depth of the station and the wavelength is between 0.07 and 0.1; assuming a Poisson ratio of 0.25, the amplitude reduction factors are 1 for vertical motion and 0.4 for horizontal motion).
- The radial and transverse components have larger S/D ratios for both surface and body waves than the vertical component.

In addition to these general observations, the S/D behavior at each station, which provides an indication of the event-to-event variability, is briefly summarized below. Finally, the average S/D ratios from each station are compared to show the observed station-to-station variability.

2.2.1 Station W25

Of all stations, station W25 had the largest S/D ratios. Recall that this station is intermediate, in terms of distance from Pahute Mesa, relative to the other stations. The average ratios of S/D PSRVs for the vertical, radial and transverse components are shown in Figure 2.2-1.

The ratios of S/D transverse PSRVs have a different behavior than the other two components at this station. After the initial increase in ratios at about 1 Hz, the ratios rapidly increase and maintain a relatively constant ratio of about 8. The standard deviations calculated for these averages are about the same as those calculated for the radial component.

The ratios calculated for the vertical component (Fig. 2.2-1) show significant reduction (increase in S/D ratio) in the observed downhole values

after a frequency of about 1.5 Hz. The ratios increase to a maximum of about 6 at a frequency of 10 Hz. At frequencies greater than 10 Hz, the ratios drop off rapidly to a constant value of about 4. Plus and minus one standard deviations (± 1 σ) shown for the vertical component (indicated as the dotted lines on Fig. 2.2-1) are relatively close to the average, indicating that the arithmetic average of the individual ratios is an accurate measure of the attenuation for this suite of events at this station.

The radial component S/D PSRV ratios show a somewhat similar behavior. The main differences are that the frequencies are shifted relative to the vertical component (the maximum ratio of 5.4 occurs at a lower frequency of about 3 Hz) and the ± 1 σ limits are greater. (The average still appears to be a reasonably accurate way to describe the attenuation behavior at this station, however.)

2.2.2 Station W28

This station is located the closest to Pahute Mesa. The amplitude reduction in downhole motions at Station W28 was the second highest in the group. The average S/D PSRV ratios are shown in Figure 2.2-2. Generally the ratios for all three components increase to a maximum value between 1 and 2 Hz (transverse - maximum of 4.3 at 1.1 Hz; vertical - maximum of 4.5 at 1.9 Hz; radial - maximum of 5.1 at 1.7 Hz) and decrease to a relatively low level for the remainder of the frequencies. The ± 1 σ bounds shown on these figures continue to indicate that the arithmetic average is an accurate representation of the attenuation phenomena. There is an unusual behavior present in the radial and transverse components at frequencies greater than 8 Hz. The S/D ratios become less than one at these frequencies, indicating that downhole motions are becoming larger than the surface values. This behavior will be discussed in more detail in a later section.

2.2.3 Station W29

The average S/D ratios calculated for W29 are shown in Figure 2.2-3. This station has the shallowest downhole station (82 m) in the group and predictably it has the least amount of amplitude reduction (smallest ratios) of the entire group (transverse - maximum of 2.1 at 4.2 Hz; vertical - maximum of 2.3 at 10.1 Hz; radial - maximum of 2.8 at 3.3 Hz). The ± 1 σ bounds are somewhat greater than for the other stations, but the use of the average ratio to describe the attenuation behavior at the station is still supported.

2.2.4 Station W30

The average S/D PSRV ratios for this station are shown in Figure 2.2-4. This station has the least amount of amplitude reduction in the downhole motions of the deep stations. This station is also the greatest distance away from the Pahute Mesa testing area. The maximum ratio calculated for the vertical component was 2.8 at a frequency of 2 Hz. The radial component had a maximum s/d ratio of 2.6 at 1.6 Hz and the transverse component had a maximum ratio of 3.2 at 7.8 Hz. The ± 1 σ bounds are generally small, as was the case for the other stations.

2.2.5 Station Averages

Figure 2.2-5 shows the comparison of the average S/D PSRV ratios calculated for each of the four downhole stations. This figure illustrates the variability both in amount of amplitude reduction at each station, as well as, the variability in frequency content at each station. It is clear from this figure that development of a regional model for the prediction of S/D behavior will require additional analyses beyond the scope of this effort.

Figure 2.2-1. Average Ratios of S/D PSRVs Calculated for Station W25

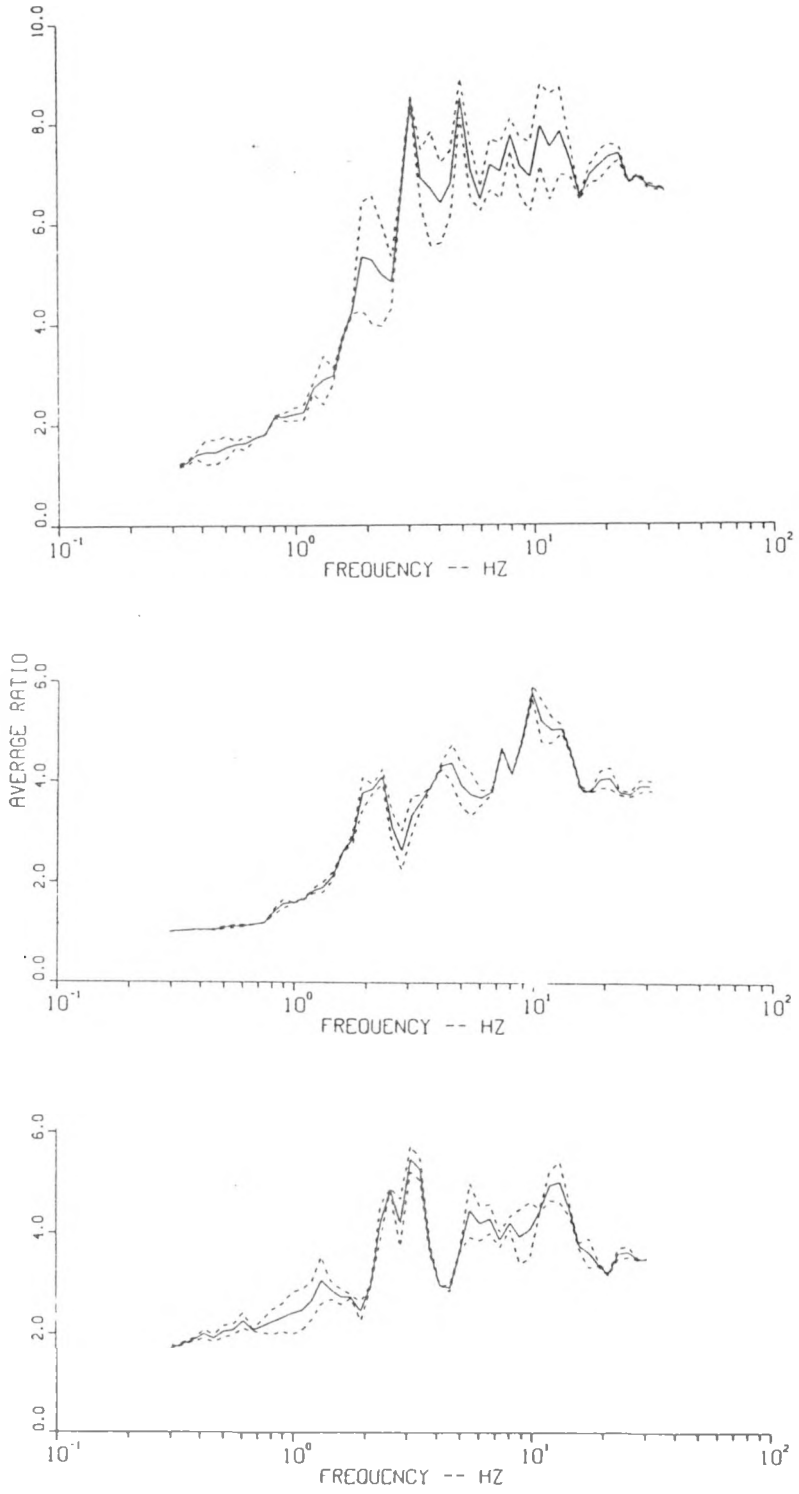

Figure 2.2-2. Average Ratios of S/D PSRVs Calculated for Station W28

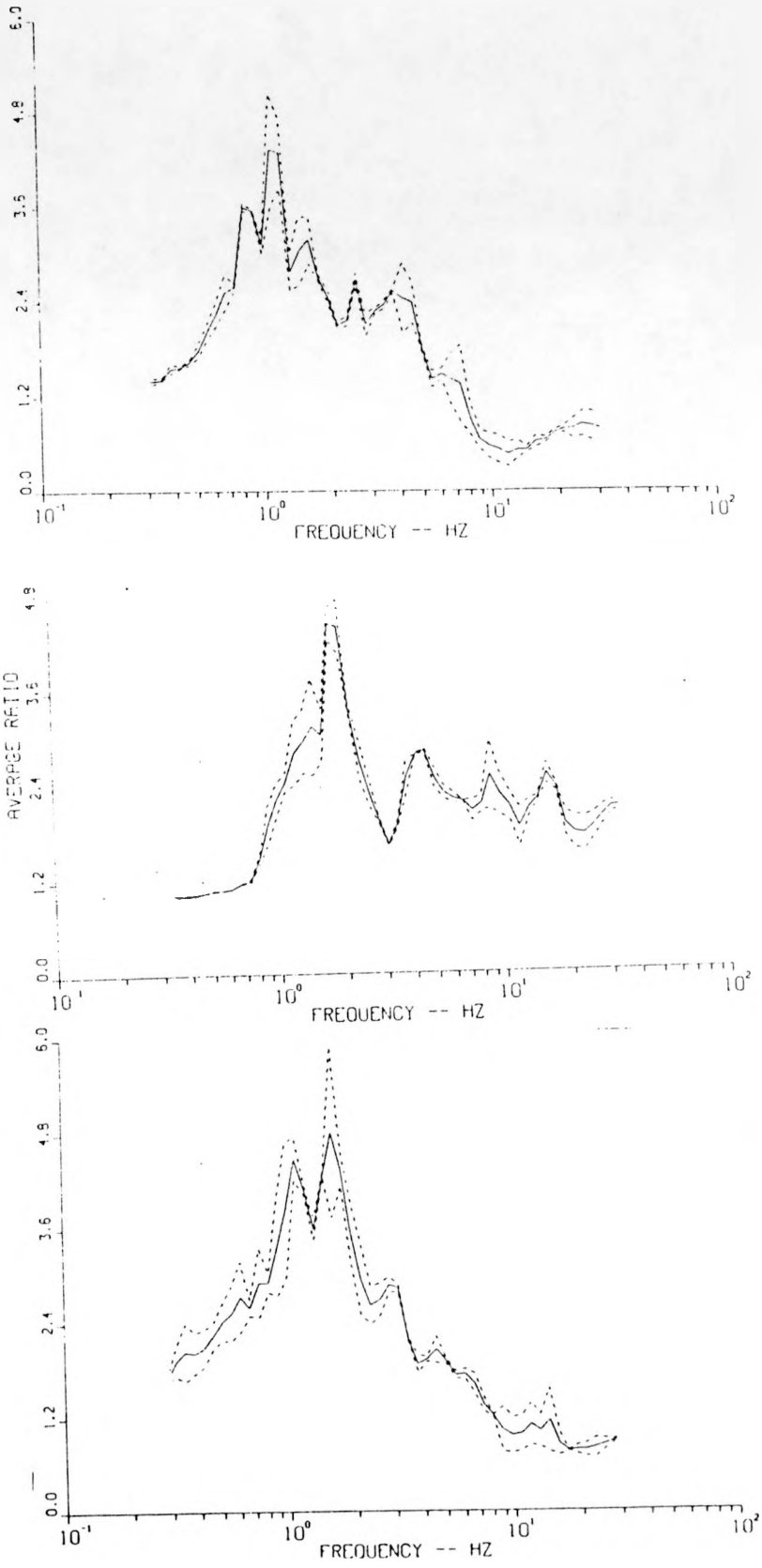

Figure 2.2-3. Average Ratios of S/D PSRVs Calculated for Station W29

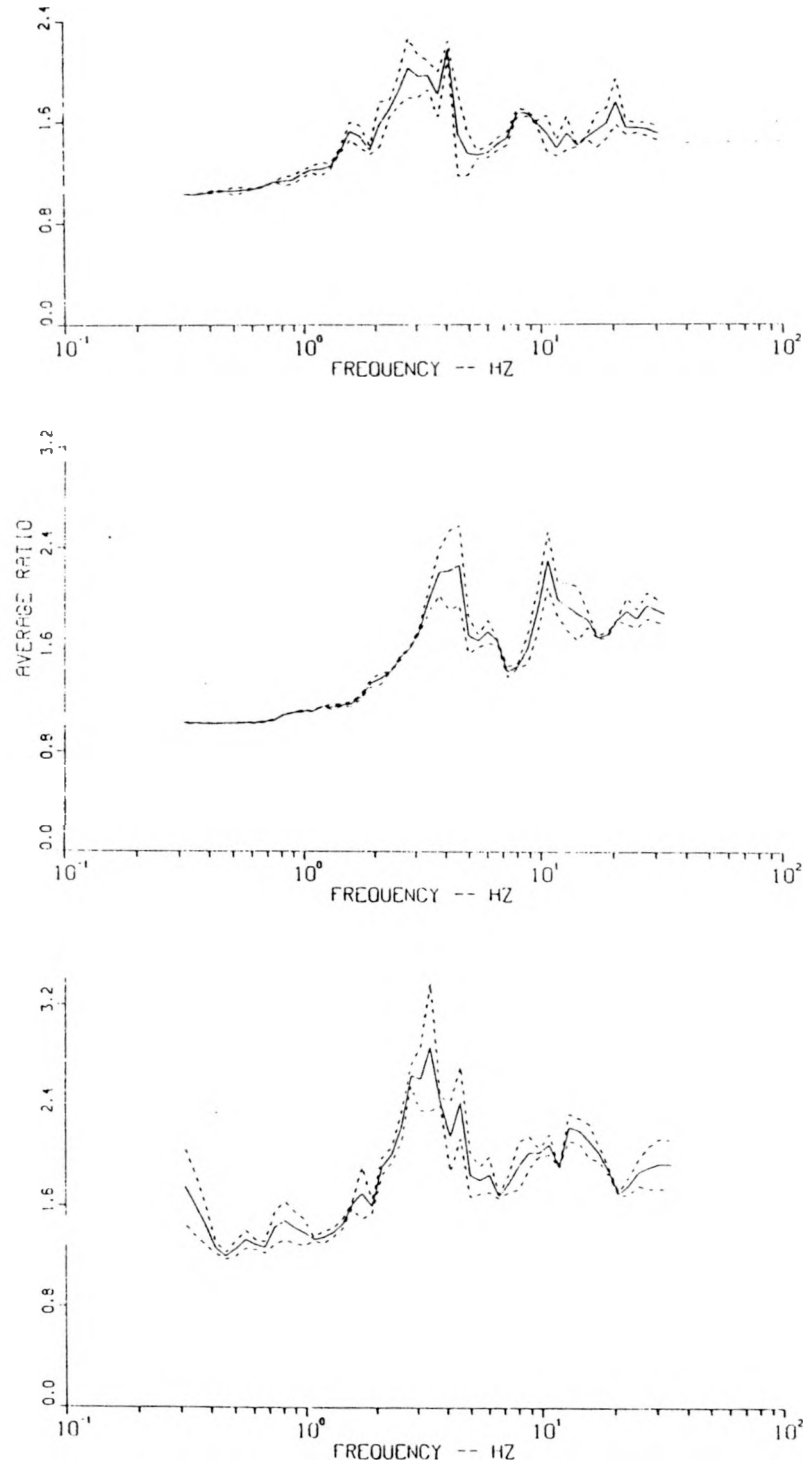

Figure 2.2-4. Average Ratios of S/D PSRVs Calculated for Station W30

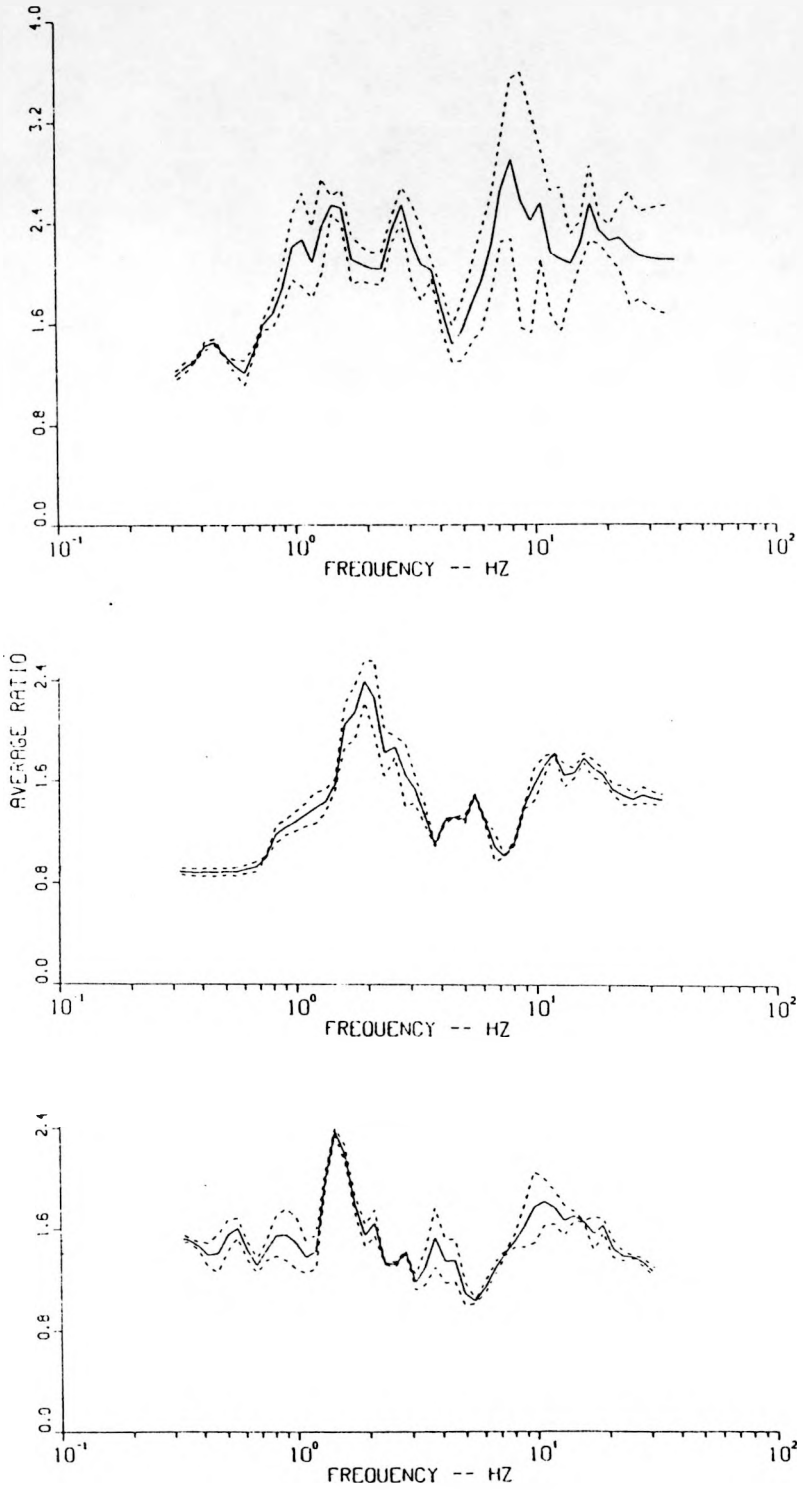

Figure 2.2-5. Comparison of Average S/D PSRV Ratios at the Yucca Mountain Stations

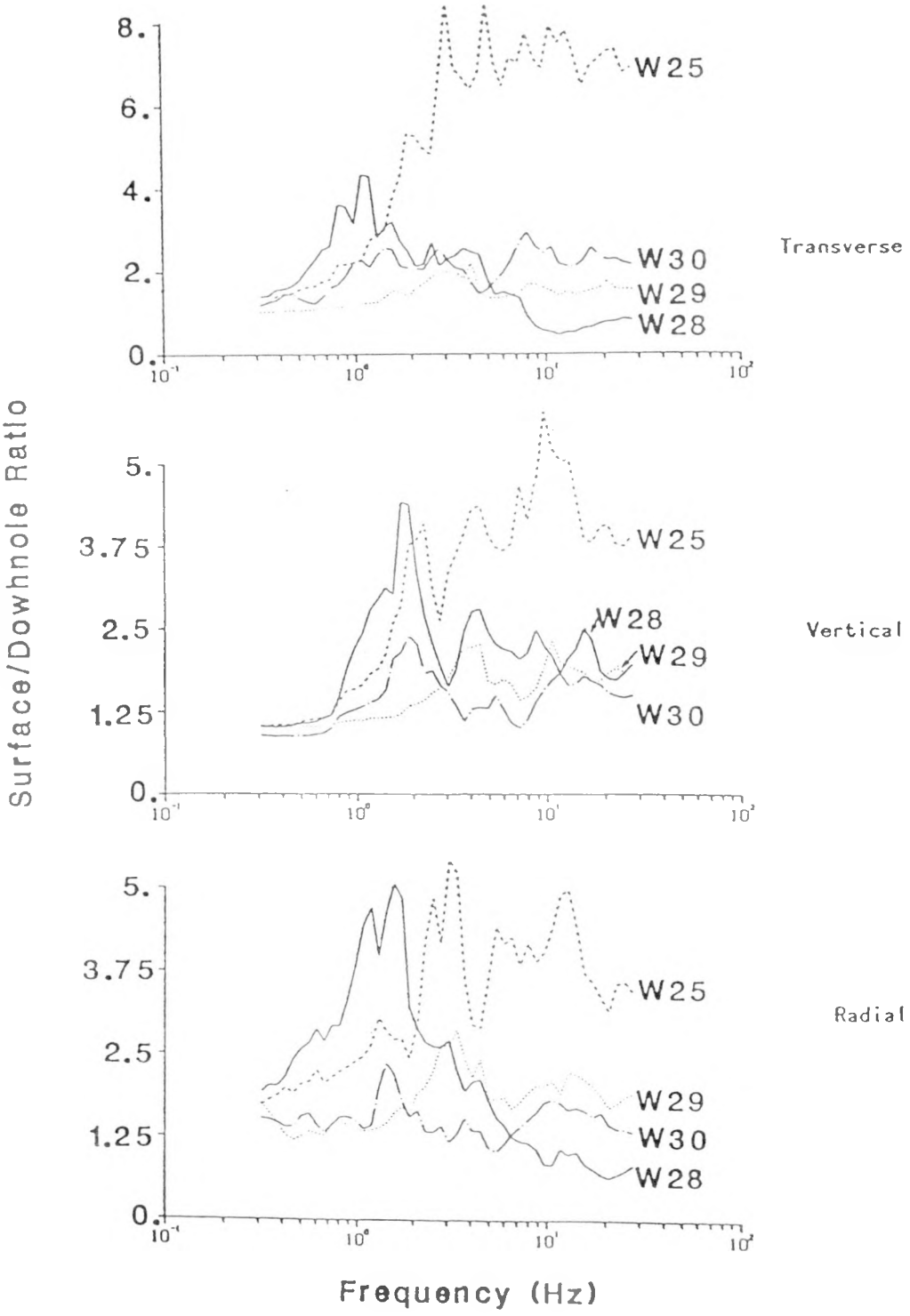

2.3 Discussion

2.3.1 Surface/Downhole Behavior

For similar materials, the S/D behavior at each of the stations would be expected to be the same. This is apparently not the case for the three deep stations (W28, W25 and W30) at Yucca Mountain. The S/D factors tend to decrease with increasing distance from the source. Although Station W25 is the intermediate station of the group in terms of distance, it shows consistently larger amplitude reduction factors than the other stations. Two plausible explanations for these observations are related to the material property differences of the surface materials at these stations and the fact that surface amplitudes decay differently with distance from the source than do the downhole amplitudes. These two explanations will be discussed in detail below.

The description of the geologic materials present on the surface at Stations W30 and W28 are classified as a moderately-to-densely welded, devitrified tuff. The surface material at Station W25, however, is classified as unconsolidated overburden (which includes alluvium, colluvium, non-welded vitric ashflow tuff). The downhole materials at Stations W25 and W30 have the same classification, while the material at Station W28 is similar, but somewhat "softer" (in a uniaxial stress-strain sense). Even though the material properties for the surface materials are not given, it is reasonable to assume (based on the geologic descriptions of the materials) that the tuff present at W28 and W30 is a more competent material with larger density and wave speeds (i.e., "stiffer") than the "tuff" present at W25. In general, peak particle velocities and displacements will be greater in a softer material and accelerations may be larger or smaller depending on the material property differences. If the surface and downhole materials were similar at all three stations, S/D factors should be about the same at each station. Because the materials on the surface differ, S/D ratios will vary. This can be illustrated using the simple concepts discussed below.

Assume an identical stress wave in two different materials. For the purposes of the following discussions, the surface material associated with stations W28 and W30 will be classified as "rock" and the materials at station W25 will be classified loosely as "alluvium". Particle velocity at a wave front can be estimated from one-dimensional wave theory as $\sigma/\rho c$ (where σ is the stress at the front, ρ is the density of the material, and c is the wave speed of the material). Rock material will have larger values of both ρ and c than alluvium. For the same given stress, peak particle velocity calculated for alluvium will be greater than peak velocity calculated for the rock (because ρc is in the denominator). The velocity time history can be differentiated to estimate acceleration. The acceleration associated with the peak velocity is determined from the peak particle velocity, rise time to peak velocity and wave shape. The rise time to peak may be estimated from the seismic and loading wave speeds of the material (the initial arrival of the signal travels at the seismic speed of the material and the peak travels at the loading speed). In general, the rise time to peak in alluvium will be greater than in rock. For the purposes of this discussion, the simplest assumption of waveshape (linear rise to peak) will be used. The acceleration is simply the ratio of the velocity and the rise time. Although the softer

alluvial material has a larger velocity, the longer rise to peak will have a tendency to compensate. Thus the acceleration values from the two types of materials will more than likely be about the same. Particle displacement may be estimated by integrating the velocity time history. A rock material will generally produce higher frequency motions. Given the higher peak velocity and the lower frequency of the softer material, the peak displacement in alluvial material will be greater than that observed in the rock.

The above discussion provides a theoretical basis for why motions in a soft material should be larger than a stiff material. This is also observed in the data. Figure 2.3-1 was developed using empirical equations from Vortman (1985). Two different data groupings were used in this comparisôn. The Group I data set was considered more representative of the "rock" behavior, while the Group II data set was more representative of the "alluvium" behavior.[6] The amplitude of the peak accelerations from the two types of materials are about the same, but the peak amplitudes of the velocities and displacements in the alluvial material are greater.

The recorded surface ground motions at W25 and W28 were compared to understand the effect of surface material differences. W28 is 2 to 3 km closer to the Pahute Mesa testing area than W25 and, because the amplitude of these motions decrease as distance from the source increases, the amplitude of the observed ground motion at W25 would be expected to be somewhat less than the motion at W28. Five events were examined at these two stations: Jefferson, Goldstone, Labquark, Serena and Salut. Ratios of peak ground motions were calculated for each quantity measured at the station (a total of nine) and an average value calculated for both the surface and downhole stations on each event. These averages are shown in Table 2.3-1. Although there was some variation on a component-by-component basis, the surface ground motions at W25 were generally greater than those at W28 (average ratios of W25/W28 for each event ranged from 1.1 to 1.5). The downhole ground motions at W25 for all components were generally less than those at W28 (average ratios for the events were 0.8 or 0.9). Therefore, S/D factors observed for W25 will be greater than for W28.

The apparent decrease in the S/D factors with increasing range from the source is most obvious in the transverse component of the ground motion, but it is also observed in the vertical and radial components as well. A contributing factor to the reduction in the S/D factors with distance is that peak motions on the surface attenuate, with distance from the source, than downhole motions. This attenuation rate is a function of the material properties as well as the geometry of the problem. An example of geometrical attenuation differences in the various components is the vibrational source on the surface of the halfspace (Richart et. al, 1970). Body wave displacement amplitudes for this geometry attenuate with range as r^{-1} at depth and r^{-2} at the surface (due to free surface effects). Surface wave displacement amplitudes have a theoretical attenuation rate of $r^{-0.5}$. (The accelerations and velocities will decay at slightly different rates.) Factoring in the attenuation due to the material properties will increase these rates somewhat.

---

6. Vortman (1985) fit the data from NTS in various groups: Group I included all data; Group II eliminated known anomalous stations which were mostly alluvium stations in the NRDS area of the NTS.

Because the amplitude of the motions observed at the surface decrease at a faster rate (with distance from the source) than motions downhole, the two amplitudes will become more similar at the greater distances. Thus the S/D factors decrease with distance.

The behavior of the amplitudes with distance from the source, of the surface and downhole motions at the Yucca Mountain stations were examined. The five events studied were Labquark, Jefferson, Salut, Serena and Goldstone. The absolute peak motions (regardless of wave type) recorded in the time history were tabulated. For each of the five events, the variation of the surface and downhole peak motions with distance away from the UNE were fit with a power curve. The attenuation rates calculated from these fits were then compared. The observed attenuation rates at the surface generally were faster than the downhole rates. Unfortunately, the majority of the fits were poor and the quantitative value of the equations questionable. For example, correlation coefficients ("goodness" of fit indicators, where 0 is no linear correlation and 1 is perfect linear correlation) calculated for the fits varied from 0.01 to 1.00, indicating a great deal of variation in the data.

2.3.2 Station W28

As mentioned earlier, an unusual signal observed in the horizontal components was observed at Station W28. This signal is characterized by a relatively large amplitude, high-frequency (8-20 Hz) acceleration in the downhole ground motion. (The acceleration amplitude of the downhole motion is generally larger than the surface acceleration amplitude at the same frequency.) An example of this signal compared to a "normal" signal is shown in Figure 2.3-2. This figure shows the radial accelerations recorded on event Tierra for stations W25 and W28. In an effort to understand the nature of this signal, S/D data from eight events were studied. In addition to the six Pahute Mesa events, two Yucca Flats UNEs were included in the analysis in an effort to determine the azimuthal dependency of the signal. The normalized PSRVs and the calculated S/D ratios for these two events are located in Appendix B. Information concerning these events is presented in Table 2.3-2. (The behavior of this signal is described and discussion of possible causes is included in this section.)

Observations

1. Seven of the eight UNEs listed in Table 2.3-2 showed varying degrees of amplification. The behavior occurs only in the horizontal plane; the largest effect appears in the transverse component of acceleration. The unaffected UNE was Hermosa (Figs. B.1-B.3). The maximum effect was exhibited by the Tierra UNE (Figs. A.29, A.35 and A.41). In the Tierra UNE, the maximum ground motion observed was downhole.

2. Shown on Figure 2.3-3 is the azimuthal extent of the observed anomaly. The angle is roughly 54°. The maximum observed effect occurs at 17° east of north (UNE Tierra). The event with the smallest observed effect was Labquark (Figs. A.28, A.34 and A.40) which is at 15.5° east of north. The boundaries of the effect (in this data set) are UNE Salut at 3° west of north and UNE Cottage (Figs. B.4-B.6) at 50° east of north. The majority of the UNEs had

shot points between the western boundary and the azimuth of maximum effect. No UNEs had shot points between the eastern boundary and maximum azimuth. One UNE (Hermosa) had a shot point east of the azimuth of Cottage; no effect was observed.

3. The location of the shot points were noted and listed in Table 2.3-2. The Pahute Mesa events were plotted on the map of the Silent Canyon Caldera (Fig. 2.3-4). The numbers on the events indicate the relative magnitude of the observed effect, where 1 indicates the event with the largest effect. A study of maximum effect versus location in the caldera showed no apparent systematic variations. Both the maximum and minimum observed effects were produced by UNEs conducted in Area 19.

4. The travel paths from the Pahute Mesa UNEs pass through the area of Timber Mountain Caldera. The geologic structure in this area has been identified as the probable cause of the acceleration anomaly in the NRDS area (Walck, 1987). It has also been postulated that this structure is responsible for small apparent acceleration anomalies at some Yucca Mountain surface stations (Vortman, 1986). The anomalous behavior observed here does not appear to be related to the other anomalies.

5. All UNEs with this anomaly have shot points above the water table. The UNE that showed no anomalous motion (Hermosa) had its shot point below the water table. There is no apparent correlation between depth above water table and observed effect.

6. Arrival times measured from the acceleration time histories and slant ranges between shot point and W-28 bottom were used to calculate apparent wave speeds for the signal. The arrival time and wavespeeds are shown in Table 2.3-2. There is no obvious correlation with the observed effect and apparent wavespeed.

7. The ground motion time histories were inspected to determine the various parameters associated with this signal. The parameters of interest are time of peak, peak acceleration, peak velocity and peak displacement. These parameters were scaled from the time histories and are listed in Table 2.3-3. For the majority of the UNEs, the maximum acceleration occurs in the first wavetrain (i.e., within the first second after arrival). For radial accelerations, only Cottage had the peak acceleration later in the waveform. For transverse accelerations, events Cottage, Jefferson and Salut had the peak acceleration occur later in the waveform. This signal produced the maximum magnitude of acceleration for all events on which it was observed. The time at which the peak radial acceleration occurred for this signal was different than the time of maximum peak in the transverse acceleration. Magnitudes of peak velocities associated with this acceleration were not the maximum of the time history (except for Tierra) and displacements associated with this signal were very small. The displacements were large enough to measure on only three of the events.

8. The direction of the maximum vector acceleration at the time of the radial peak acceleration and at the time of the transverse peak acceleration was calculated. The results are shown in Figures 2.3-5 and 2.3-6. Figure 2.3-5 shows the direction at the time of the radial peak. With the exception of Labquark, the direction of all signals is generally the same. The majority of the events cover an angle of about 65°. The direction at the time of the maximum transverse peak acceleration shows more scatter in the direction of motion, a spread of about 166°, excluding Labquark (Fig. 2.3-6). An overlap of direction for some events is apparent. These do not appear to correlate with magnitude of effect.

9. Table 2.3-4 summarizes the study of the PSRVs for these events. or most of the events, this high-frequency signal is well defined in the PSRV of the transverse component. The peak transverse amplitude occurs between 8.9 and 15 Hz for all events. The width of this high-frequency spike generally fell between 6-20 Hz for all events. This high-frequency signal in the radial PSRV was not as well defined as for the transverse PSRV. The width of the high frequency spike is somewhat more than observed for the transverse component (6 - 25 Hz). The frequency of the peak amplitude was about the same on most of the events.

   The magnitudes of the PSRV amplitudes are also shown in Table 2.3-4. This table shows the relative magnitudes with respect to the spectrum of the companion surface acceleration as well as the maximum amplitude of the bottom spectrum. For most events the high-frequency signal is a significant element of the downhole radial and transverse motion. With respect to the surface accelerations, the signal appears to be significant for only the Tierra event.

10. This station is located in USGS exploratory boring USW G-2. The geologic material at the gage depth was described in Section 1.0. Further stratigraphic detail is contained in the boring log (Moldanado and Koether, 1983). The section of that log which includes the station is shown in Figure 2.3-7. The station is located in the Topopah Spring Member of the Paintbrush Tuff at a depth of 368 m. Breciated fault zones were noted above and below the station depth. In addition, the station is included in a lithophysae zone with an increase of lithophysae near the station depth. The core index used as an indication of competent or incompetent rock (presented on Fig. 2.3-7) shows the station at an abrupt change from so-called competent to incompetent rock.

11. The station was installed in a different manner from other downhole stations. The usual mode of installation is to equip the canister with a gripper (i.e., remote-controlled feet that expand to hold the canister in place). In this instance, the drill hole was plugged and the canister placed on the plug. Then sand was rained down around the gage.

Discussion

The observed behavior could be caused by any number of sources. These sources can be placed into two broad general categories: instrumentation/installation problems and actual ground motion phenomena.

The instrumentation/installation problems include "ringing" of components as a result of the ground motion signal or installation problems due to the difficulty of placing a gage at such a large depth. Remember, this station is the nonstandard installation (with respect to the other installations; note, however, that this is an accepted method of installation). The station was installed in such a way that some errors could have gone unnoticed (i.e., soil that was supposed to be placed around the canister may not have made it down to the canister or the canister might not have been founded securely on the plug). Some degree of noise, which may indicate ringing in the system, has been noted by field technicians during the operation of this station for most of the shots recorded. Instrumentation/installation problems are implicated as a cause of the observed behavior.

Two geologic factors, namely travel path and station geology, provide support to the hypothesis that the observed behavior is actual ground motion phenomena. The travel path geology for the majority of UNEs is through an area known to have produced anomalous behavior for other stations in the NRDS and Yucca Mountain areas. Further, the geology noted in the drilling log has enough variation to indicate that the station geology might also be affecting the ground motion.

The geologic circumstances at this station are such that ground motions at these frequencies would be amplified. The material properties for the TsW1 and TsW2 (Nimick and Schwartz, 1987) were used to derive the P-wave and S-wave velocities. The ratios of these velocities and the densities of the two materials were used in conjunction with Figure 2.3-8 (taken from Grant and West, 1965). This figure shows the reflection coefficients for the P-wave and the SV-waves for the instance where the wave is traveling from a stiff material to a soft material. (This is the case at W28, where the motions recorded in TsW1 are transmitted from TsW2.) Note that although these curves are generated for a Poisson's ratio of 0.25 the qualitative behavior will be the same for all values of Poisson's ratio. These two components are the most likely candidates for generating the high frequency motions. The reflection coefficients are a function of the angle of incidence and the ratios of the seismic P- and S-wave velocities and the mass densities of the two media (α and ρ, noted in the figure). For the materials of interest here, the reflection coefficients are about 0.1 for angles of incidence from 0° to 60°. This indicates roughly 90 percent of the incident signal is transmitted to the softer material. Therefore, most of the high-frequency signal will be transmitted to the interface of the two materials. Depending upon the distance of the station is away from the interface and the attenuation characteristics of the medium, this could account for the presence of the enhanced high frequencies. Such is not the case for the other deep stations as they are installed in the stiffer TsW2 material and underlain by a softer material (Fig. 1.0-3).

Although neither installation/instrumentation nor ground motion phenomena can be discounted completely, several observations support the theory that

this behavior is the result of the actual ground motion phenomena. First, the signal appears only in the horizontal plane. If there was a ringing problem it would be expected to show up in all three gages in that canister. Second, the apparent directional nature of the signal is not a usual characteristic of an instrumentation problem. It would seem that an instrumentation problem would be similar for each event and not exhibit the variability observed here. Third, an instrumentation problem should appear for all UNEs; appearing on all but one (with no other correlation) is inconsistent with an instrumentation problem.

This station was recently replaced. The old instrumentation was inspected and no faults were found. A specially fabricated canister was reinstalled with newly calibrated gages using the method consistent with the other installations in the Yucca Mountain area. This new canister was installed at a slightly shallower depth (358 m vs 375 m) but still in the same material.

Since the original draft of this report was prepared, a total of eight events have been recorded using the new canister installed at this station. Figure 2.3-9 shows the comparison of the average S/D PSRV ratios and the $\pm 1\sigma$ bounds of this new data set and the average S/D PSRV ratios of the original data set. In general, all components have similar shape (new set vs existing set). The S/D ratios of the new set are less that the existing set because of the fact that the instrumentation in the new set was installed at a shallower depth. While the degree of high frequency amplification is less in the new set, it is still present. Based on these data, it appears that anomalous behavior is ground motion phenomena and not instrumentation problems.

Currently, the major limitation is lack of data for a complete analysis. A definitive answer is unlikely to be reached based on the available data. The anomalous signal is probably related to a structural feature, either near the station or in the travel path, which will not be identified with eight experiments recorded at a single location. Because this signal is of relatively small magnitude and occurs only at one station, it appears to be of little significance from a practical (design-oriented) point of view. However, the cause of the behavior should be understood in order to make definitive statements about its impact on the seismic wave transmission in the vicinity of Yucca Mountain.

Additional work planned in the study of this anomaly is in two areas. First, any new UNEs recorded at this station will be added to the existing data base and analyzed. Second, the details of the travel path modeling completed or under way in the study of the NRDS anomaly will be reviewed to determine any commonalities that might exist in the two problems.

Table 2.3-1 Average Ratios of Ground Motions Measured at Stations W25 and W28 for 5 Events

Event	W25/W28 Surface	W25/W28 Downhole
Labquark	1.1	0.84
Jefferson	1.4	0.93
Serena	1.5	0.85
Salut	1.1	0.88
Goldstone	1.4	0.89

Table 2.3-2 Basic Information Concerning UNEs Recorded at Station W28 Downhole

Event	Location	Date	Slant Range km	Time of Arrival s	Apparent Wavespeed	Comments
Tierra	Pahute Mesa-Area 19	12/15/84	45.594	8.74	5220	Max. Observed Effect
Cottage	Yucca Flat-Area 8	3/23/85	50.643	8.13	6229	Small Effect
Hermosa	Yucca Flat-Area 7	4/ 2/85	44.347	7.85	5649	No Effect
Salut	Pahute Mesa-Area 20	6/12/85	39.844	7.75	5141	Small Effect
Serena	Pahute Mesa-Area 20	7/25/85	45.282	8.90	5088	Intermediate Effect
Goldstone	Pahute Mesa-Area 20	12/28/85	38.662	7.90	4894	Small Effect
Jefferson	Pahute Mesa-Area 20	4/22/85	41.601	8.25	5043	Small Effect
Labquark	Pahute Mesa-Area 19	9/30/86	47.525	9.00	5281	Min. Observed Effect

Table 2.3-3 Times and Peak Ground Motion Parameters Associated With Anomalous Signal Observed at W28 Downhole

Event	Time of Peak Acceleration s (TP)		Time of Arrival s (TA)	Δt (TP-TA) s		Peak Acceleration m/s^2		Peak Velocity m/s		Peak Displacement cm	
	Radial	Transverse		Rad.	Trns.	Radial	Transverse	Radial	Transverse	Radial	Transverse
Tierra	9.14	9.33	8.74	0.40	0.59	0.14	0.12	0.0046	0.0045	0.01	0.01
Cottage	11.10	15.20	8.13	2.97	7.07	0.015	0.014	0.0005	0.0004	-	-
Hermosa	-	-	7.85	-	-	-	-	-	-	-	-
Salut	8.25	14.80	7.75	0.50	7.05	0.05	0.05	0.0011	0.0009	-	-
Serena	9.11	9.22	8.90	0.21	0.32	0.09	0.07	0.0026	0.0024	0.005	0.006
Goldstone	8.93	8.42	7.90	1.03	0.52	0.07	0.06	0.0019	0.0022	-	-
Jefferson	8.71	14.40	8.25	0.46	6.15	0.04	0.05	0.0008	0.00014	-	-
Labquark	9.80	9.80	9.00	0.80	0.80	0.03	0.04	0.0017	0.0014	0.001	0.001

Table 2.3-4 Summary of Major Parameters Describing Anomalous Signal at W28 Downhole

Frequency Behavior of Anomalous Signal

Event	Frequency of Peak		Frequency Range	
	Radial	Transverse	Radial	Transverse
Labquark	9.5	9.5	7.5-12	7 -20
Tierra	9.0	8.9	5.5-20	5 -20
Salut	8 ?	9.5	6 -25	6 -25
Jefferson	8 ?	12	6 -25	7.2-20
Serena	9	9	4 -20	5 -16
Goldstone	7.5	11	6.5-25	6 -20
Cottage	8	15	6 -20	6 -20
Hermosa	-	-	-	-

Magnitude of Anomalous Signal Relative to the Maximum Psuedo Velocity of the Surface Measurement

Event	Radial	Transverse
Labquark	0.06	0.1
Tierra	0.57	1.5
Salut	0.08	0.17
Jefferson	0.07	0.13
Serena	0.2	0.3
Goldstone	0.16	0.22
Cottage	0.08	0.08
Hermosa	-	-

Magnitude of Anomalous Signal Relative to the Maximum Pseudo Velocity of the Downhole Measurement

Event	Radial	Transverse
Labquark	0.12	0.11
Tierra	1.0	1.0
Salut	0.26	0.38
Jefferson	0.28	0.28
Serena	0.69	0.73
Goldstone	0.48	0.38
Cottage	0.19	0.14
Hermosa	-	-

Figure 2.3-1. Comparison of Peak Vector Ground Motions Calculated From Equations Presented in Vortman (1986) for 150 kt (Group I Equations Used for Rock; Group II Equations Used for Alluvium)

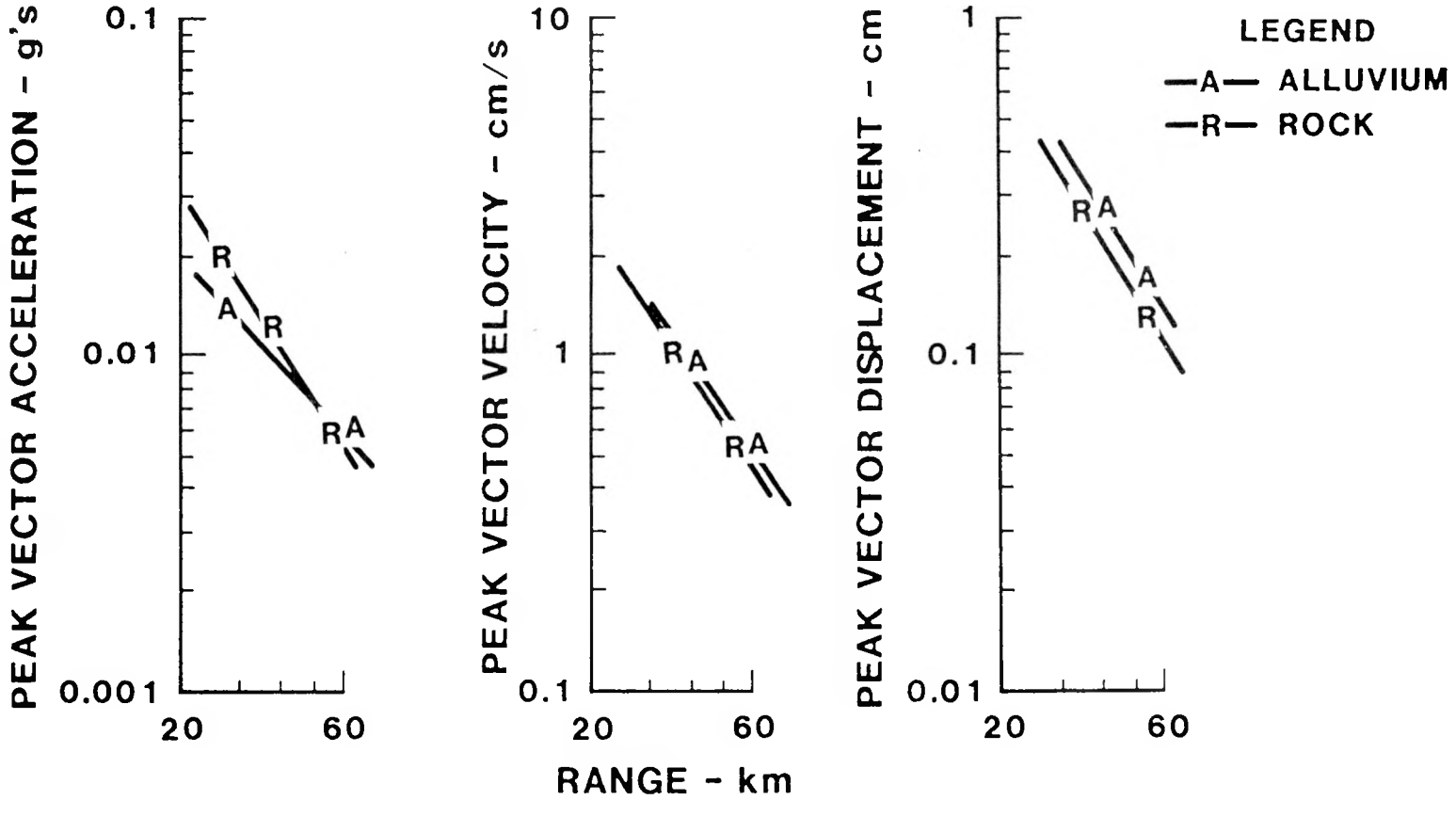

Figure 2.3-2 Comparison of "Typical" (W25) Downhole Ground Motions and Those Observed at W28 - Event Tierra

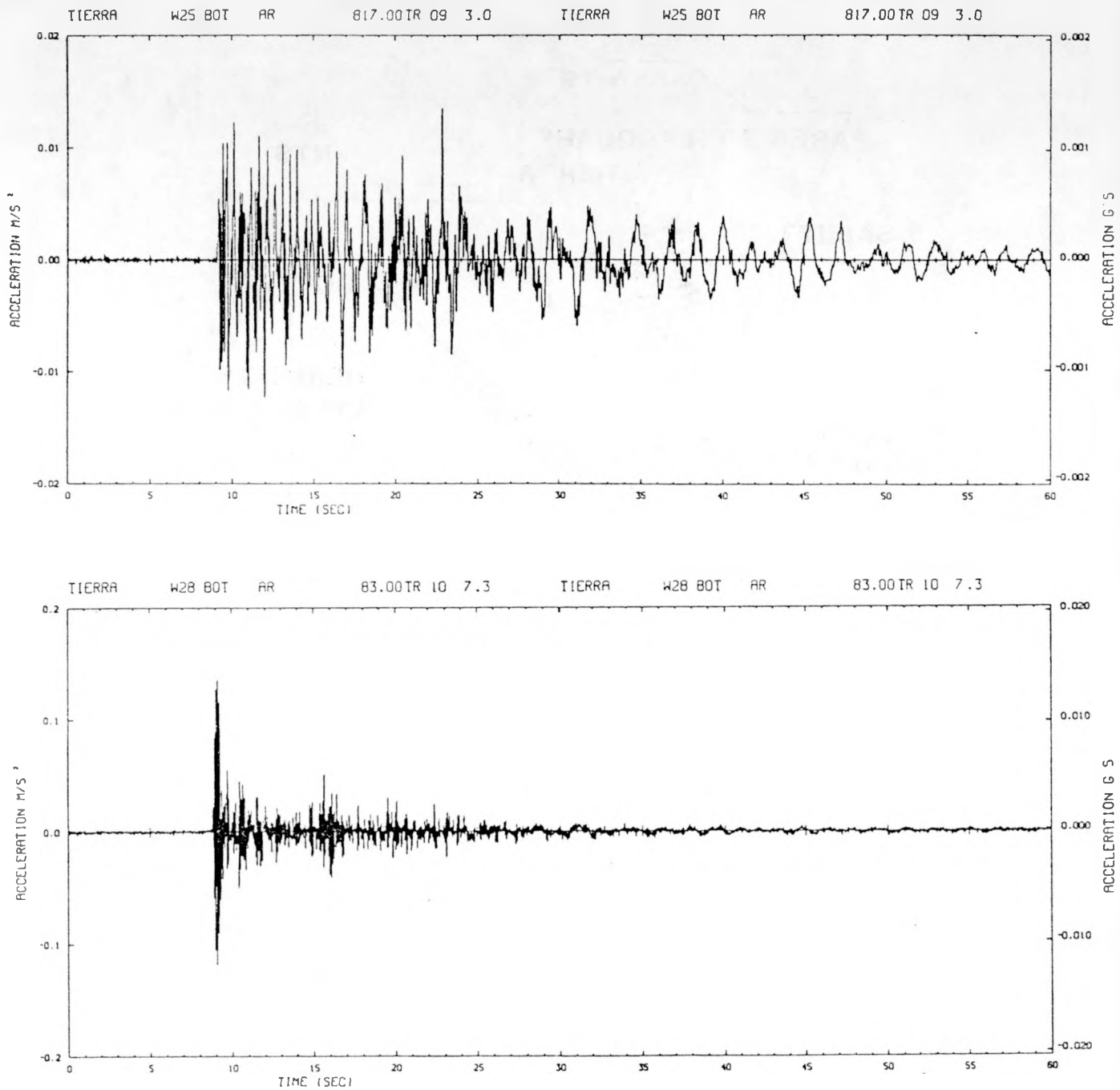

Figure 2.3-3. Azimuthal Extent of High Frequency Anomaly at Station 28 Downhole With Azimuths of Maximum and Minimum Effect Indicated

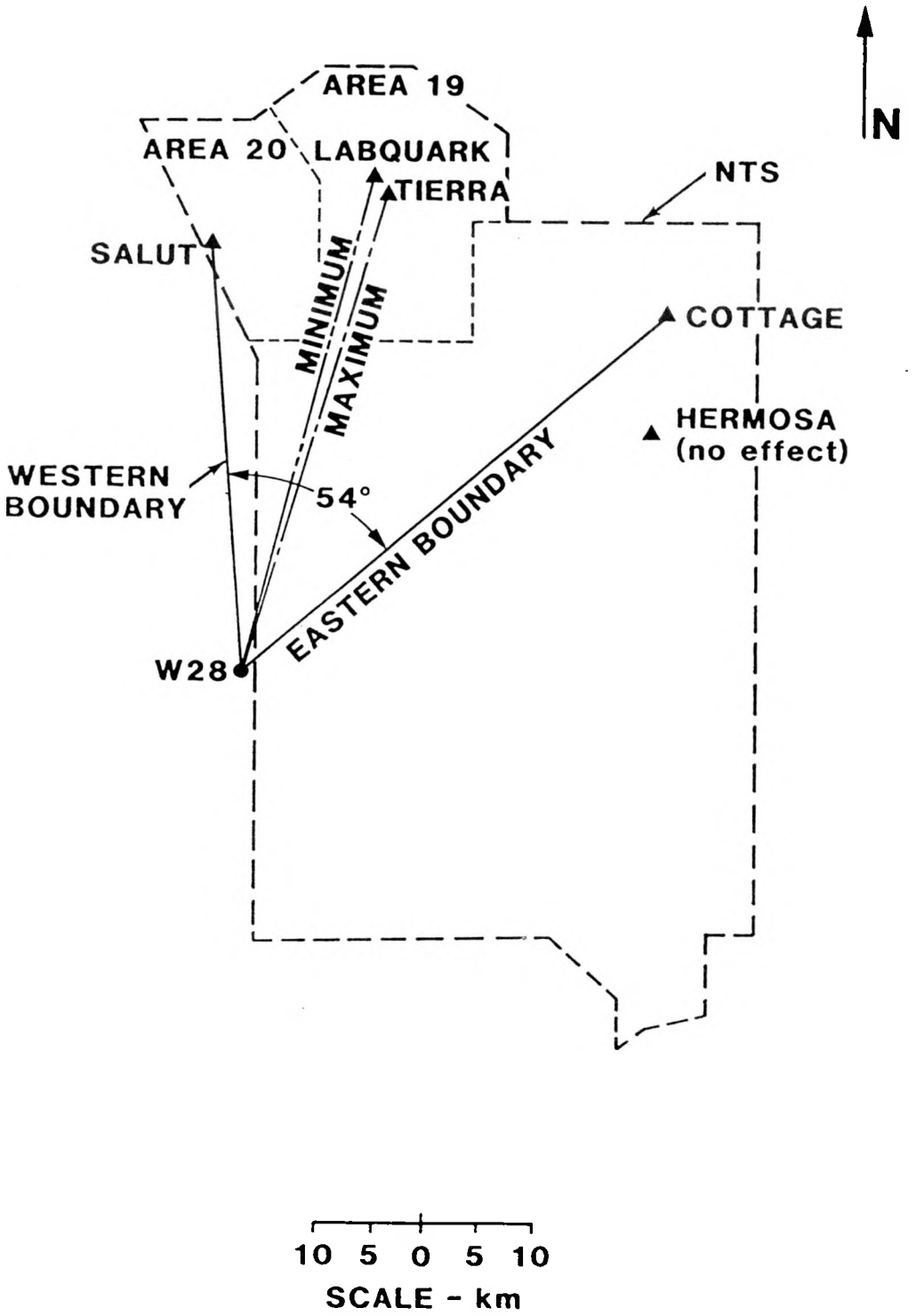

Figure 2.3-4. Relative Location of the Pahute Mesa UNEs That Produced Anomalus Signal at Station W28 Downhole (Circled Numbers Indicate Relative Size of the Effect - 1 is the largest and 6 is the smallest)

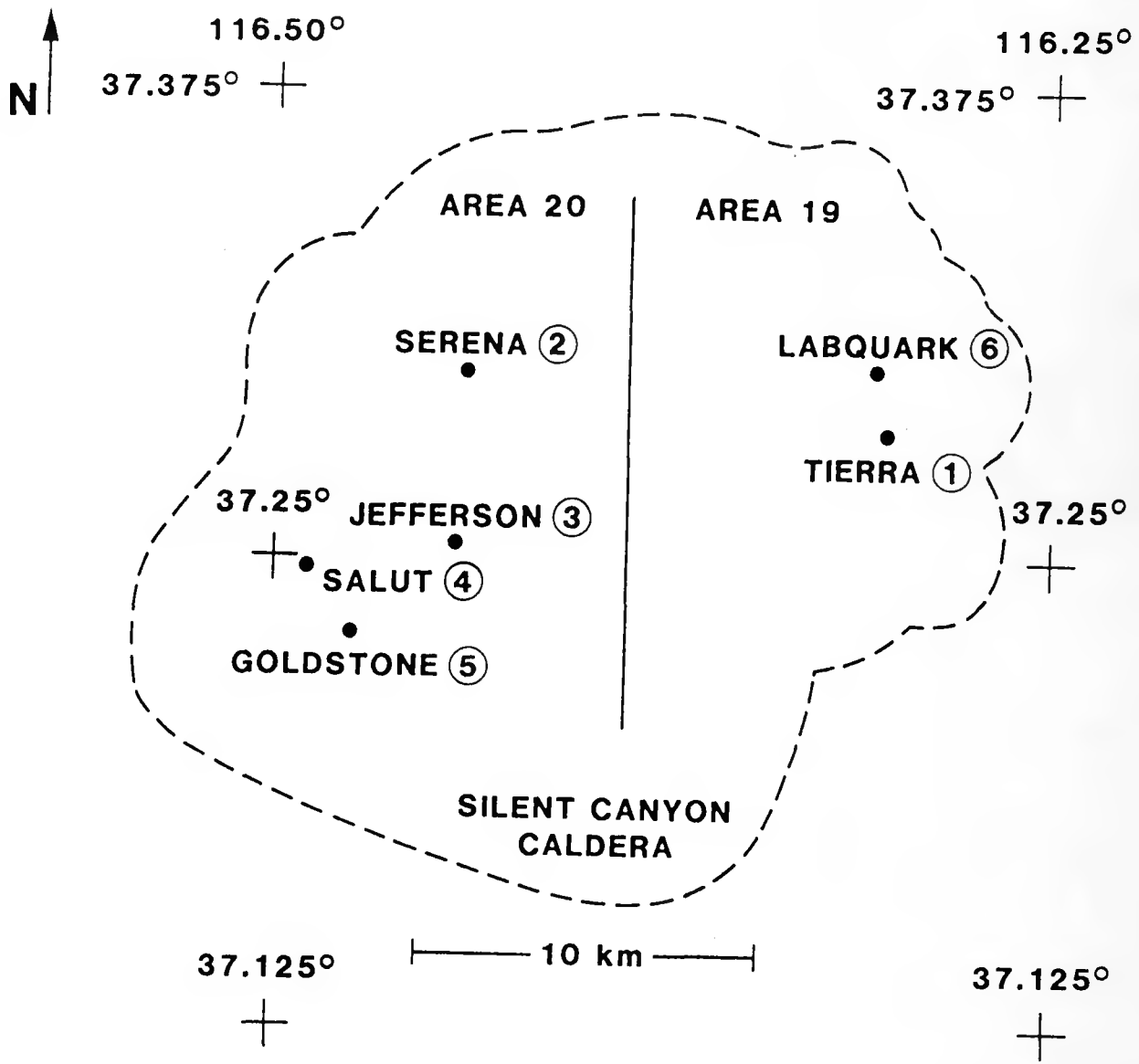

Figure 2.3-5. Direction of Early Time Horizontal Motion at the Time of Maximum Radial Acceleration

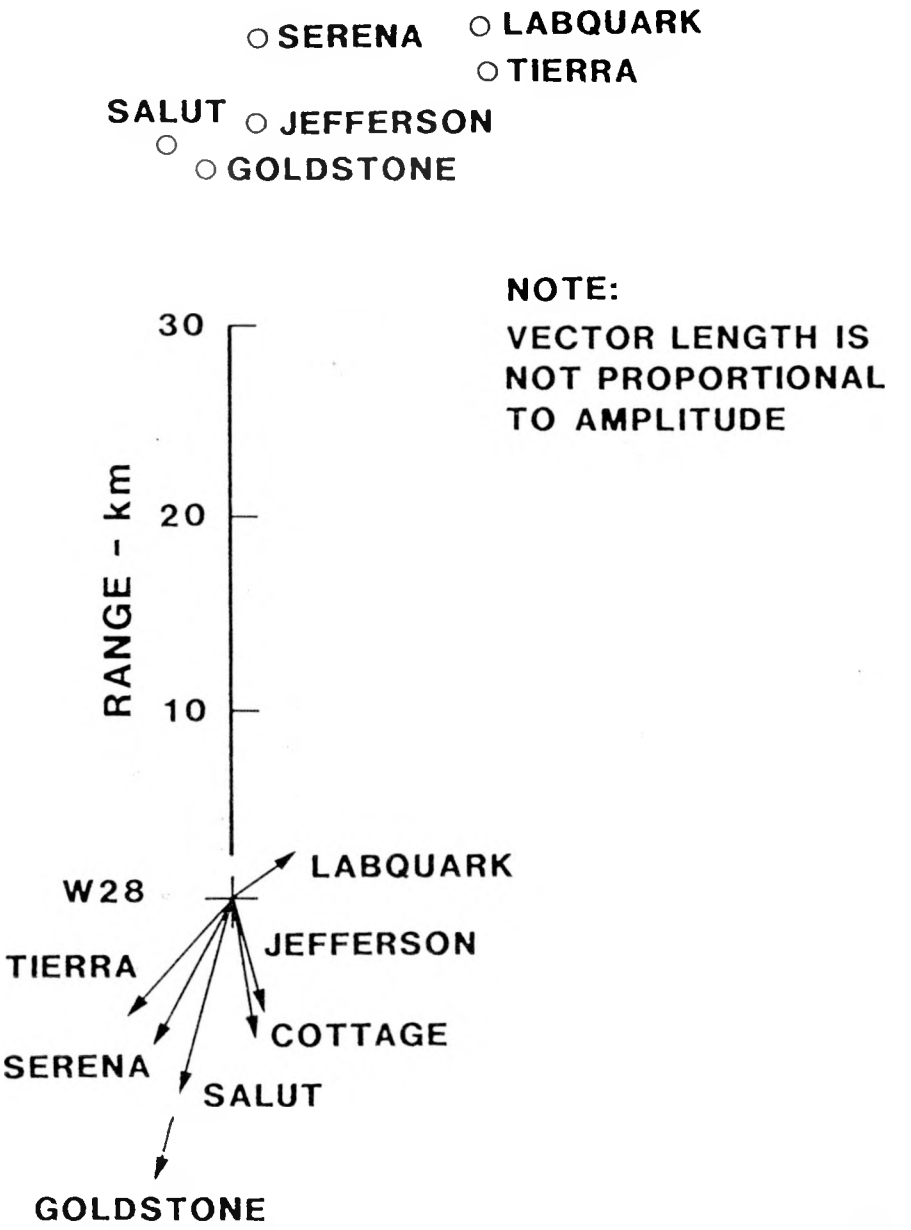

Figure 2.3-6. Direction of Early Time Horizontal Motion at the Time of Maximum Transverse Acceleration

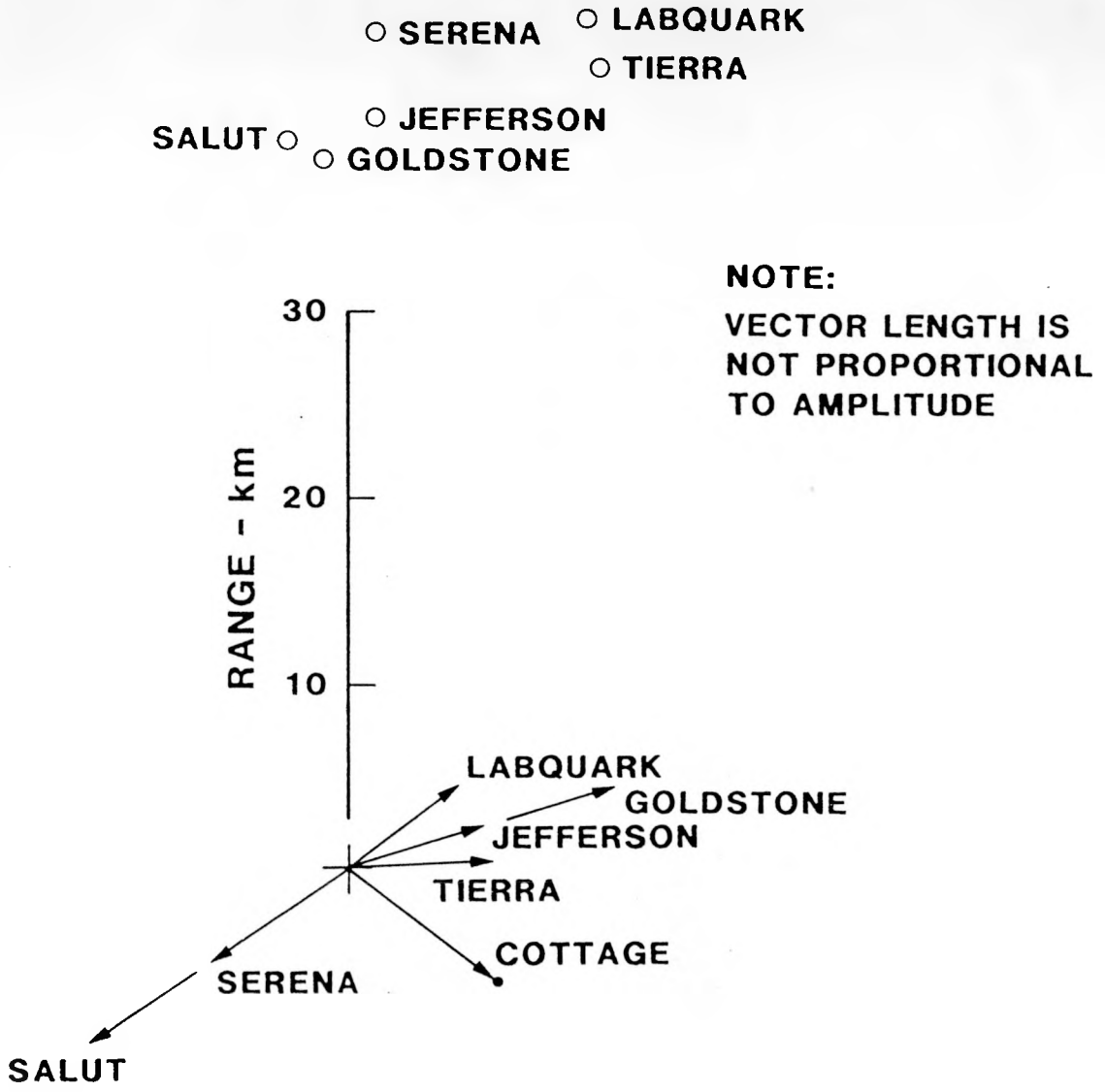

Figure 2.3-7. Drilling Log of Hole USW G-2 (Ref. 11)

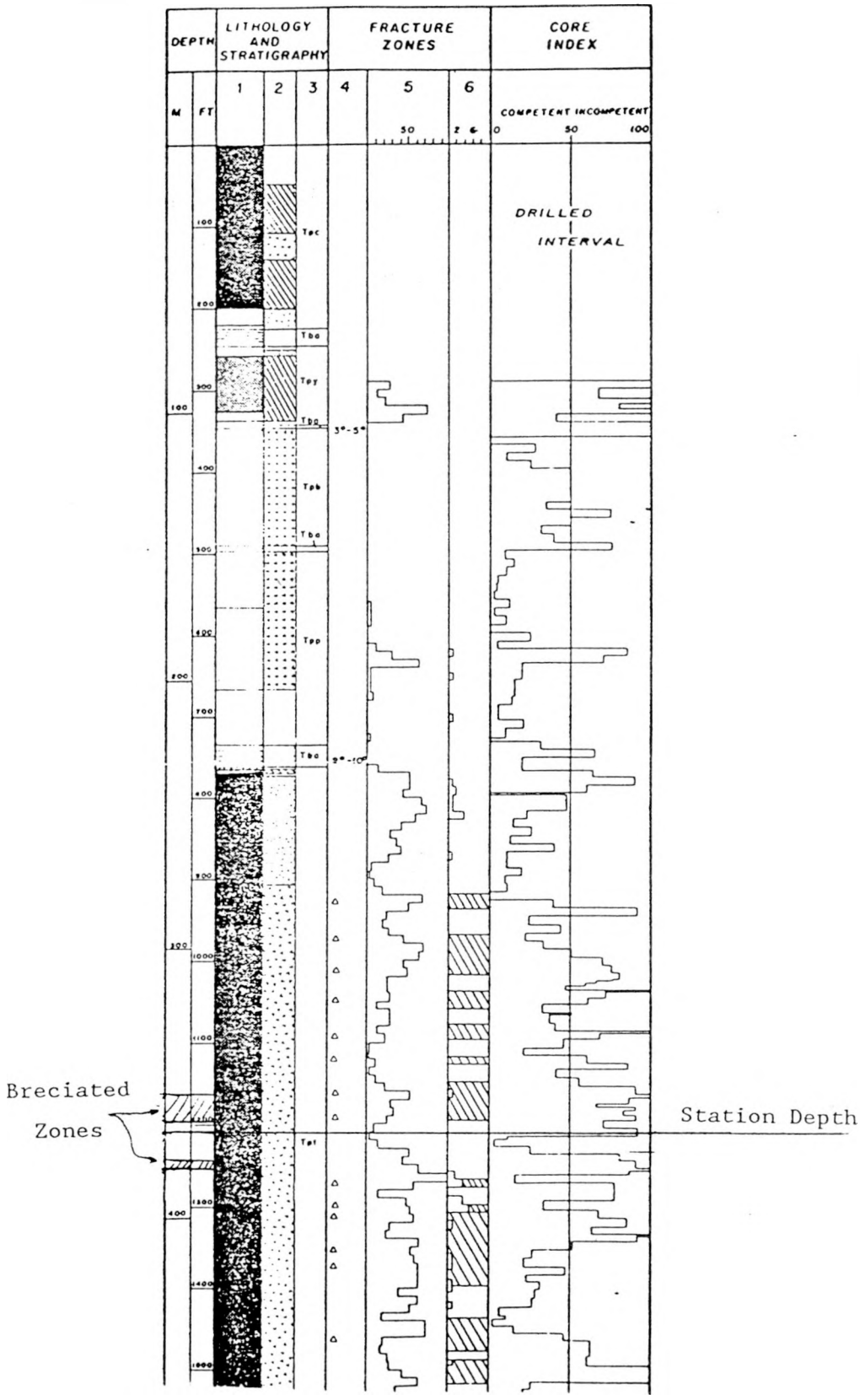

Figure 2.3-8. Reflection Coefficients for Plane P- and SV-waves at a Solid-Solid Interface $\alpha_2 < \alpha_1$ (Wave Going From Hard Material Into Soft Material -- Grant and West, 1965)

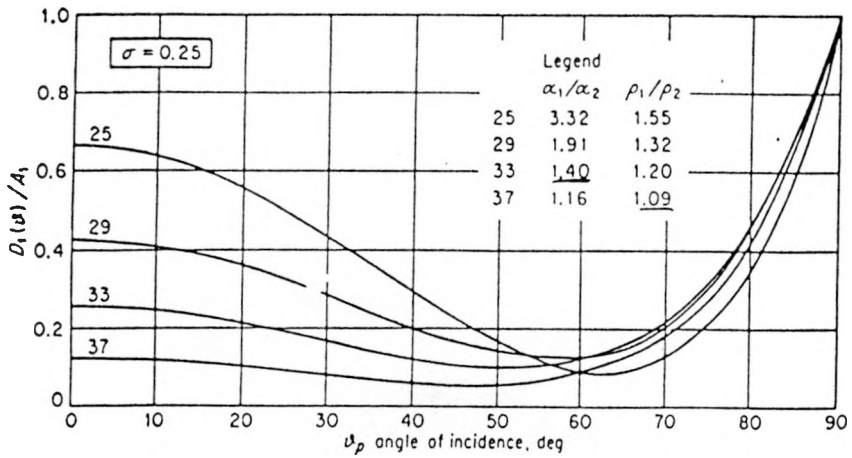

P-wave Reflection coefficients

(for W28 α_1/α_2~ 1.4 and p_1/p_2 ~ 1.09)

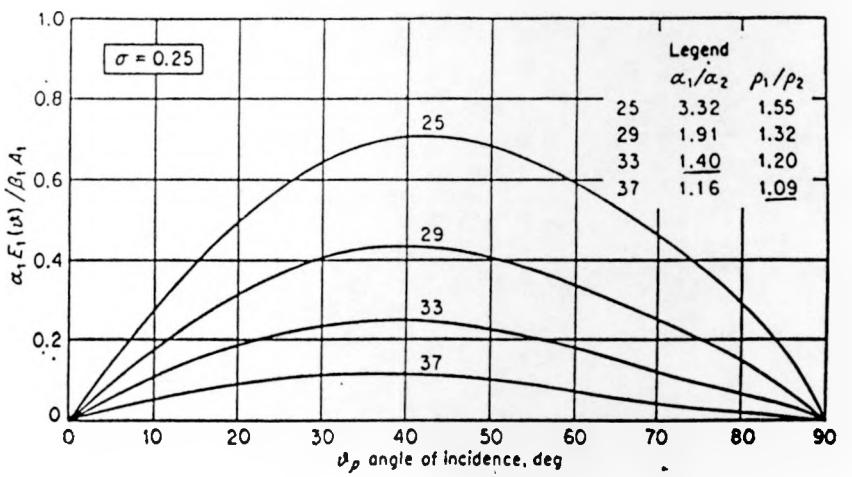

SV-wave Reflection Coefficients

(for W28 α_1/α_2 ~ 1.4 and p_1/p_2 ~ 1.09)

Figure 2.3-9 Comparison of Data from This Study and "New" Data from W28

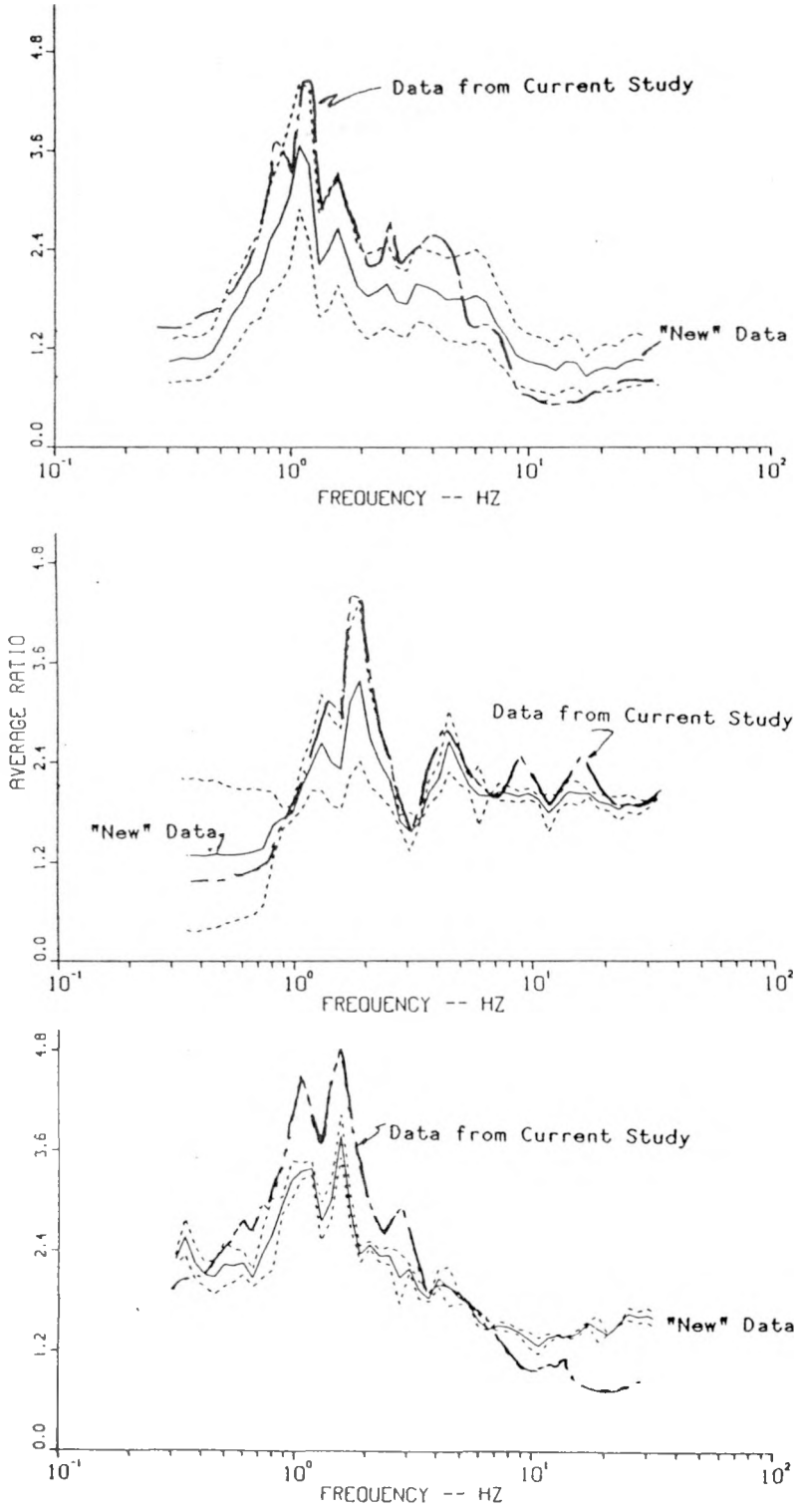

3.0 CONCLUSIONS AND RECOMMENDATIONS

The major conclusions drawn from this study are summarized below:

- PSRV ratios are a convenient way to describe the S/D behavior because they provide information on the attenuation of the entire ground motion signal rather than a single peak.

- Apparent inconsistencies in the regional S/D behavior at Yucca Mountain can be explained by the differences in the geologic materials at the stations.

- Due to the variability observed in the PSRVs from station to station, prediction of downhole behavior is most accurately accomplished by developing predictions for individual stations. Further analysis will be required to develop a general prediction approach.

- Anomalous ground motion observed at station W28 appears to be actual phenomena. The most probable cause at this point is the combination of the travel path and the stratigraphy at the station. While the amplitude of this signal is insignificant from the design view point, an understanding of this signal in the broader context of seismic wave transmission in the Yucca Mountain area is required.

The recommendations for further study are as follows:

- A prediction procedure for surface PSRVs should be developed. The ratios of S/D PSRV values discussed in this report can be used to predict downhole PSRVs. Prediction equations should be developed for both the Yucca Flats and Pahute Mesa testing areas.

- Plausible two-dimensional velocity models for the travel paths between Yucca Mountain and the two testing areas should be developed. This can be accomplished using data recorded at Yucca Mountain, known geologic properties, two-dimensional seismic travel time, and synthetic seismogram techniques.

- The PDS of these and newly acquired S/D data should be analyzed in an effort to determine geologic structure at these stations. This work coupled with the two-dimensional modeling could be used to develop plausible regional models for Yucca Mountain.

4.0 References

Grant, F. S. and West, G. F., 1965, Interpretation Theory in Applied Geophysics, McGraw-Hill Book Company, Chapter 3, pp. 58 and 59 (NNA.901127.0199)

Long, J. W., et. al., 1983, Prediction of Downhole Waveforms, SAND82-2478, Sandia National Laboratories (NNA.870518.0063).

Maldonado, F. and Koether, S. L., 1983, Stratigraphy, Structure, and Some Petrographic Features of Tertiary Volcanic Rocks at the USW G-2 Drill Hole, Yucca Mountain, Nye County, Nevada. USGS-OFR-83-732, United States Department of the Interior Geological Survey (HQS.880517.1329).

Nimick F. B. and B. M. Schwartz, 1987, Bulk Thermal and Mechanical Properties of the Topopah Spring Member of the Paintbrush Tuff, Yucca Mountain, Nevada, SAND85-0762, Sandia National Laboratories (NNA.871013.0012).

Ortiz, T. S., et. al., 1985, A Three-Dimensional Model of Reference Thermal/Mechanical and Hydrological Stratigraphy at Yucca Mountain, Southern Nevada, SAND84-1076, Sandia National Laboratories (NNA.890315.0013).

Richart, F. E., Jr., Hall, J. R., Jr., and Woods, R. D., 1970, Vibrations of Soils and Foundations, Prentice-Hall Inc (NNA.900502.0053).

URS/Blume and Associates, Engineers, 1985, Review of Seismic Studies for the Prospective Yucca Mountain Nuclear Waste Repository, SAND83-7458, Sandia National Laboratories (NNA.890713.0193).

Vortman, L. J. and Long, J. W., 1982a, The Effects of Repository Depth on Ground Motion - The Pahute Mesa Data, SAND82-0174, Sandia National Laboratories (HQS.880517.1549).

Vortman, L. J. and Long, J. W., 1982b, Effects of Ground Motion on Repository Depth - The Yucca Flat Data, SAND82-1647, Sandia National Laboratories (HQS.880517.1911).

Vortman, L. J., 1986, Ground Motion ProduceJ at Yucca Mountain from Pahute Mesa Underground Nuclear Explosions, SAND85-1605, Sandia National Laboratories (HQS.880517.2896).

Walck, M. C., 1988, "Modeling of Anomalous Ground Motion Observed at Jackass Flats, Nevada Test Site," (abstract), Seism. Res. Lett., 59, 31 (NNA.891106.0220).

APPENDIX A

COMPARISON OF NORMALIZED PSRVS AND CALCULATED RATIOS OF S/D PSRVS

This appendix contains all the normalized PSRVs and calculated ratios of s/d PSRVs discussed in this report. The normalized PSRVs and ratios for each event are presented in one figure. On the plots of normalized PSRVs, the solid line is the downhole PSRV and the dashed line is the surface PSRV. The stations are in numerical order and for each station the vertical PSRVs are presented first, the radial PSRVs next, and the transverse PSRVs last.

Figure A.1. **Relative Normalized PSRVs and Ratios of Surface/Downhole PSRVs for Vertical Motions, Station W25, Event Labquark**

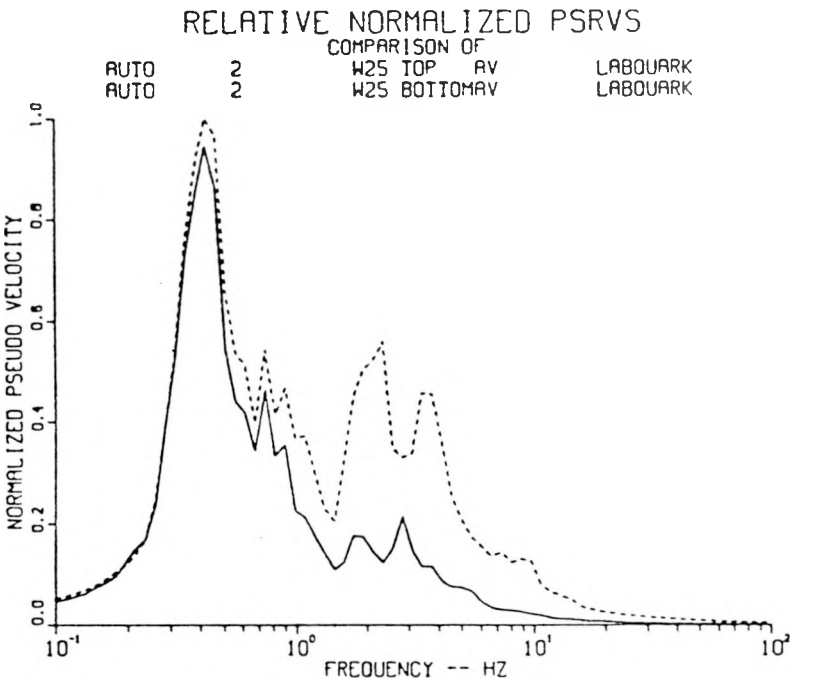

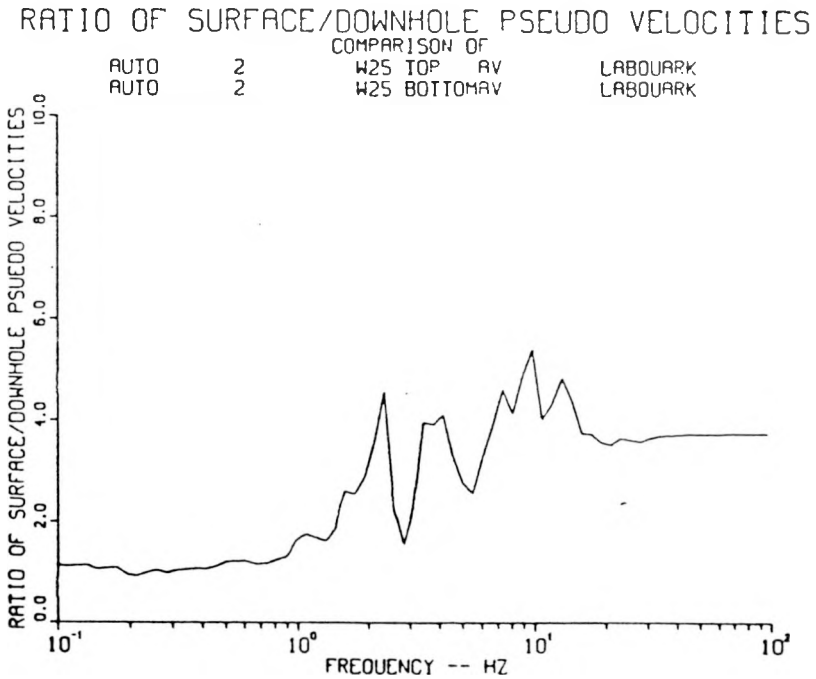

Figure A.2. Relative Normalized PSRVs and Ratios of Surface/Downhole PSRVs for Vertical Motions, Station W25, Event Chancellor

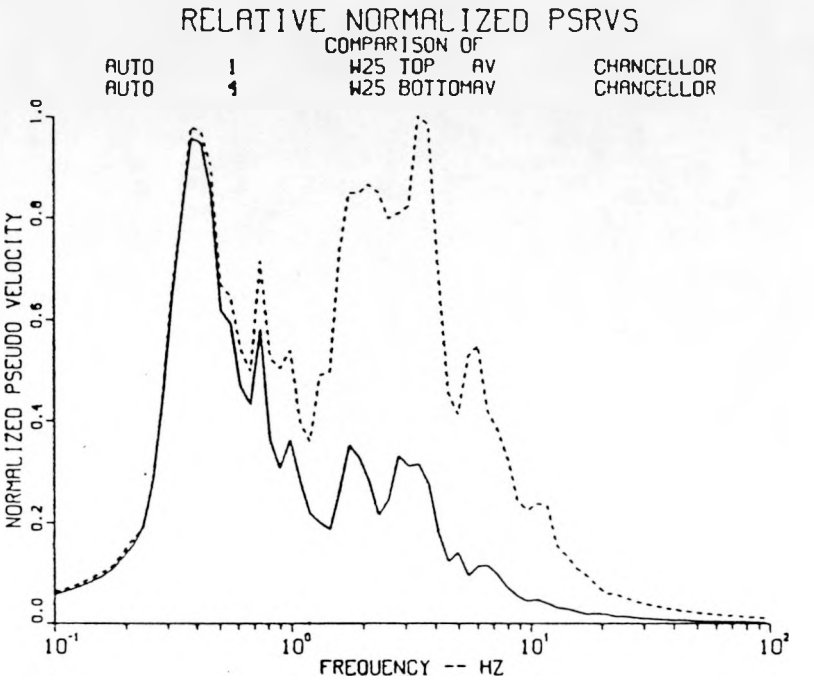

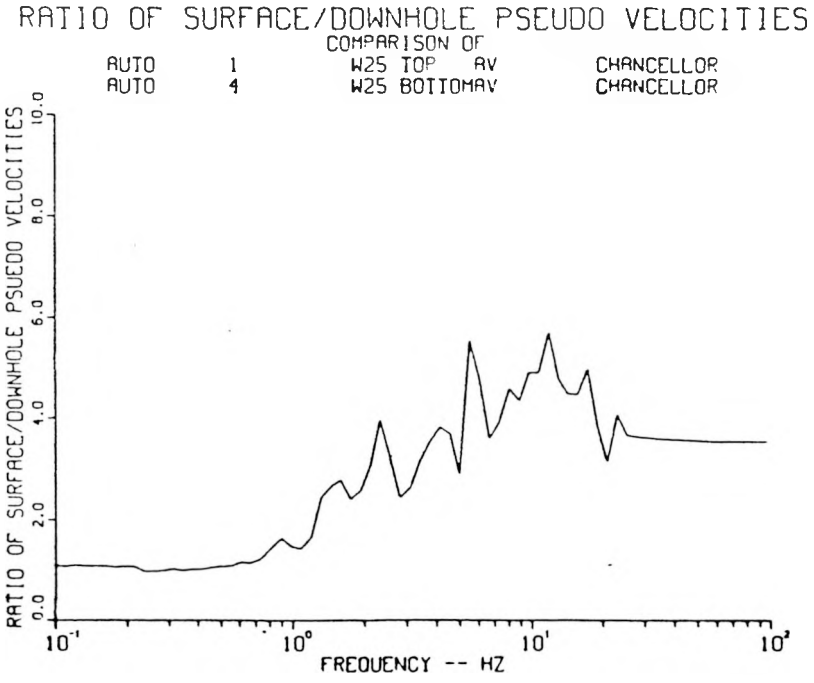

Figure A.3. Relative Normalized PSRVs and Ratios of Surface/Downhole PSRVs for Vertical Motions, Station W25, Event Salut

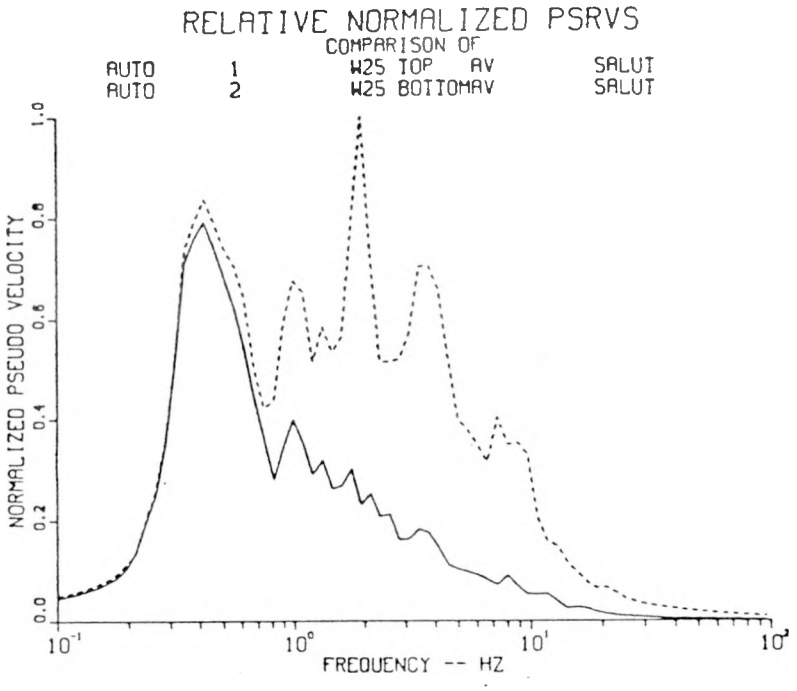

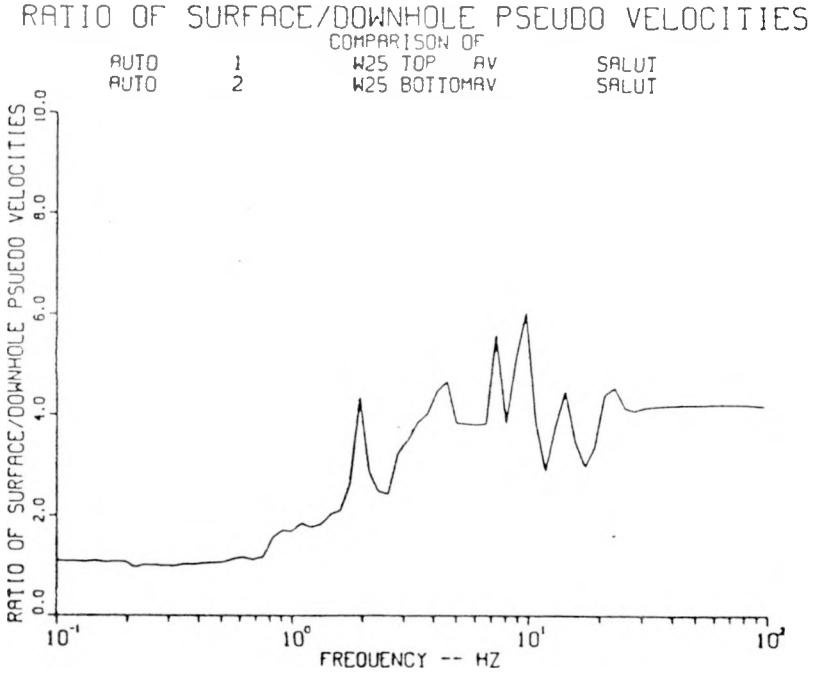

Figure A.4. Relative Normalized PSRVs and Ratios of Surface/Downhole PSRVs for Vertical Motions, Station W25, Event Kappeli

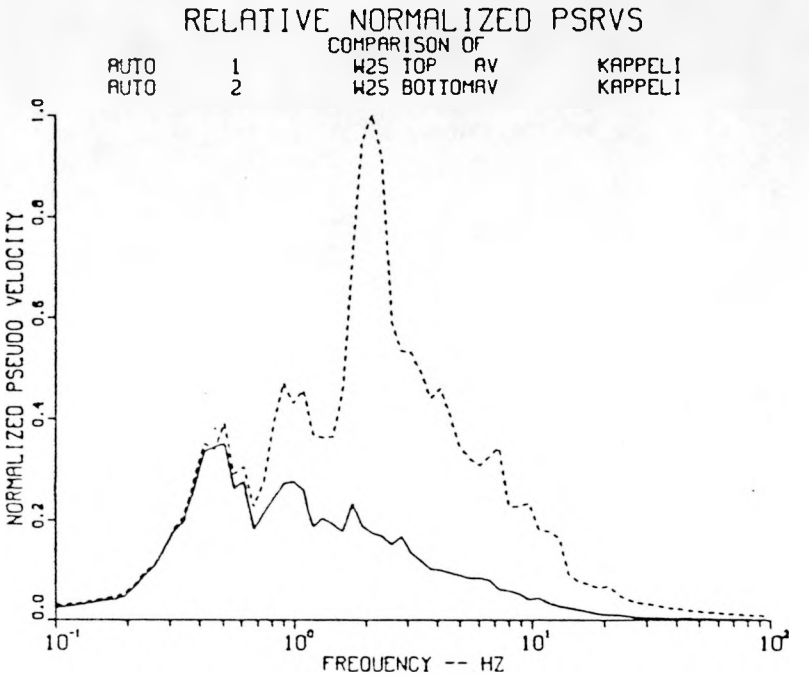

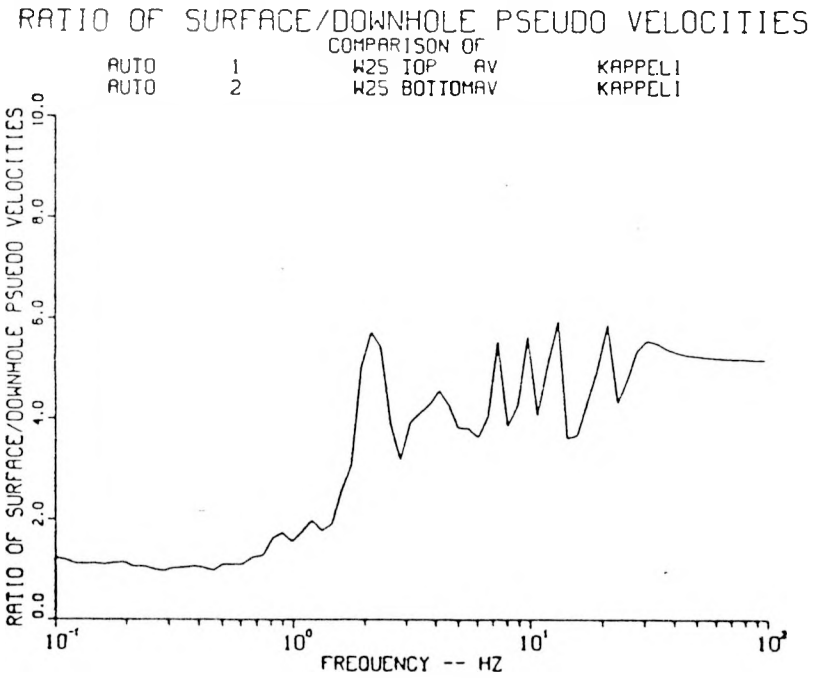

Figure A.5. **Relative Normalized PSRVs and Ratios of Surface/Downhole PSRVs for Vertical Motions, Station W25, Event Jefferson**

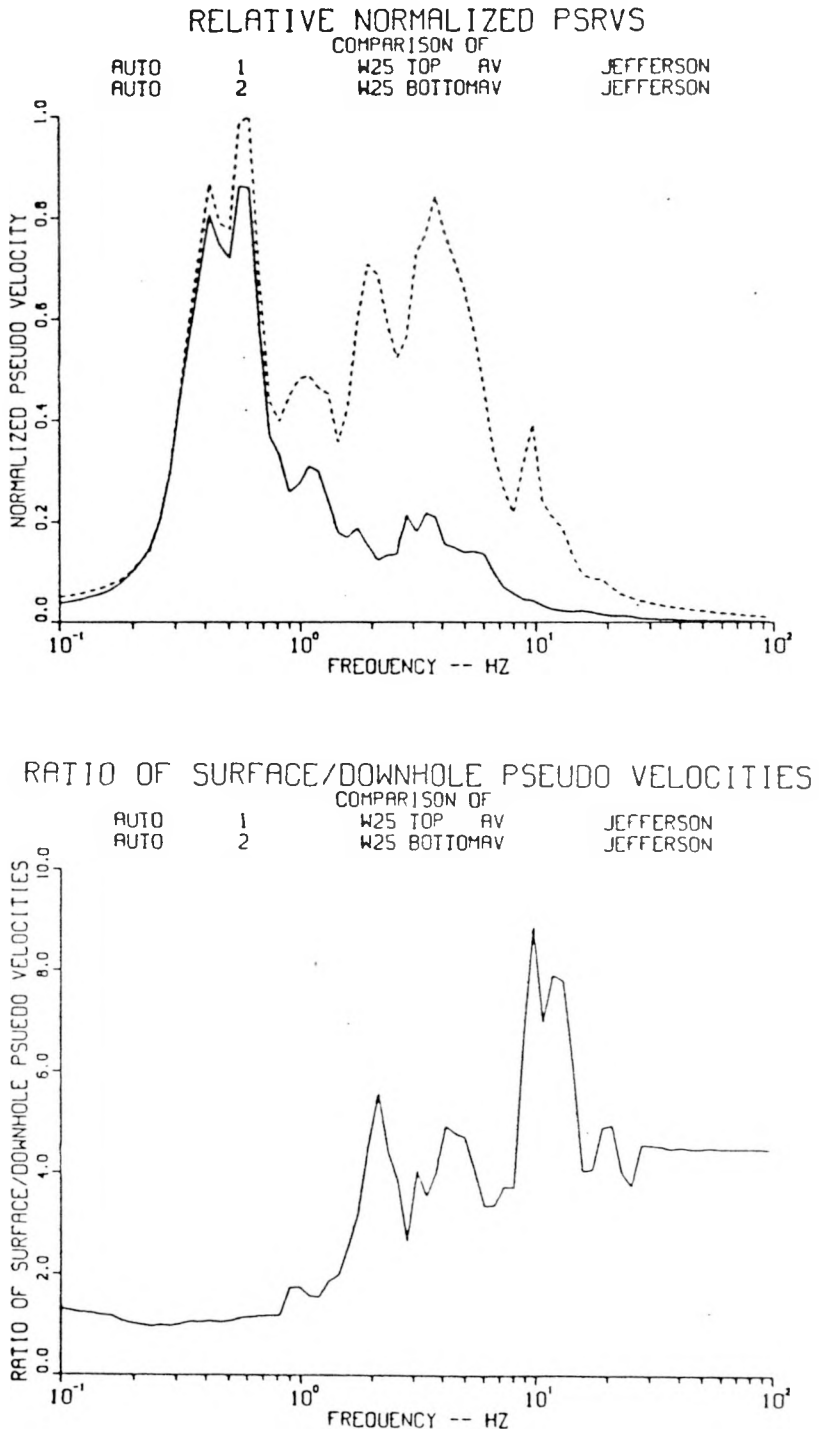

Figure A.6. Relative Normalized PSRVs and Ratios of Surface/Downhole PSRVs for Vertical Motions, Station W25, Event Serena

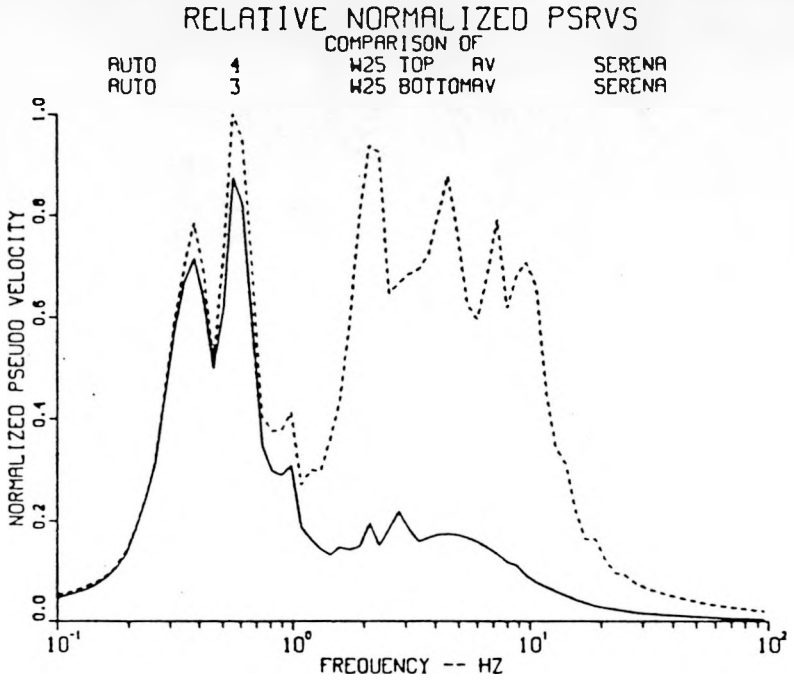

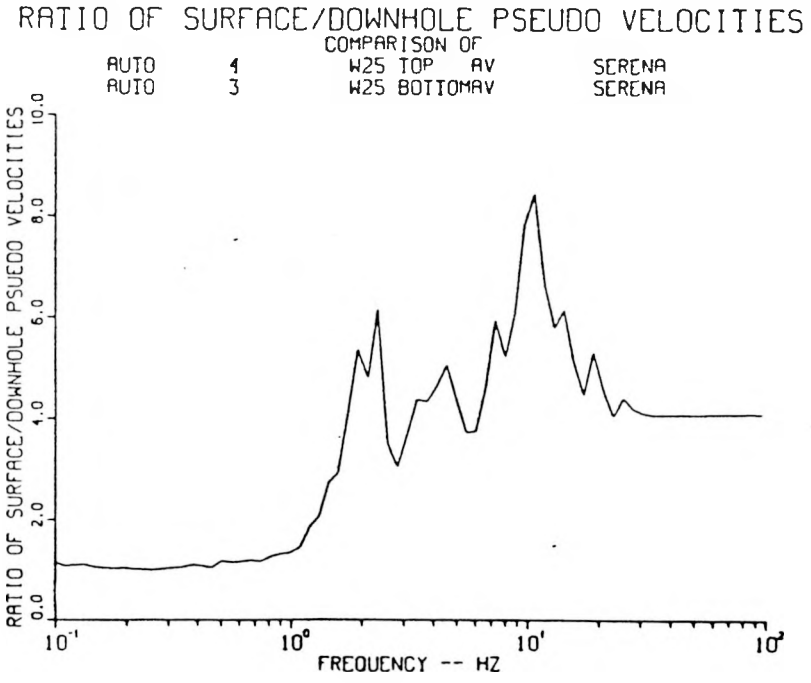

Figure A.7. Relative Normalized PSRVs and Ratios of Surface/Downhole PSRVs for Vertical Motions, Station W25, Event Goldstone

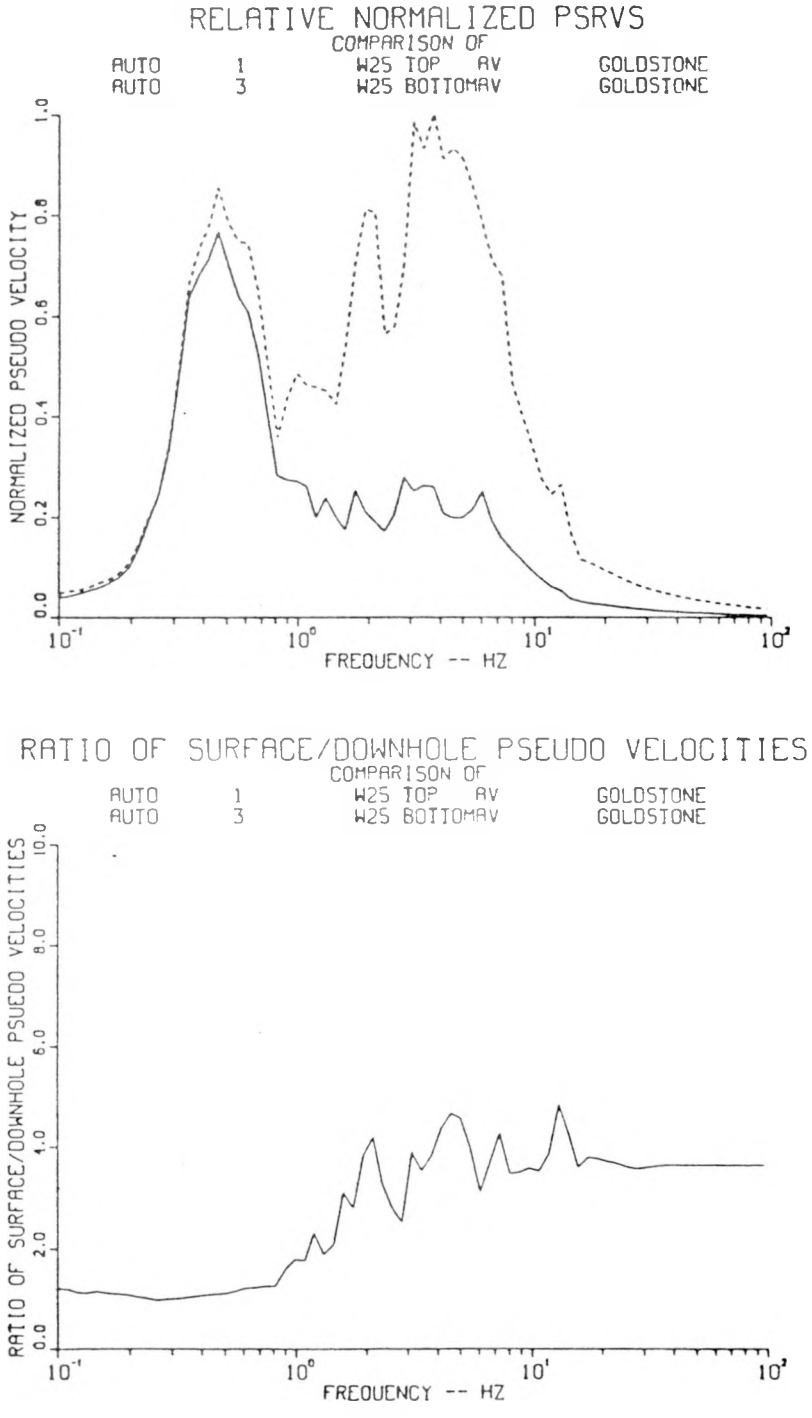

Figure A.8. Relative Normalized PSRVs and Ratios of Surface/Downhole PSRVs for Vertical Motions, Station W25, Event Egmont

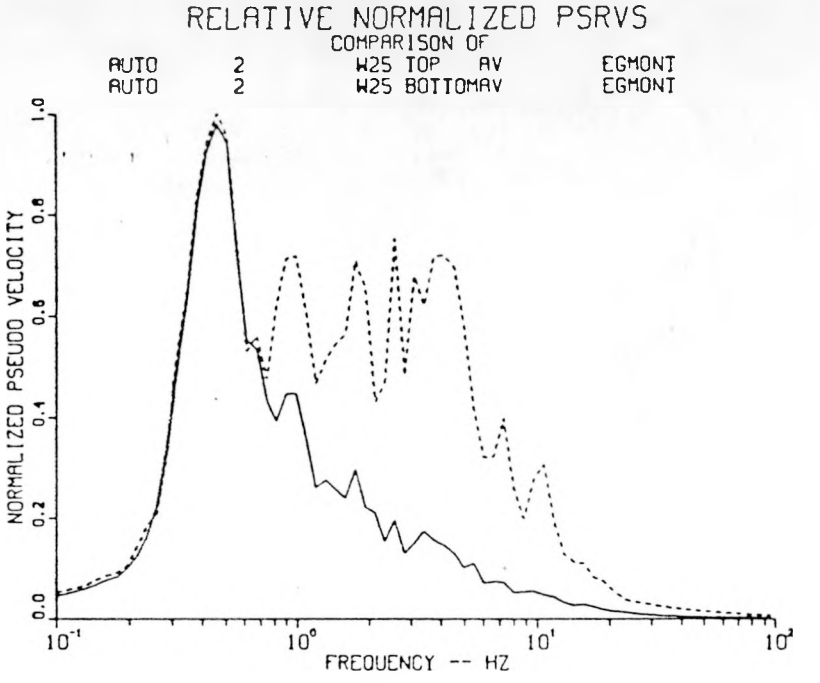

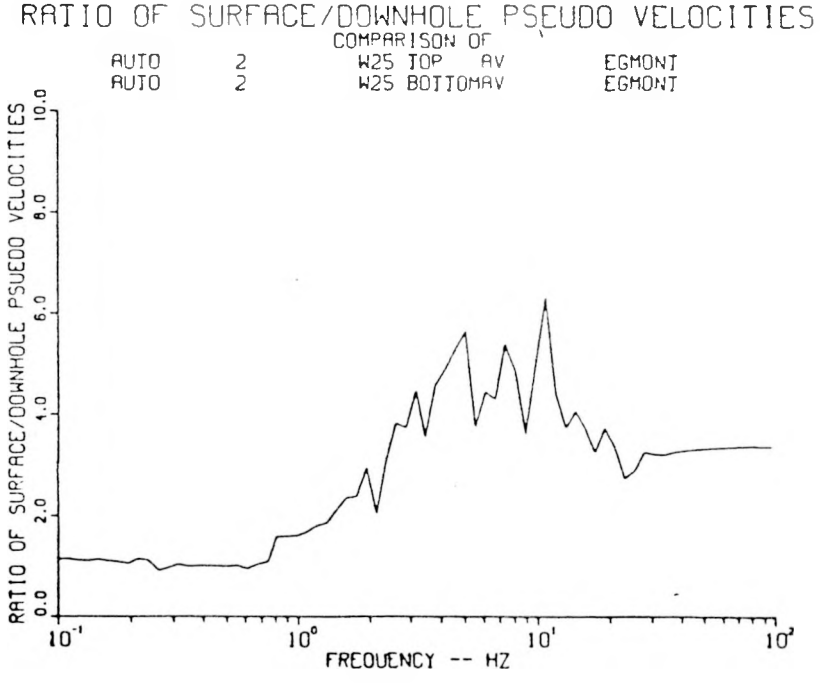

Figure A.9. Relative Normalized PSRVs and Ratios of Surface/Downhole PSRVs for Vertical Motions, Station W25, Event Towanda

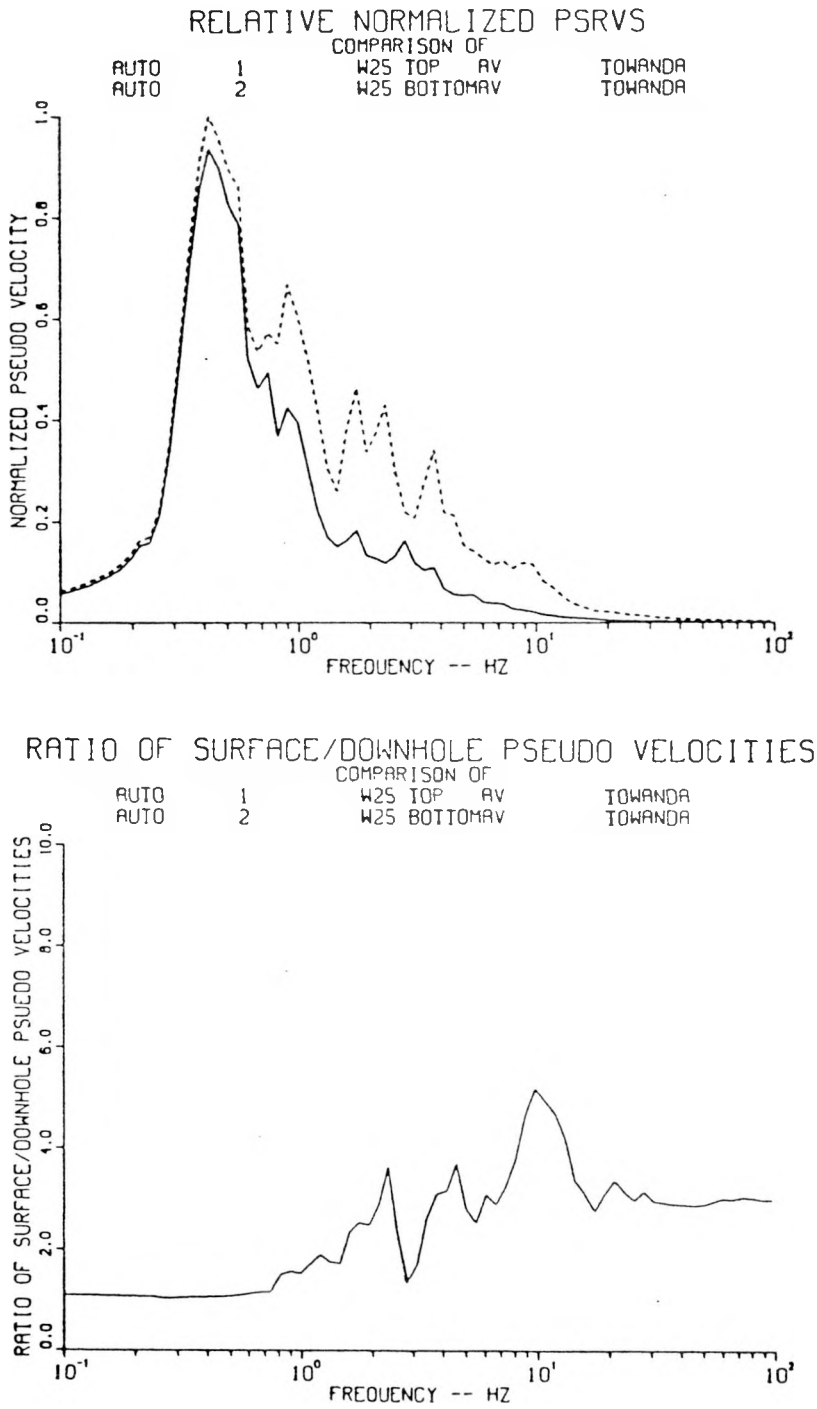

Figure A.10. Relative Normalized PSRVs and Ratios of Surface/Downhole PSRVs for Vertical Motions, Station W25, Event Labquark

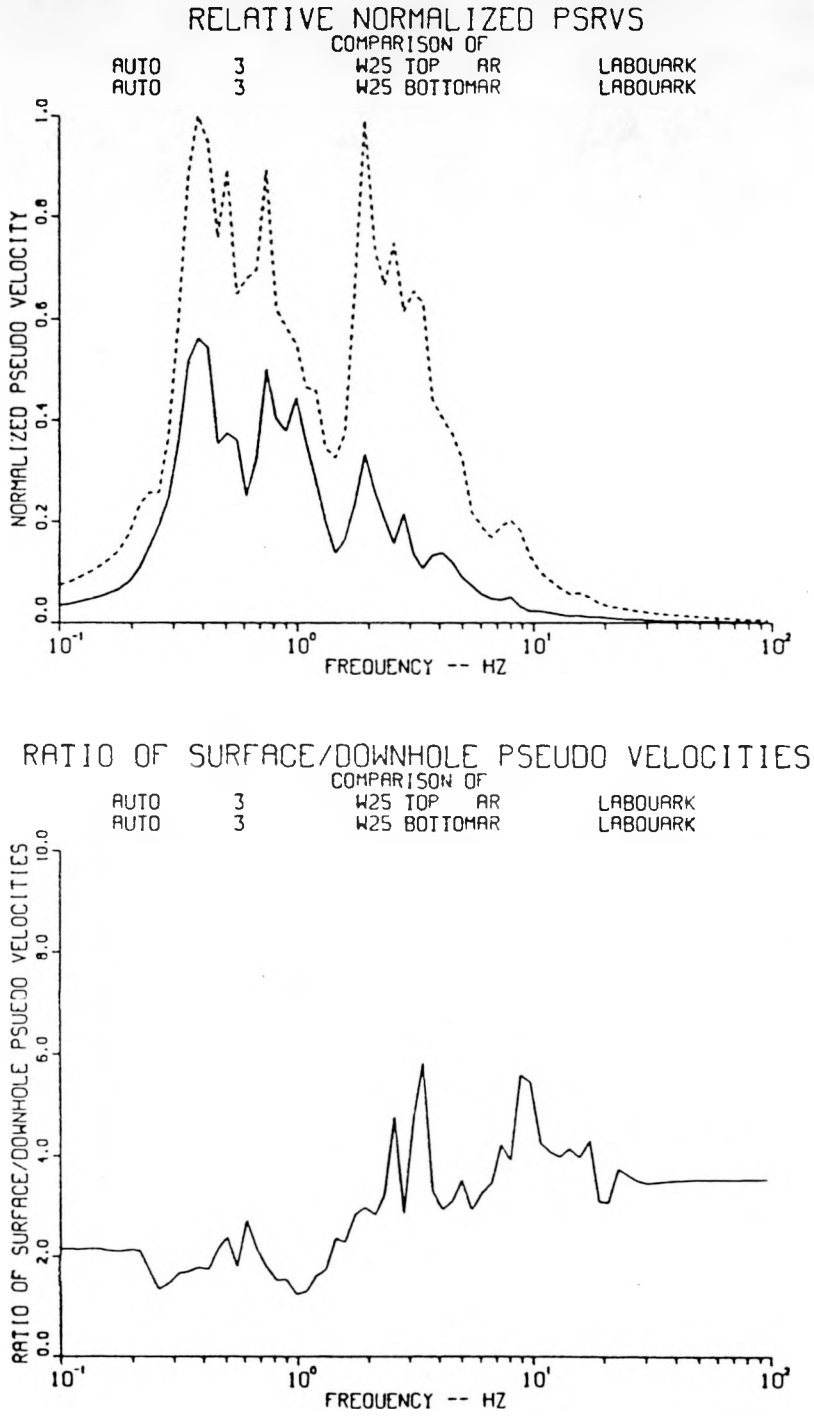

Figure A.11. Relative Normalized PSRVs and Ratios of Surface/Downhole PSRVs for Radial Motions, Station W25, Event Chancellor

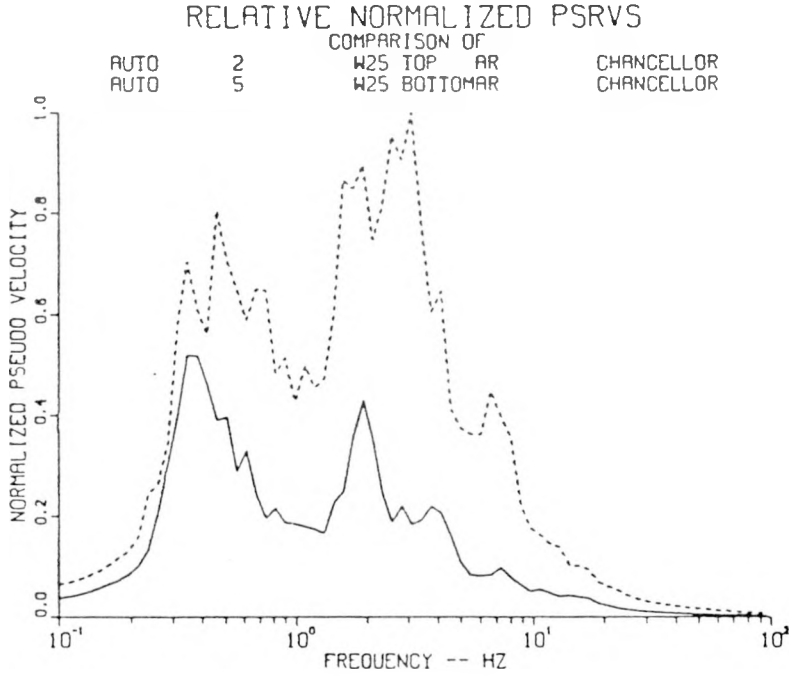

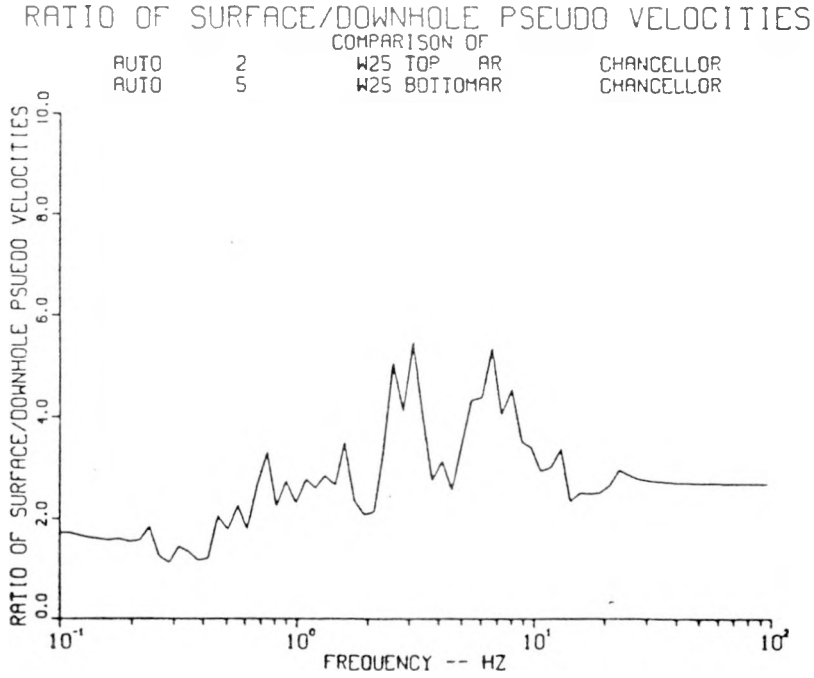

Figure A.12. Relative Normalized PSRVs and Ratios of Surface/Downhole PSRVs for Radial Motions, Station W25, Event Salut

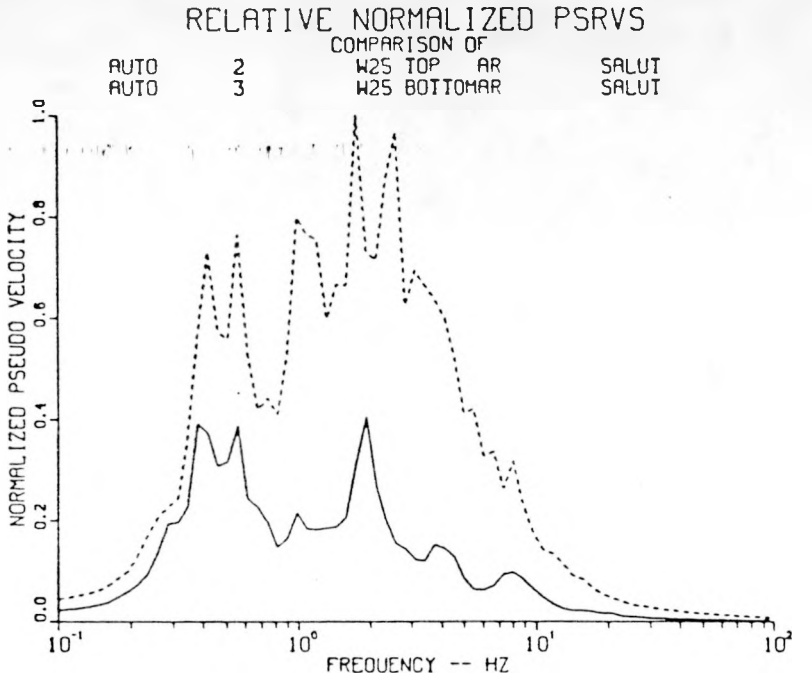

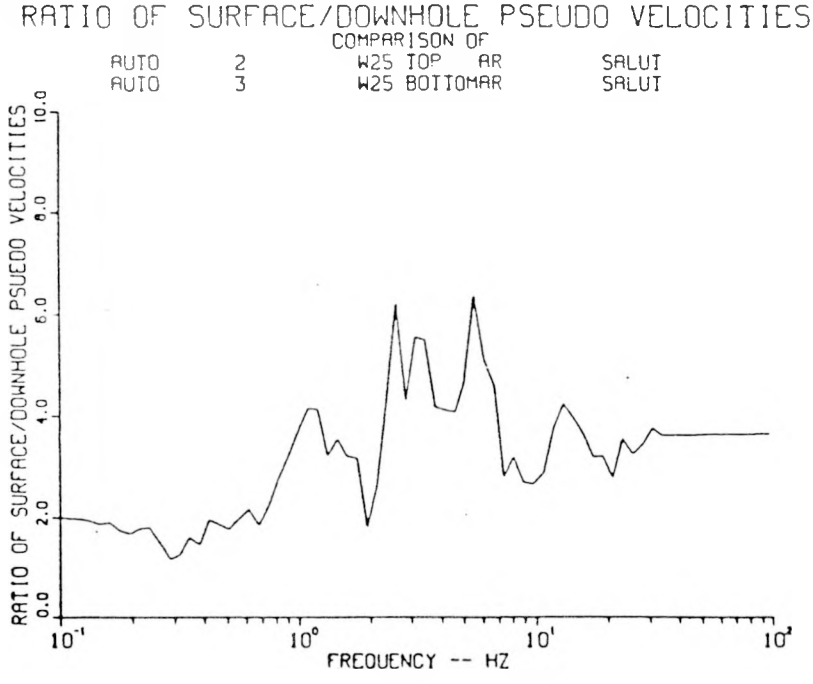

Figure A.13. Relative Normalized PSRVs and Ratios of Surface/Downhole PSRVs for Radial Motions, Station W25, Event Kappeli

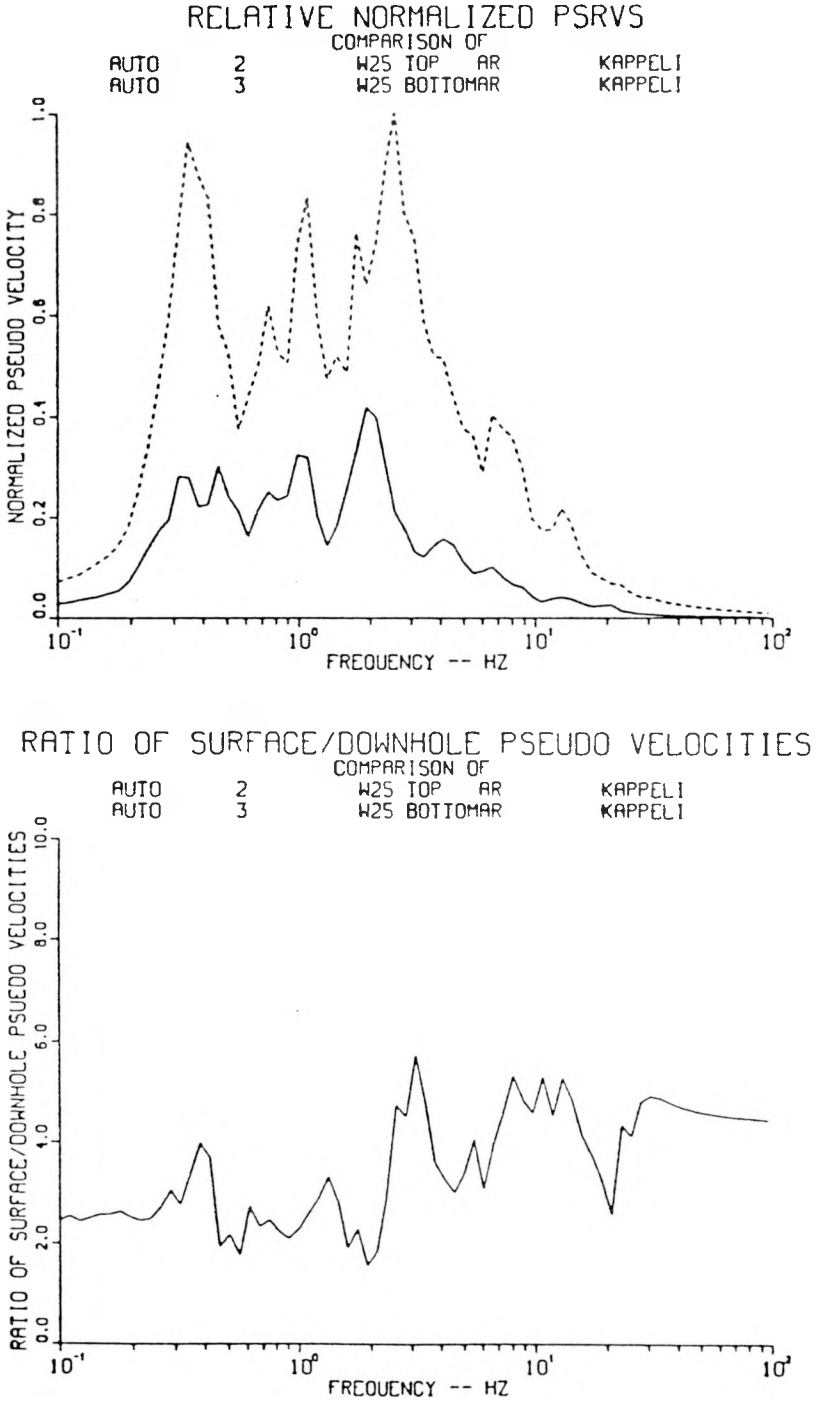

Figure A.14. Relative Normalized PSRVs and Ratios of Surface/Downhole PSRVs for Radial Motions, Station W25, Event Jefferson

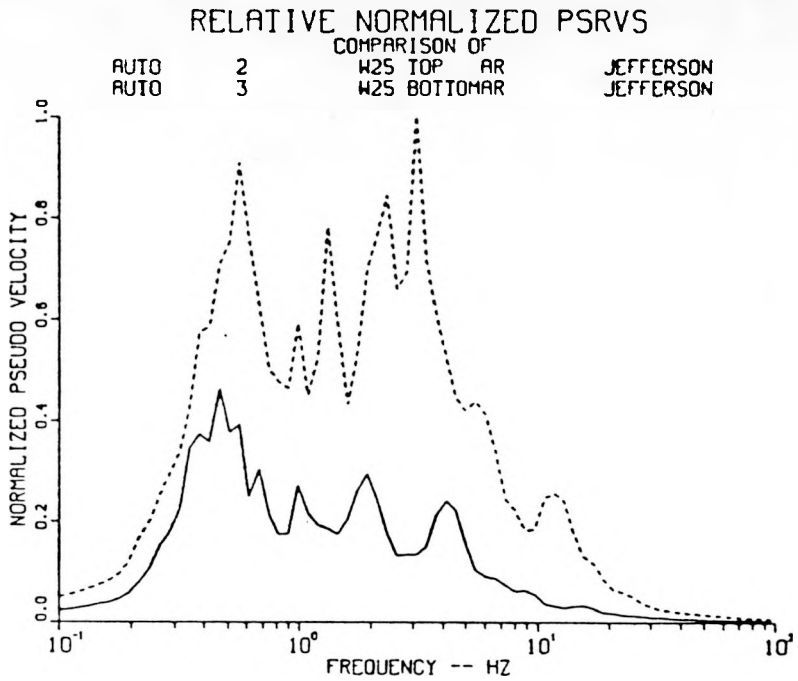

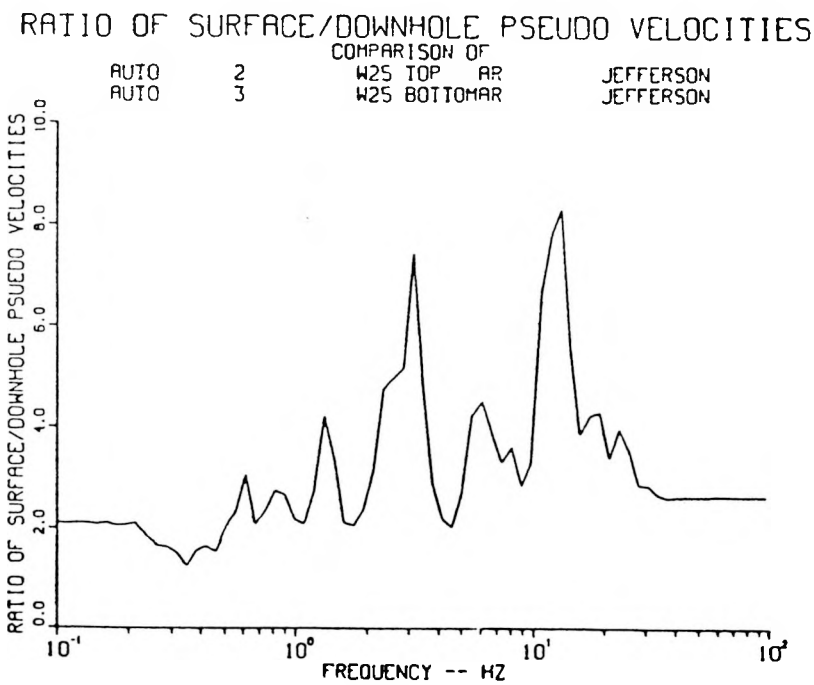

Figure A.15. Relative Normalized PSRVs and Ratios of Surface/Downhole PSRVs for Radial Motions, Station W25, Event Serena

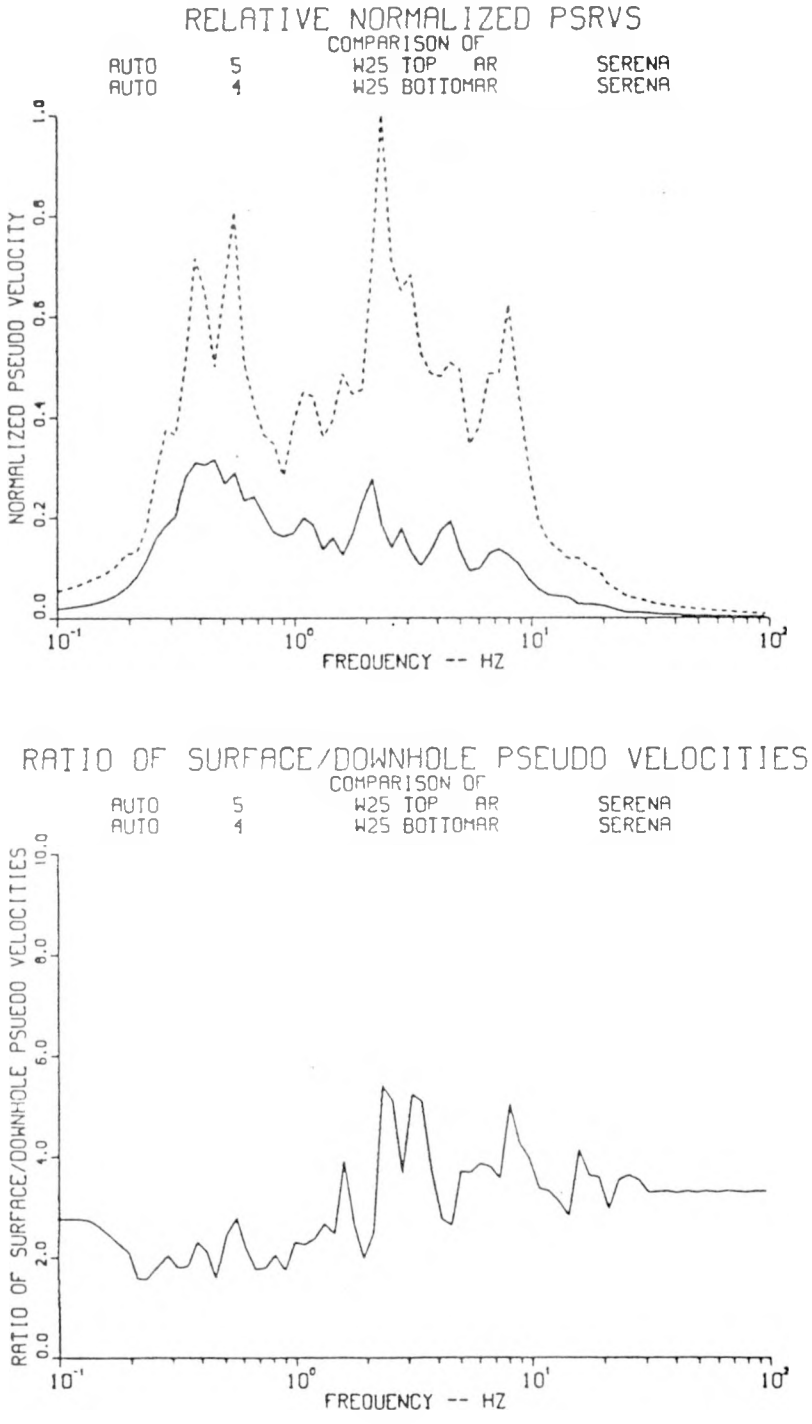

Figure A.16. Relative Normalized PSRVs and Ratios of Surface/Downhole PSRVs for Radial Motions, Station W25, Event Goldstone

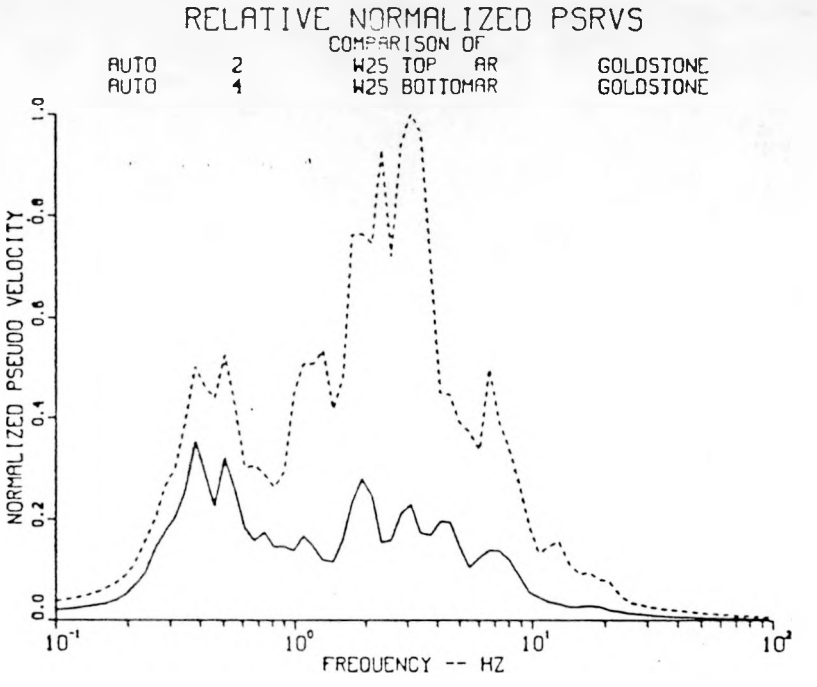

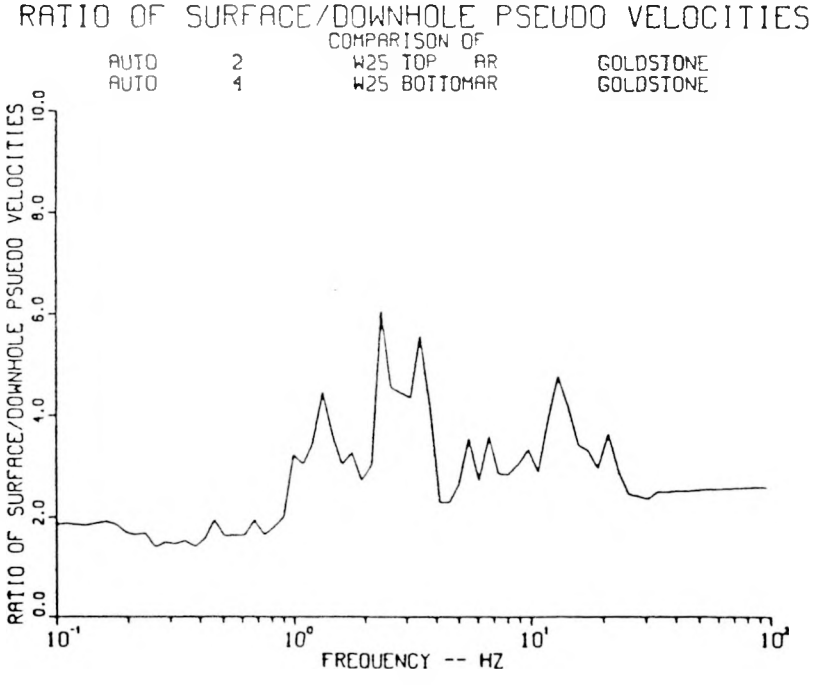

Figure A.17. Relative Normalized PSRVs and Ratios of Surface/Downhole PSRVs for Radial Motions, Station W25, Event Egmont

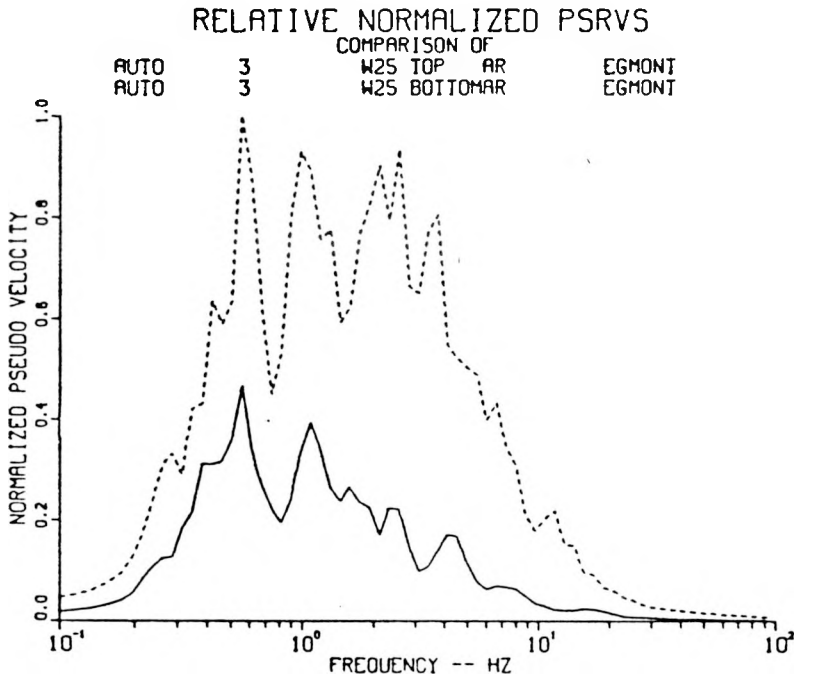

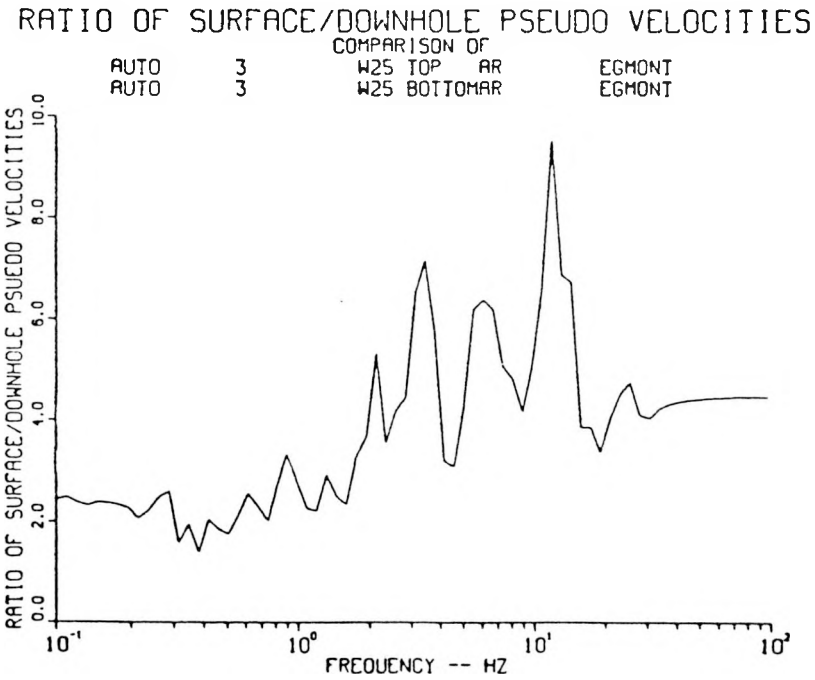

Figure A.18. Relative Normalized PSRVs and Ratios of Surface/Downhole PSRVs for Radial Motions, Station W25, Event Towanda

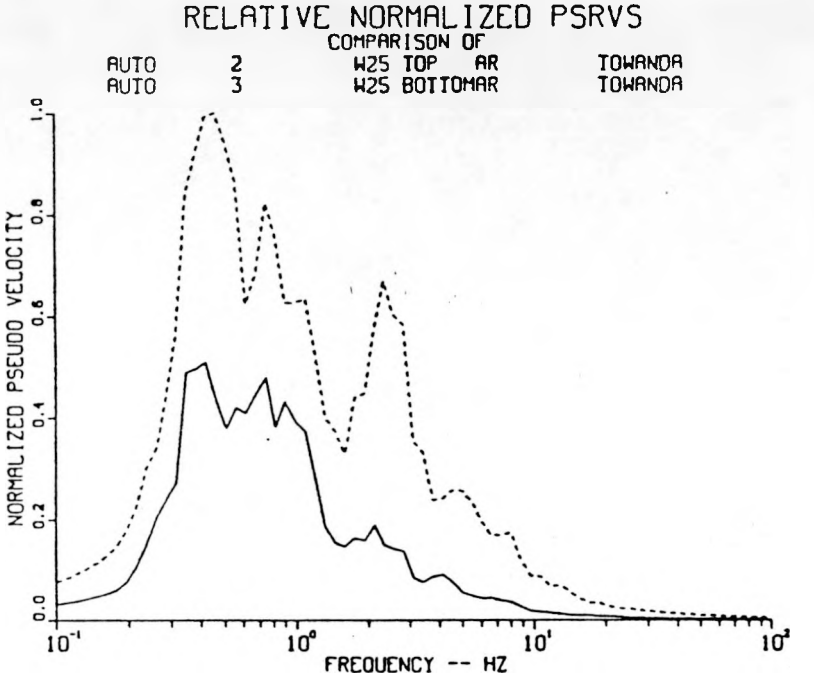

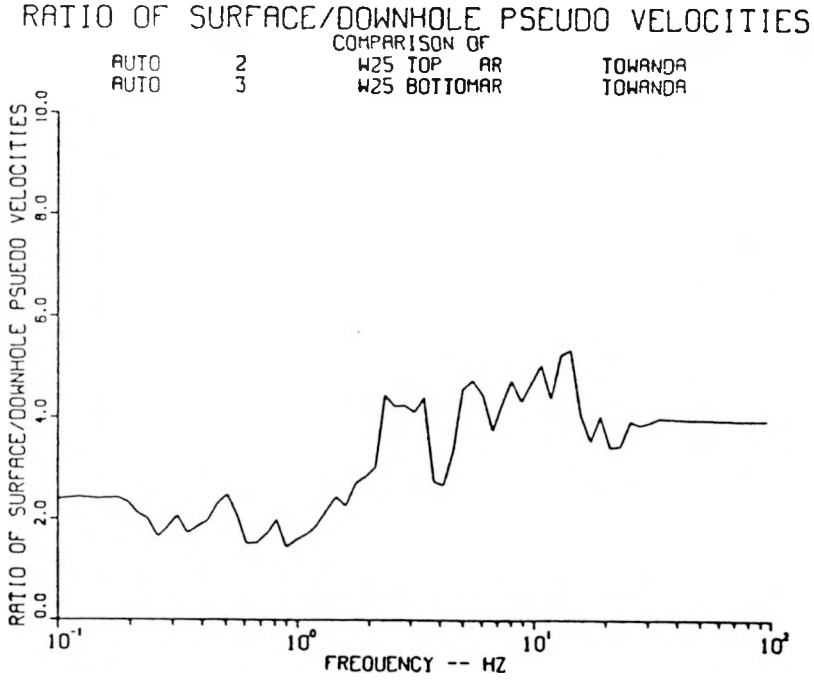

Figure A.19. Relative Normalized PSRVs and Ratios of Surface/Downhole PSRVs for Transverse Motions, Station W25, Event Labquark

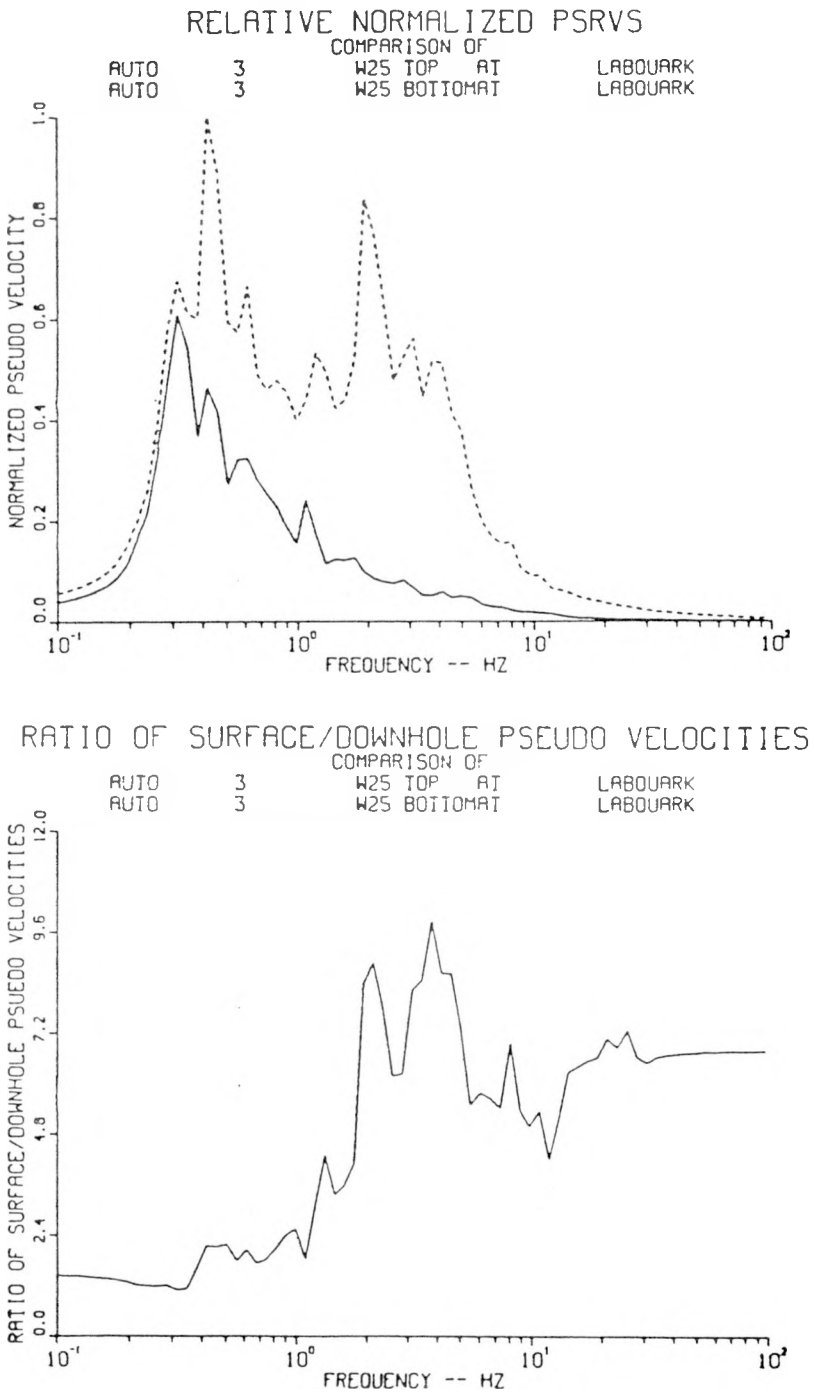

Figure A.20. Relative Normalized PSRVs and Ratios of Surface/Downhole PSRVs for Transverse Motions, Station W25, Event Chancellor

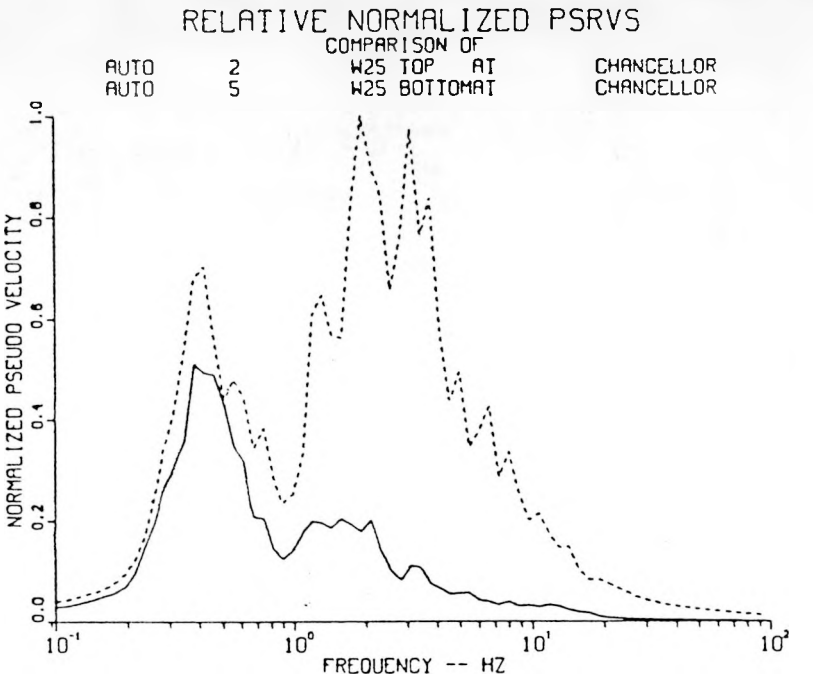

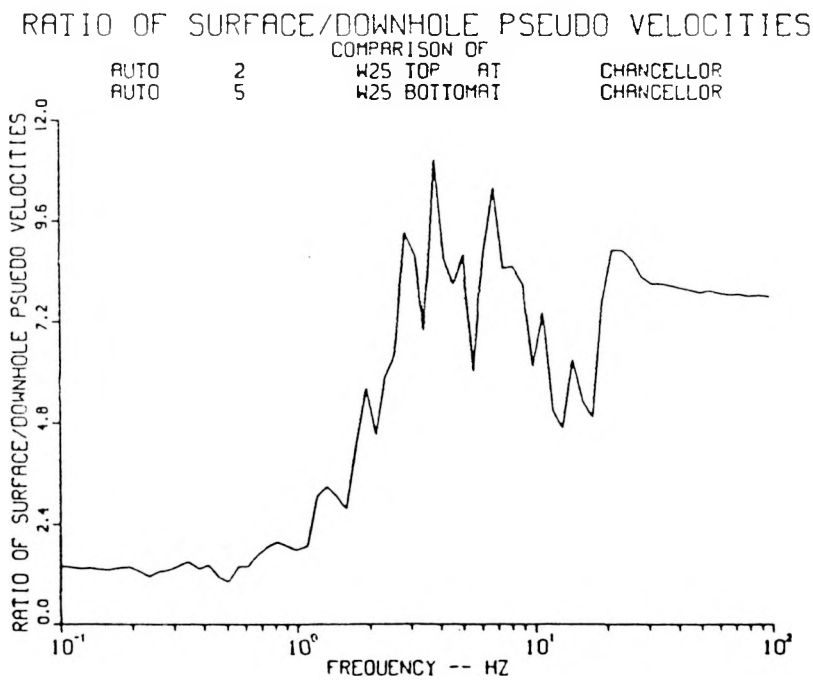

Figure A.21. Relative Normalized PSRVs and Ratios of Surface/Downhole PSRVs for Transverse Motions, Station W25, Event Salut

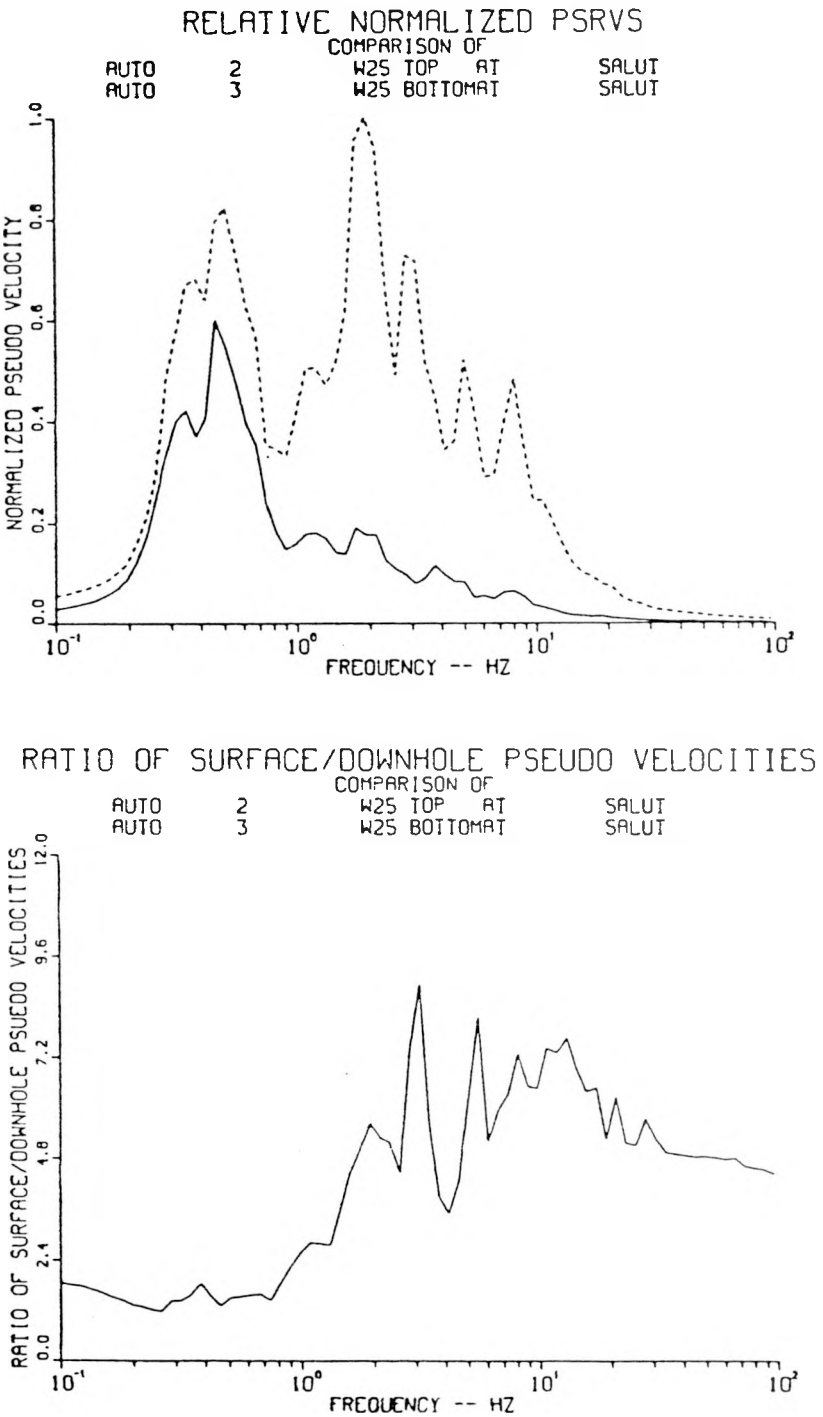

Figure A.22. Relative Normalized PSRVs and Ratios of Surface/Downhole PSRVs for Transverse Motions, Station W25, Event Kappeli

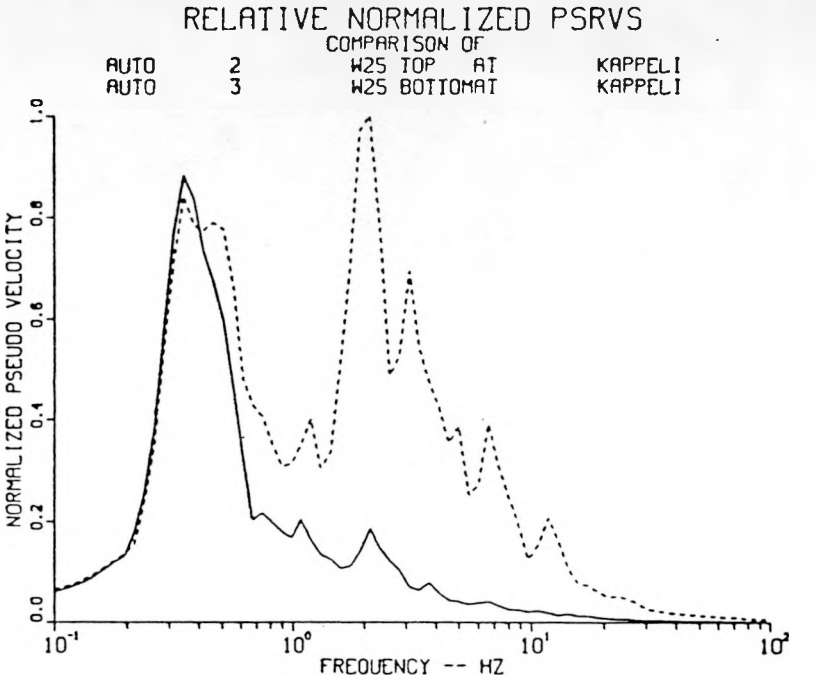

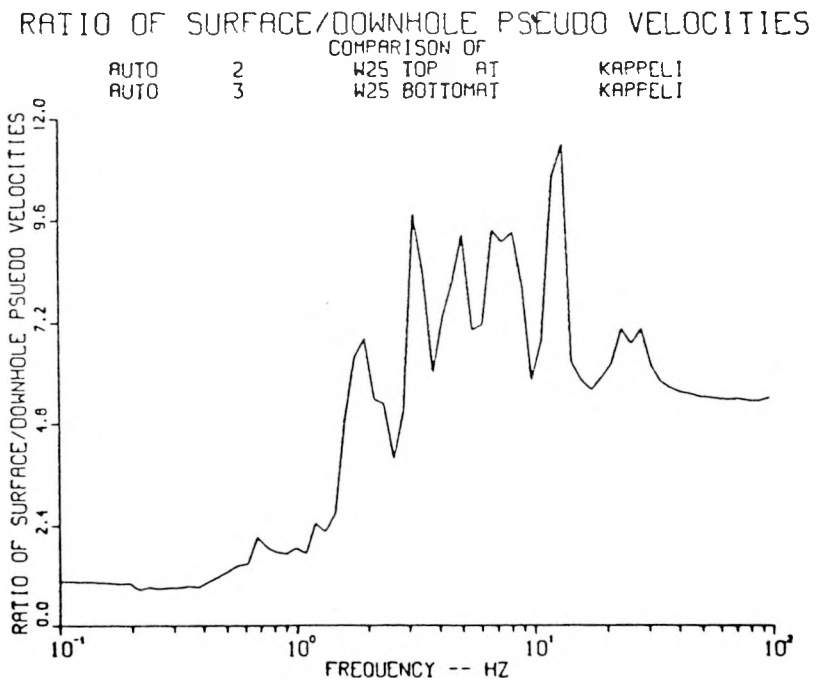

Figure A.23. Relative Normalized PSRVs and Ratios of Surface/Downhole PSRVs for Transverse Motions, Station W25, Event Jefferson

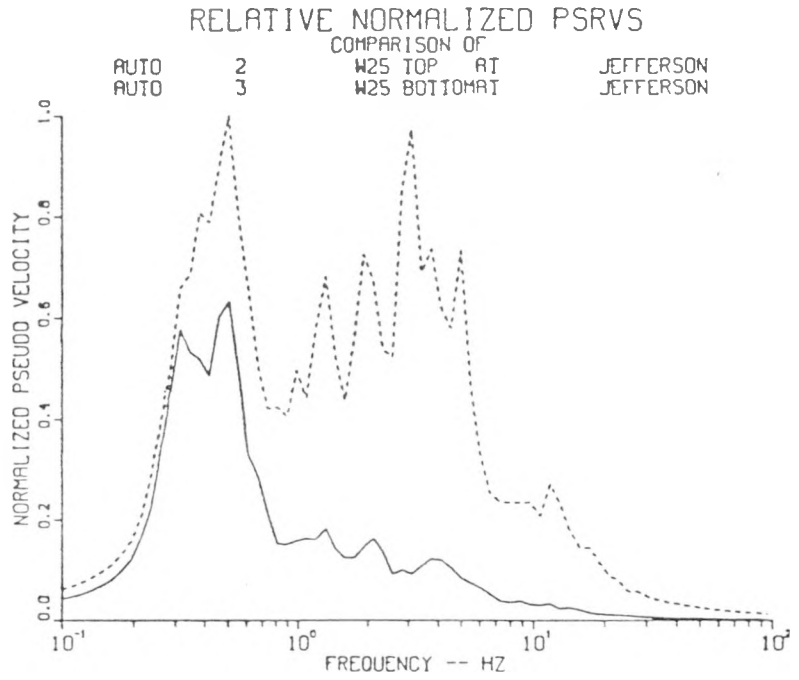

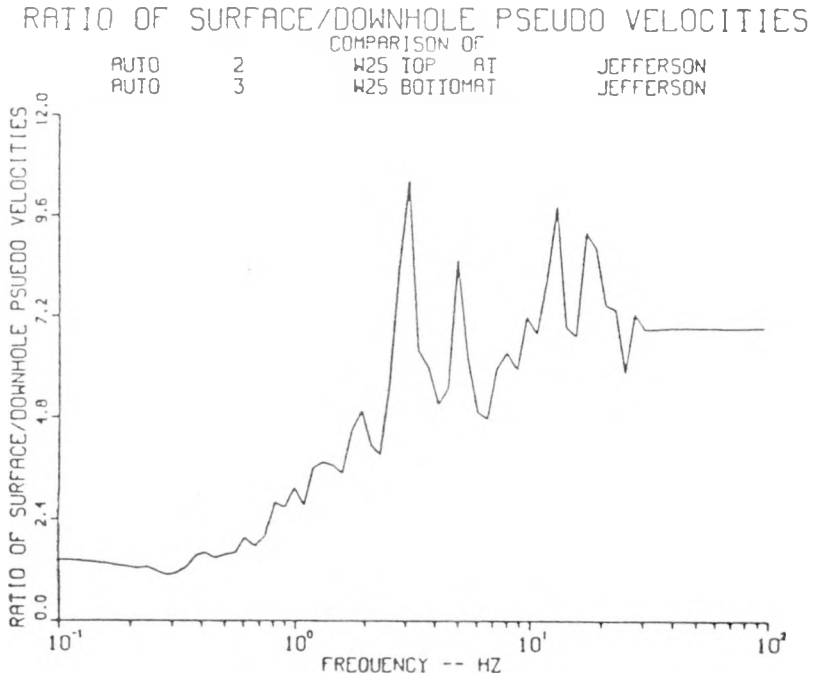

Figure A.24. Relative Normalized PSRVs and Ratios of Surface/Downhole PSRVs for Transverse Motions, Station W25, Event Serena

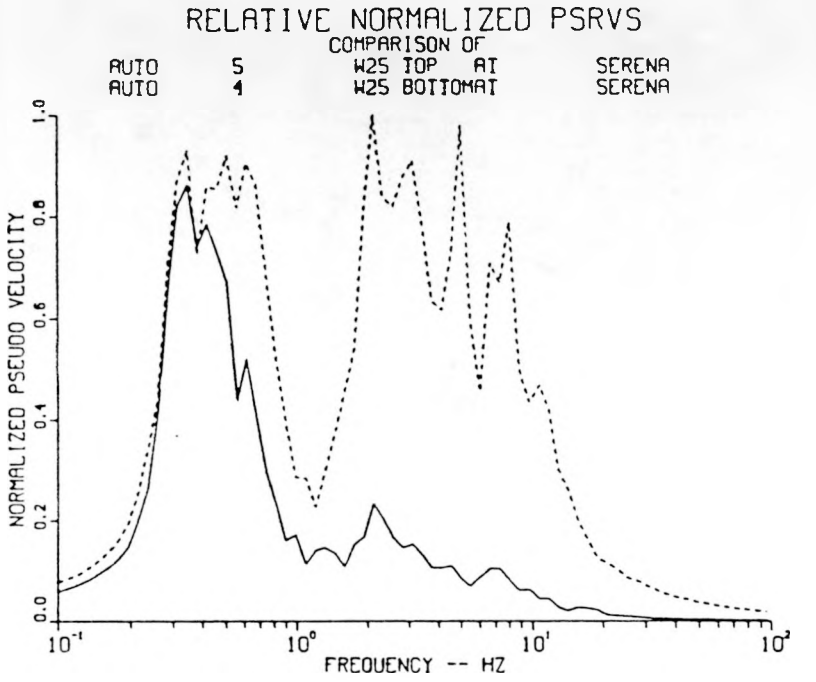

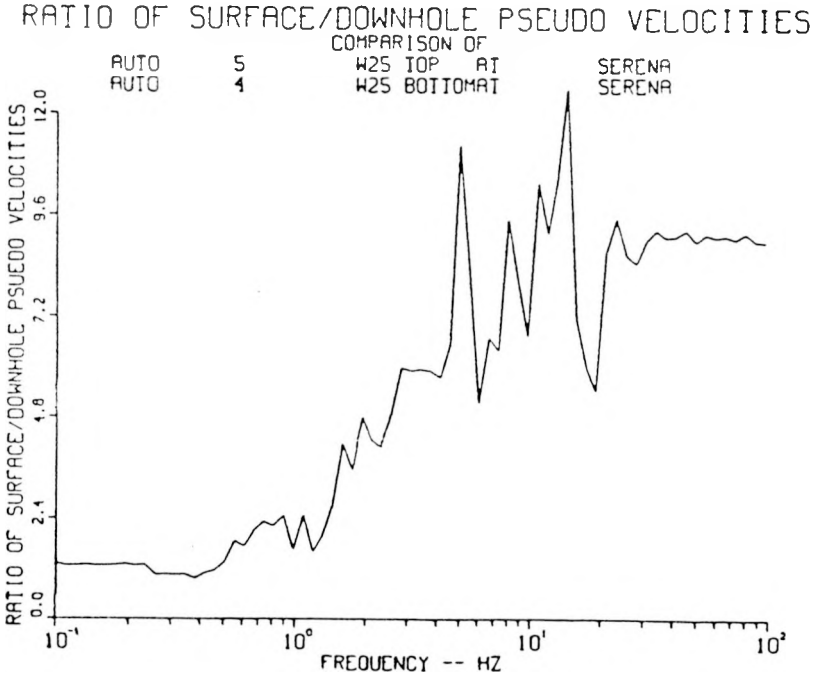

Figure A.25. Relative Normalized PSRVs and Ratios of Surface/Downhole PSRVs for Transverse Motions, Station W25, Event Goldstone

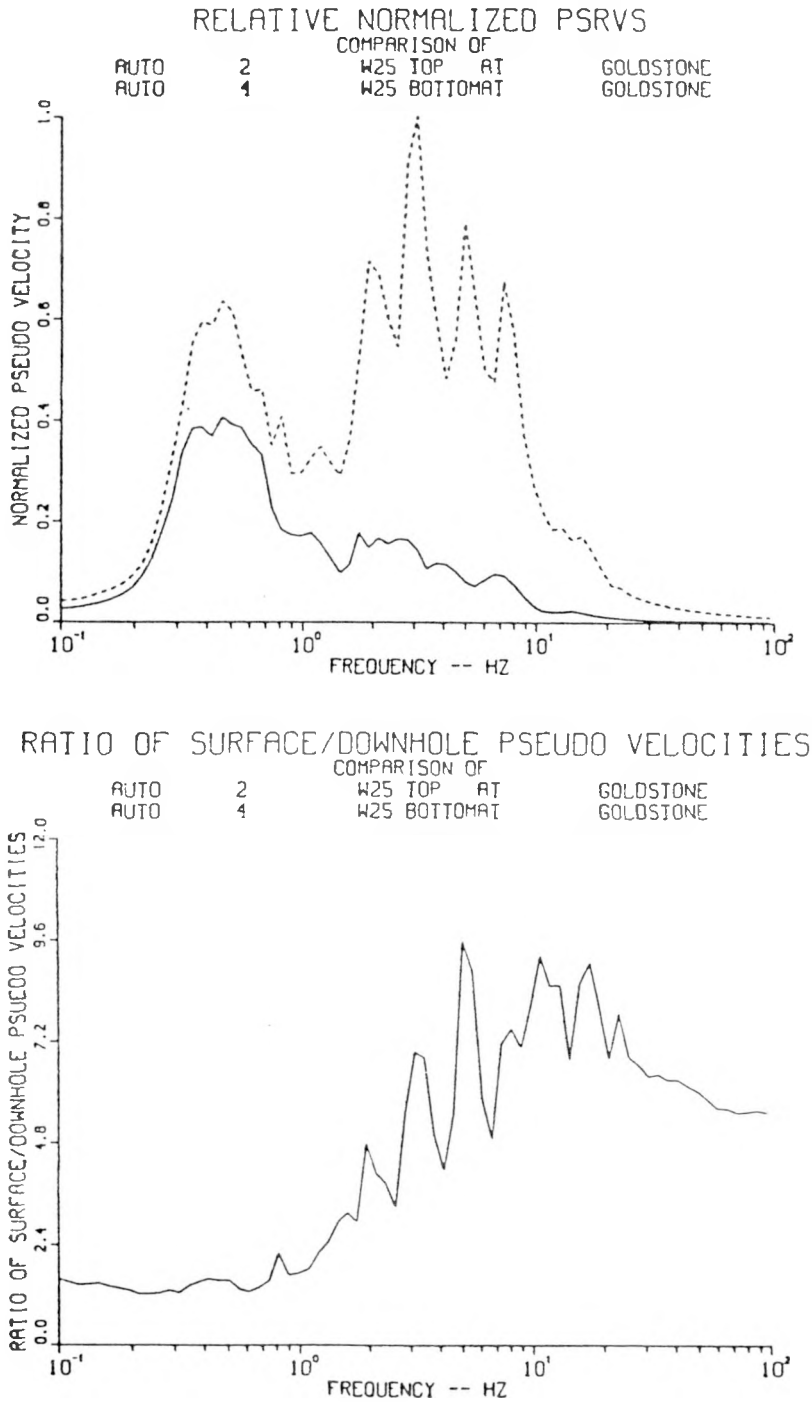

Figure A.26. Relative Normalized PSRVs and Ratios of Surface/Downhole PSRVs for Transverse Motions, Station W25, Event Egmont

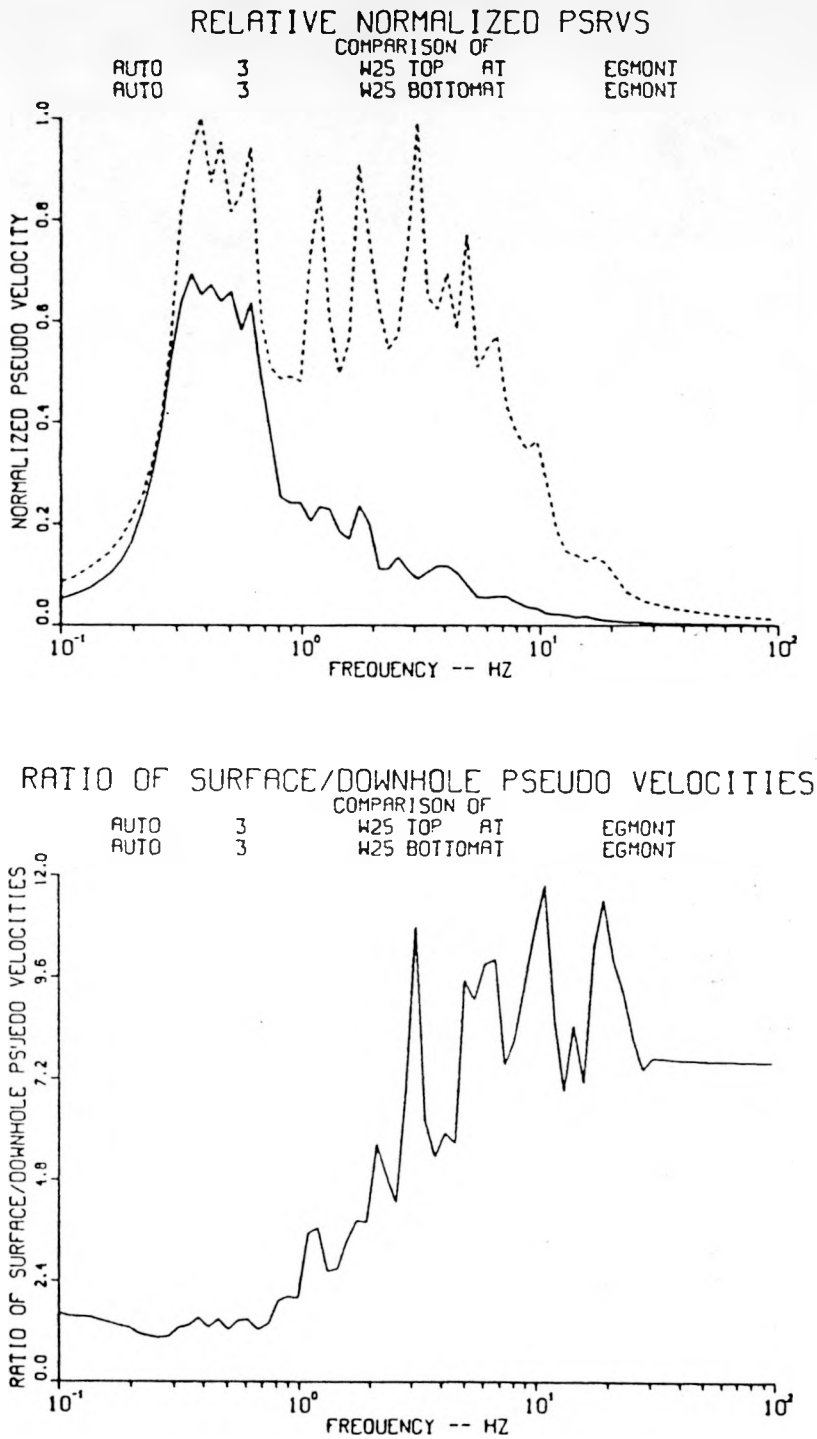

Figure A.27. Relative Normalized PSRVs and Ratios of Surface/Downhole PSRVs for Transverse Motions, Station W25, Event Towanda

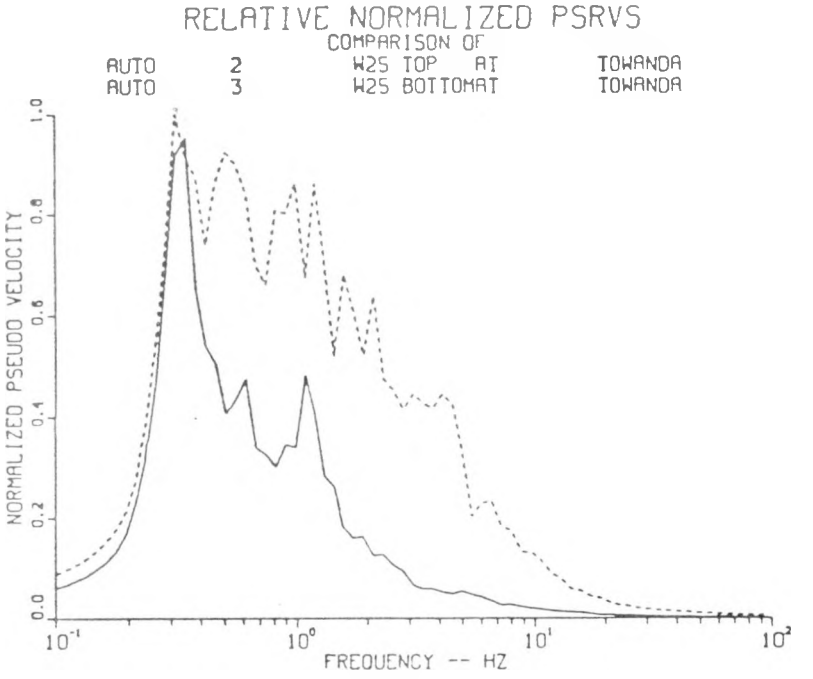

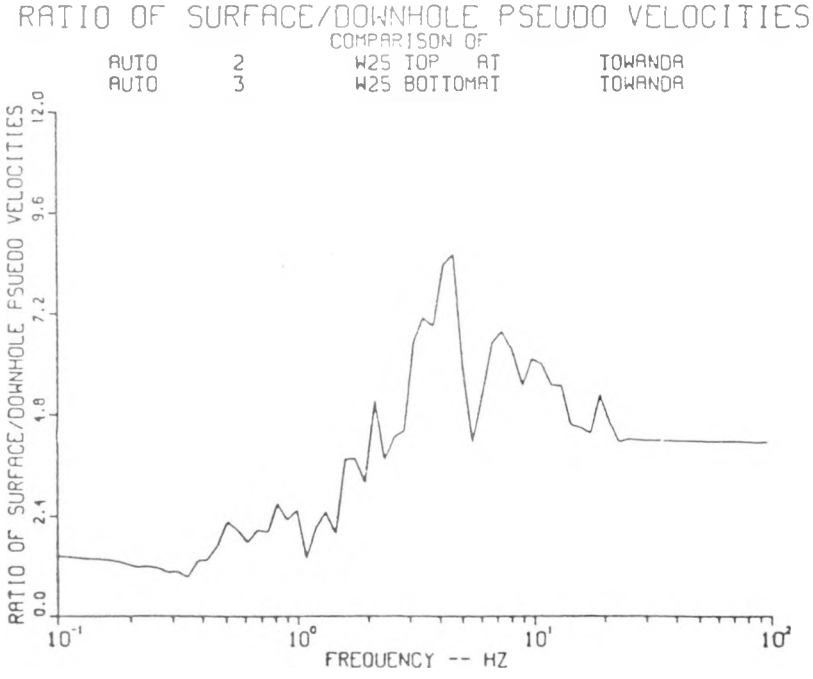

Figure A.28. Relative Normalized PSRVs and Ratios of Surface/Downhole PSRVs for Vertical Motions, Station W28, Event Labquark

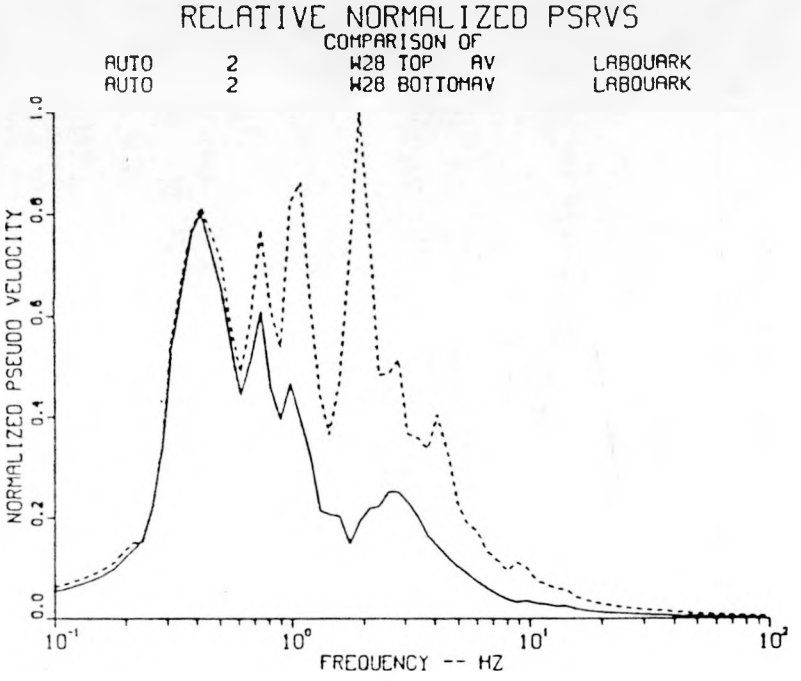

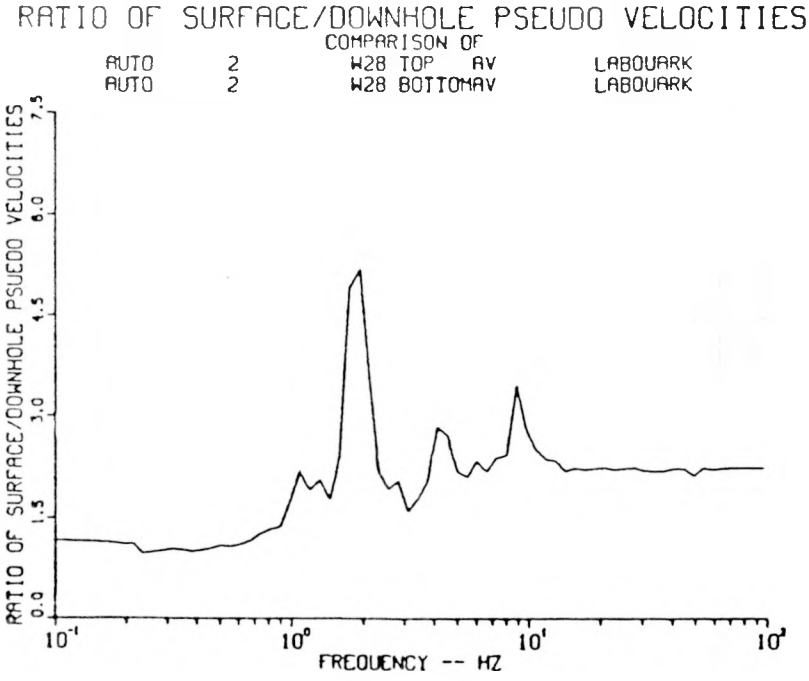

Figure A.29. Relative Normalized PSRVs and Ratios of Surface/Downhole PSRVs for Vertical Motions, Station W28, Event Tierra

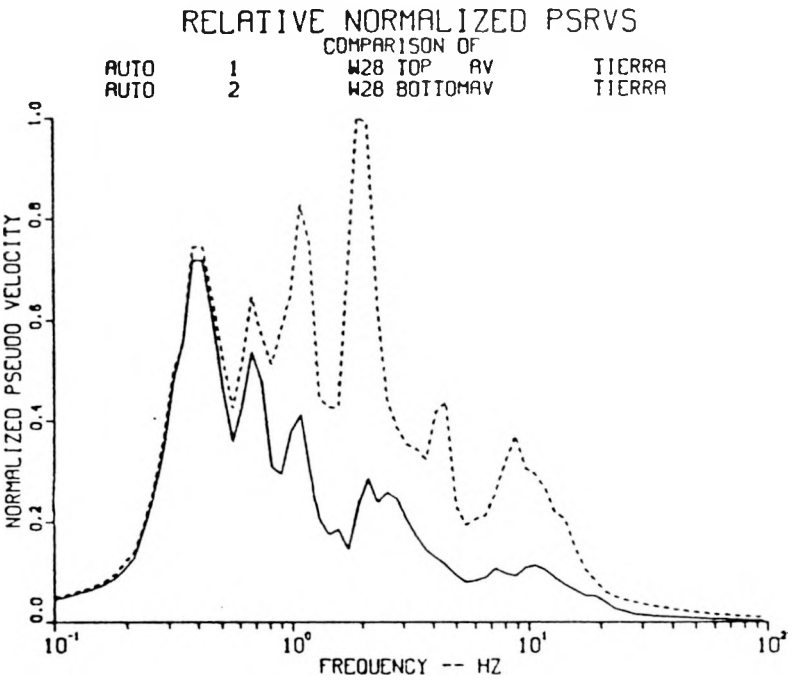

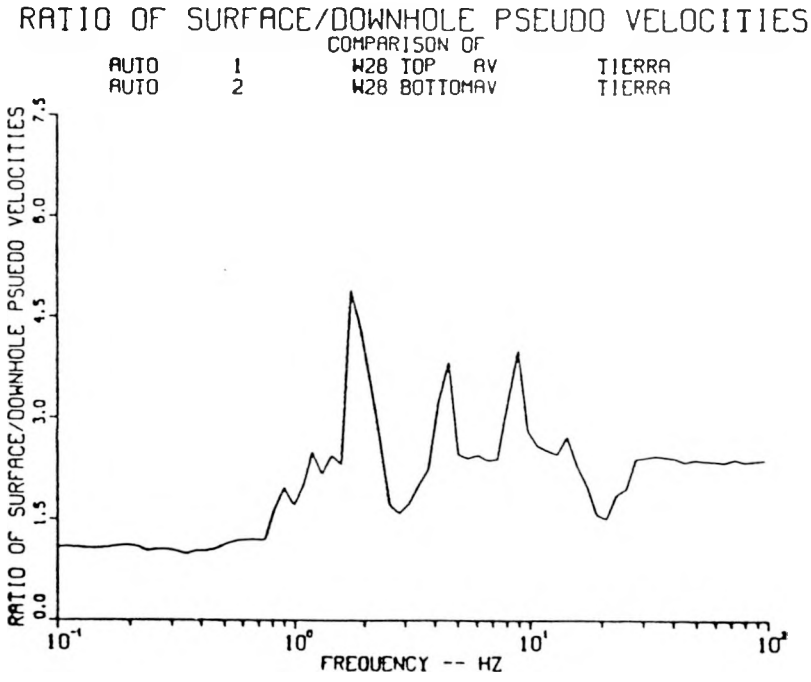

Figure A.30. Relative Normalized PSRVs and Ratios of Surface/Downhole PSRVs for Vertical Motions, Station W28, Event Salut

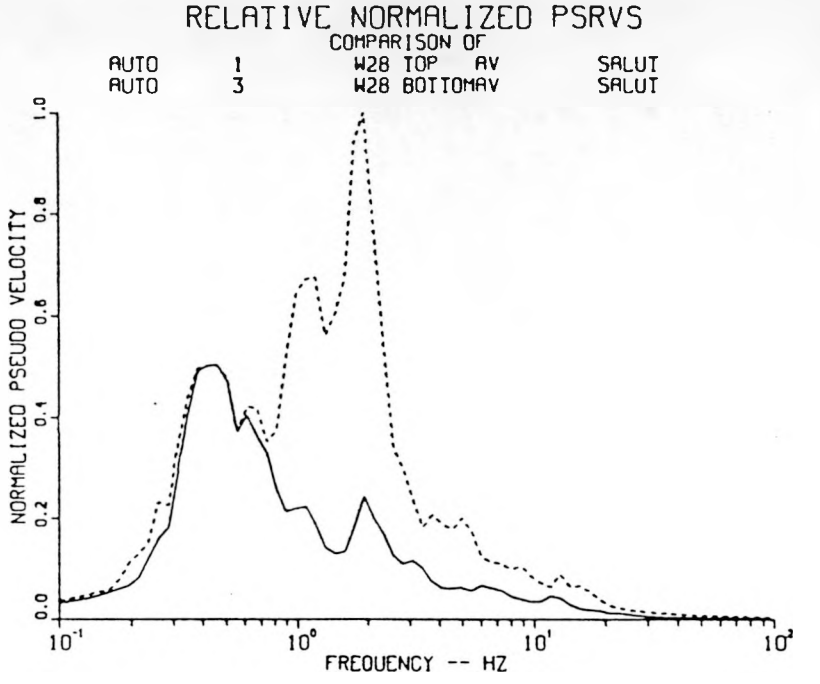

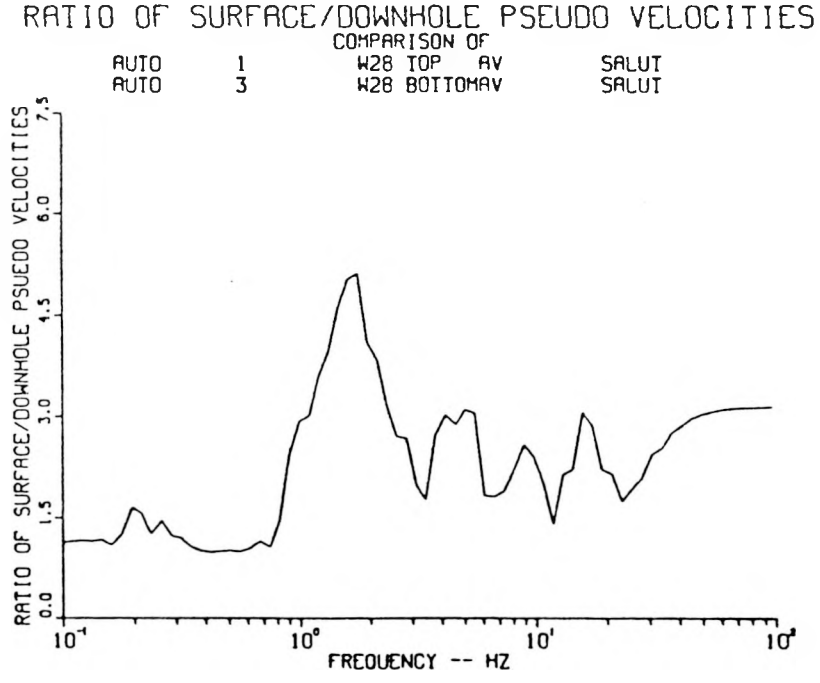

Figure A.31. Relative Normalized PSRVs and Ratios of Surface/Downhole PSRVs for Vertical Motions, Station W28, Event Jefferson

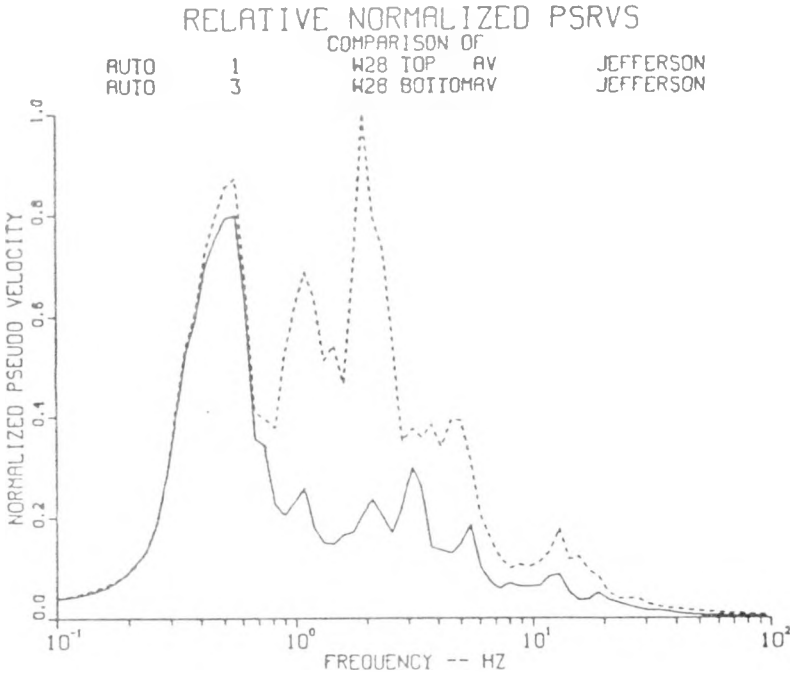

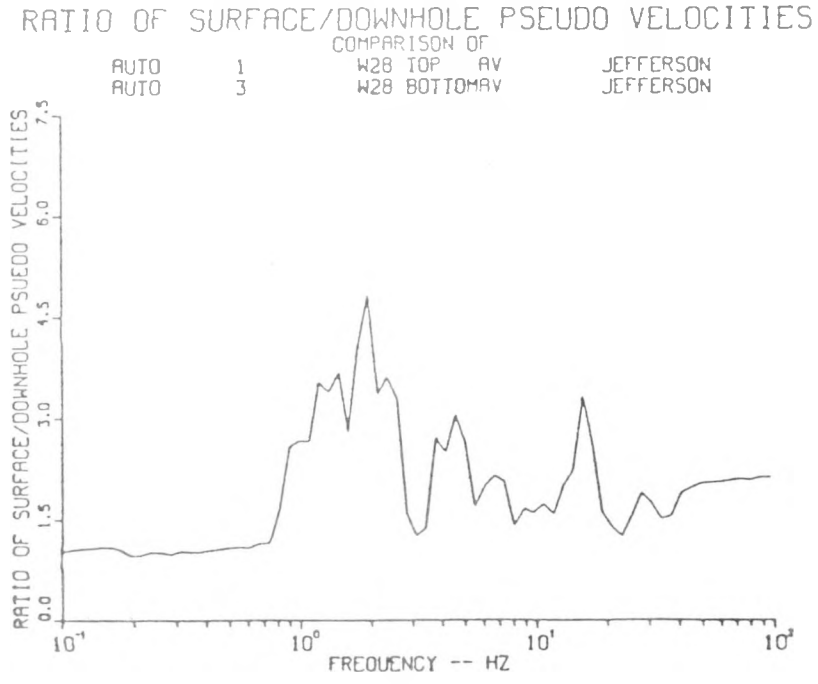

Figure A.32. Relative Normalized PSRVs and Ratios of Surface/Downhole PSRVs for Vertical Motions, Station W28, Event Serena

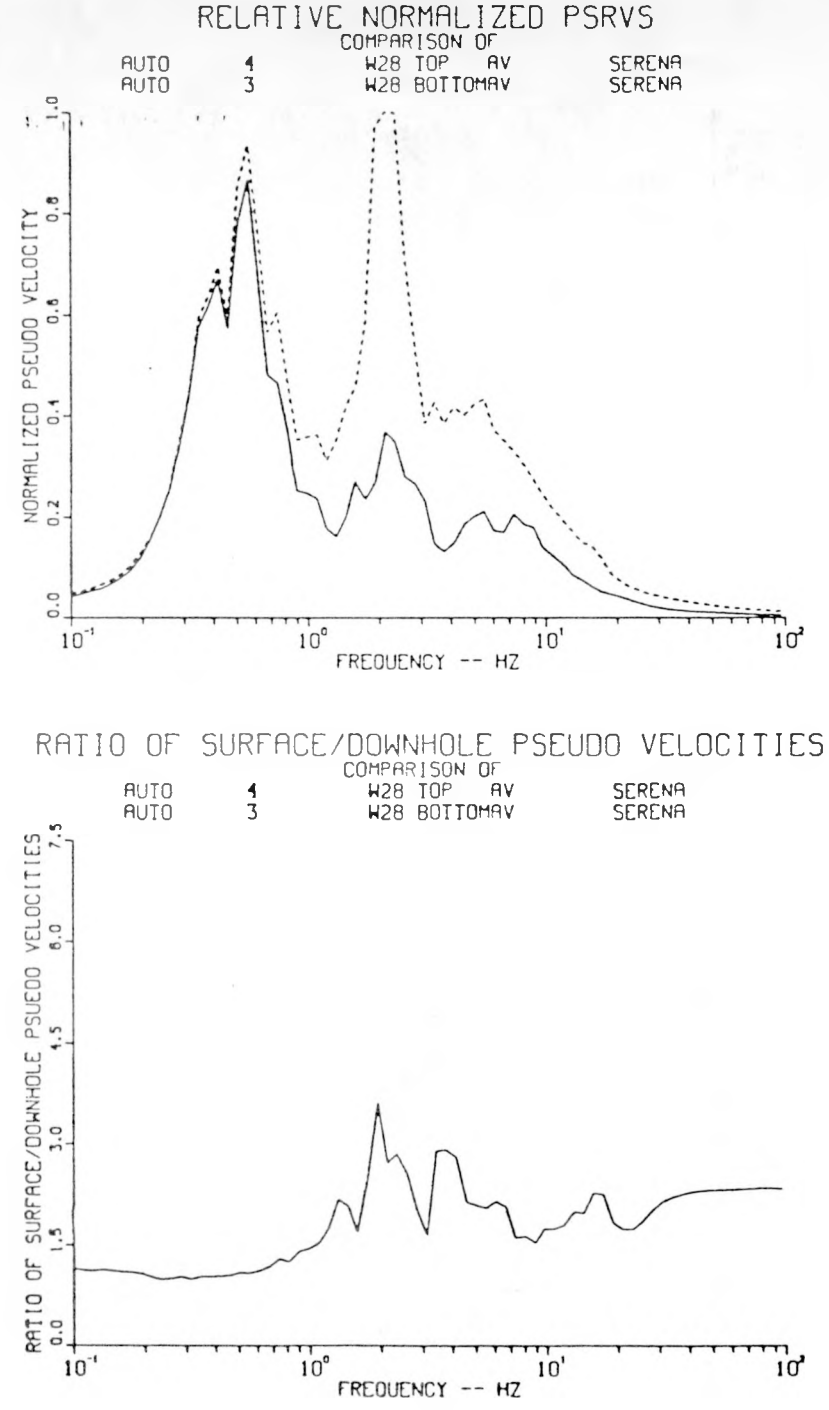

Figure A.33. Relative Normalized PSRVs and Ratios of Surface/Downhole PSRVs for Vertical Motions, Station W28, Event Goldstone

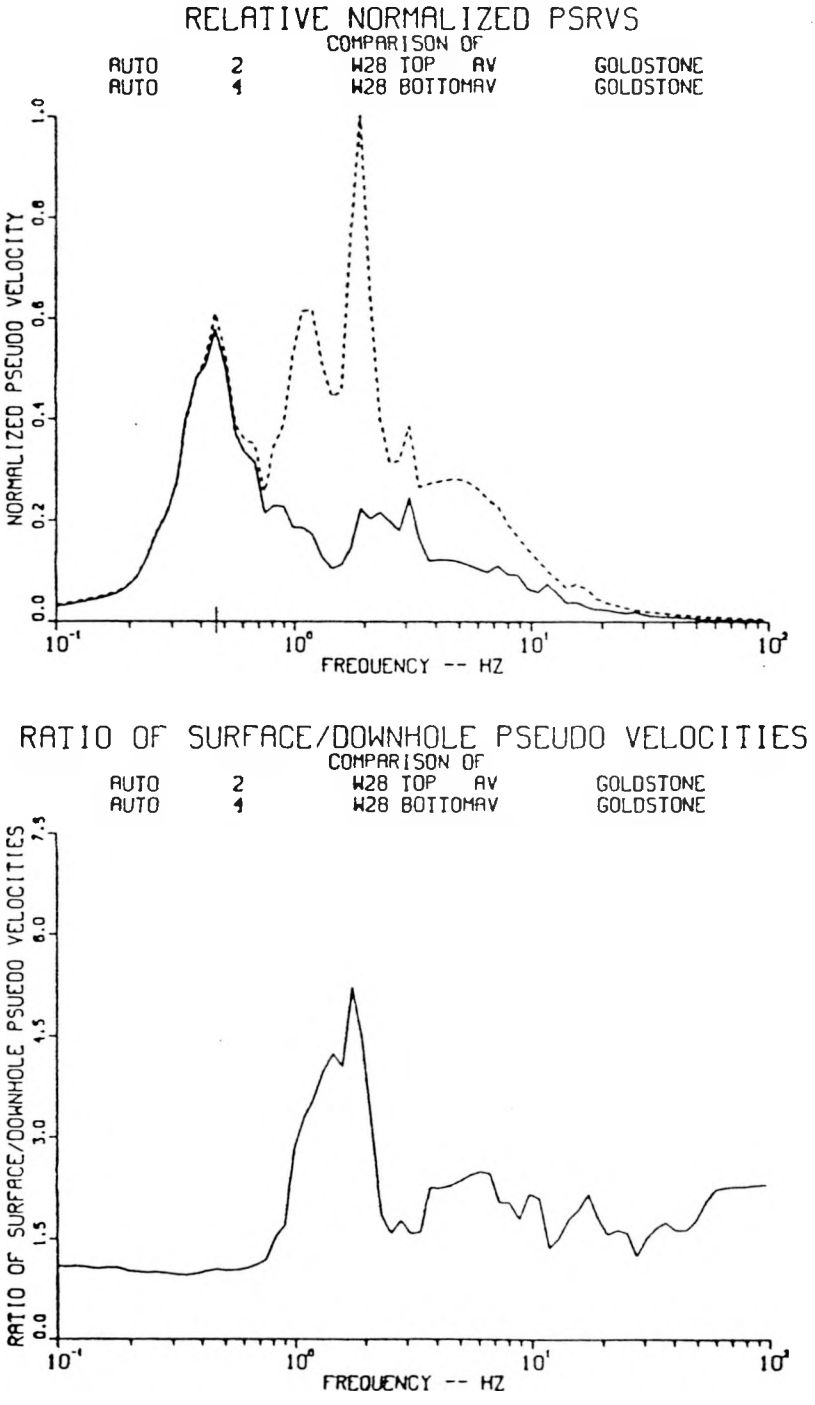

Figure A.34. Relative Normalized PSRVs and Ratios of Surface/Downhole PSRVs for Radial Motions, Station W28, Event Labquark

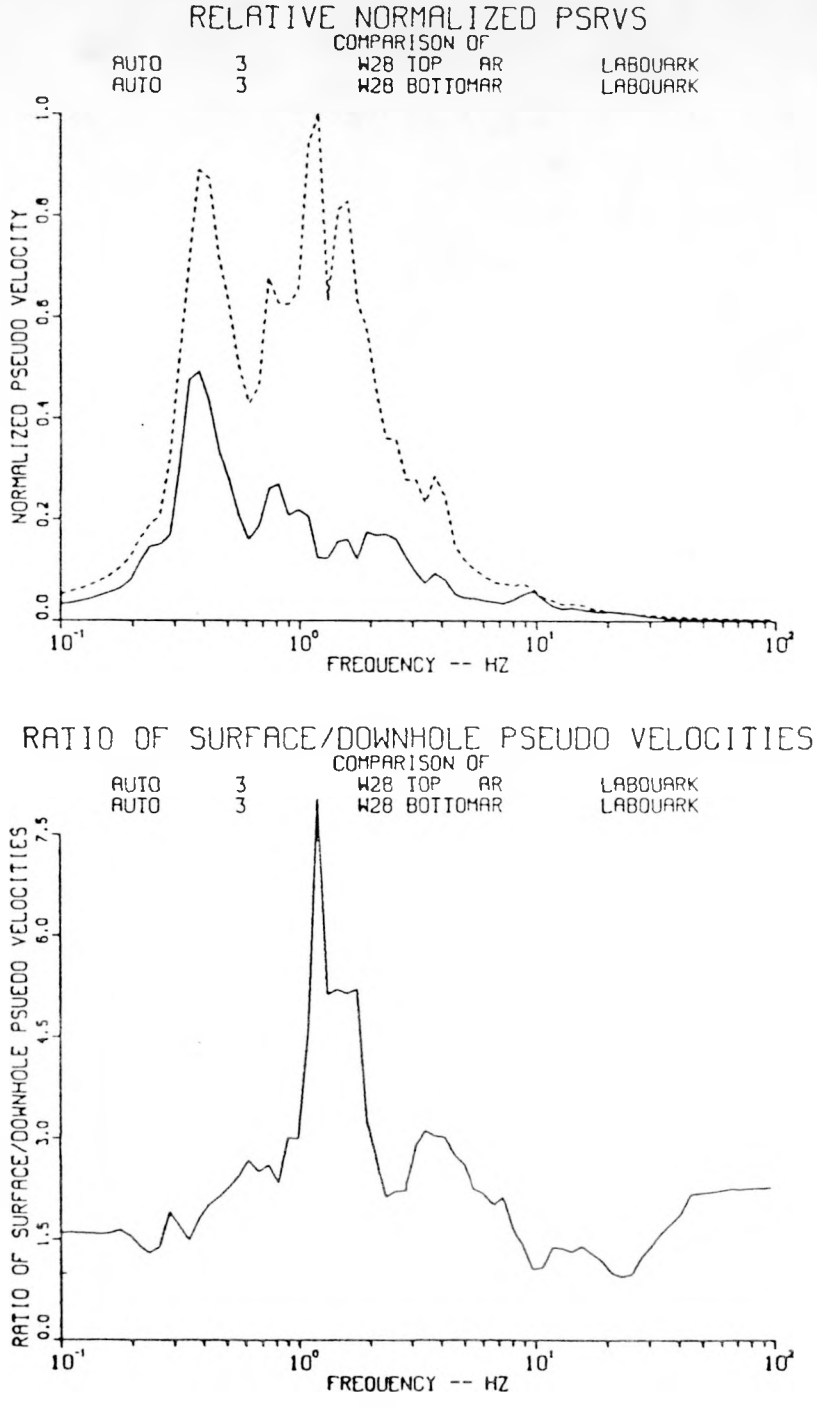

Figure A.35. Relative Normalized PSRVs and Ratios of Surface/Downhole PSRVs for Radial Motions, Station W28, Event Tierra

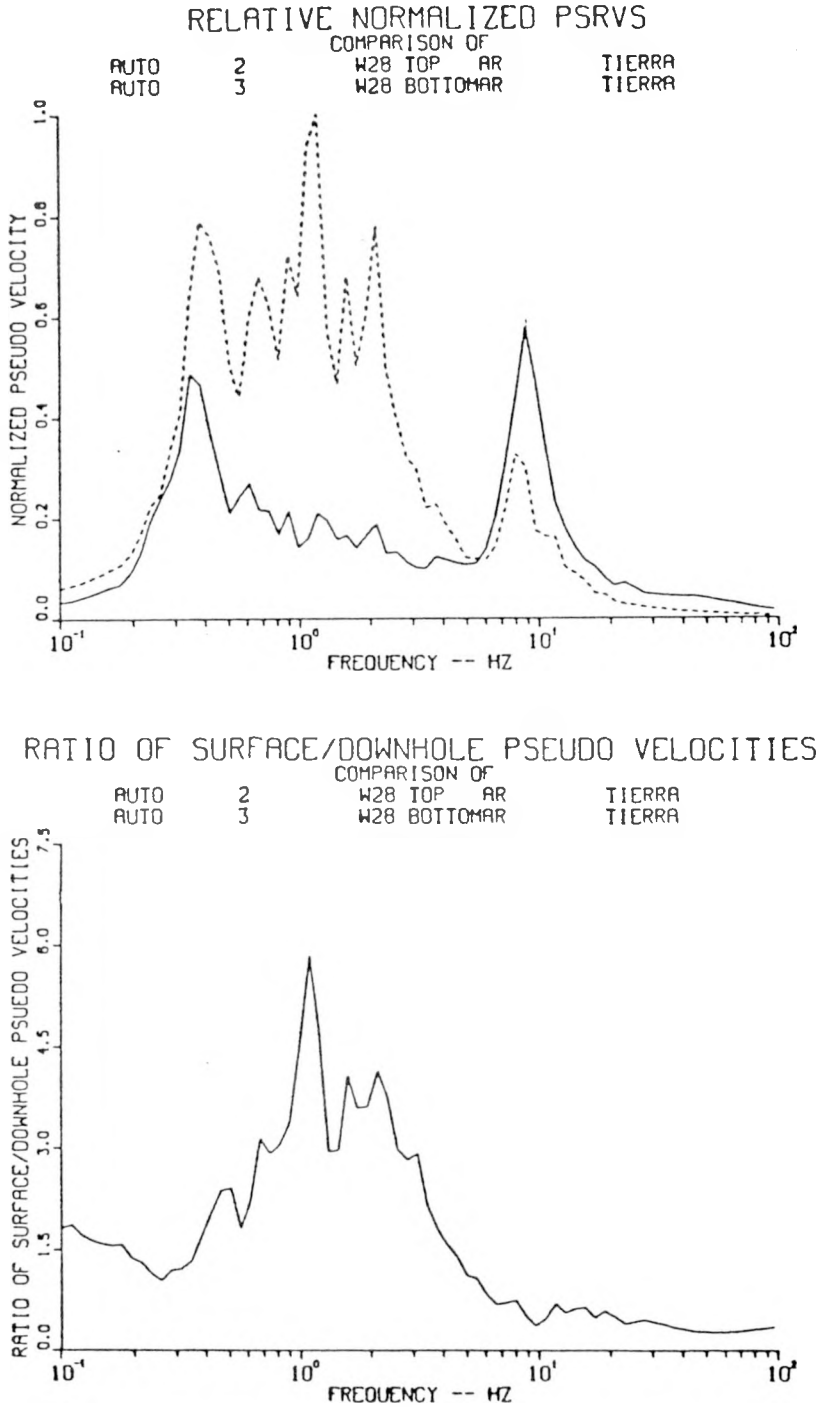

Figure A.36. Relative Normalized PSRVs and Ratios of Surface/Downhole PSRVs for Radial Motions, Station W28, Event Salut

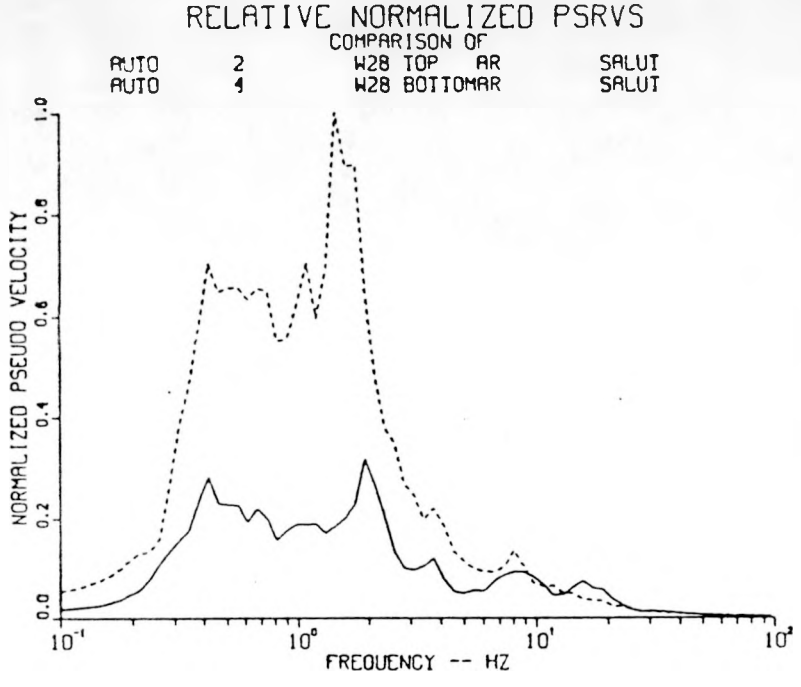

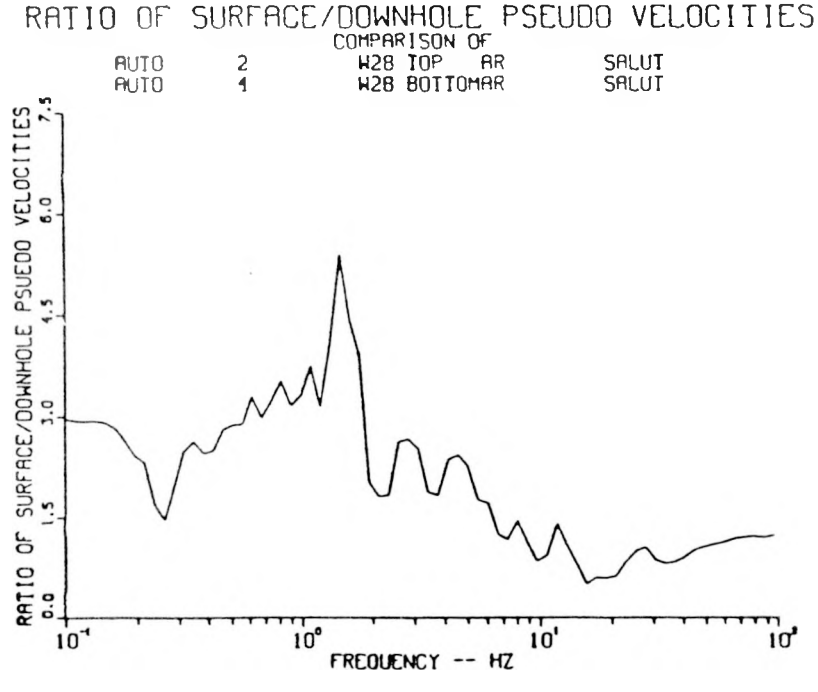

Figure A.37. Relative Normalized PSRVs and Ratios of Surface/Downhole PSRVs for Radial Motions, Station W28, Event Jefferson

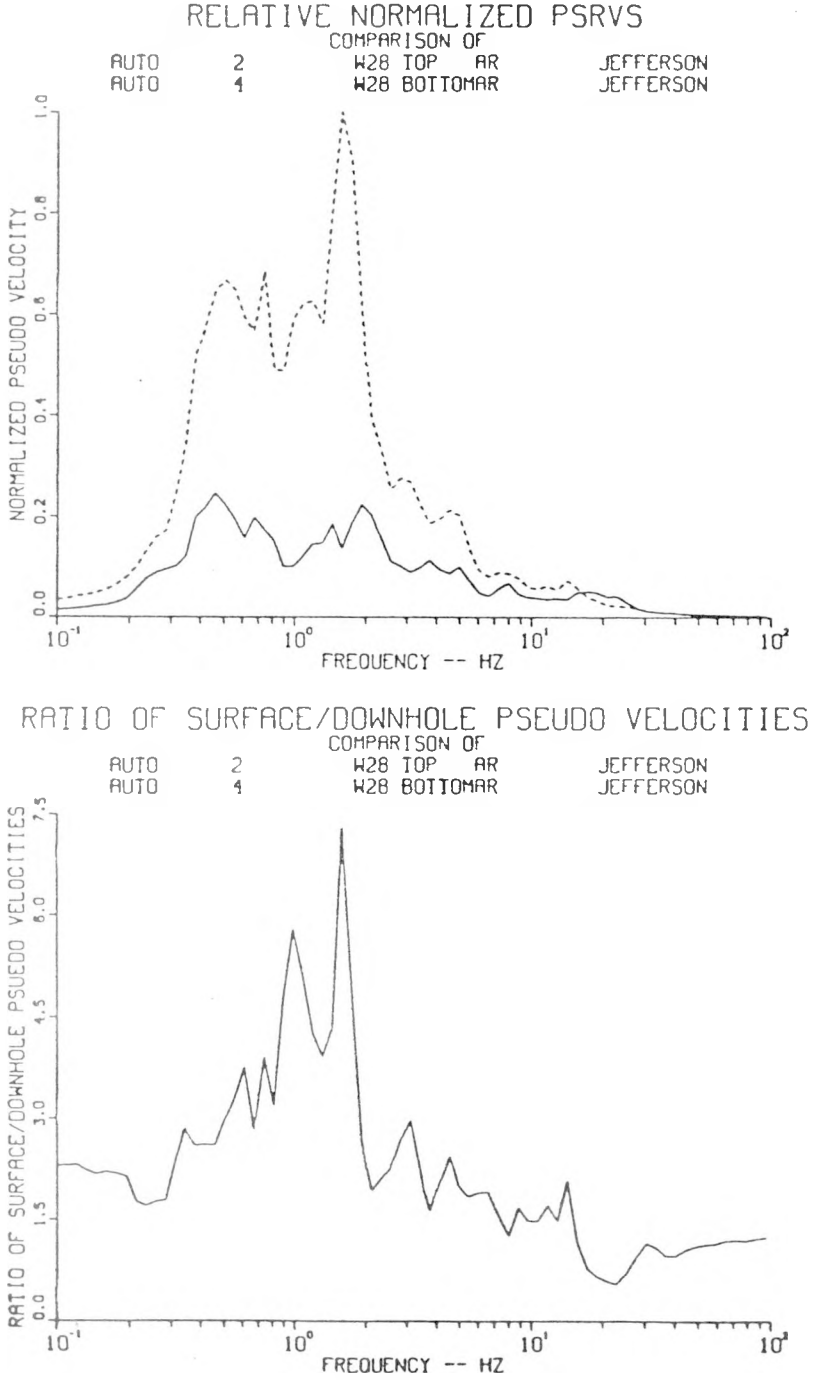

Figure A.38. Relative Normalized PSRVs and Ratios of Surface/Downhole PSRVs for Radial Motions, Station W28, Event Serena

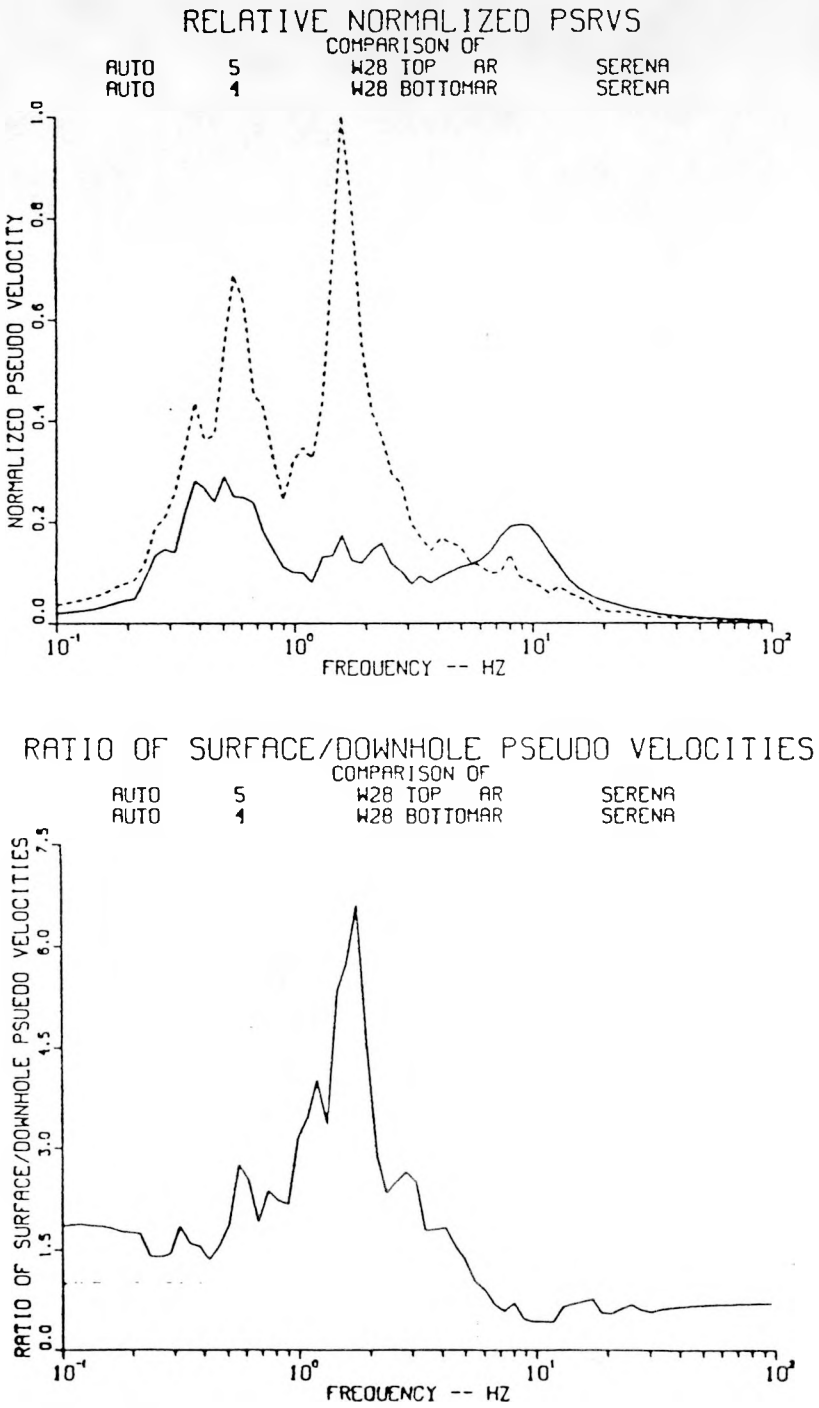

Figure A.39. Relative Normalized PSRVs and Ratios of Surface/Downhole PSRVs for Radial Motions, Station W28, Event Goldstone

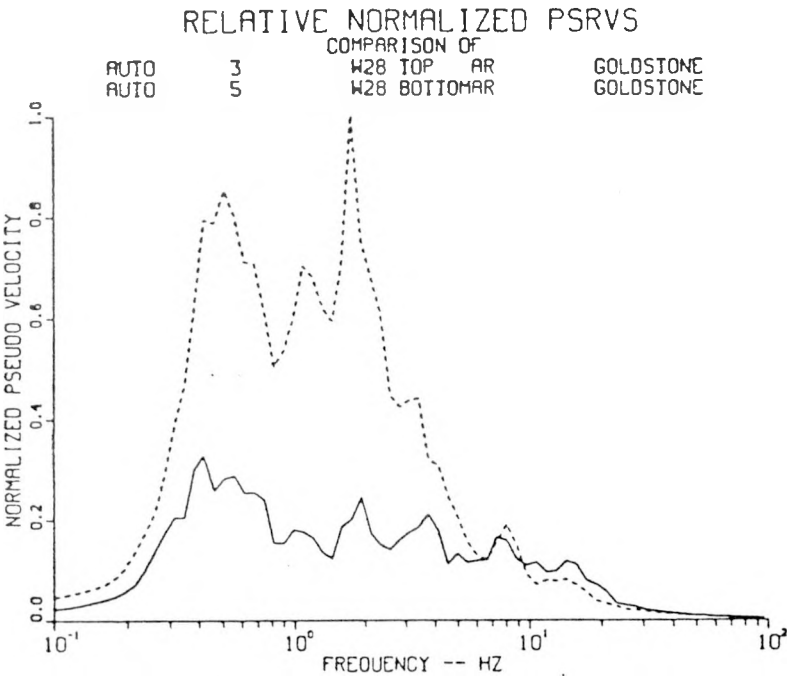

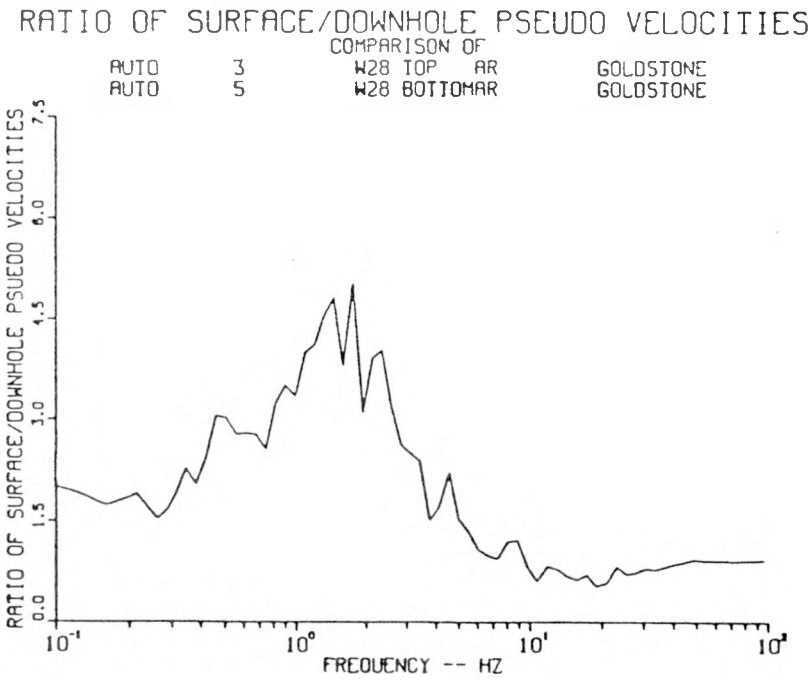

Figure A.40. Relative Normalized PSRVs and Ratios of Surface/Downhole PSRVs for Transverse Motions, Station W28, Event Labquark

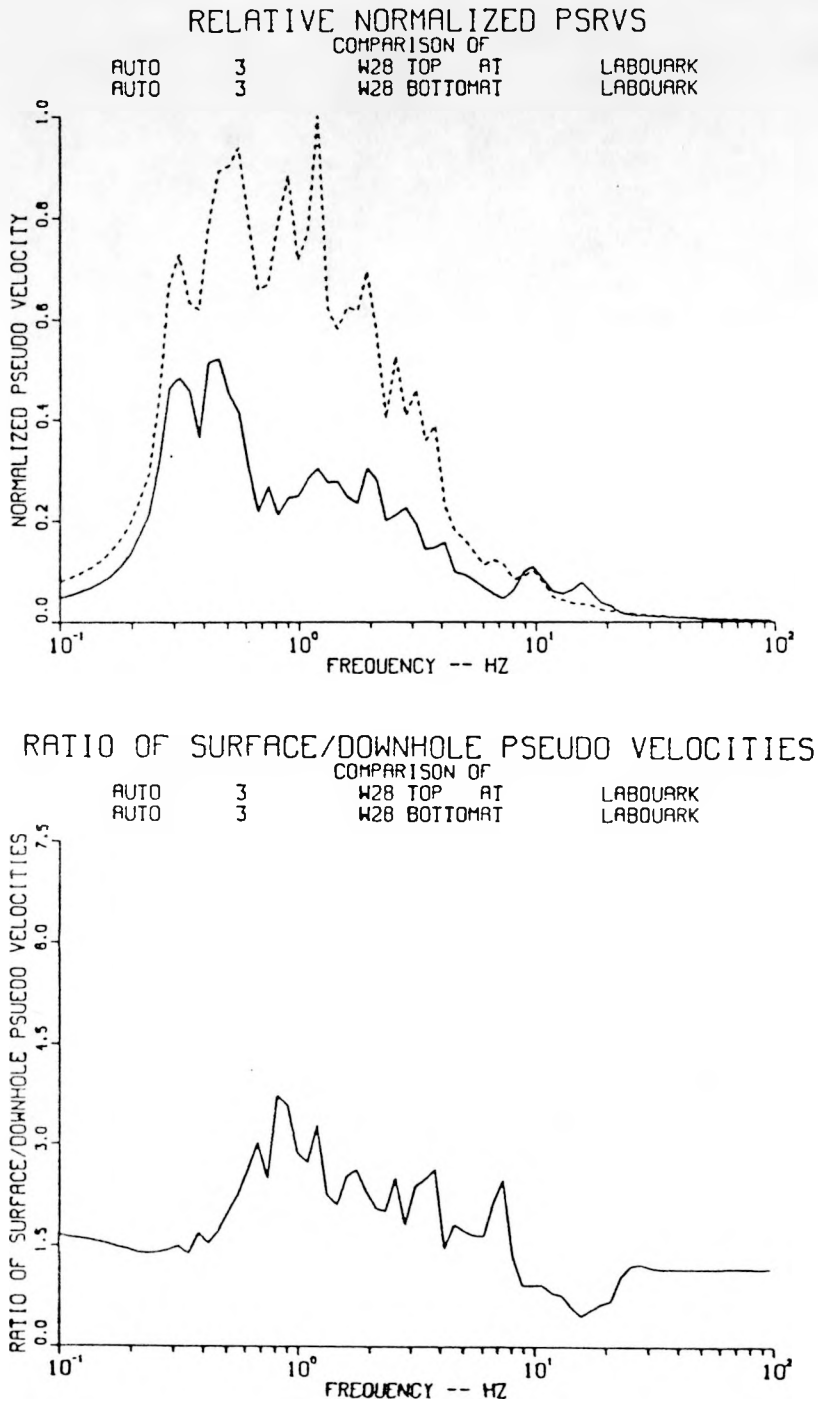

Figure A.41. Relative Normalized PSRVs and Ratios of Surface/Downhole PSRVs for Transverse Motions, Station W28, Event Tierra

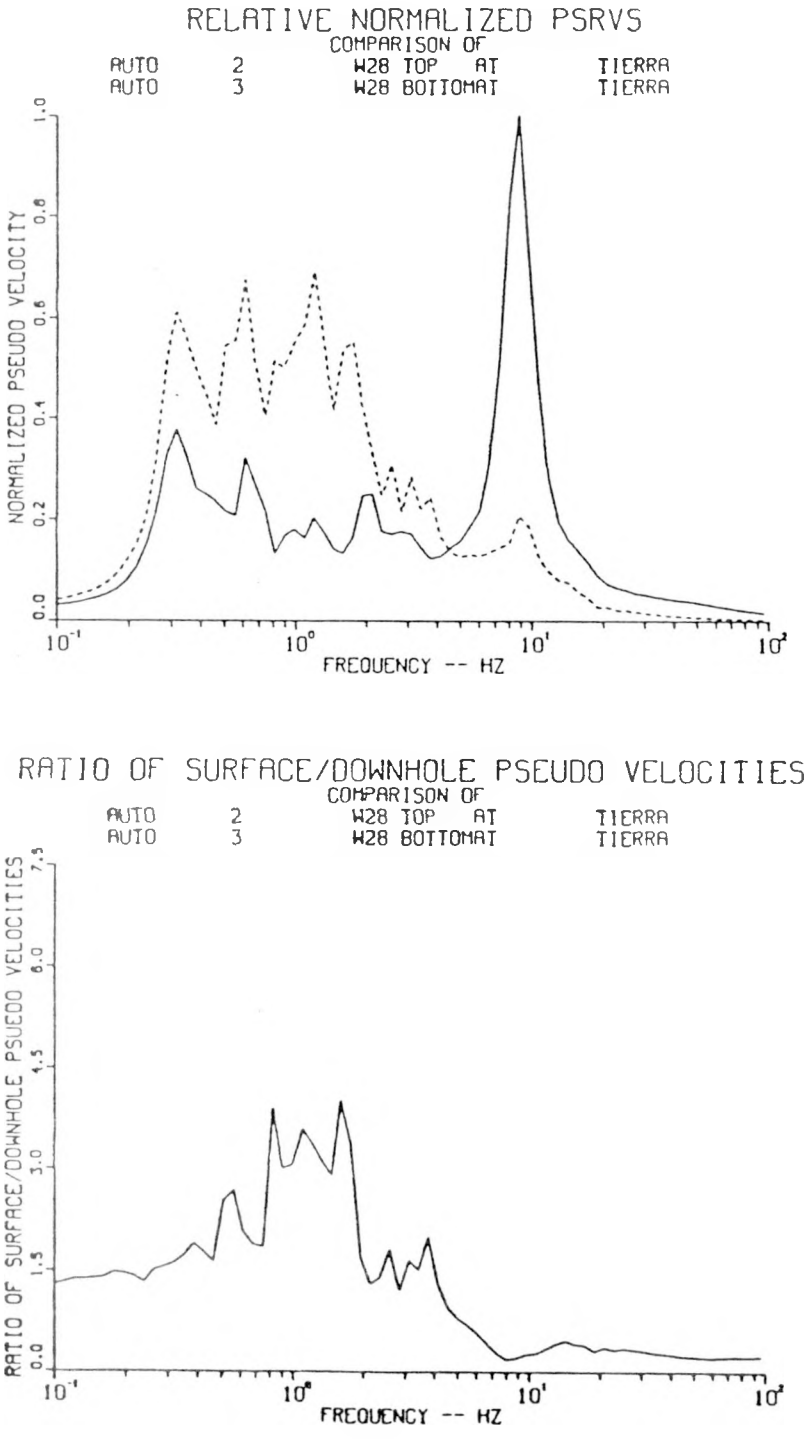

Figure A.42. Relative Normalized PSRVs and Ratios of Surface/Downhole PSRVs for Transverse Motions, Station W28, Event Salut

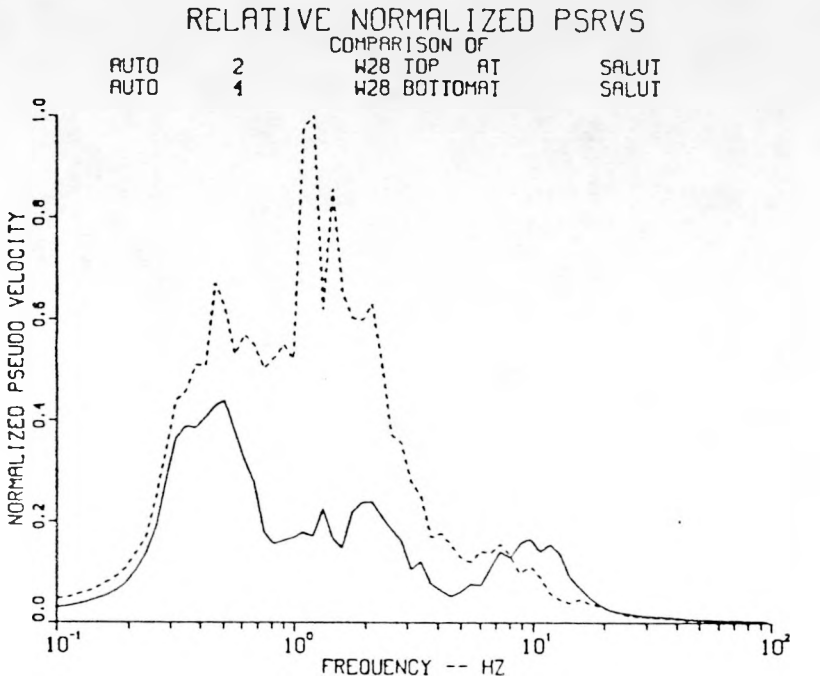

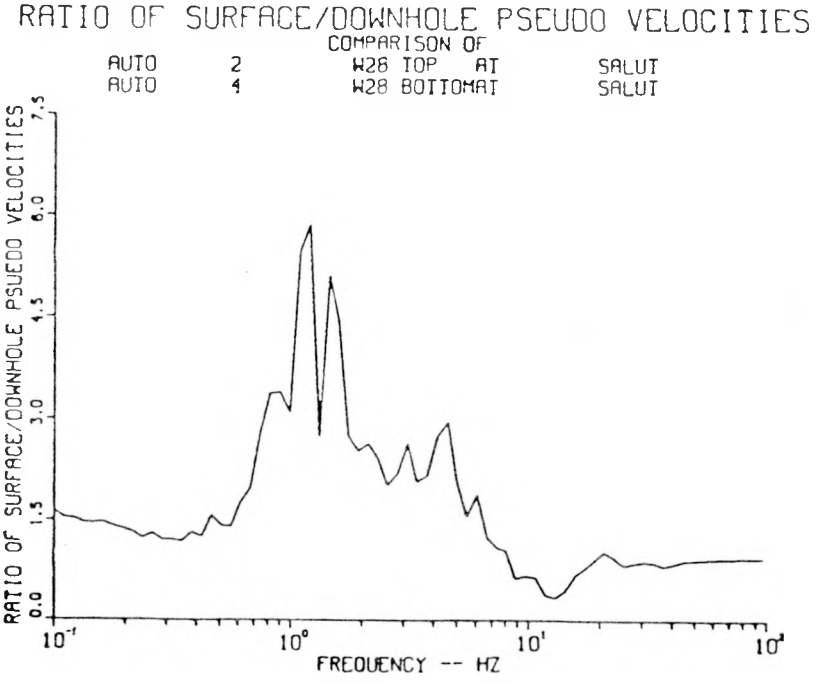

Figure A.43. Relative Normalized PSRVs and Ratios of Surface/Downhole PSRVs for Transverse Motions, Station W28, Event Jefferson

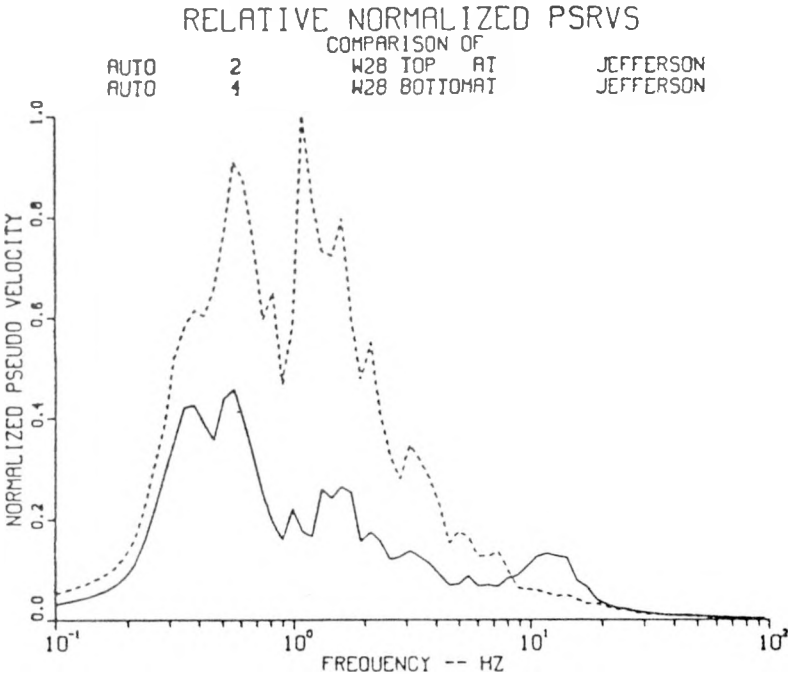

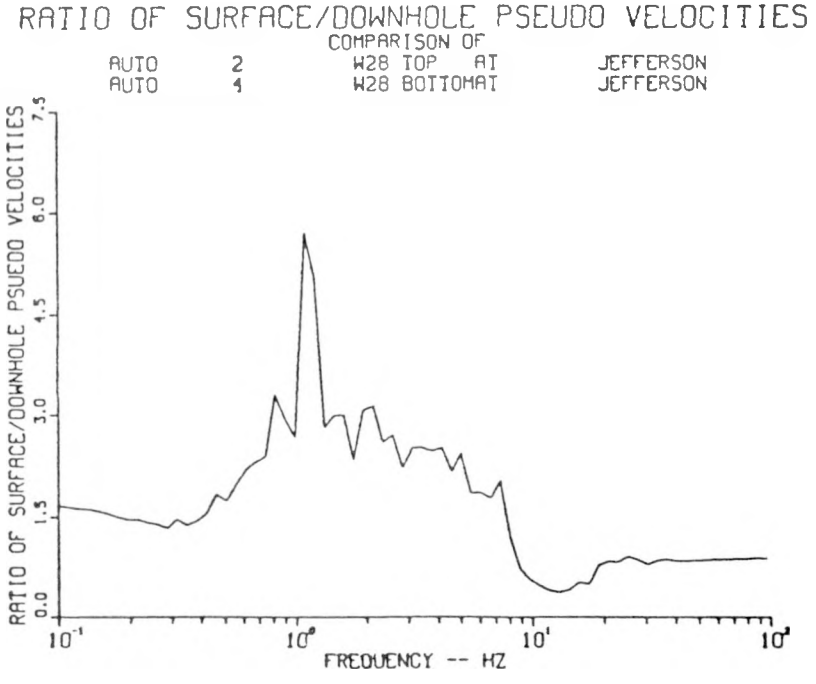

Figure A.44. Relative Normalized PSRVs and Ratios of Surface/Downhole PSRVs for Transverse Motions, Station W28, Event Serena

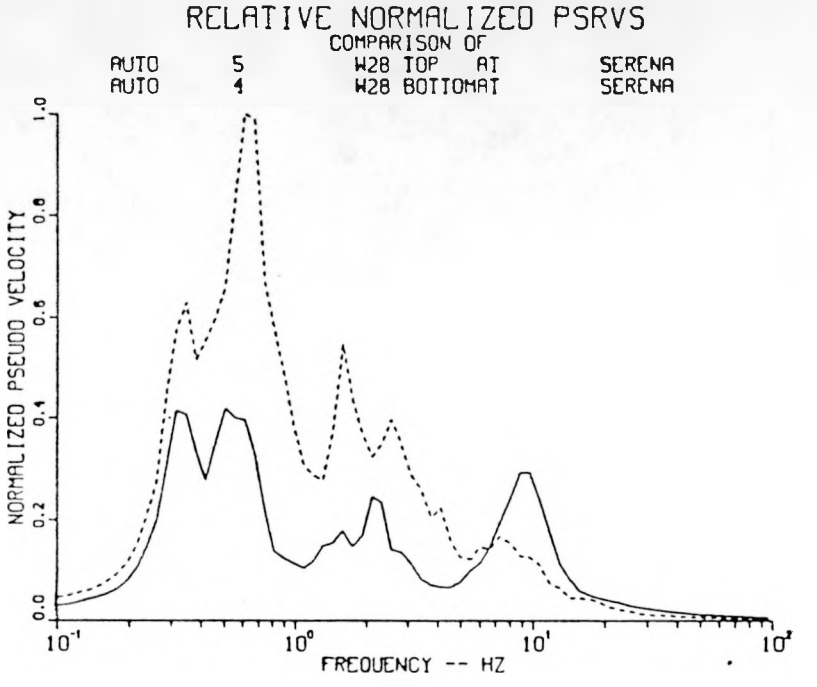

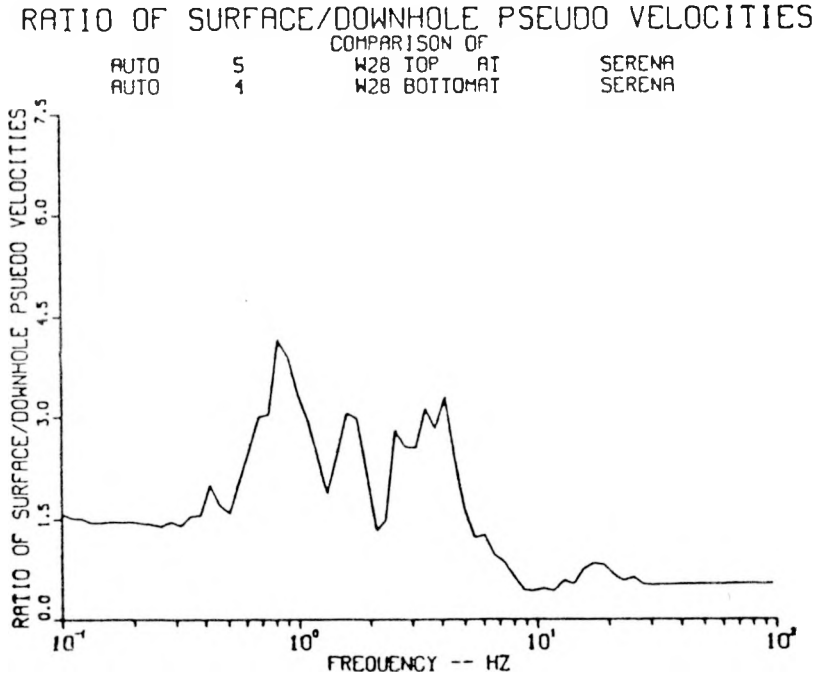

Figure A.45. Relative Normalized PSRVs and Ratios of Surface/Downhole PSRVs for Transverse Motions, Station W28, Event Goldstone

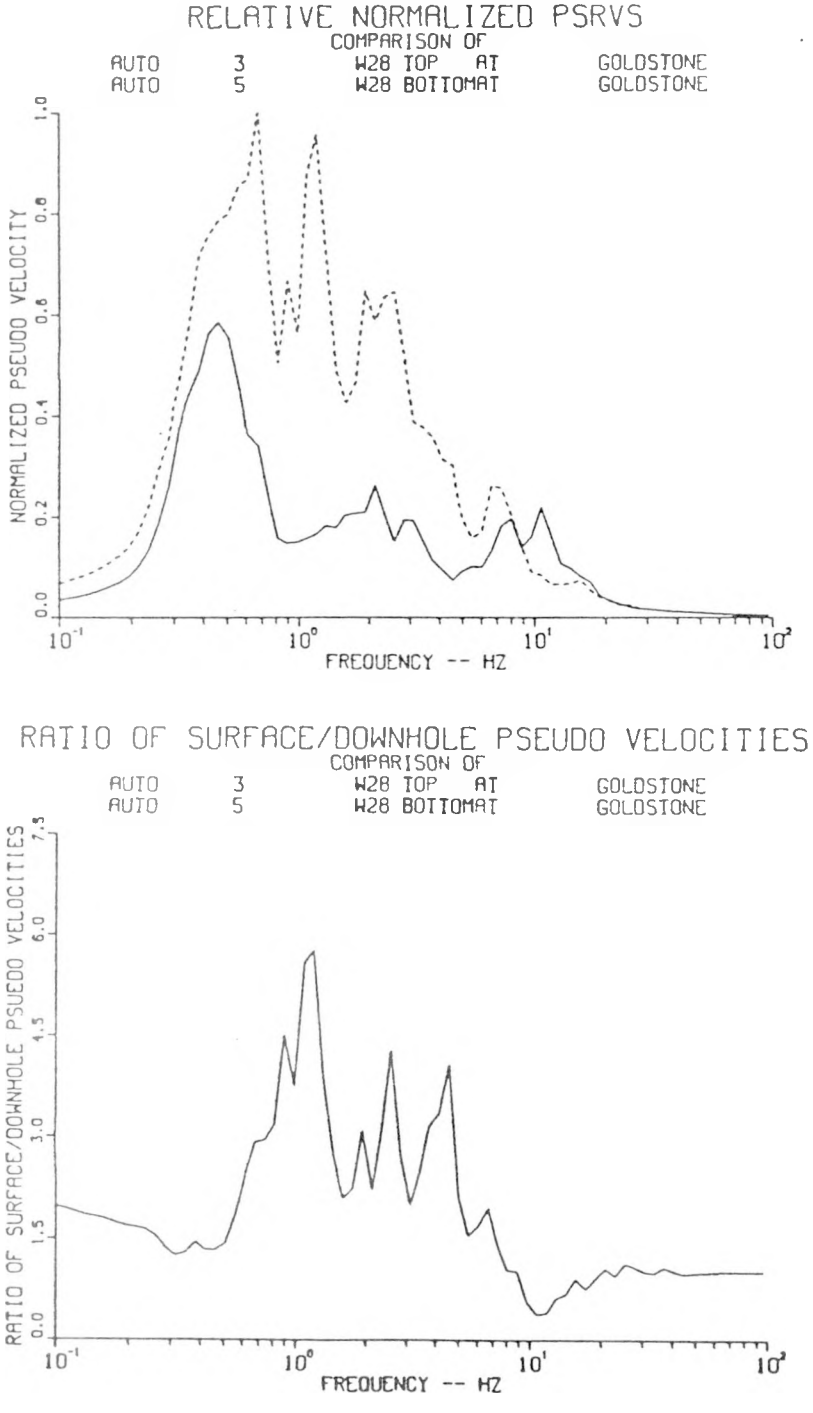

Figure A.46. Relative Normalized PSRVs and Ratios of Surface/Downhole PSRVs for Vertical Motions, Station W29, Event Labquark

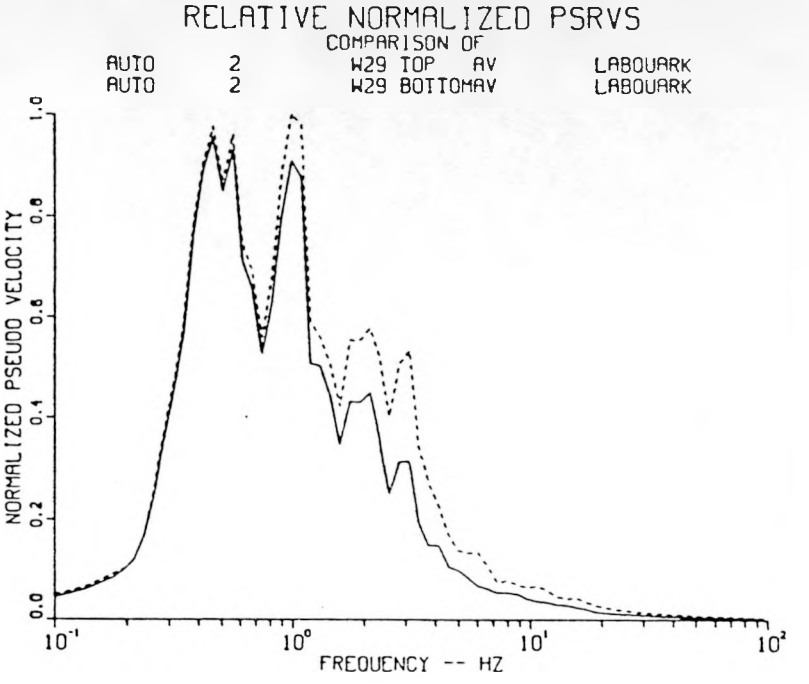

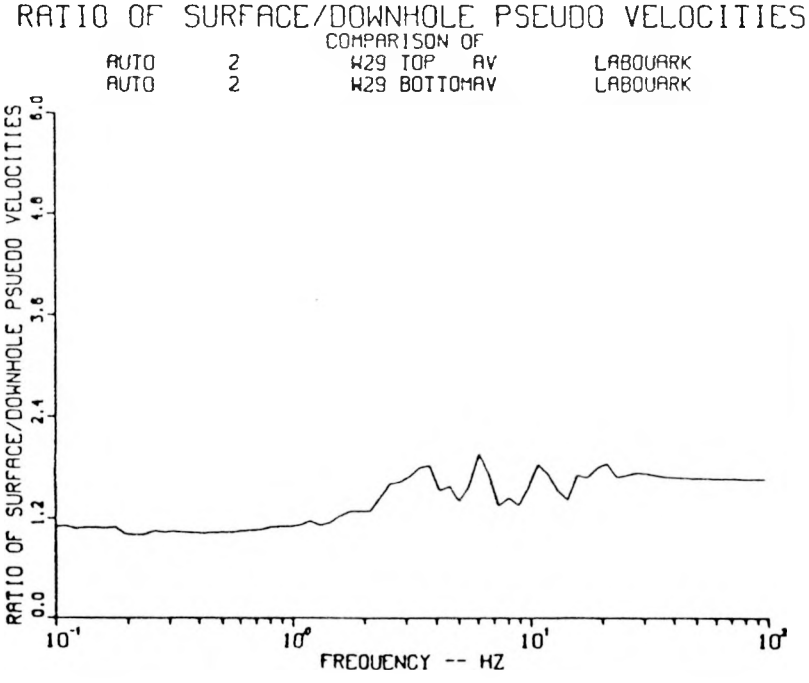

Figure A.47. Relative Normalized PSRVs and Ratios of Surface/Downhole PSRVs for Vertical Motions, Station W29, Event Salut

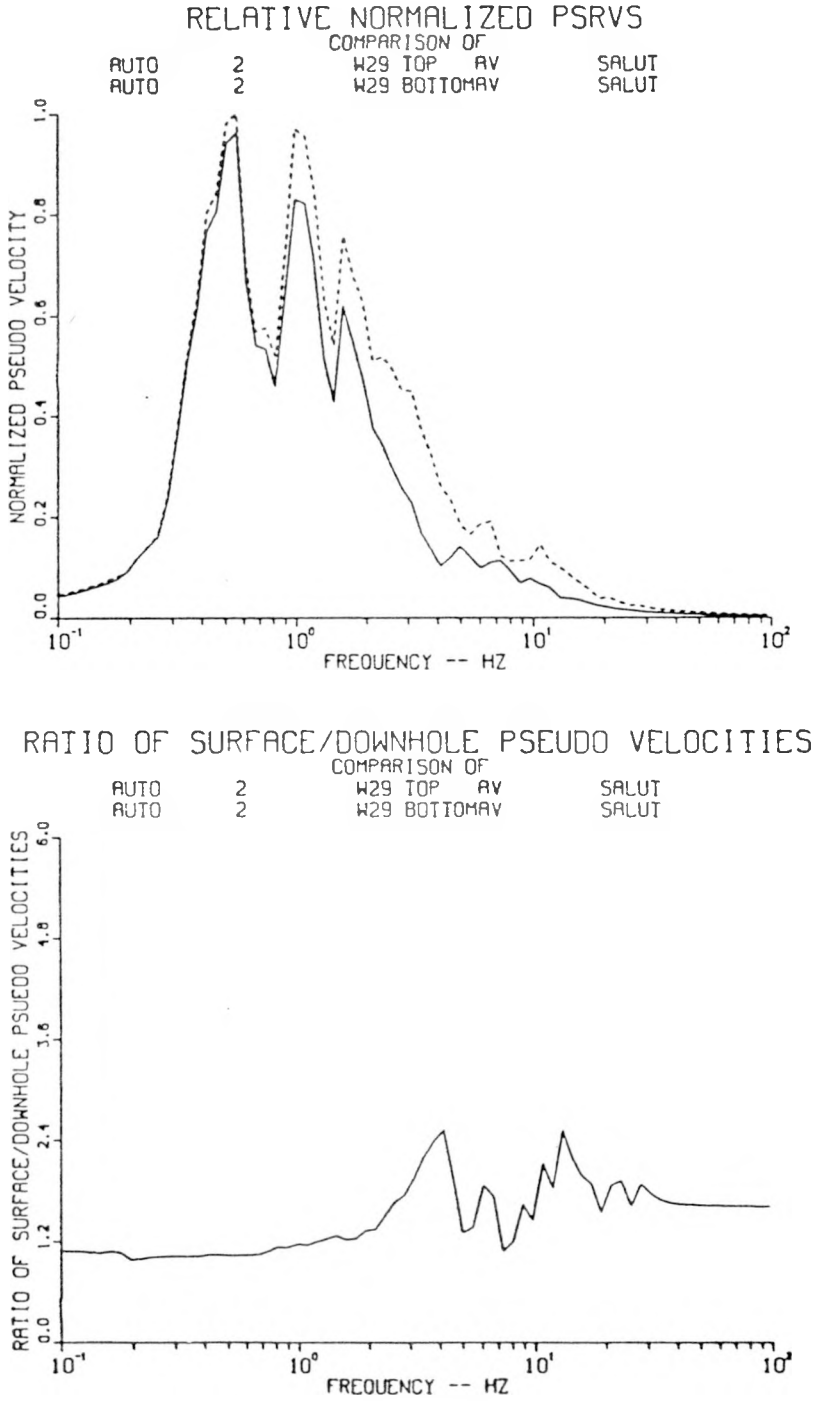

Figure A.48. Relative Normalized PSRVs and Ratios of Surface/Downhole PSRVs for Vertical Motions, Station W29, Event Jefferson

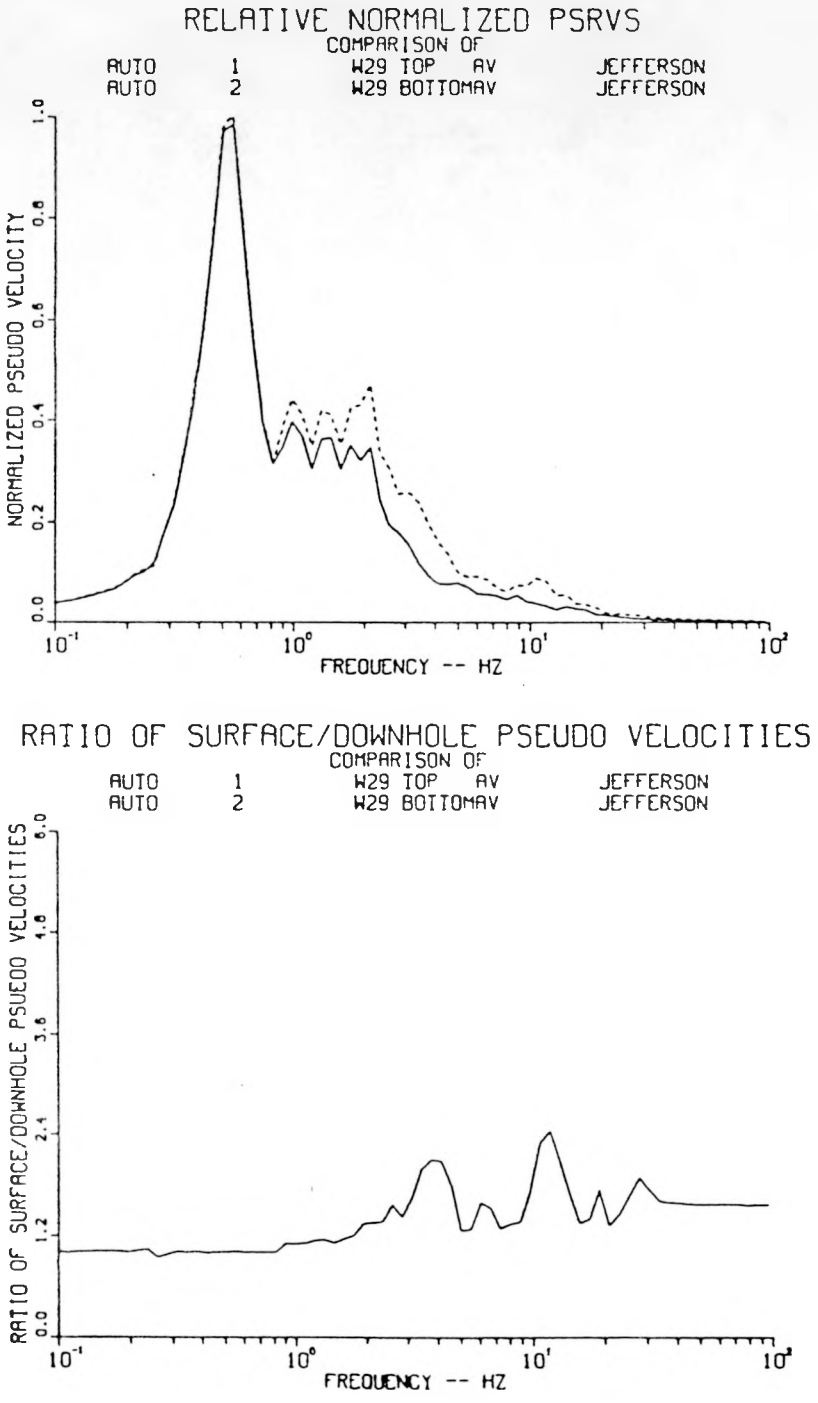

Figure A.49. Relative Normalized PSRVs and Ratios of Surface/Downhole PSRVs for Vertical Motions, Station W29, Event Serena

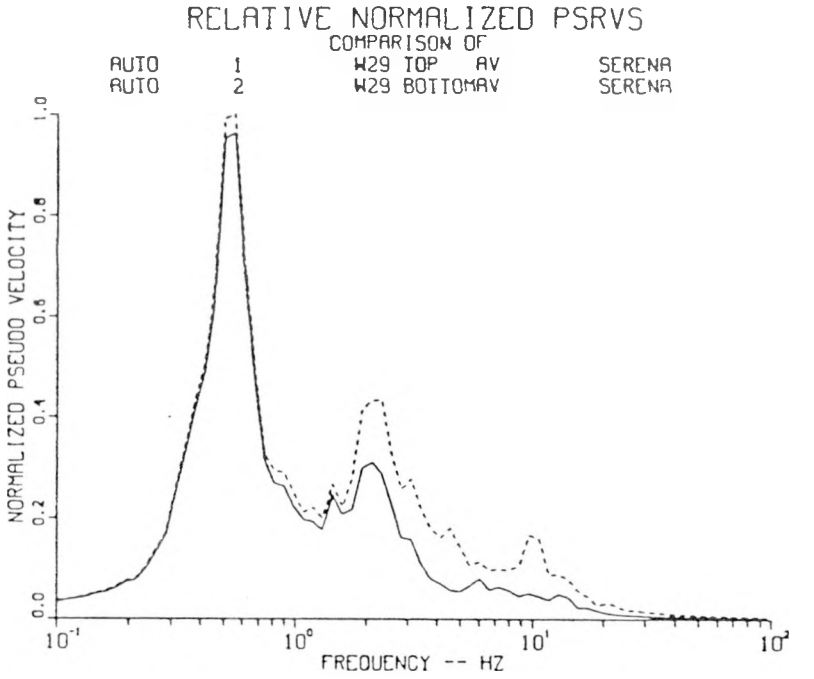

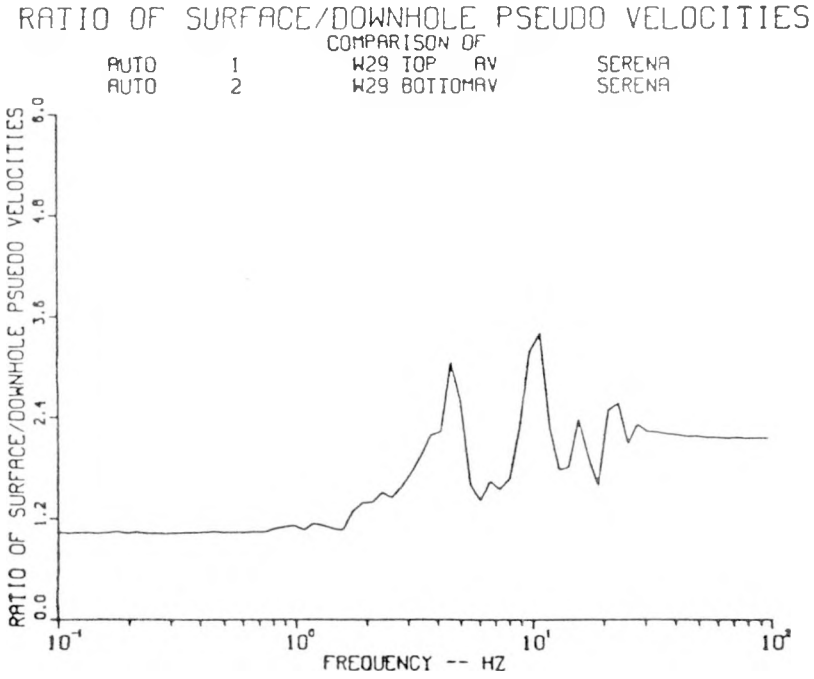

Figure A.50. Relative Normalized PSRVs and Ratios of Surface/Downhole PSRVs for Vertical Motions, Station W29, Event Goldstone

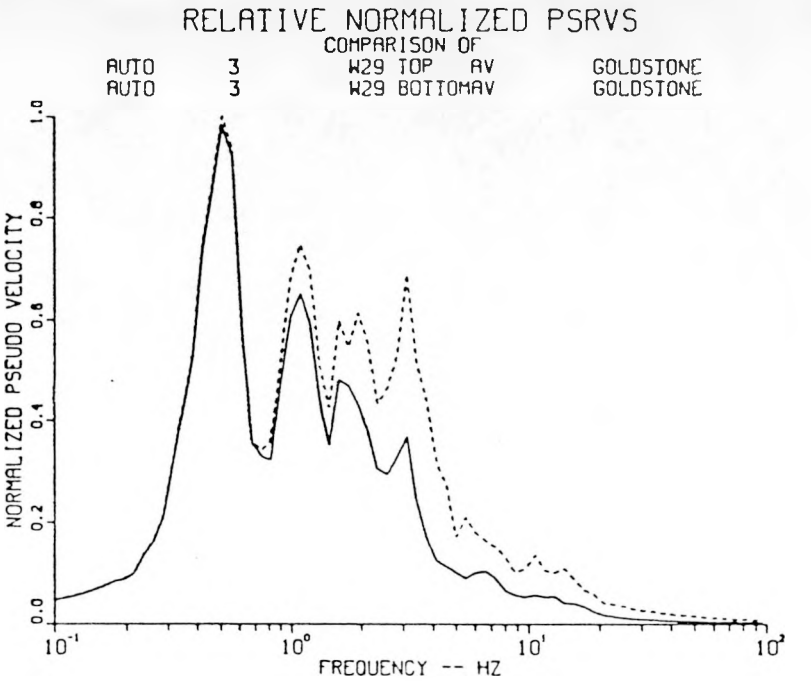

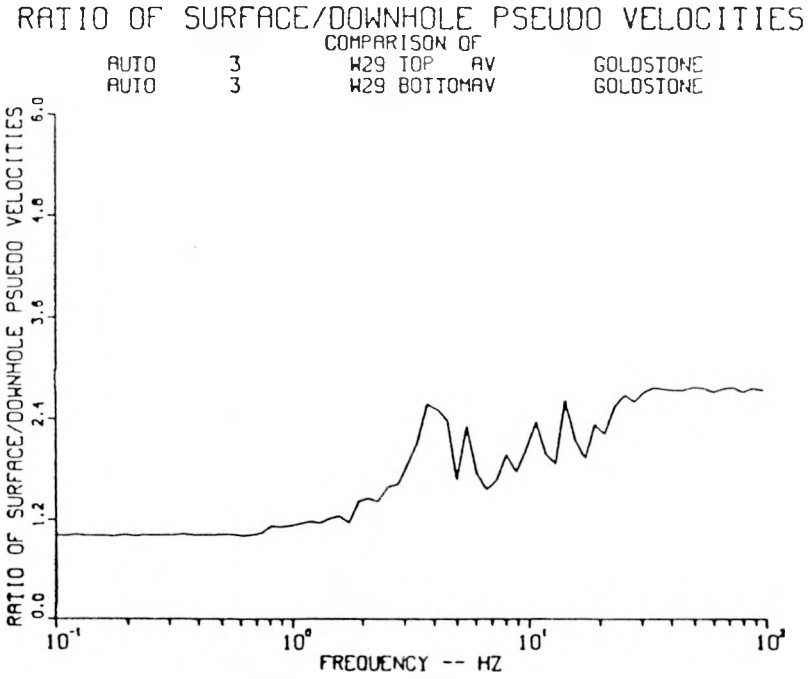

Figure A.51. Relative Normalized PSRVs and Ratios of Surface/Downhole PSRVs for Vertical Motions, Station W29, Event Towanda

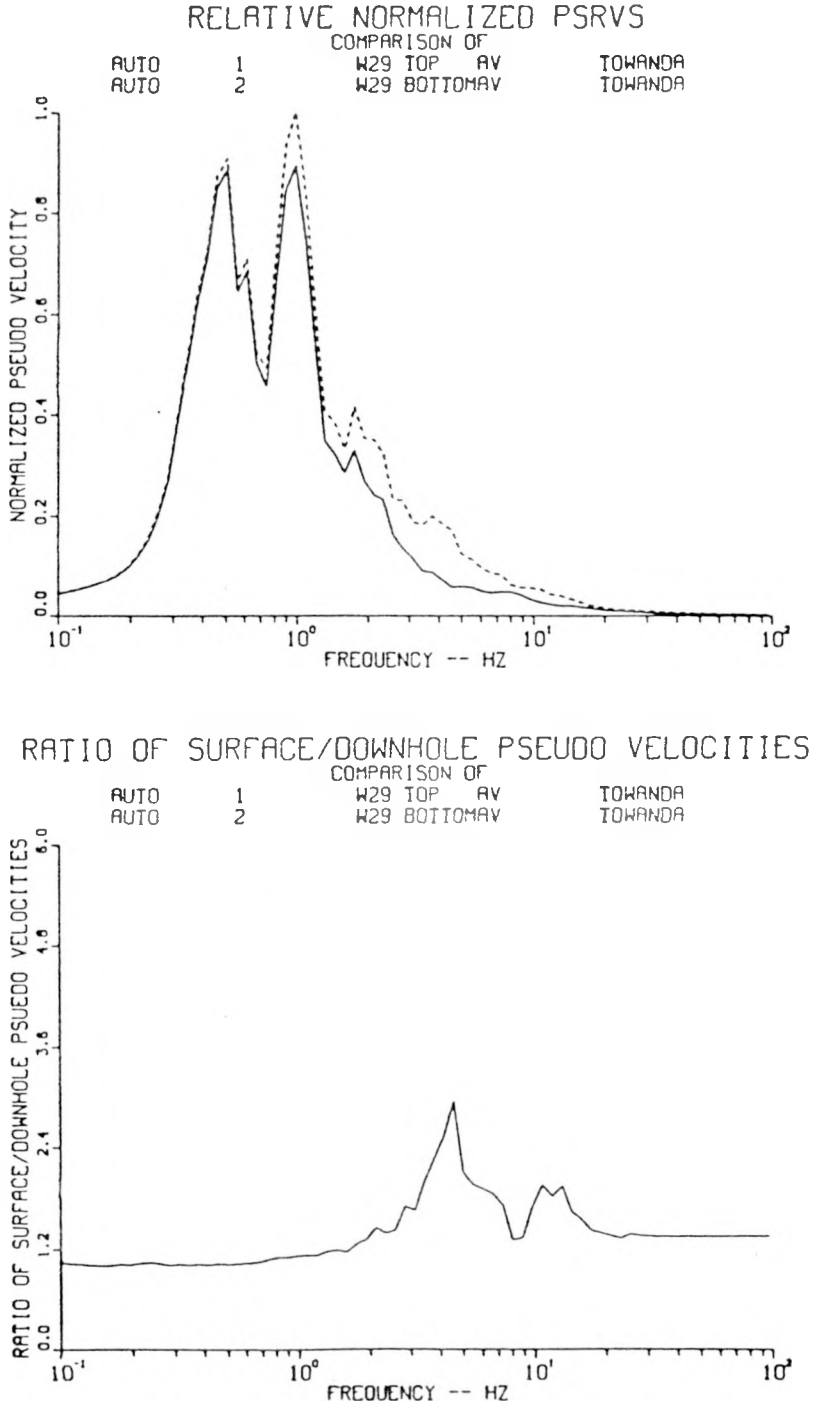

Figure A.52. Relative Normalized PSRVs and Ratios of Surface/Downhole PSRVs for Radial Motions, Station W29, Event Labquark

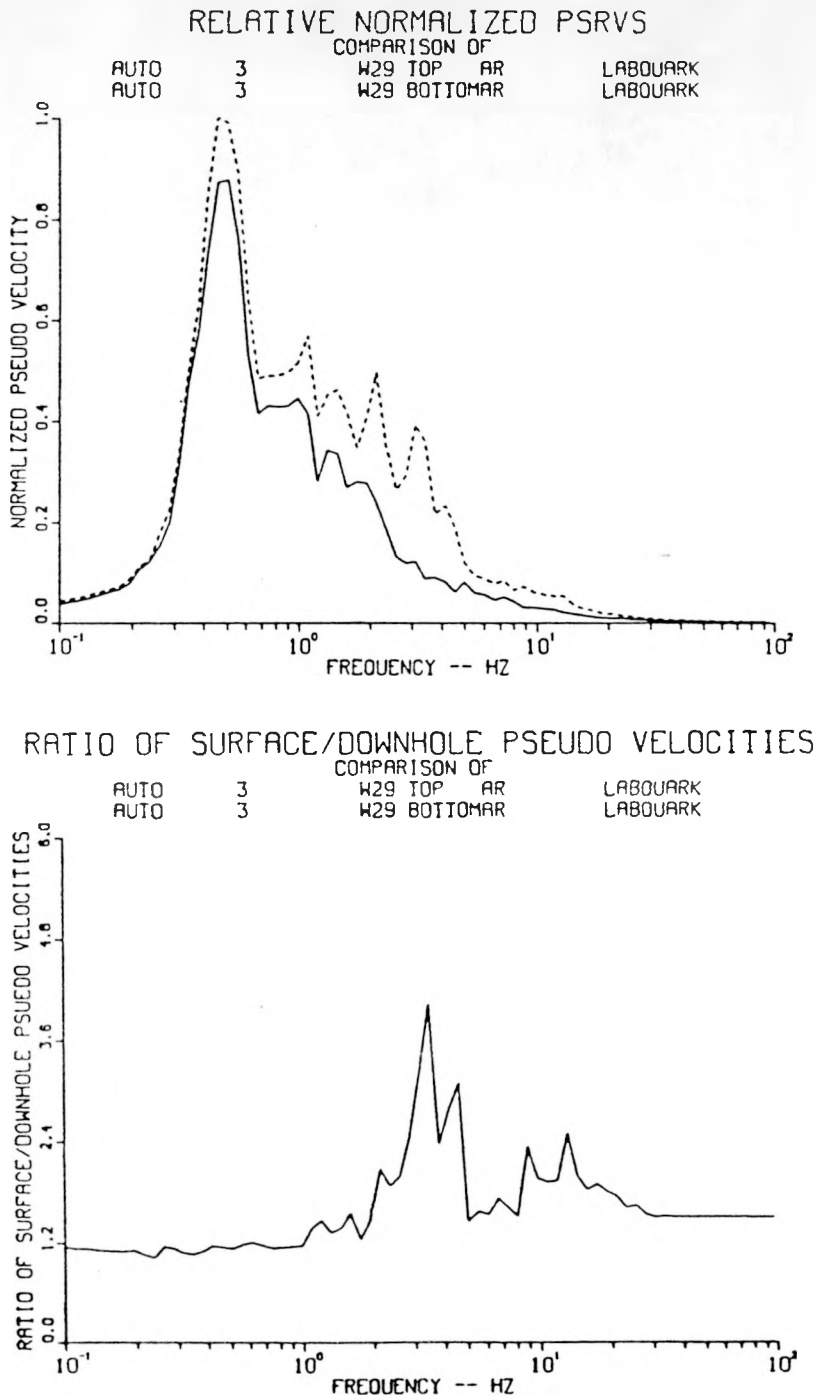

Figure A.53. Relative Normalized PSRVs and Ratios of Surface/Downhole PSRVs for Radial Motions, Station W29, Event Salut

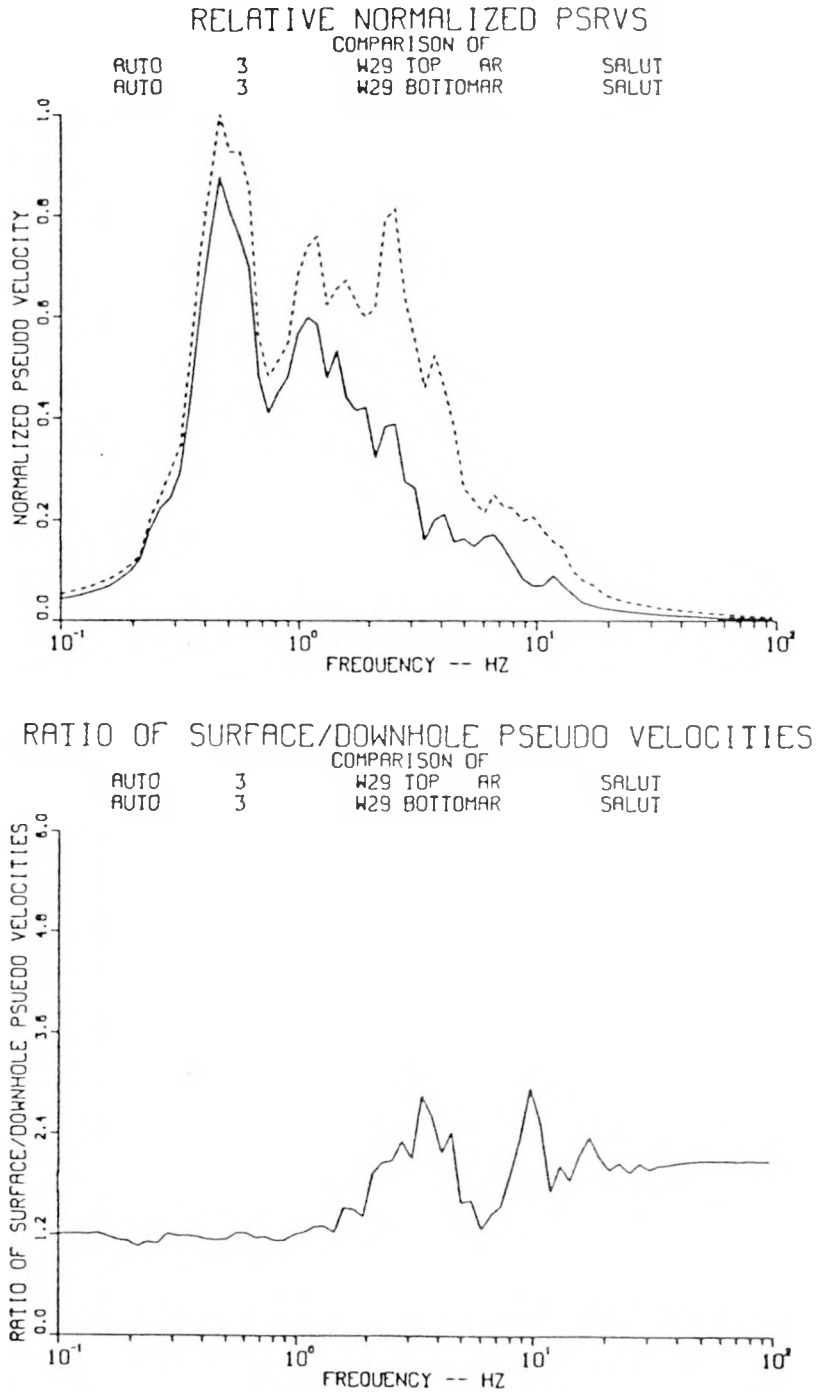

Figure A.54. Relative Normalized PSRVs and Ratios of Surface/Downhole PSRVs for Radial Motions, Station W29, Event Jefferson

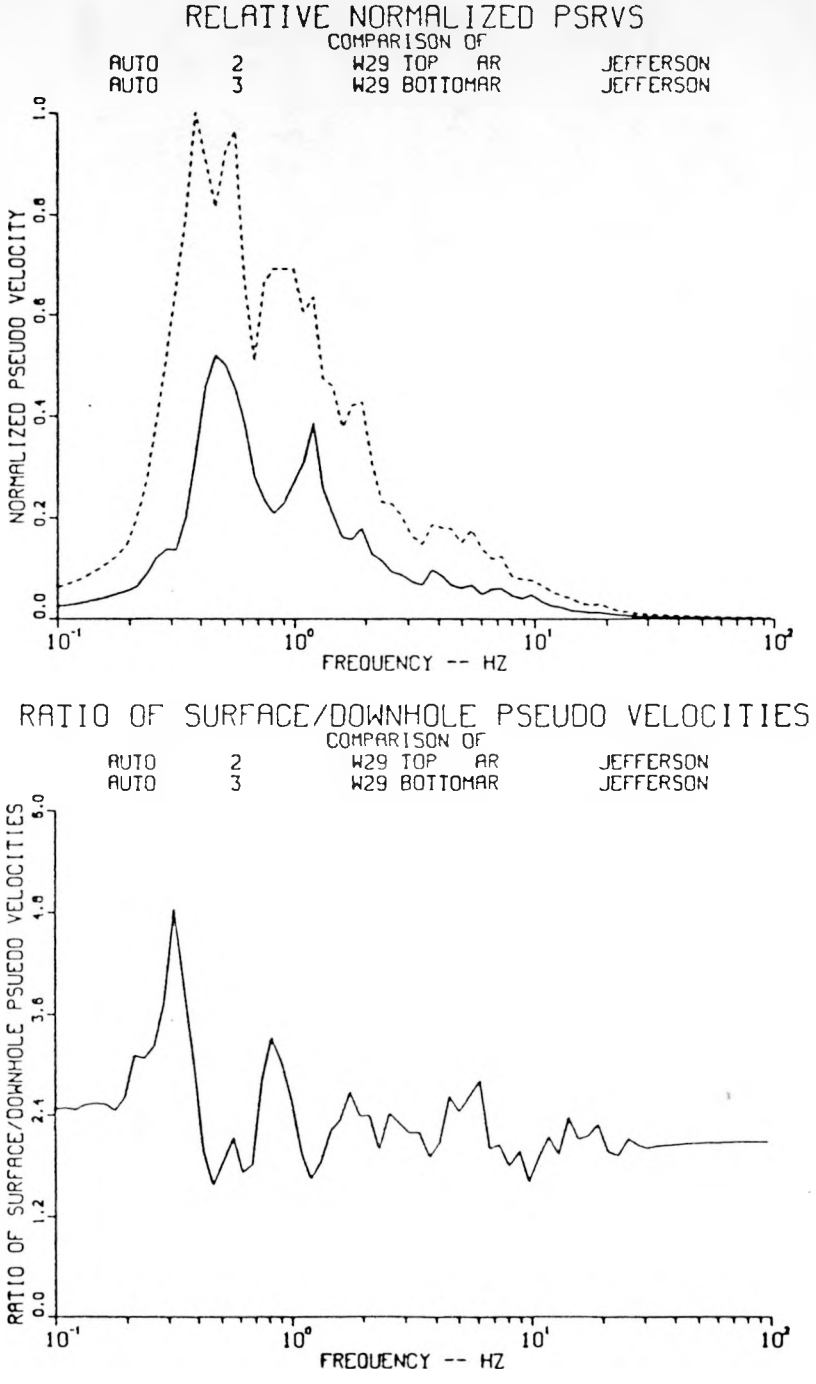

Figure A.55. Relative Normalized PSRVs and Ratios of Surface/Downhole PSRVs for Radial Motions, Station W29, Event Serena

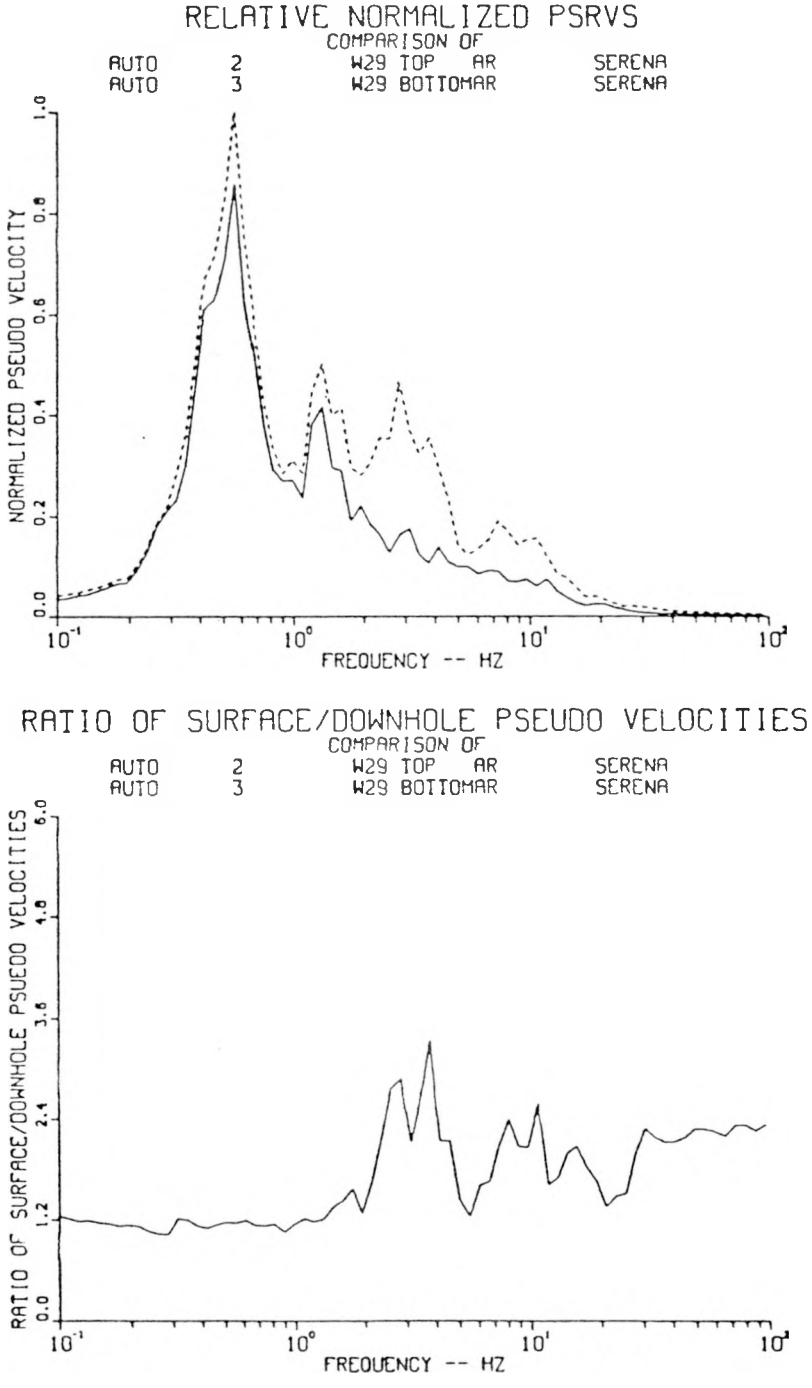

Figure A.56. Relative Normalized PSRVs and Ratios of Surface/Downhole PSRVs for Radial Motions, Station W29, Event Goldstone

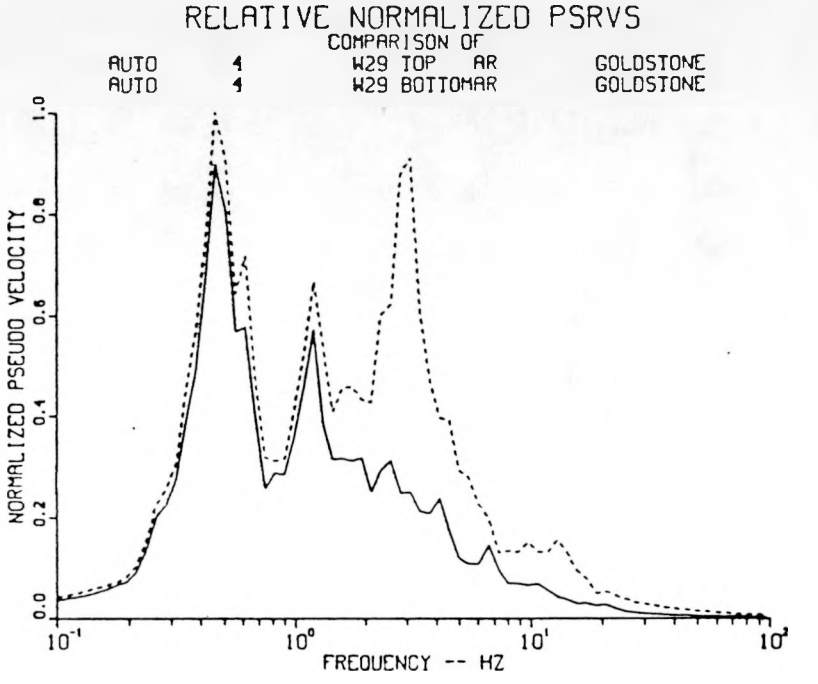

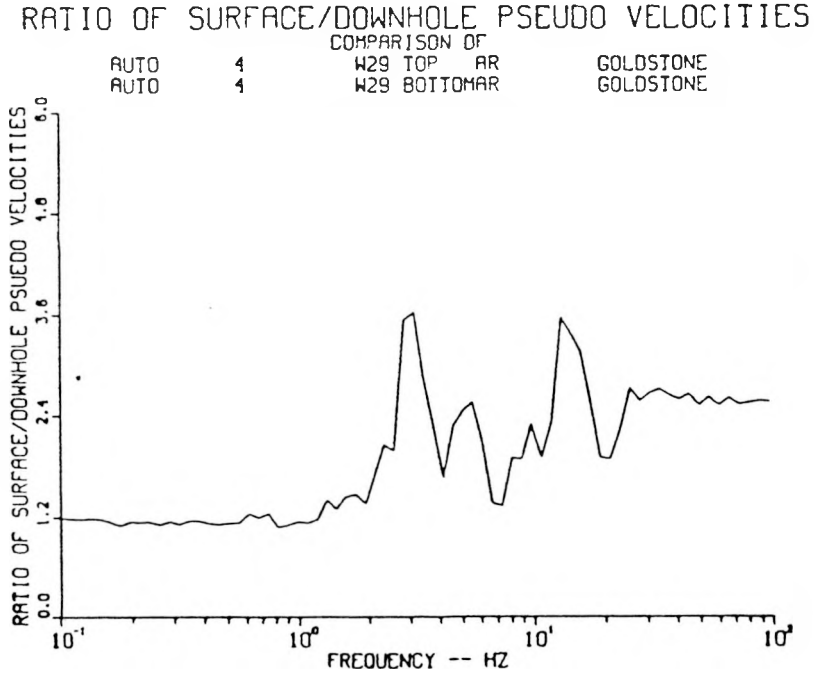

Figure A.57. Relative Normalized PSRVs and Ratios of Surface/Downhole PSRVs for Radial Motions, Station W29, Event Towanda

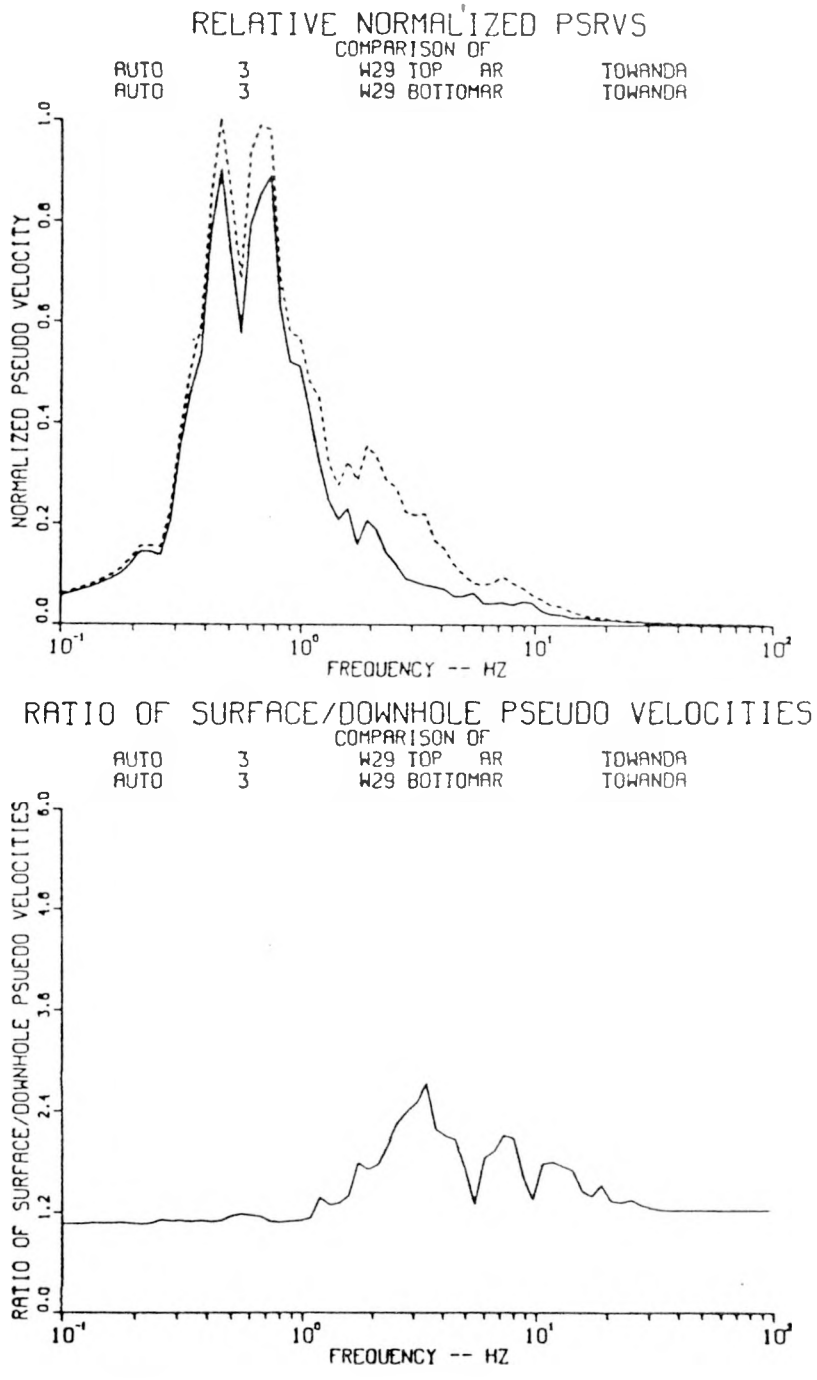

Figure A.58. Relative Normalized PSRVs and Ratios of Surface/Downhole PSRVs for Transverse Motions, Station W29, Event Labquark

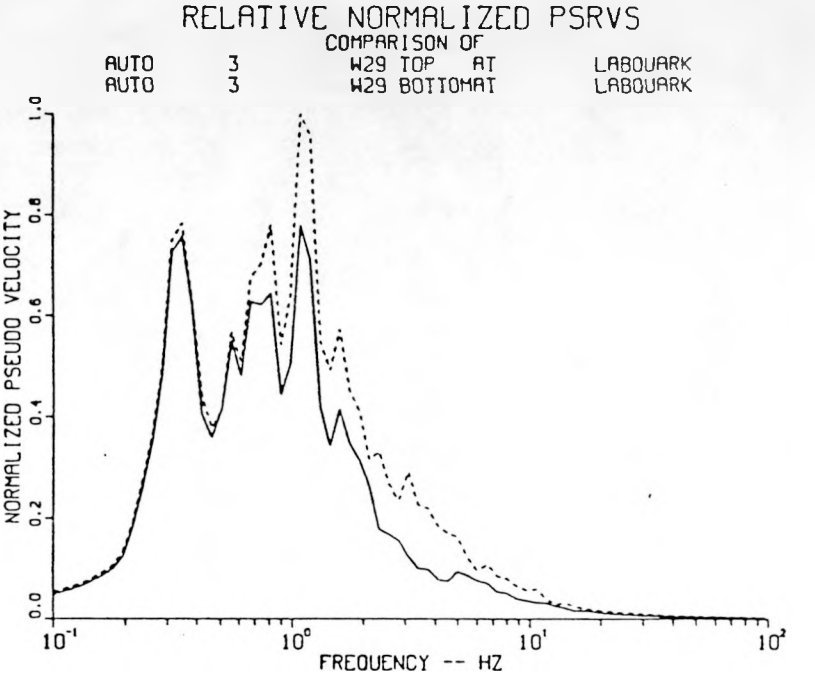

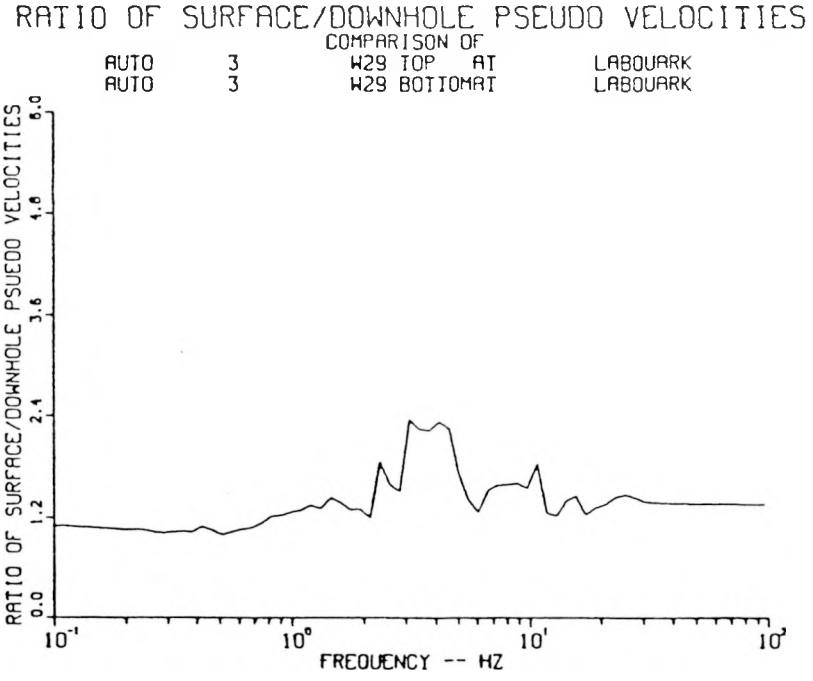

Figure A.59. Relative Normalized PSRVs and Ratios of Surface/Downhole PSRVs for Transverse Motions, Station W29, Event Salut

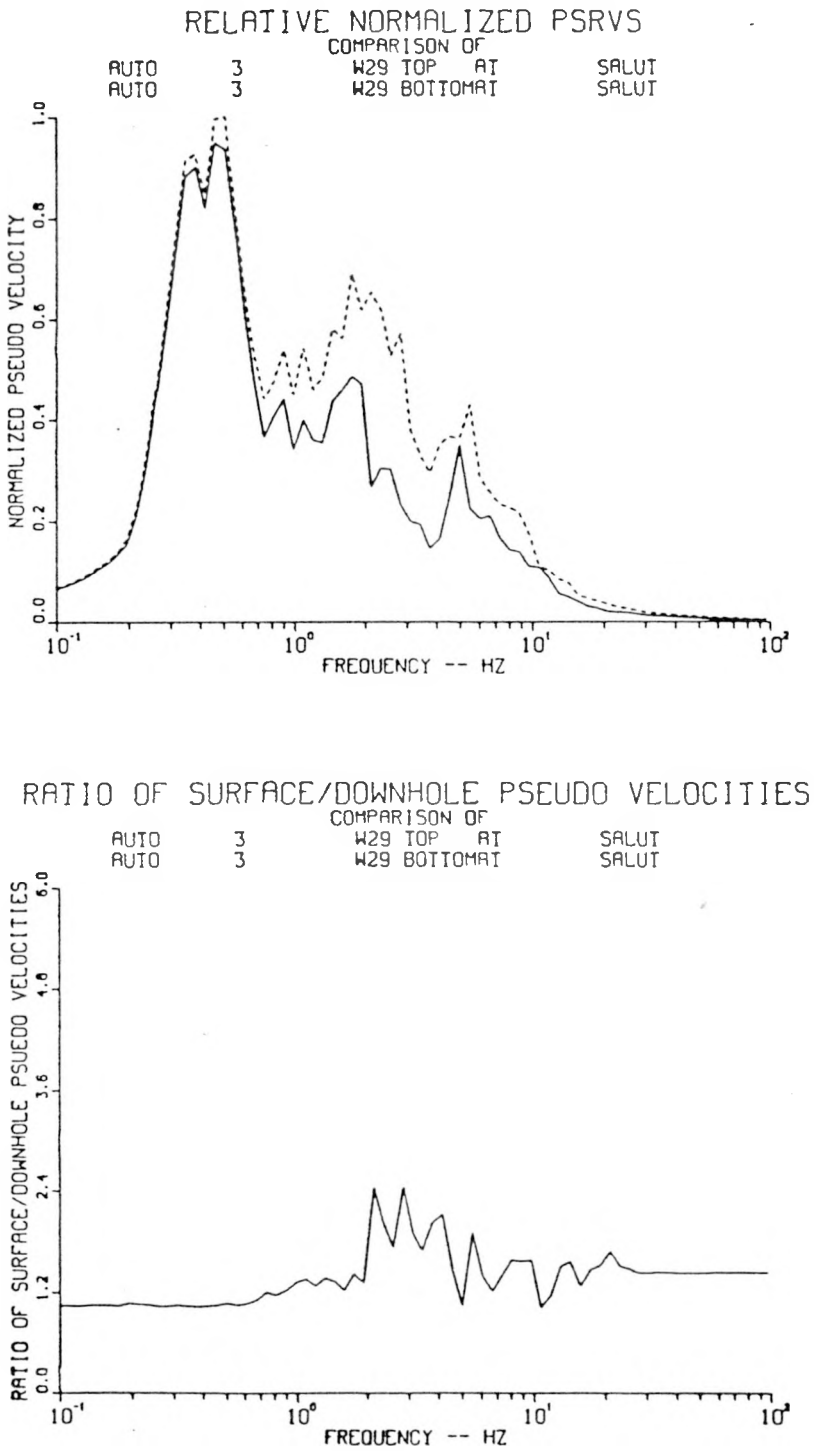

Figure A.60. Relative Normalized PSRVs and Ratios of Surface/Downhole PSRVs for Transverse Motions, Station W29, Event Jefferson

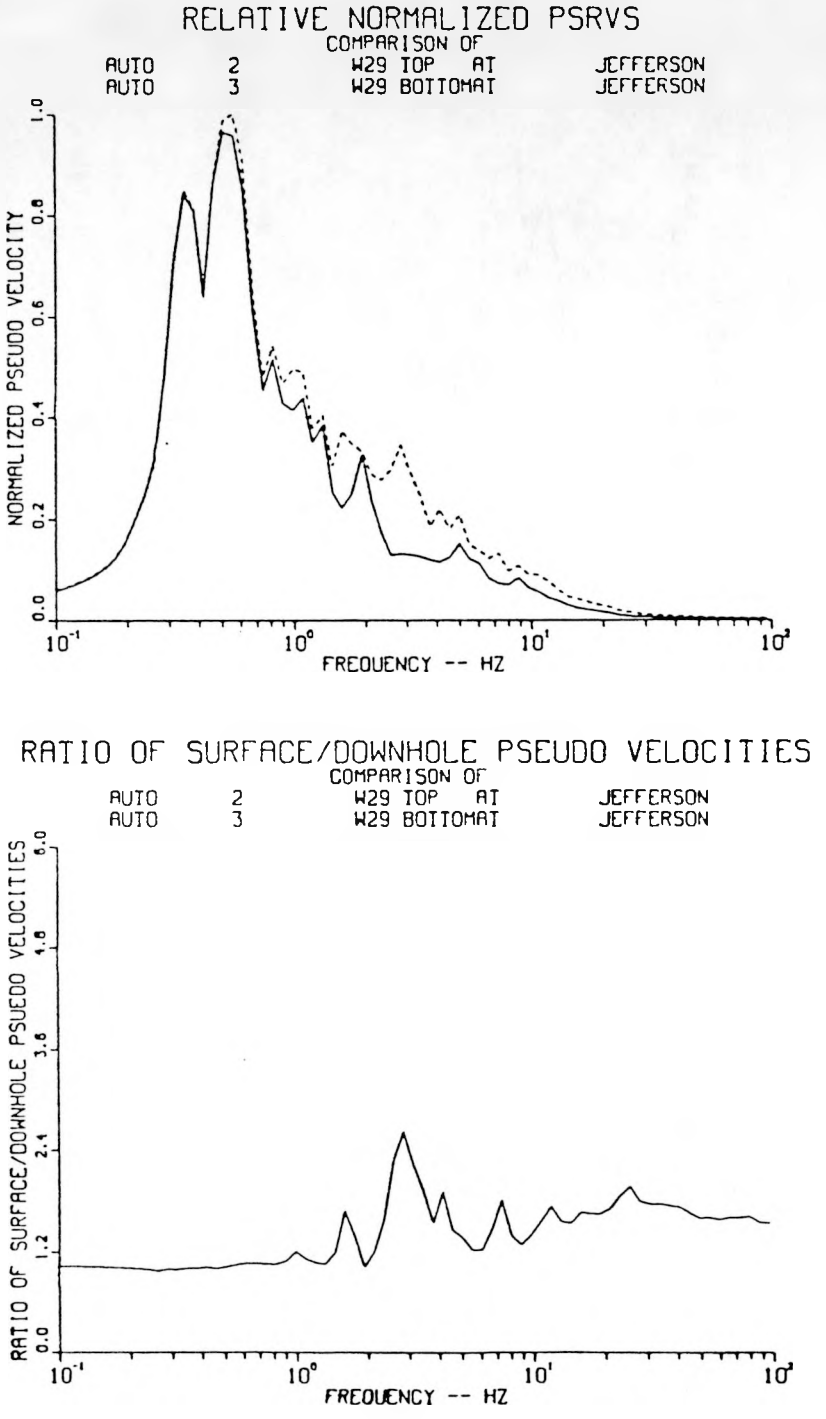

Figure A.61. Relative Normalized PSRVs and Ratios of Surface/Downhole PSRVs for Transverse Motions, Station W29, Event Serena

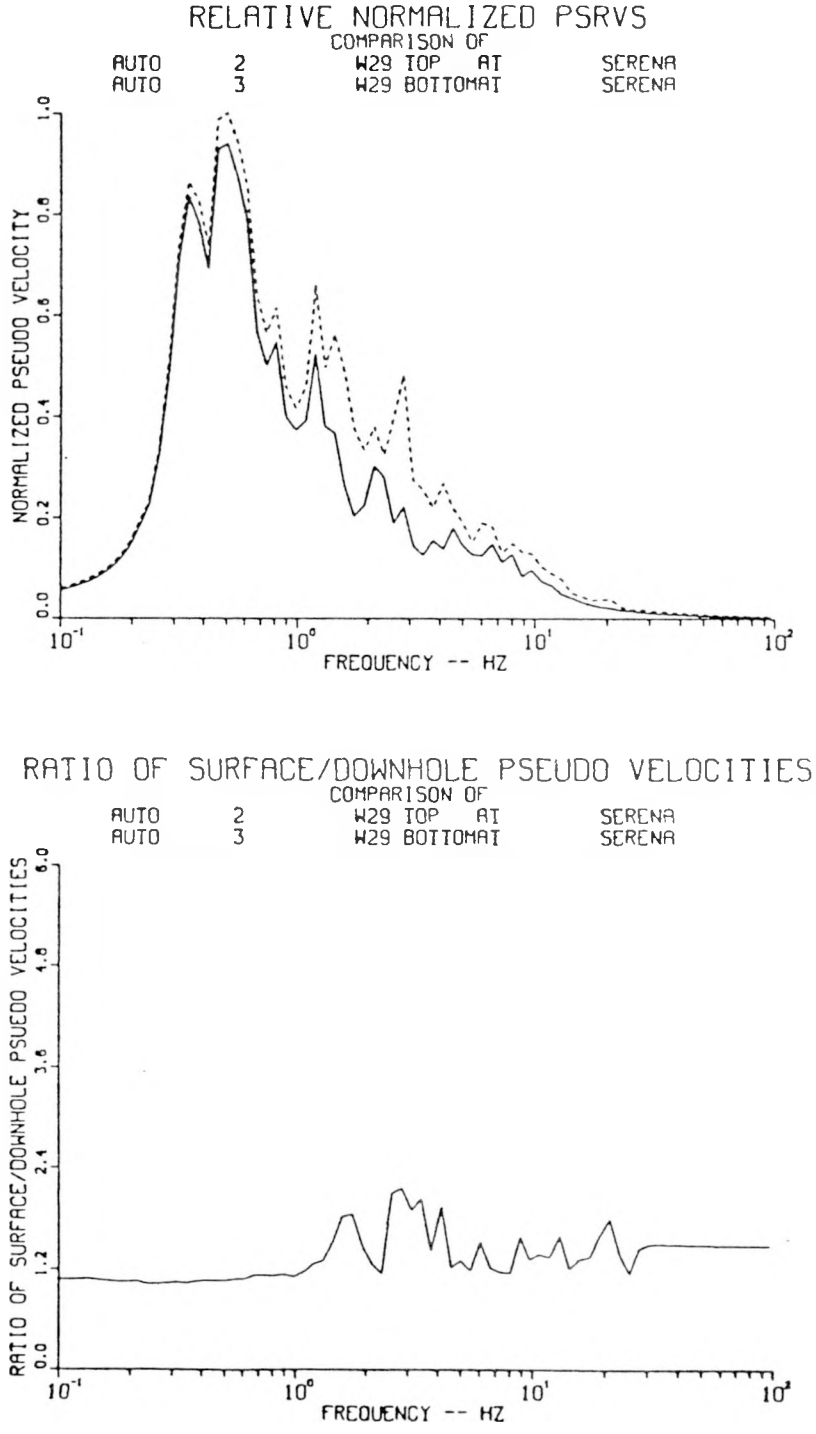

Figure A.62. Relative Normalized PSRVs and Ratios of Surface/Downhole PSRVs for Transverse Motions, Station W29, Event Goldstone

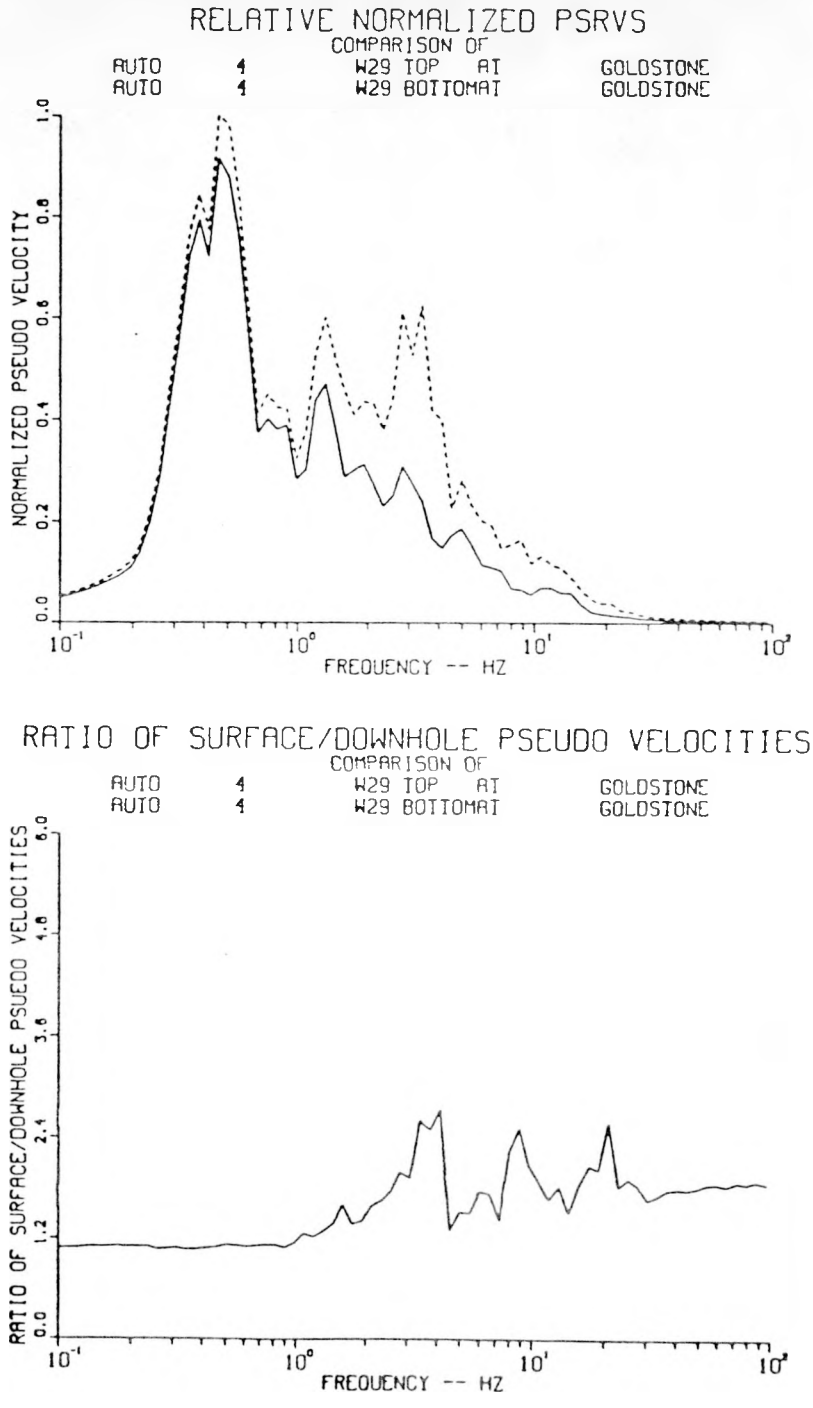

Figure A.63. Relative Normalized PSRVs and Ratios of Surface/Downhole PSRVs for Transverse Motions, Station W29, Event Towanda

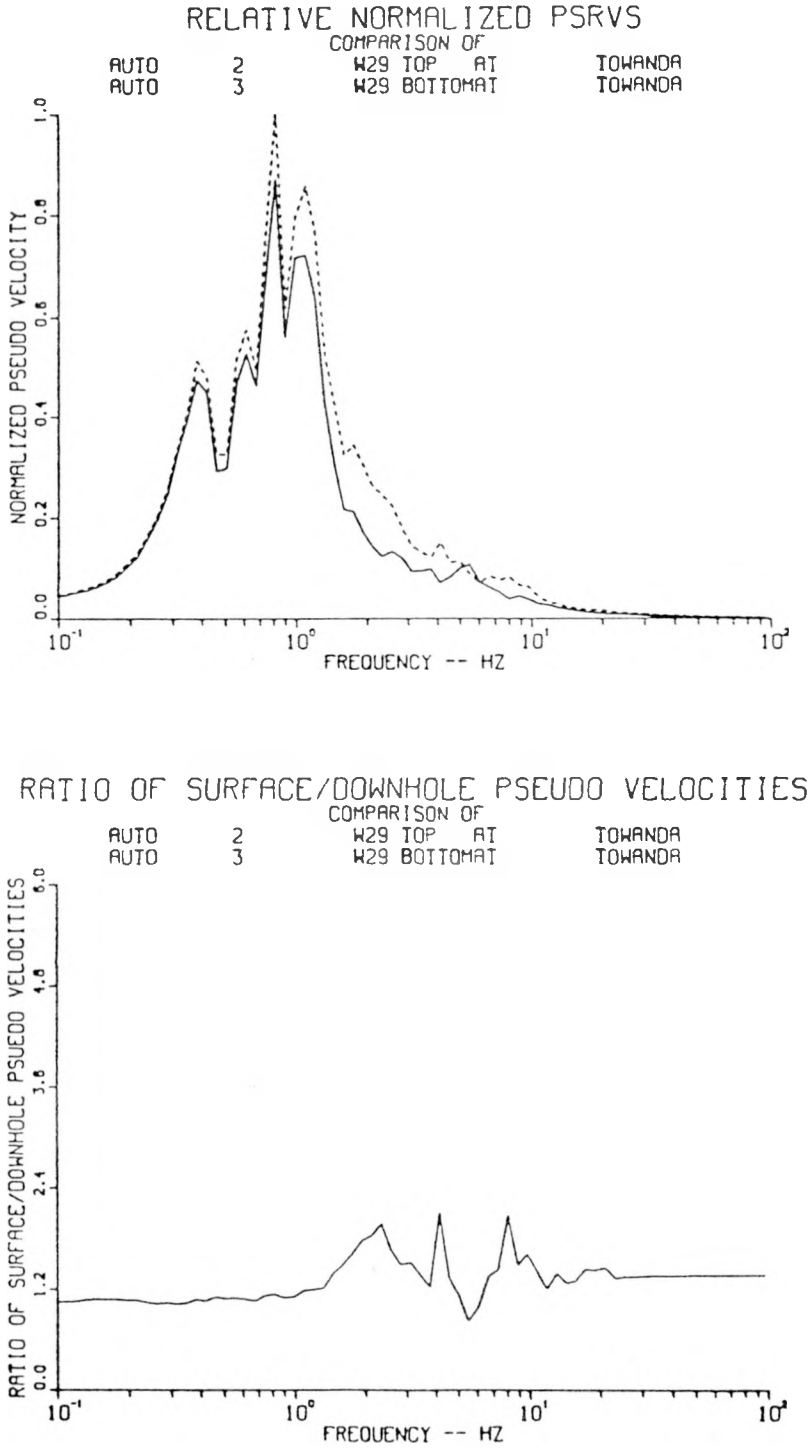

Figure A.64. Relative Normalized PSRVs and Ratios of Surface/Downhole PSRVs for Vertical Motions, Station W12(30), Event Labquark

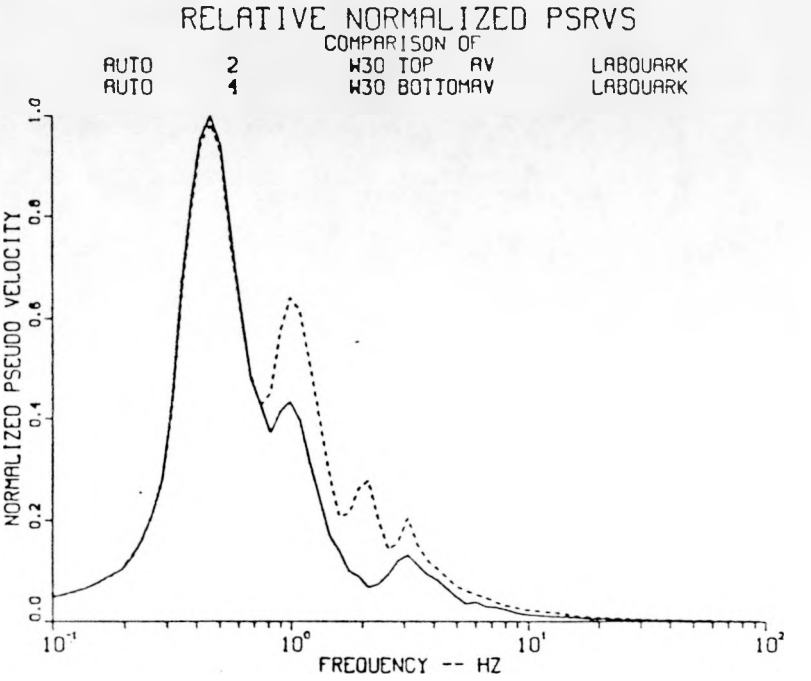

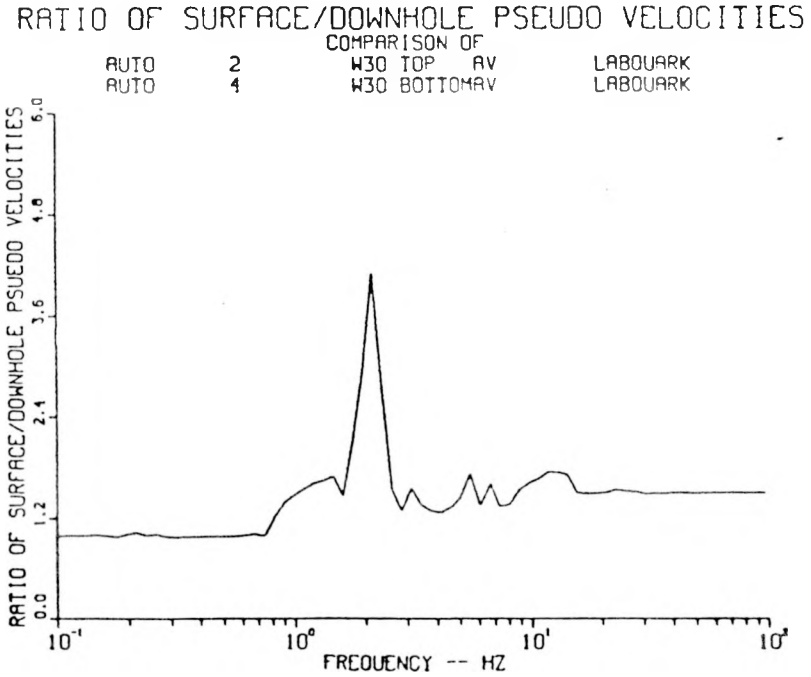

Figure A.65. Relative Normalized PSRVs and Ratios of Surface/Downhole PSRVs for Vertical Motions, Station W12(30), Event Chancellor

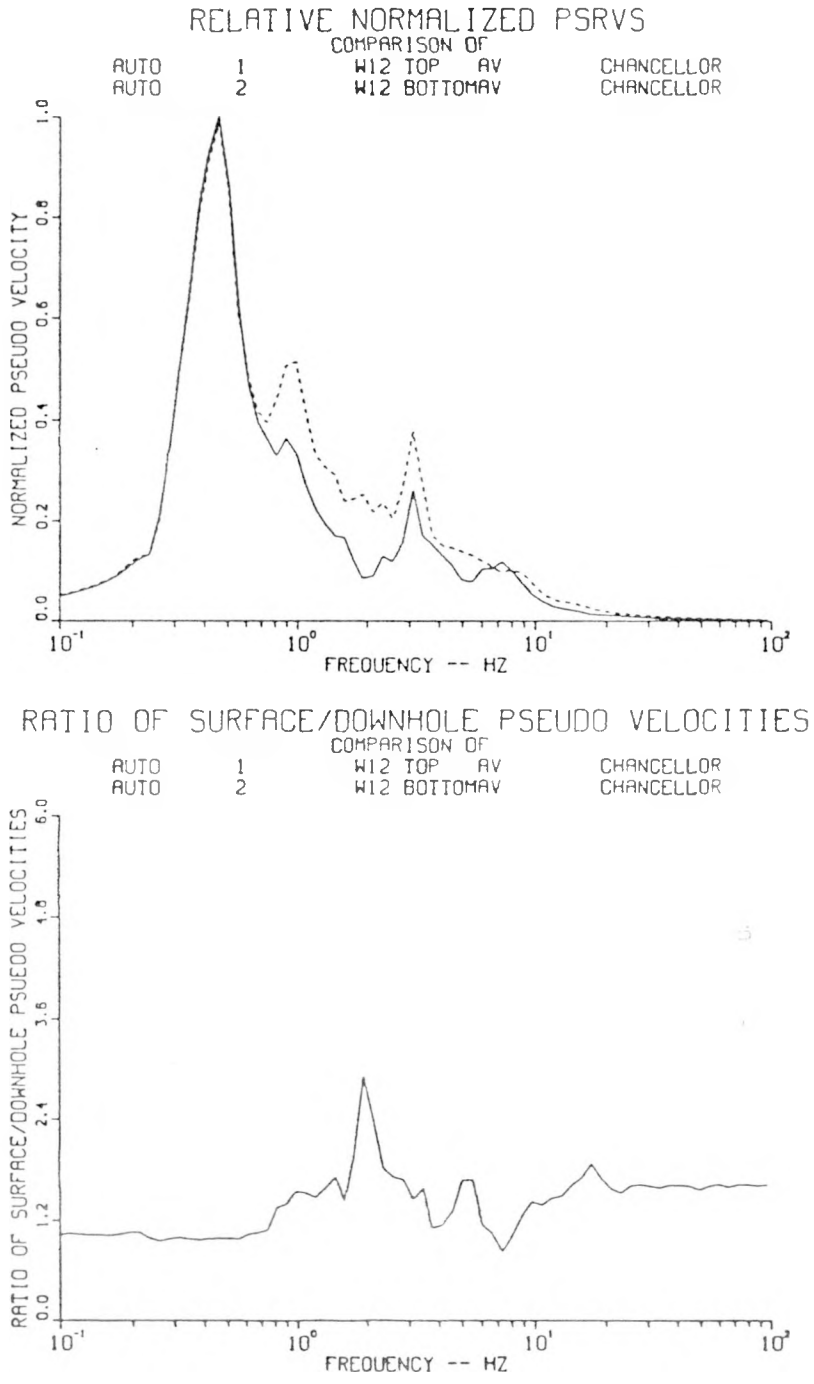

Figure A.66. Relative Normalized PSRVs and Ratios of Surface/Downhole PSRVs for Vertical Motions, Station W12(30), Event Salut

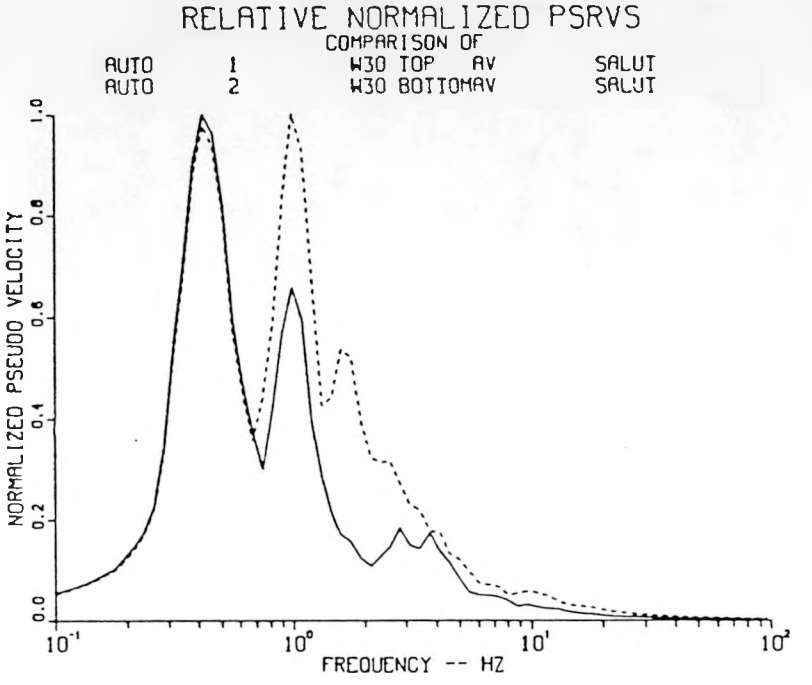

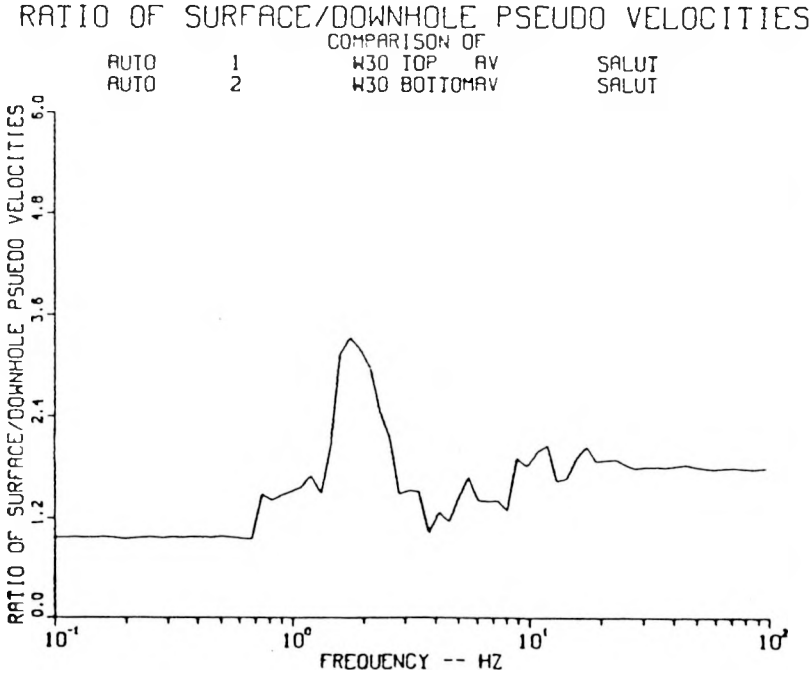

Figure A.67. Relative Normalized PSRVs and Ratios of Surface/Downhole PSRVs for Vertical Motions, Station W12(30), Event Kappeli

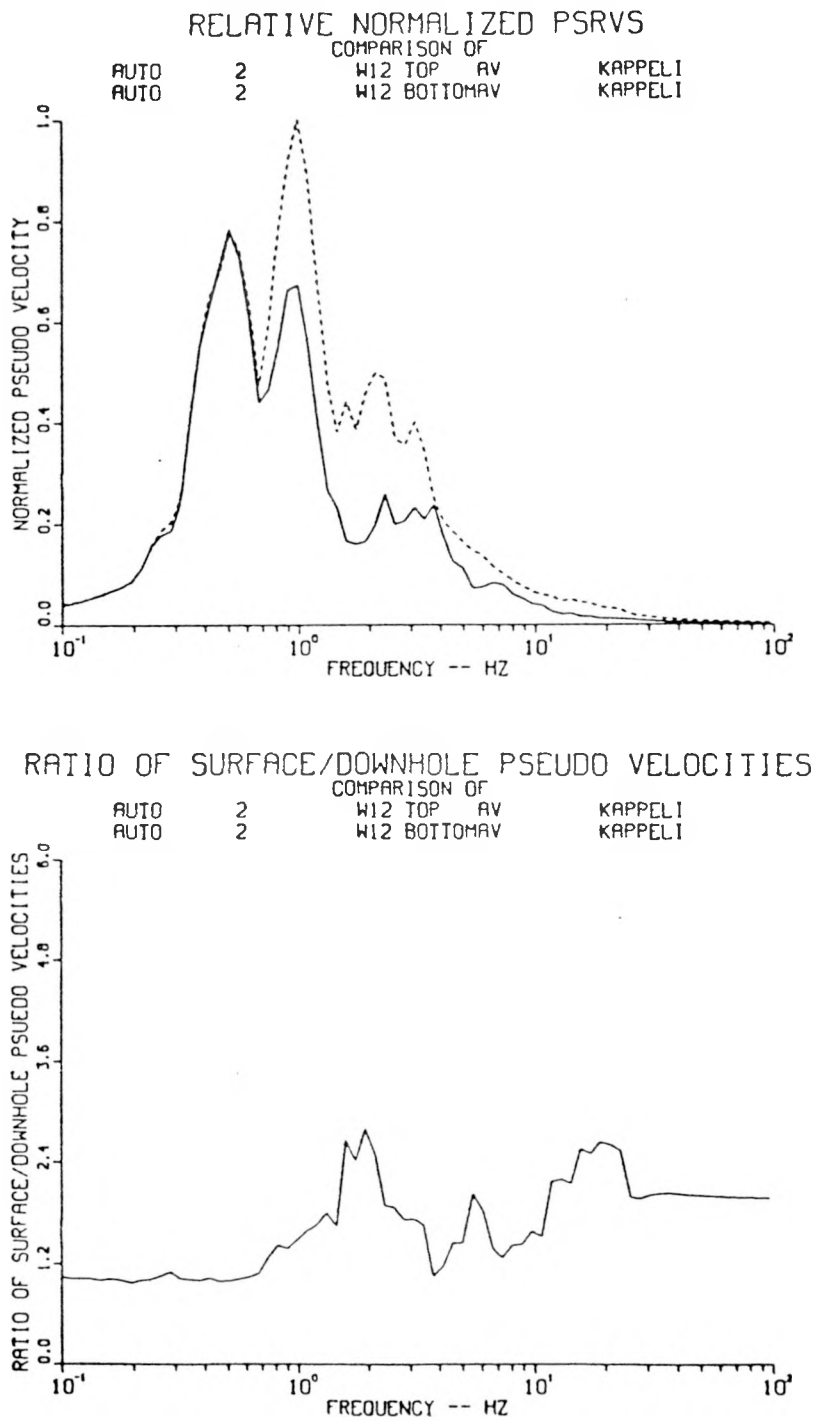

Figure A.68. Relative Normalized PSRVs and Ratios of Surface/Downhole PSRVs for Vertical Motions, Station W12(30), Event Jefferson

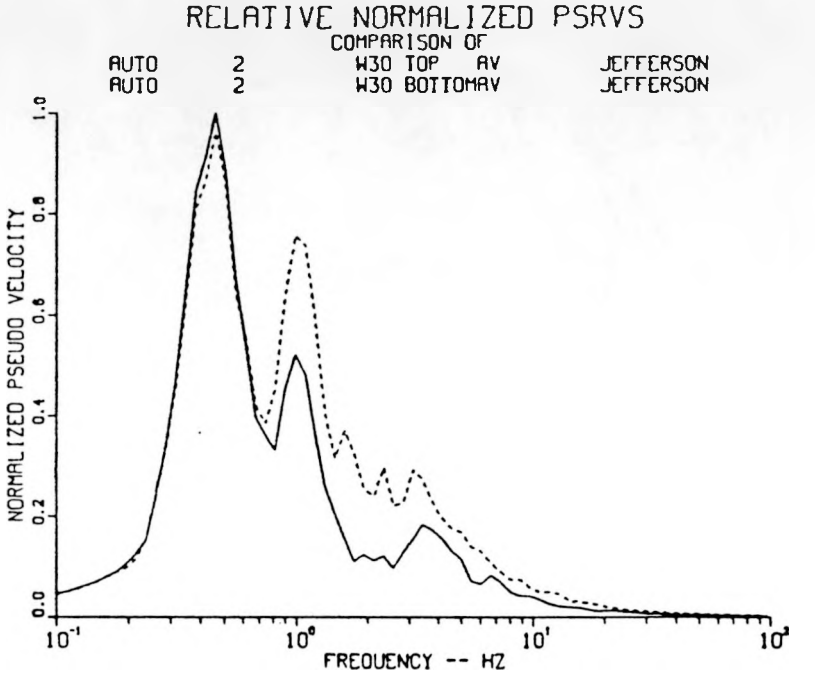

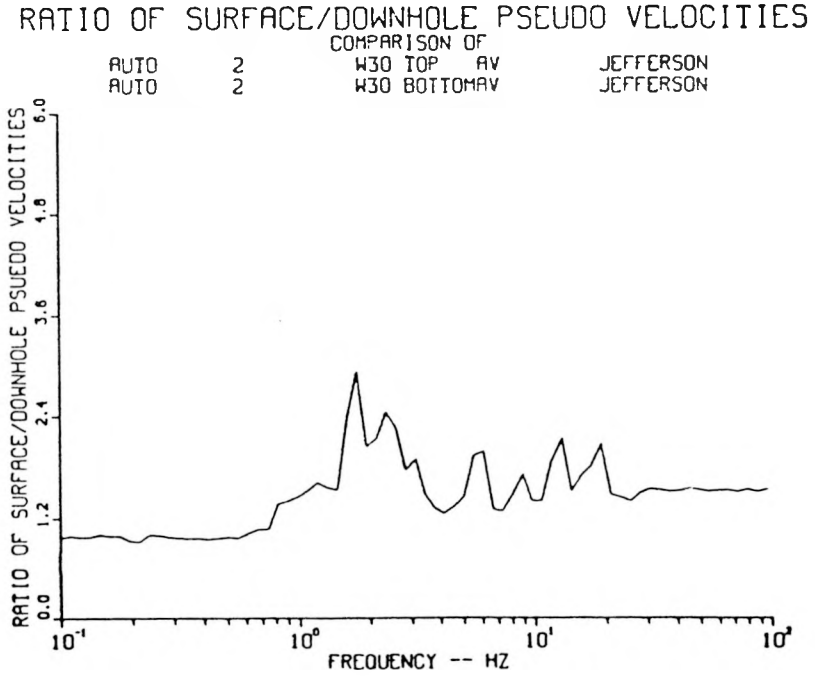

Figure A.69. Relative Normalized PSRVs and Ratios of Surface/Downhole PSRVs for Vertical Motions, Station W12(30), Event Serena

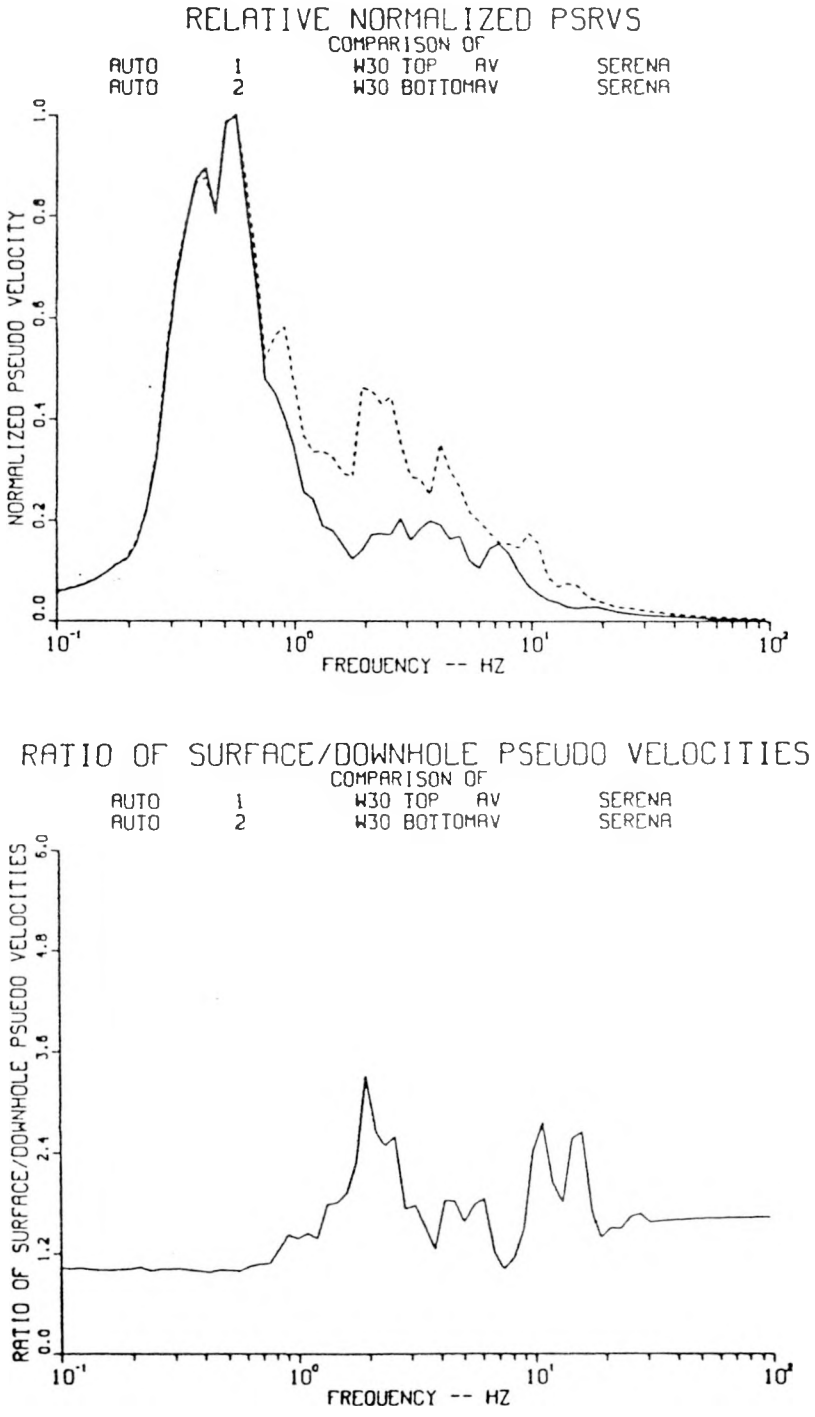

Figure A.70. Relative Normalized PSRVs and Ratios of Surface/Downhole PSRVs for Vertical Motions, Station W12(30), Event Goldstone

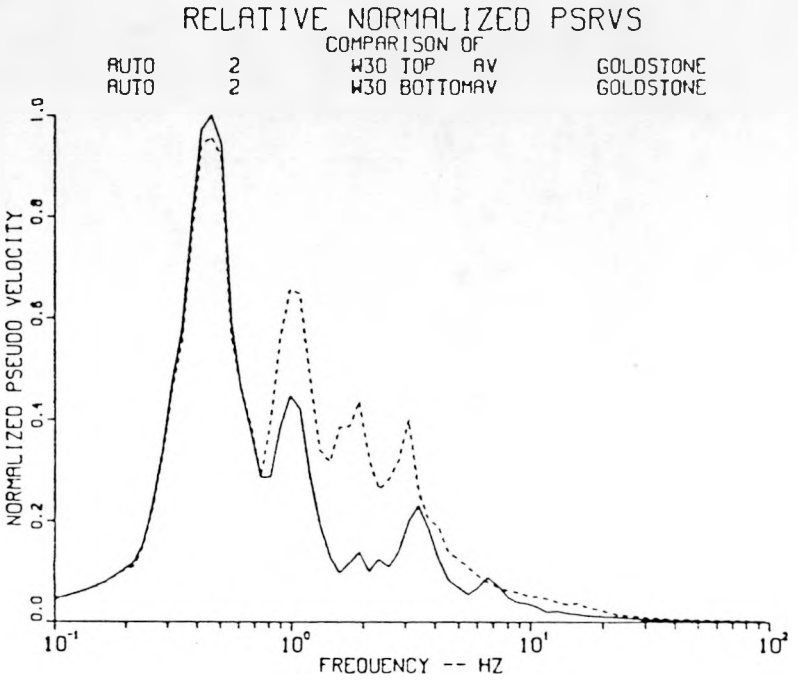

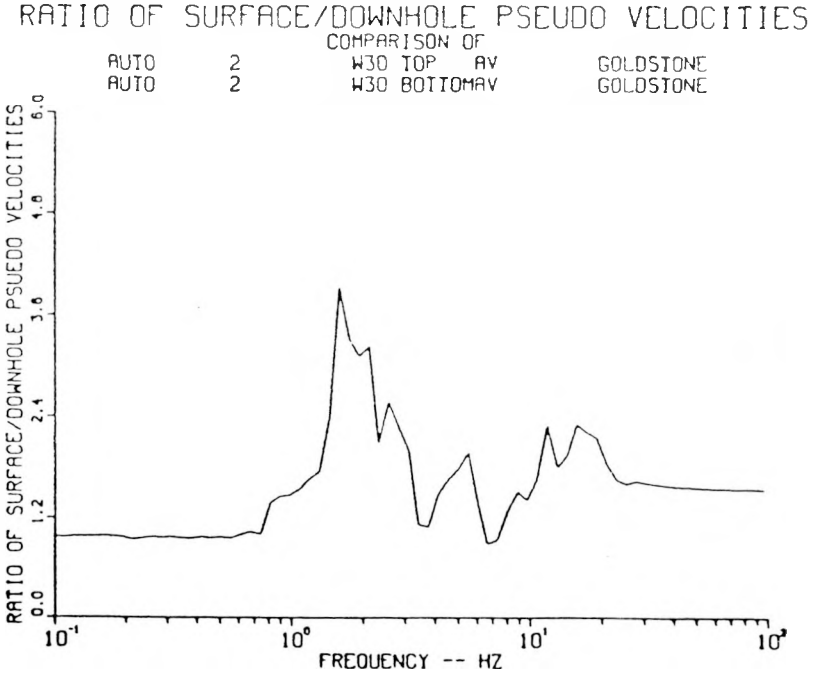

Figure A.71. Relative Normalized PSRVs and Ratios of Surface/Downhole PSRVs for Vertical Motions, Station W12(30), Event Cabra

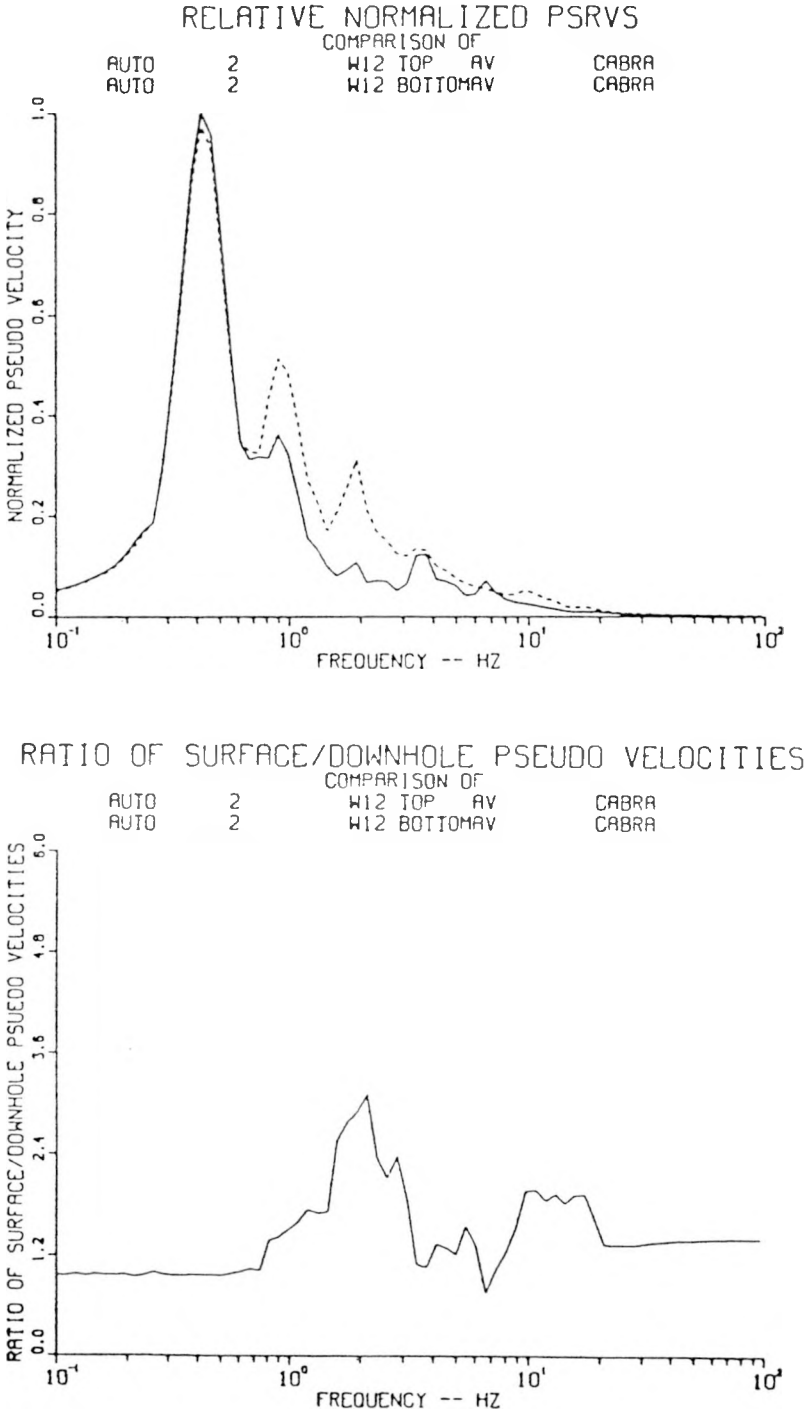

Figure A.72. Relative Normalized PSRVs and Ratios of Surface/Downhole PSRVs for Vertical Motions, Station W12(30), Event Towanda

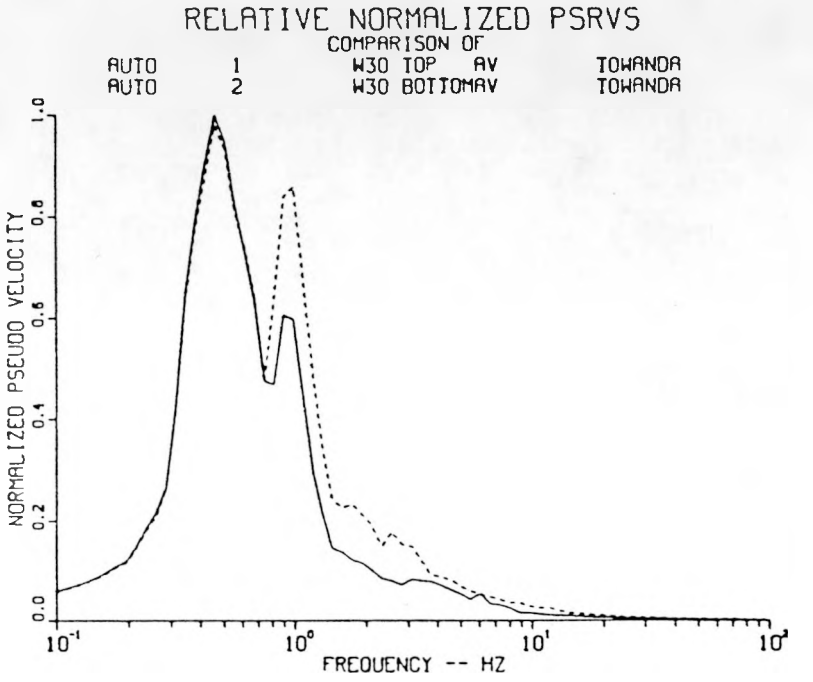

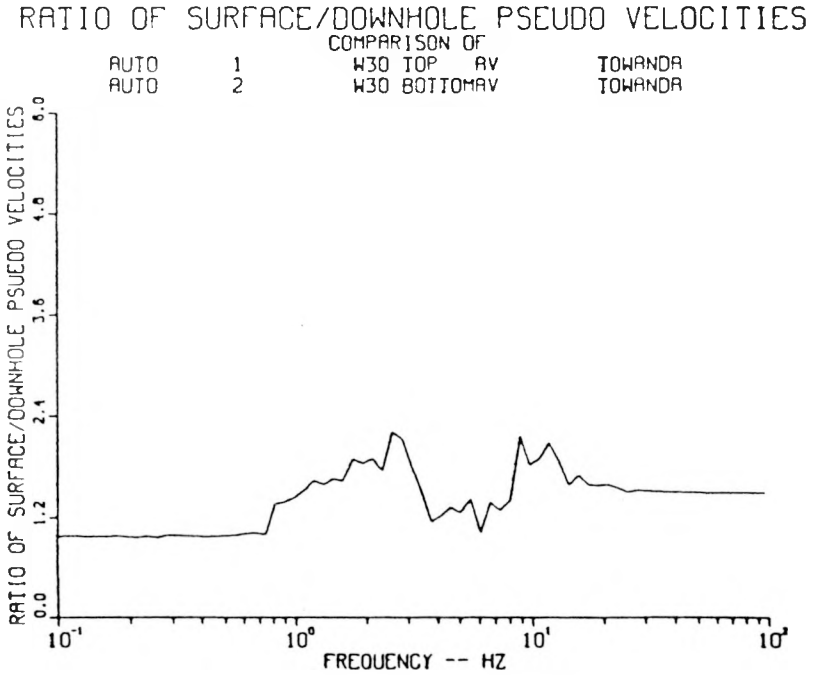

Figure A.73. Relative Normalized PSRVs and Ratios of Surface/Downhole PSRVs for Radial Motions, Station W12(30), Event Labquark

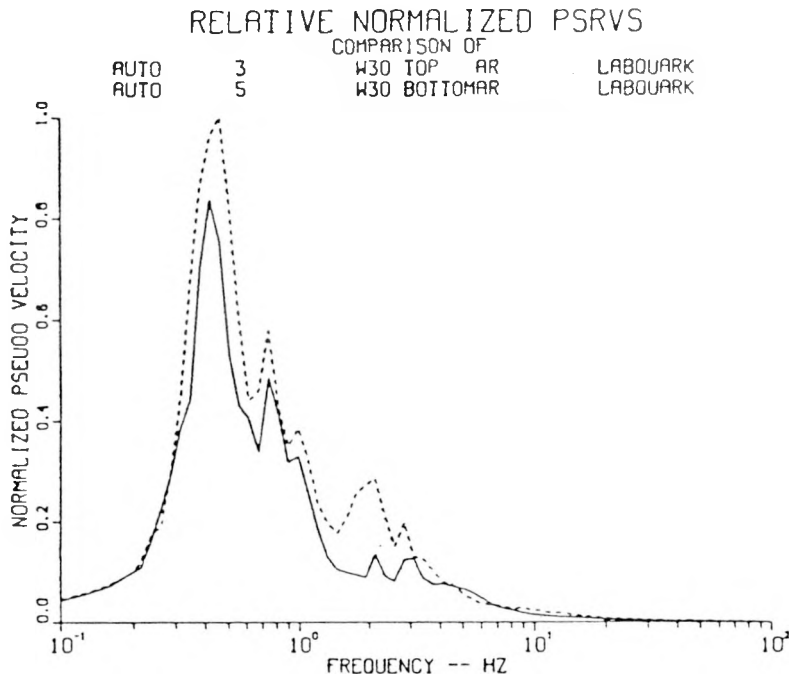

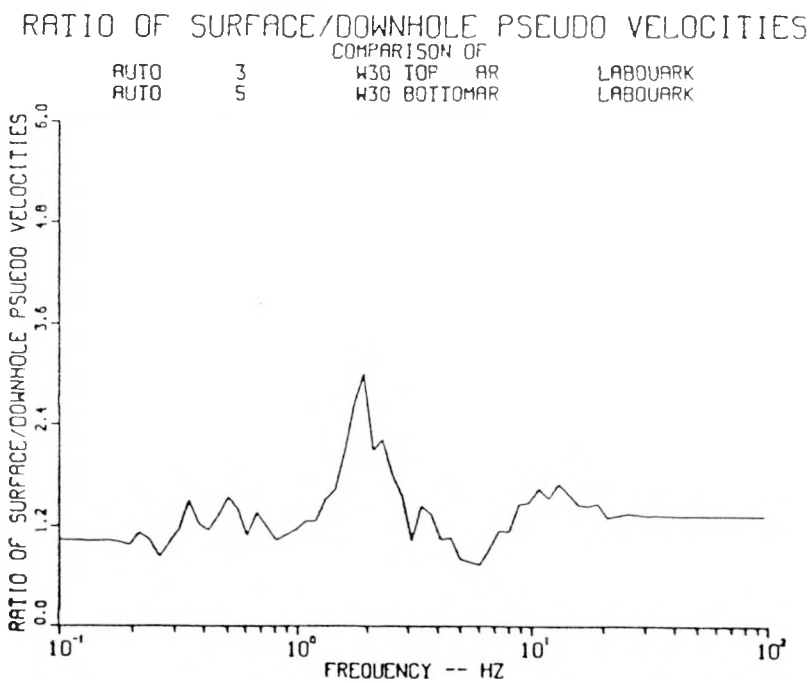

Figure A.74. Relative Normalized PSRVs and Ratios of Surface/Downhole PSRVs for Radial Motions, Station W12(30), Event Chancellor

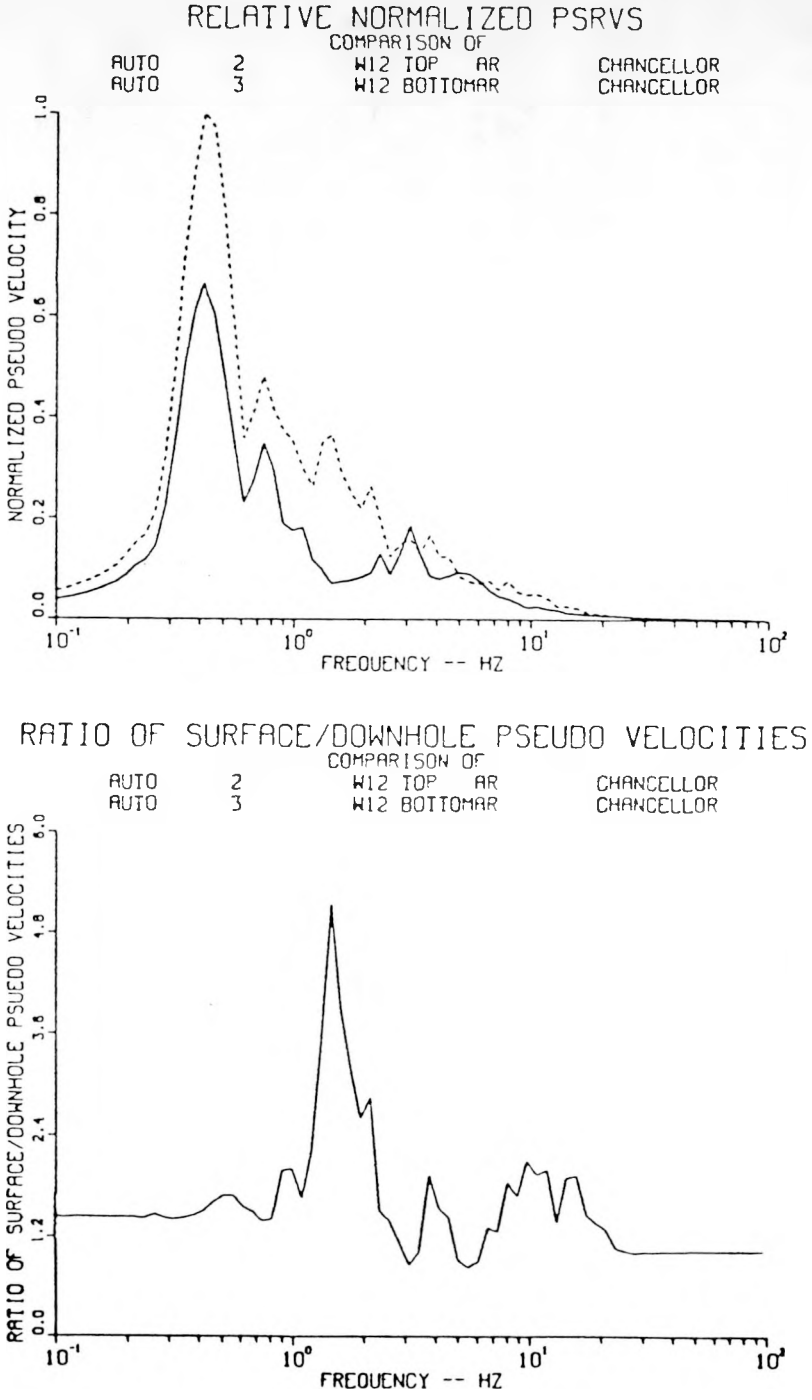

Figure A.75. Relative Normalized PSRVs and Ratios of Surface/Downhole PSRVs for Radial Motions, Station W12(30), Event Salut

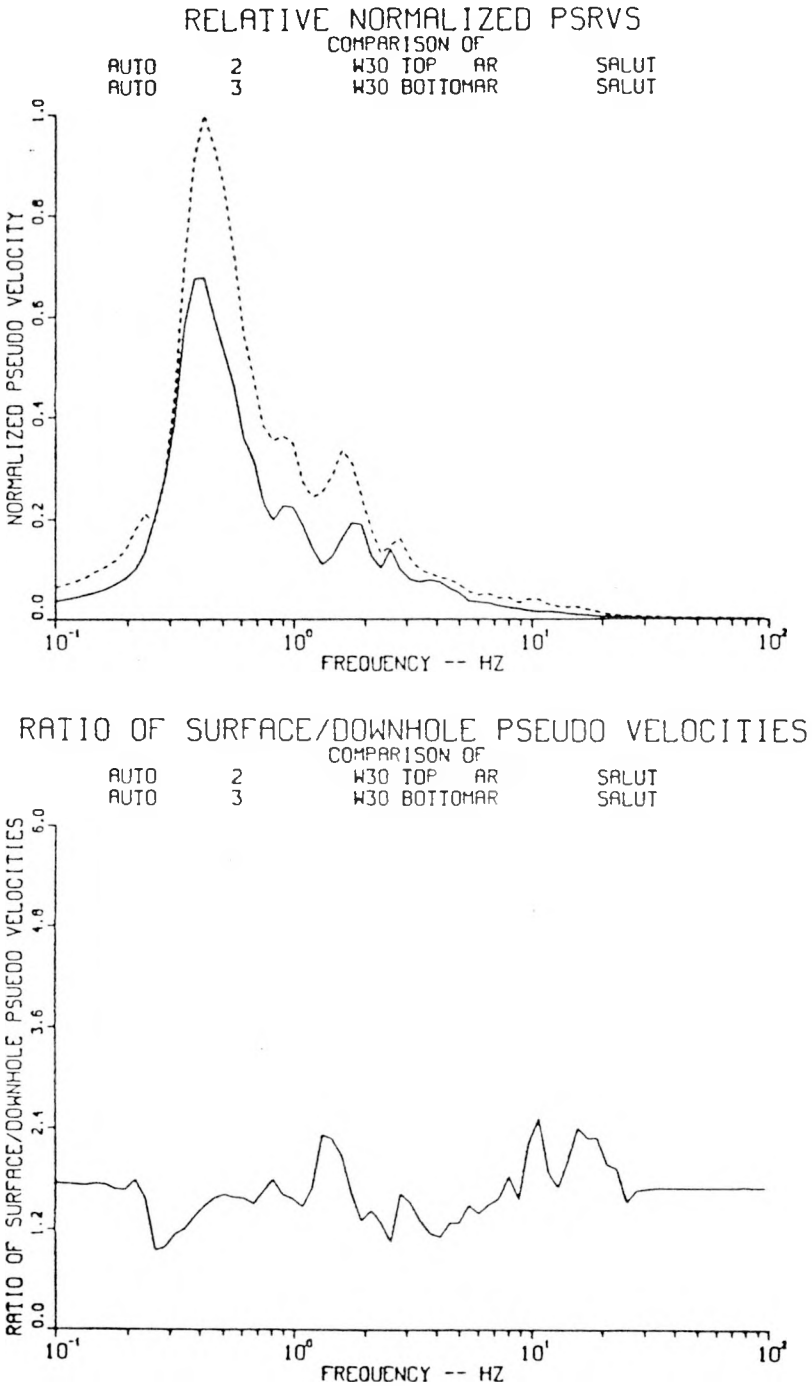

Figure A.76. Relative Normalized PSRVs and Ratios of Surface/Downhole PSRVs for Radial Motions, Station W12(30), Event Kappeli

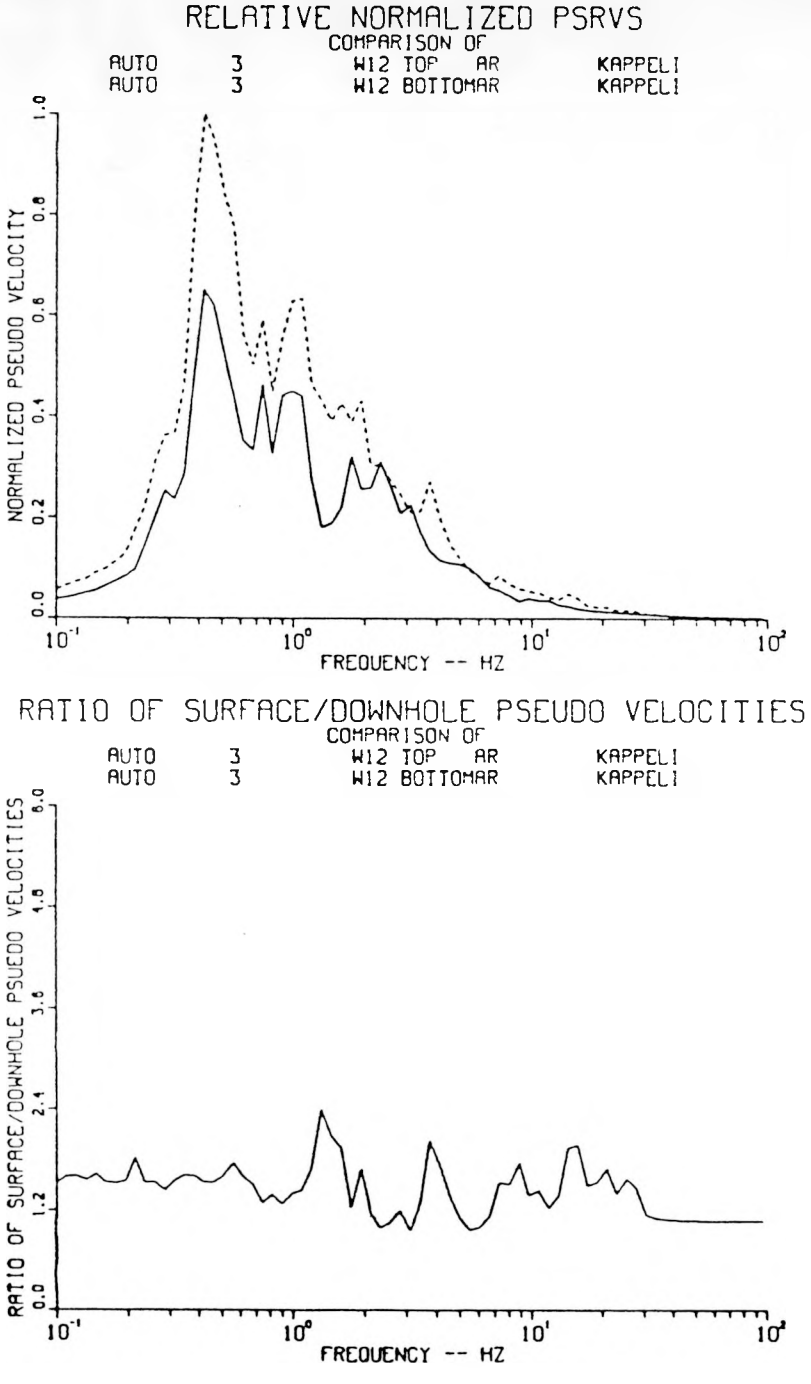

Figure A.77. Relative Normalized PSRVs and Ratios of Surface/Downhole PSRVs for Radial Motions, Station W12(30), Event Jefferson

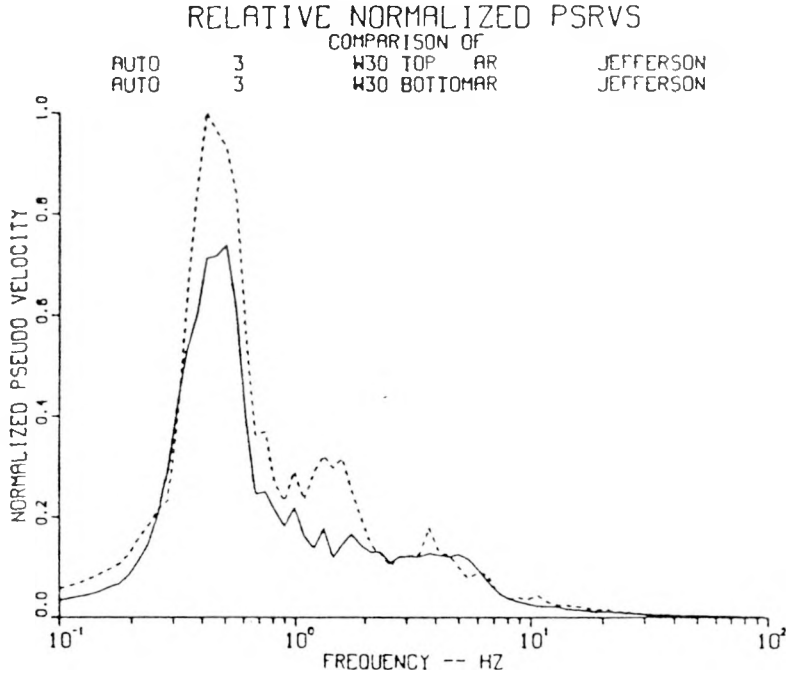

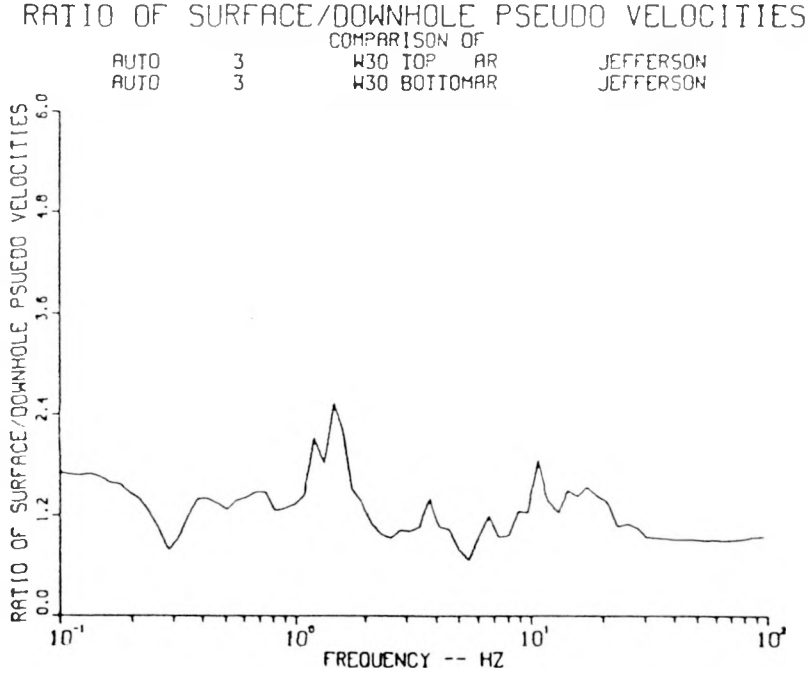

Figure A.78. Relative Normalized PSRVs and Ratios of Surface/Downhole PSRVs for Radial Motions, Station W12(30), Event Serena

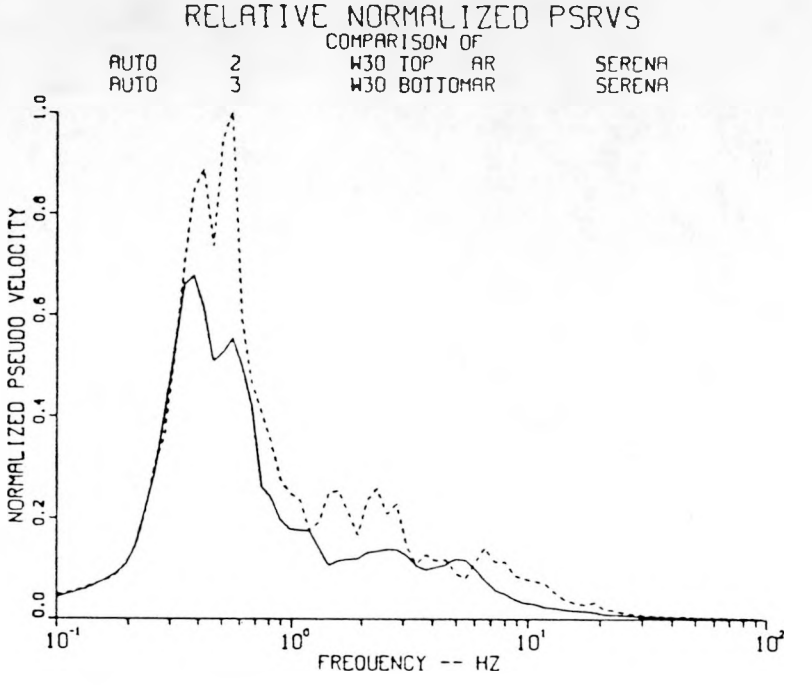

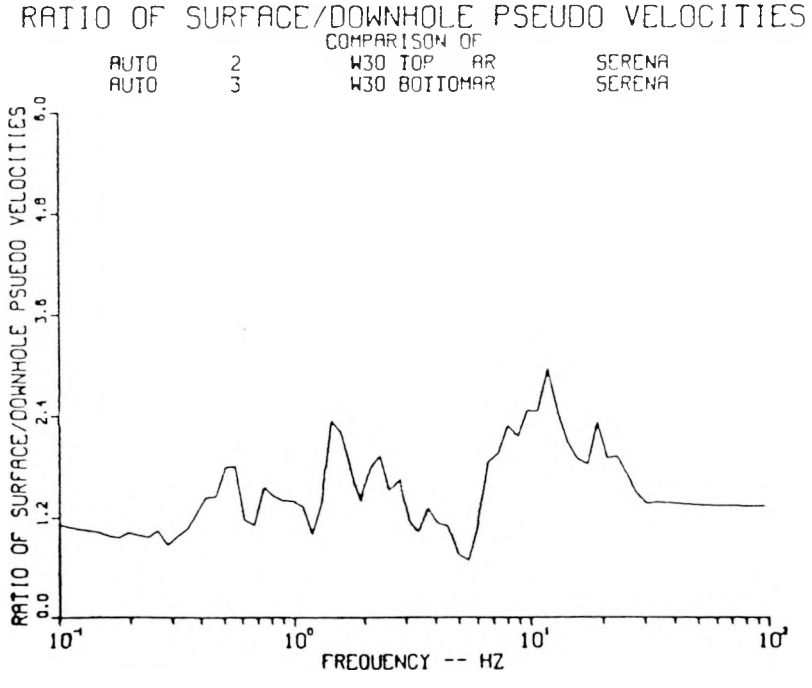

Figure A.79. Relative Normalized PSRVs and Ratios of Surface/Downhole PSRVs for Radial Motions, Station W12(30), Event Goldstone

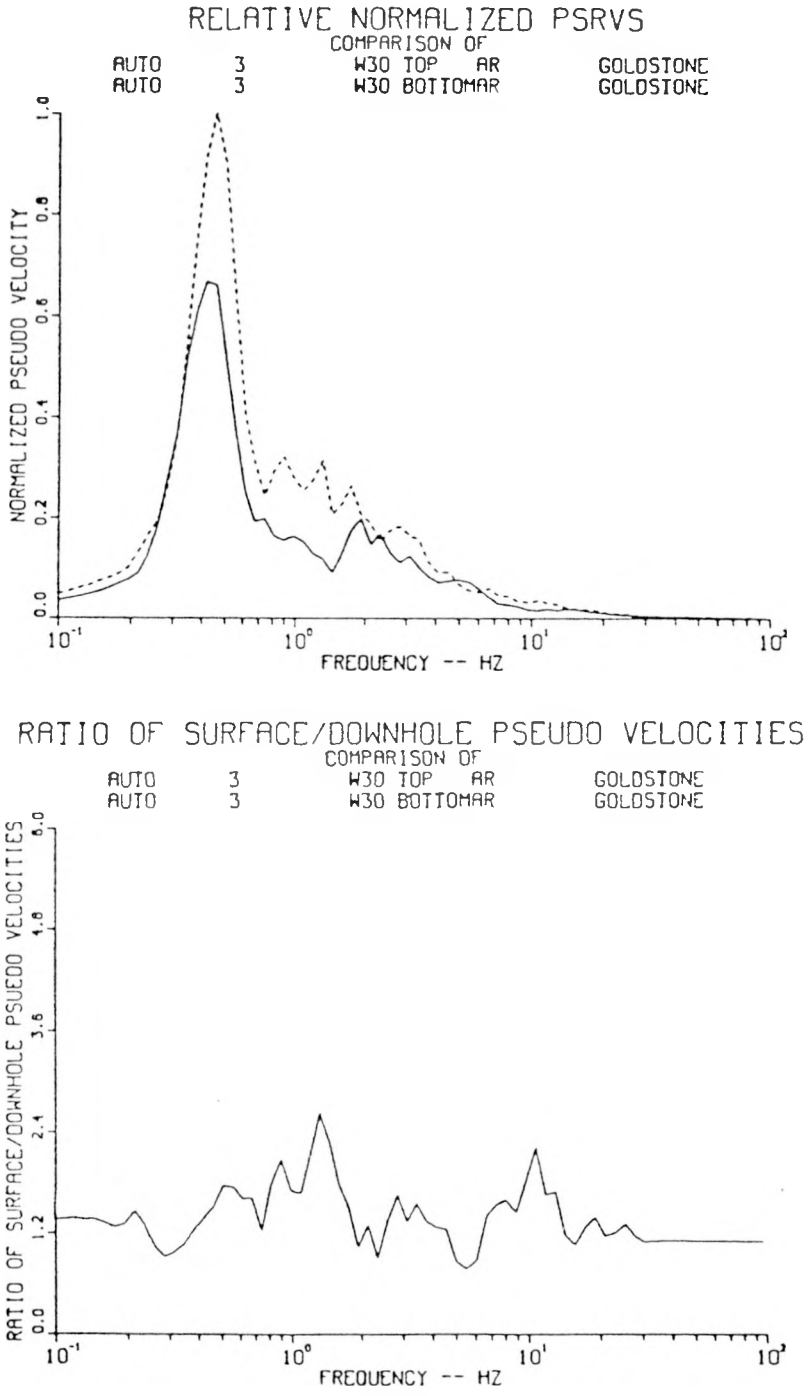

Figure A.80. Relative Normalized PSRVs and Ratios of Surface/Downhole PSRVs for Radial Motions, Station W12(30), Event Cabra

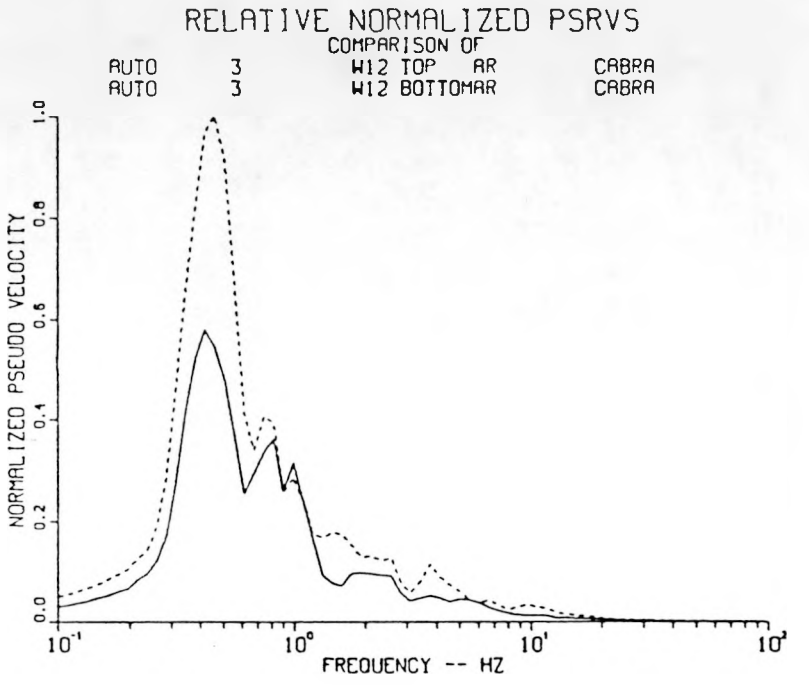

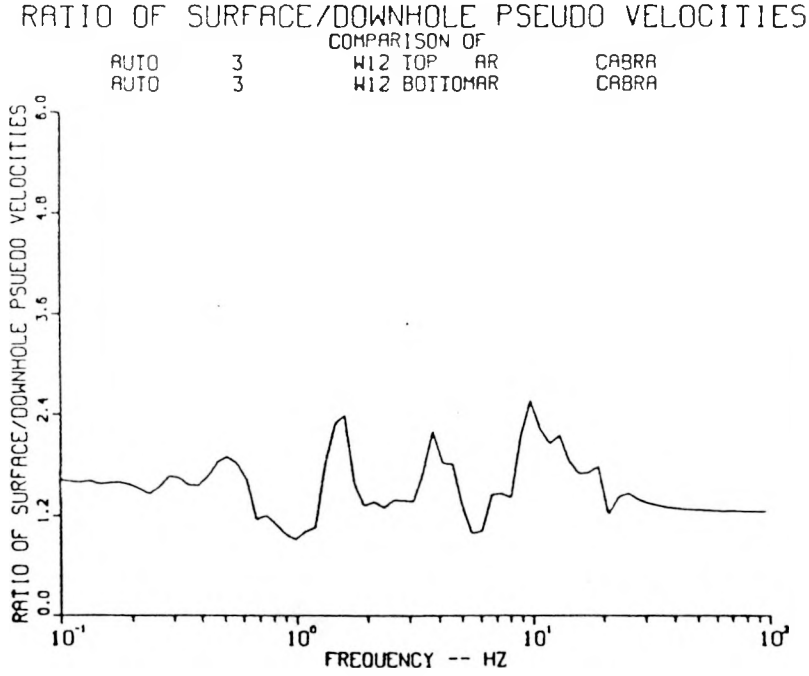

Figure A.81. Relative Normalized PSRVs and Ratios of Surface/Downhole PSRVs for Radial Motions, Station W12(30), Event Towanda

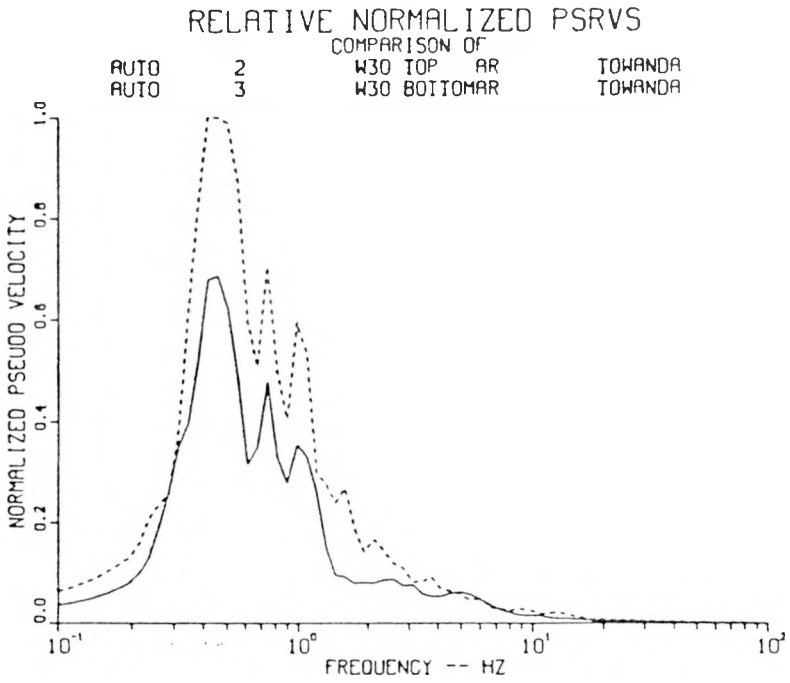

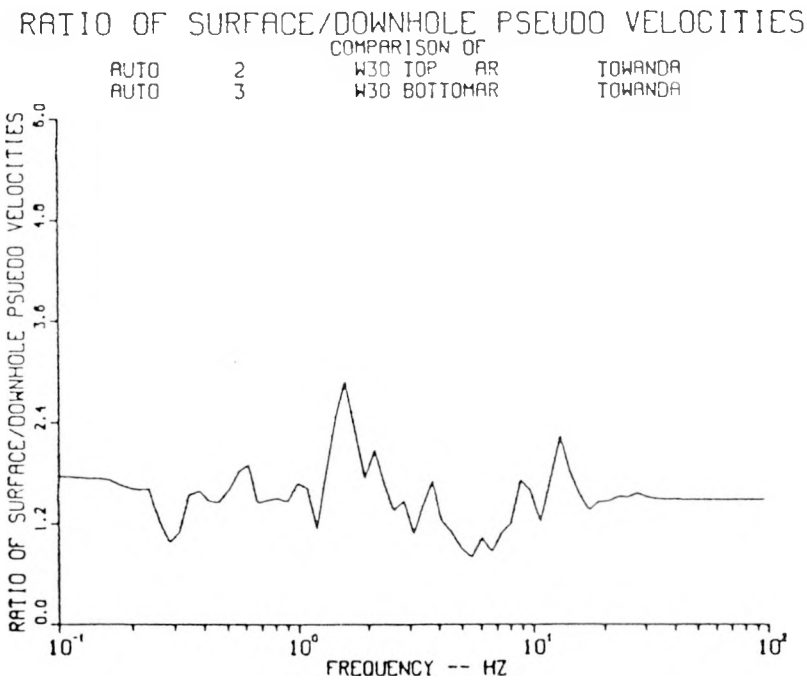

Figure A.82. Relative Normalized PSRVs and Ratios of Surface/Downhole PSRVs for Transverse Motions, Station W12(30), Event Labquark

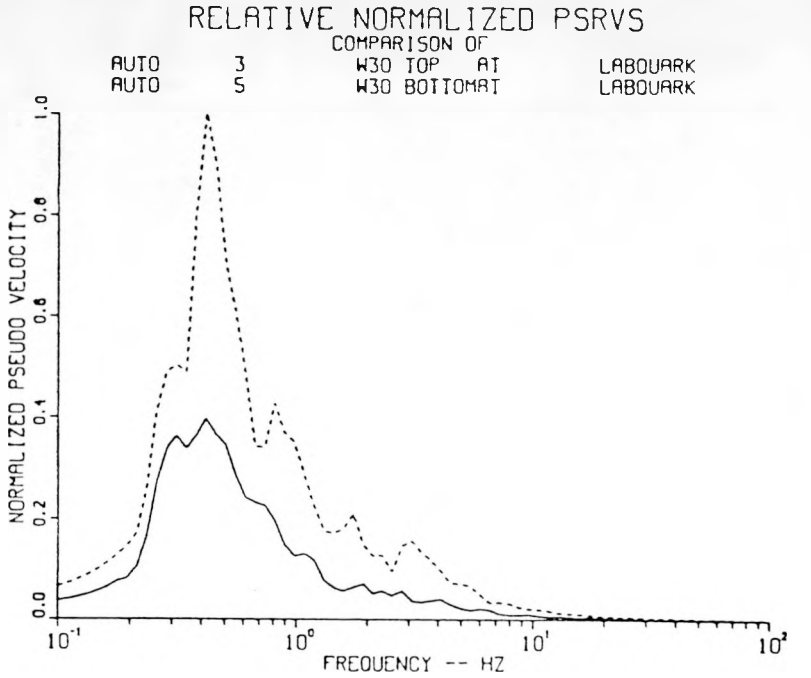

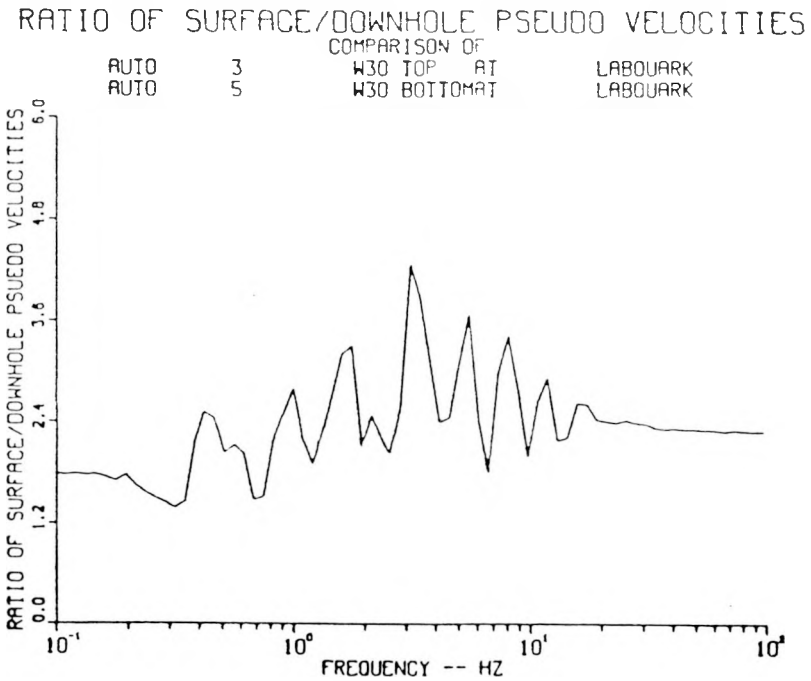

Figure A.83. Relative Normalized PSRVs and Ratios of Surface/Downhole PSRVs for Transverse Motions, Station W12(30), Event Chancellor

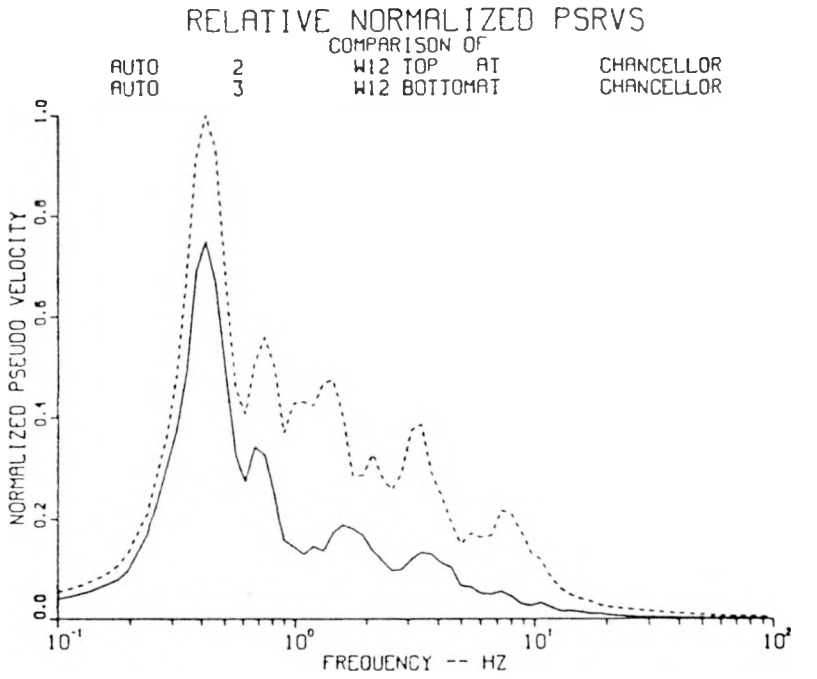

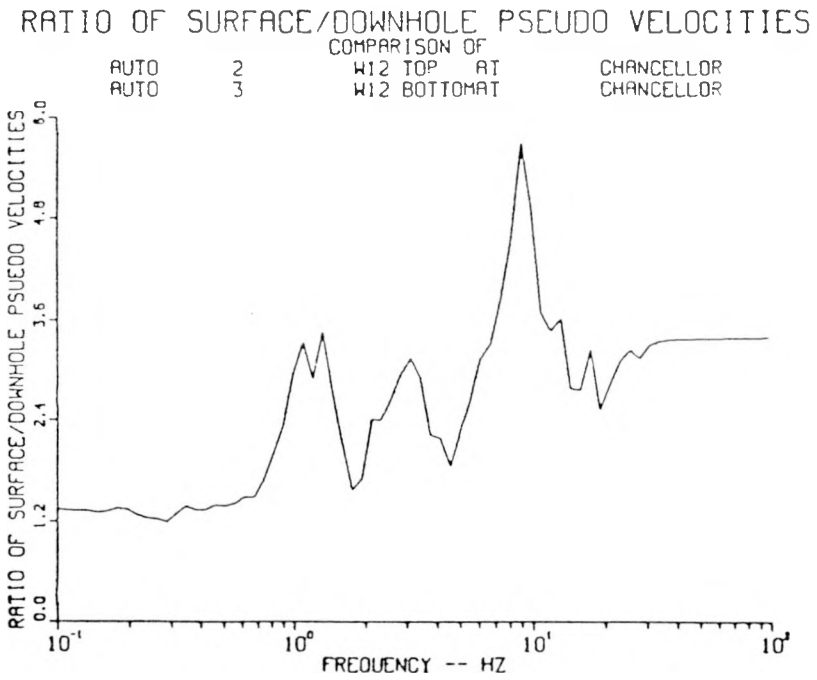

Figure A.84. Relative Normalized PSRVs and Ratios of Surface/Downhole PSRVs for Transverse Motions, Station W12(30), Event Salut

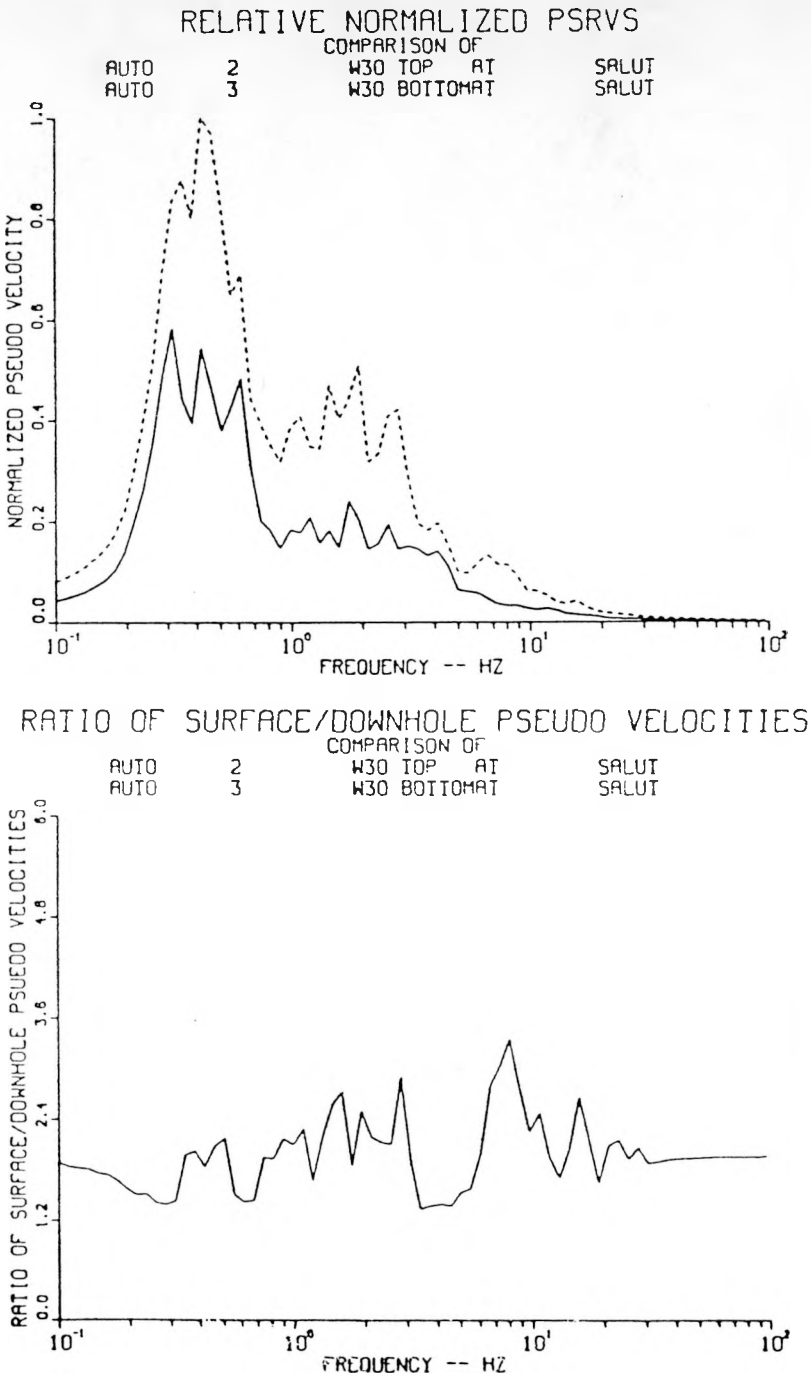

Figure A.85. Relative Normalized PSRVs and Ratios of Surface/Downhole PSRVs for Transverse Motions, Station W12(30), Event Kappeli

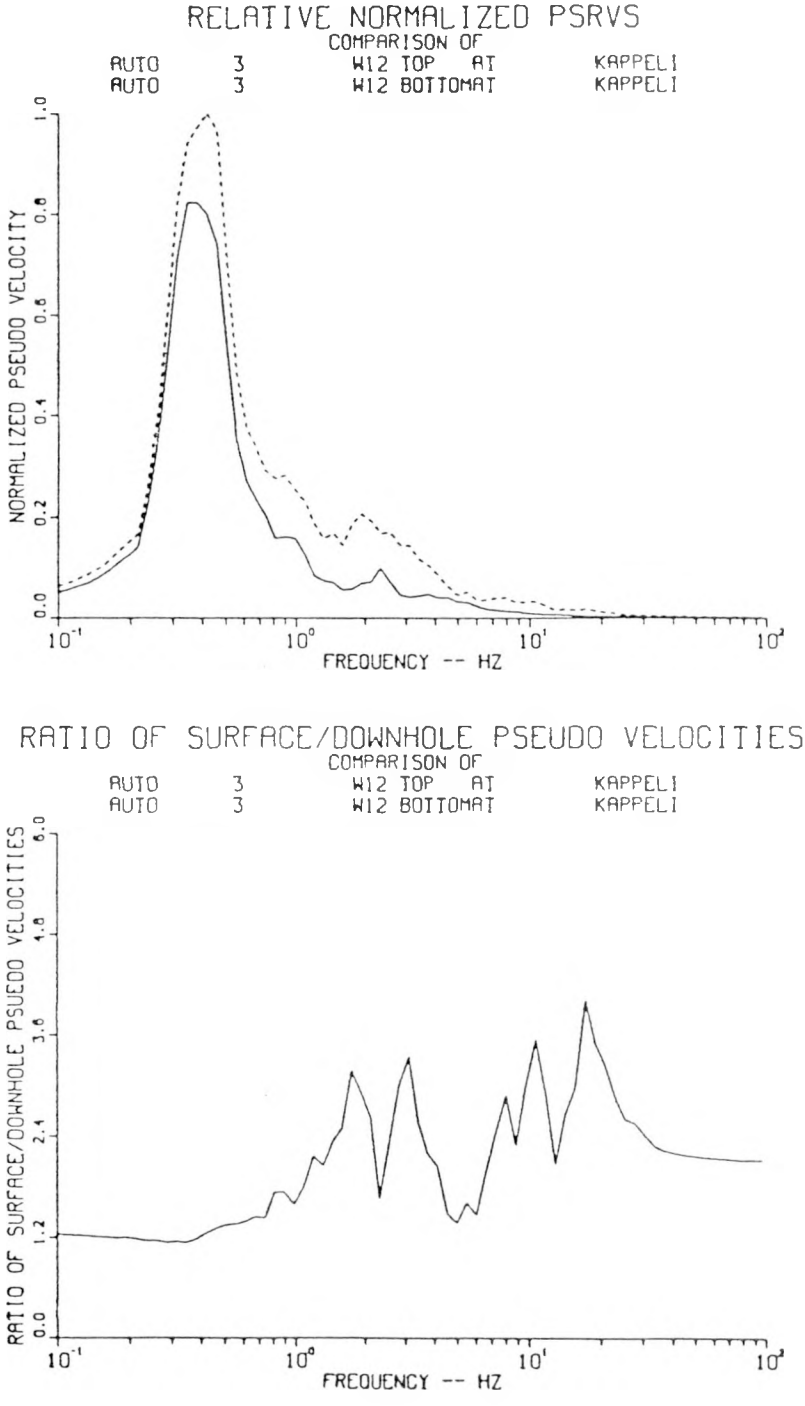

Figure A.86. Relative Normalized PSRVs and Ratios of Surface/Downhole PSRVs for Transverse Motions, Station W12(30), Event Jefferson

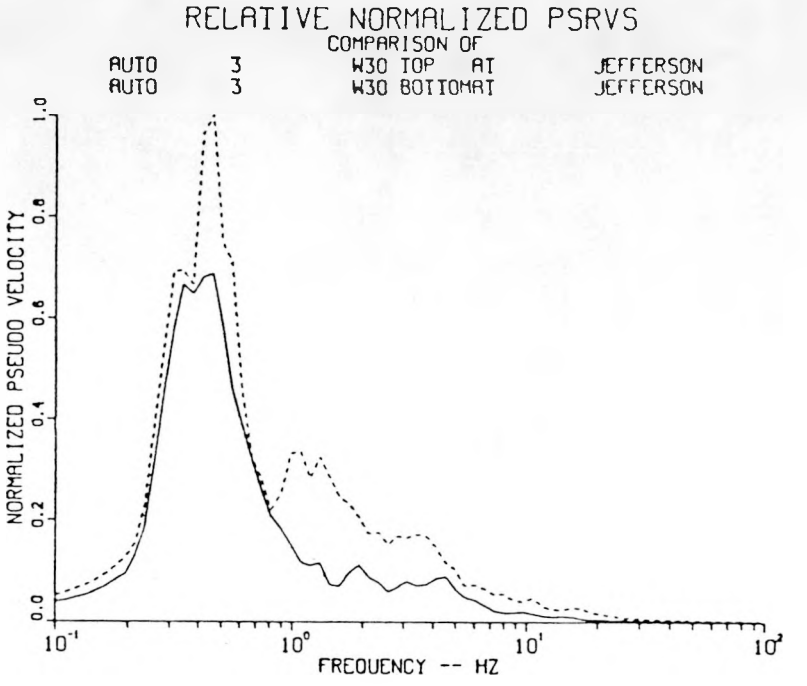

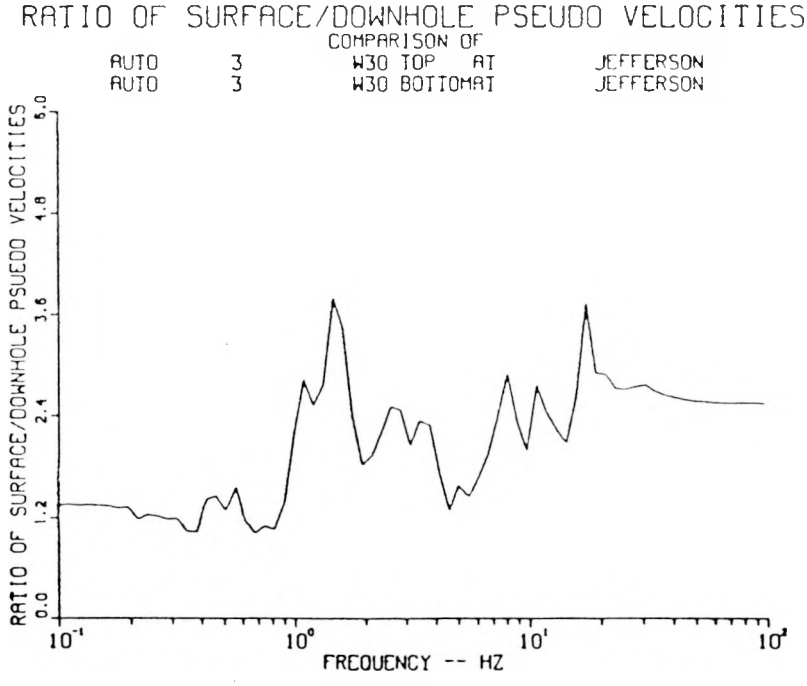

Figure A.87. Relative Normalized PSRVs and Ratios of Surface/Downhole PSRVs for Transverse Motions, Station W12(30), Event Serena

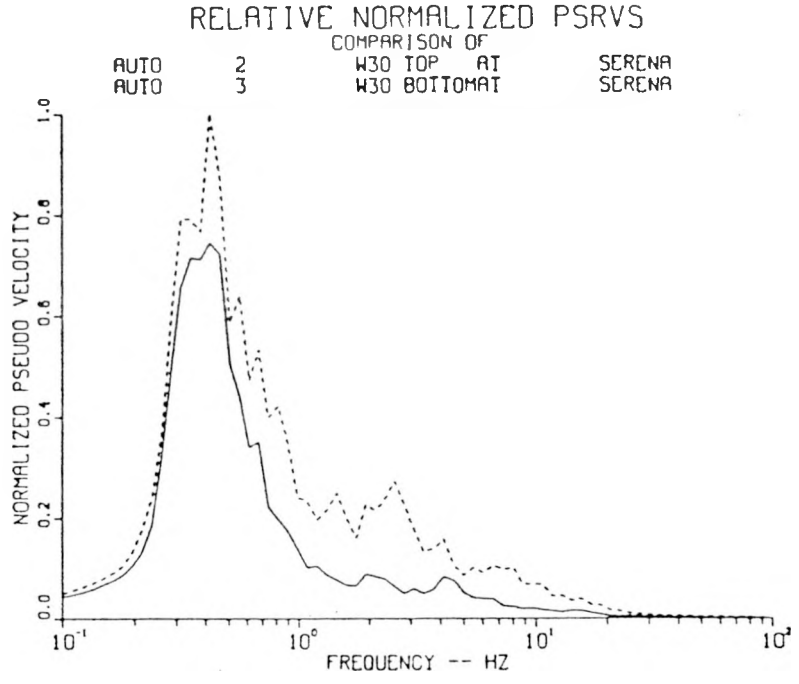

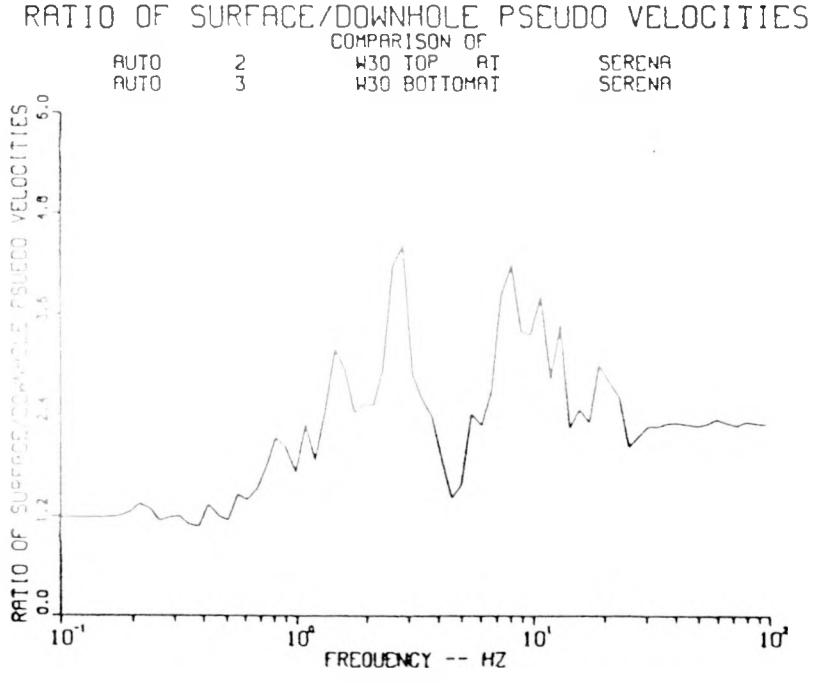

Figure A.88. Relative Normalized PSRVs and Ratios of Surface/Downhole PSRVs for Transverse Motions, Station W12(30), Event Goldstone

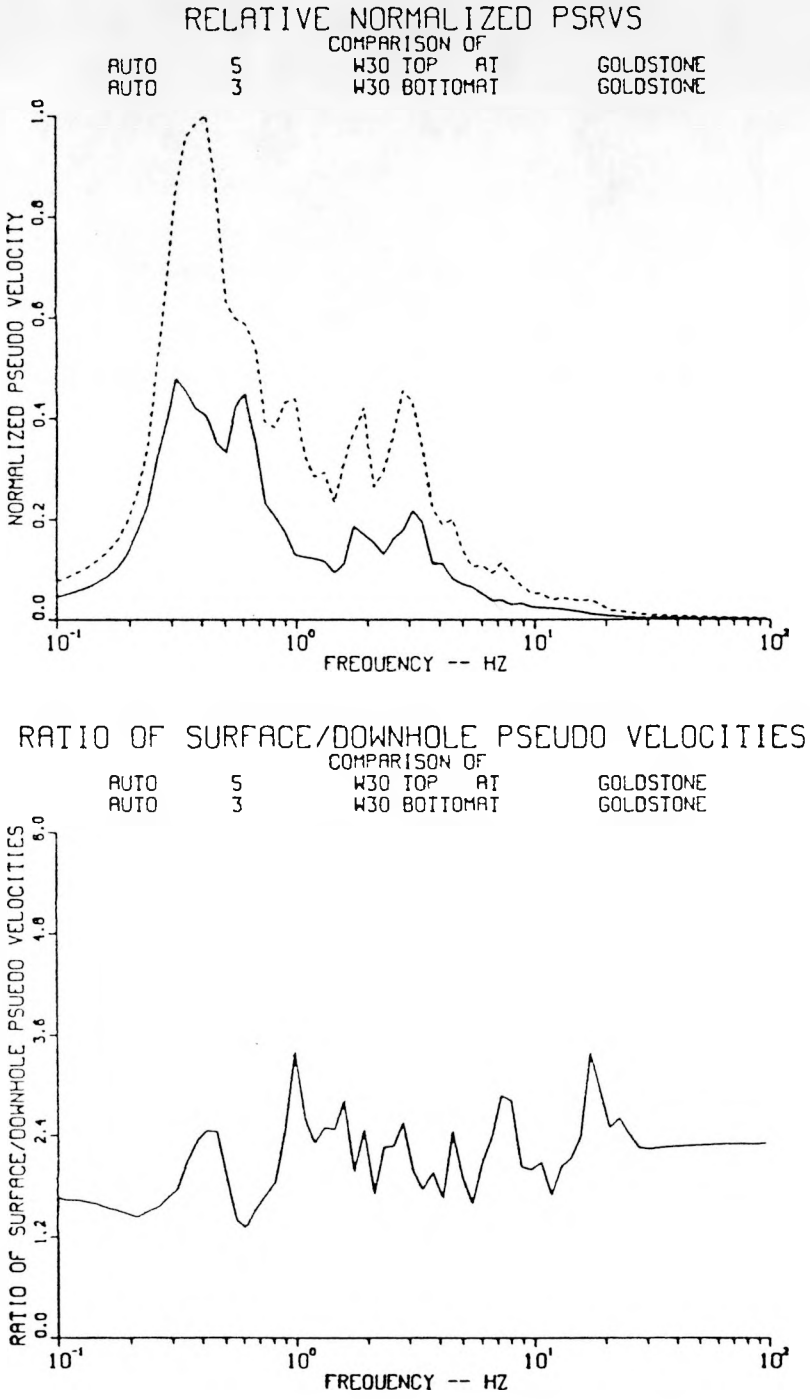

Figure A.89. Relative Normalized PSRVs and Ratios of Surface/Downhole PSRVs for Transverse Motions, Station W12(30), Event Cabra

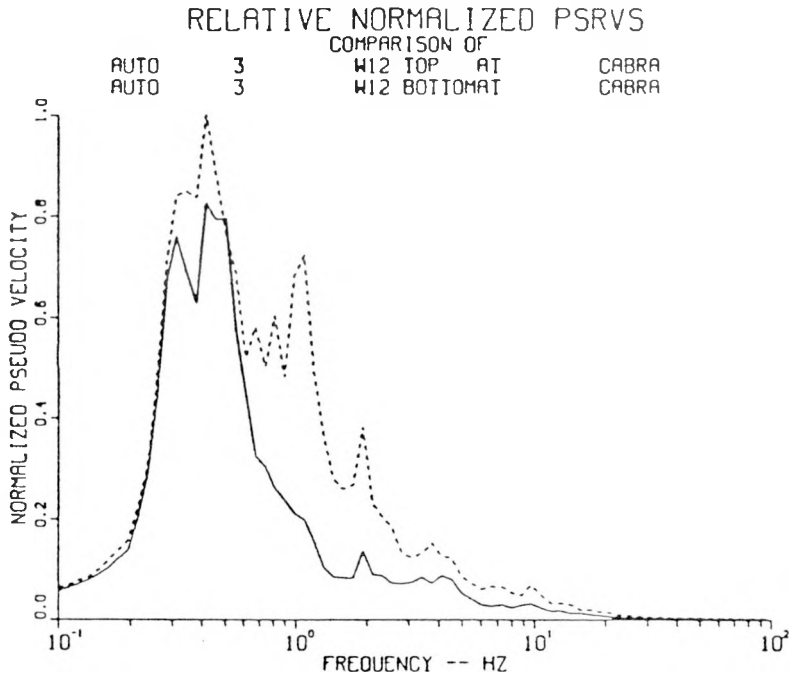

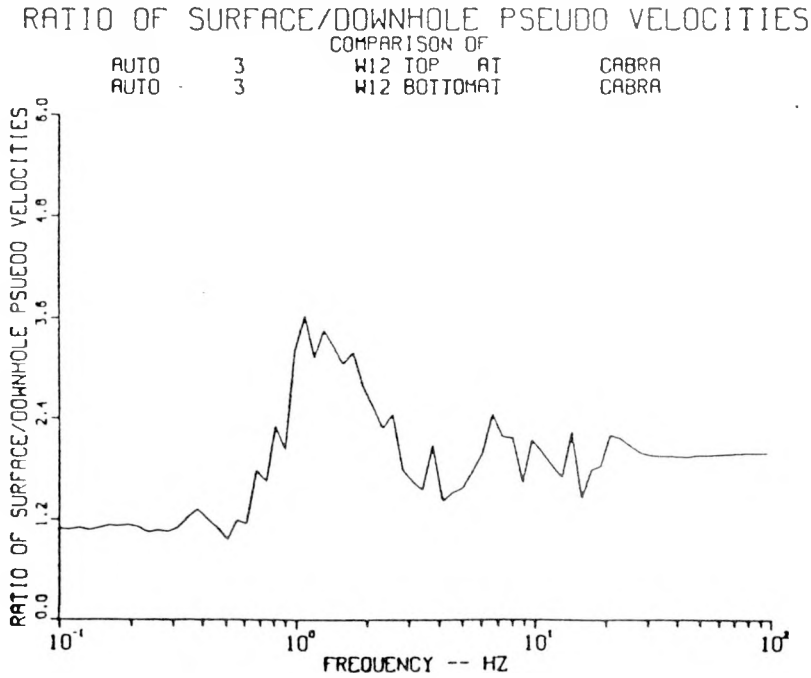

Figure A.90. Relative Normalized PSRVs and Ratios of Surface/Downhole PSRVs for Transverse Motions, Station W12(30), Event Towanda

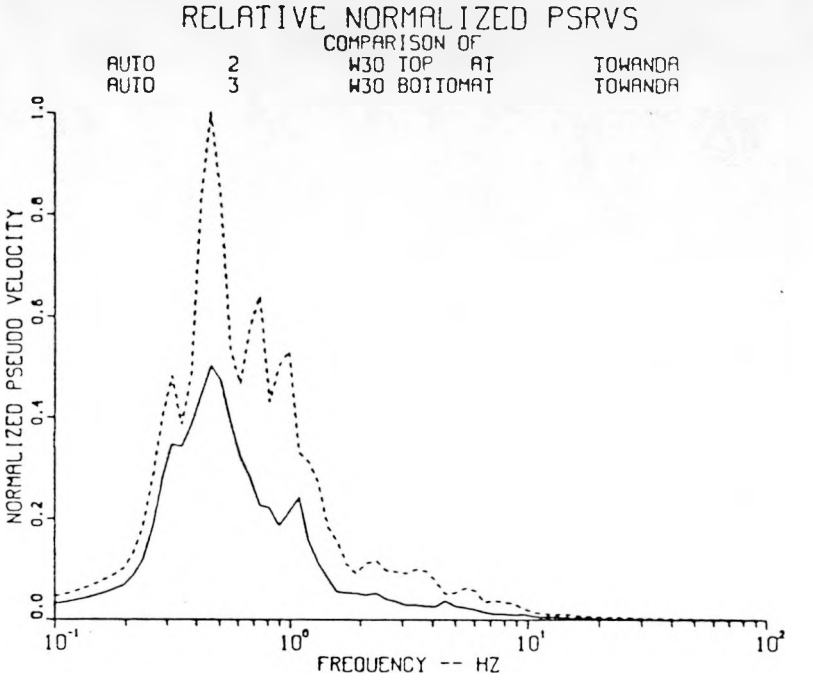

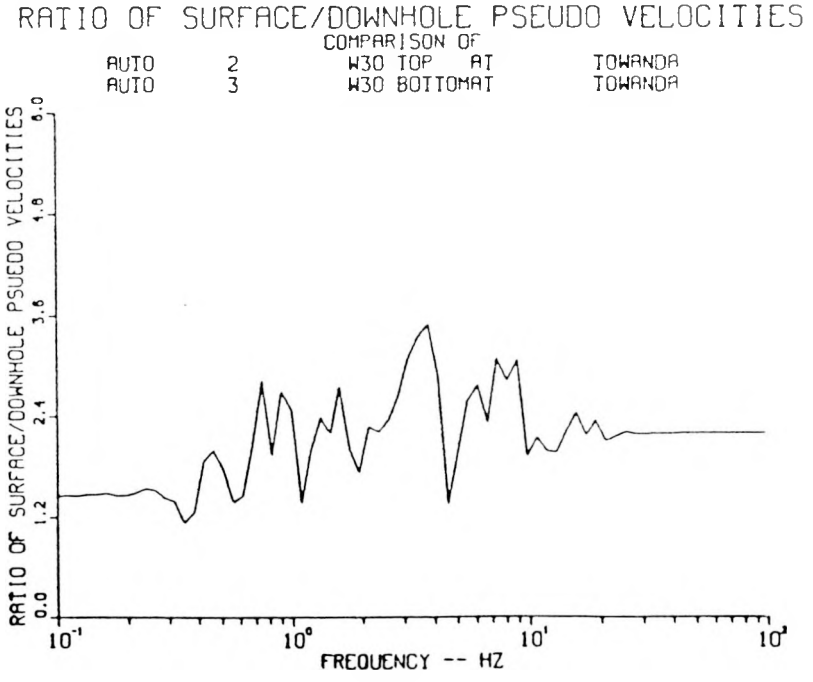

DO NOT MICROFILM
THIS PAGE

APPENDIX B

NORMALIZED PSRVS AND CALCULATED RATIOS OF S/D RATIOS FOR TWO YUCCA FLATS UNES RECORDED AT STATION W28

This appendix contains the normalized PSRVs and s/d ratios for Events Cottage and Hermosa. The PSRVs and the ratios are presented on one page with the three components for Hermosa presented first. The dashed lines on the normalized PSRVs are the surface PSRV, while the downhole PSRV is indicated by the solid line.

Figure B.1. Relative Normalized PSRVs and Ratios of Surface/Downhole PSRVs for Vertical Motions, Station W28, Event Hermosa

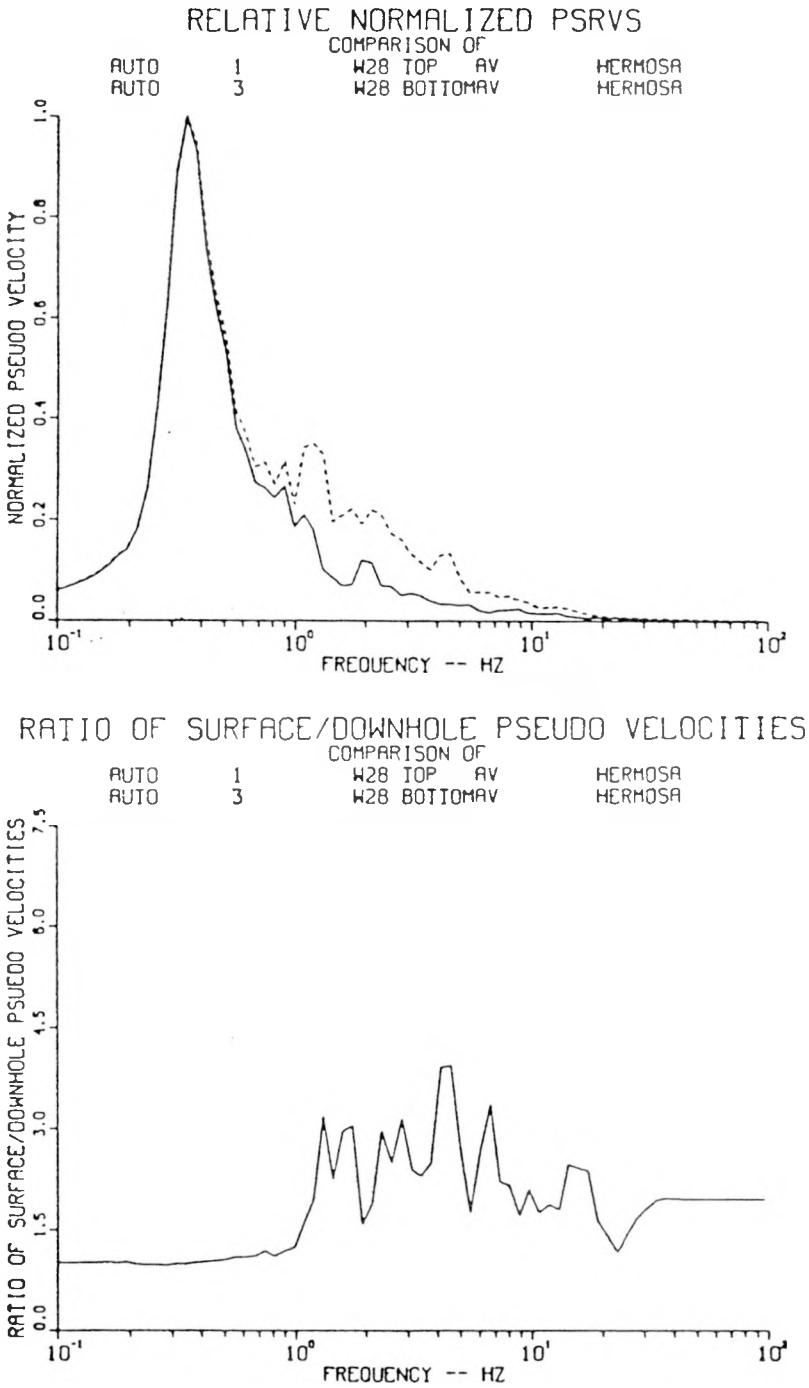

Figure B.2. Relative Normalized PSRVs and Ratios of Surface/Downhole PSRVs for Radial Motions, Station W28, Event Hermosa

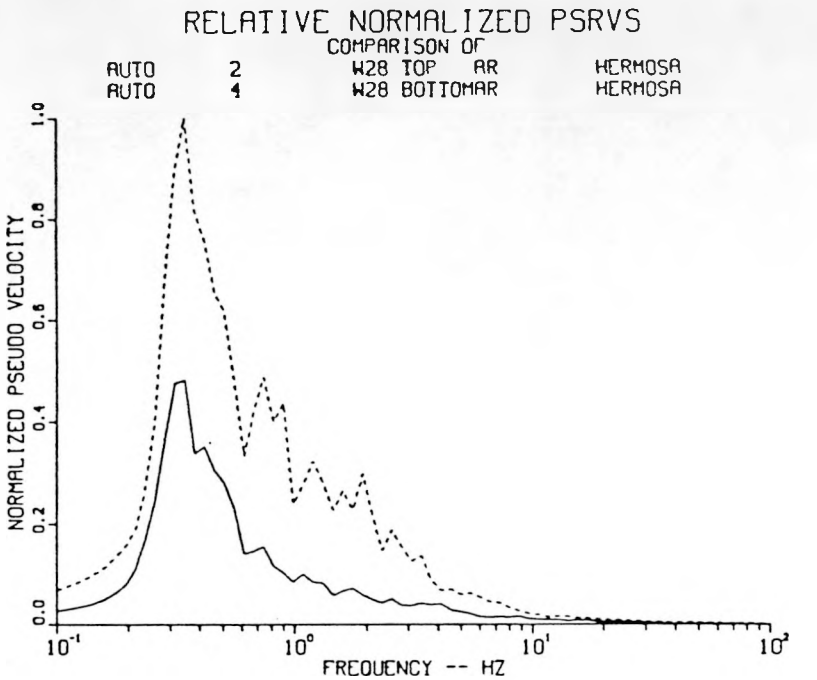

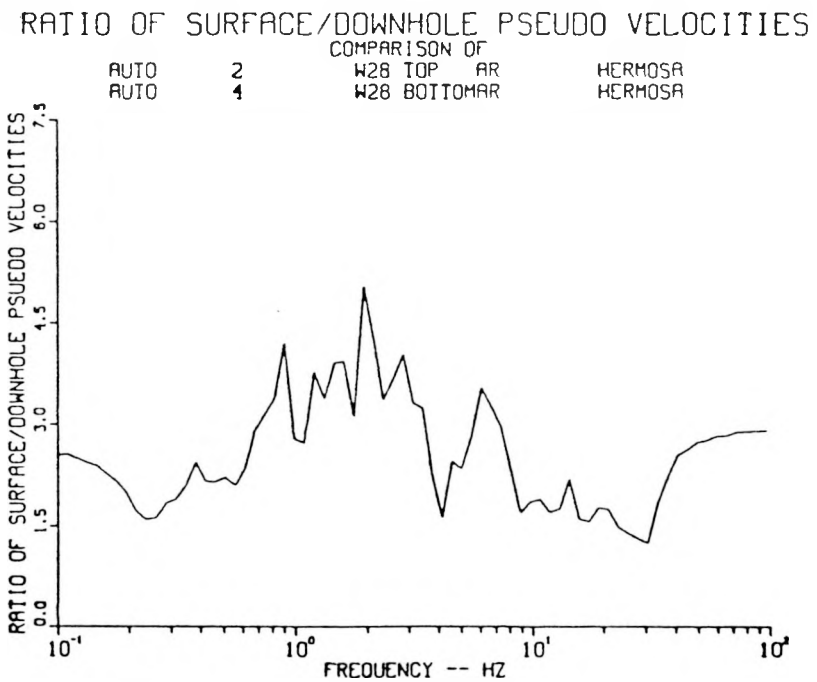

Figure B.3. Relative Normalized PSRVs and Ratios of Surface/Downhole PSRVs for Transverse Motions, Station W28, Event Hermosa

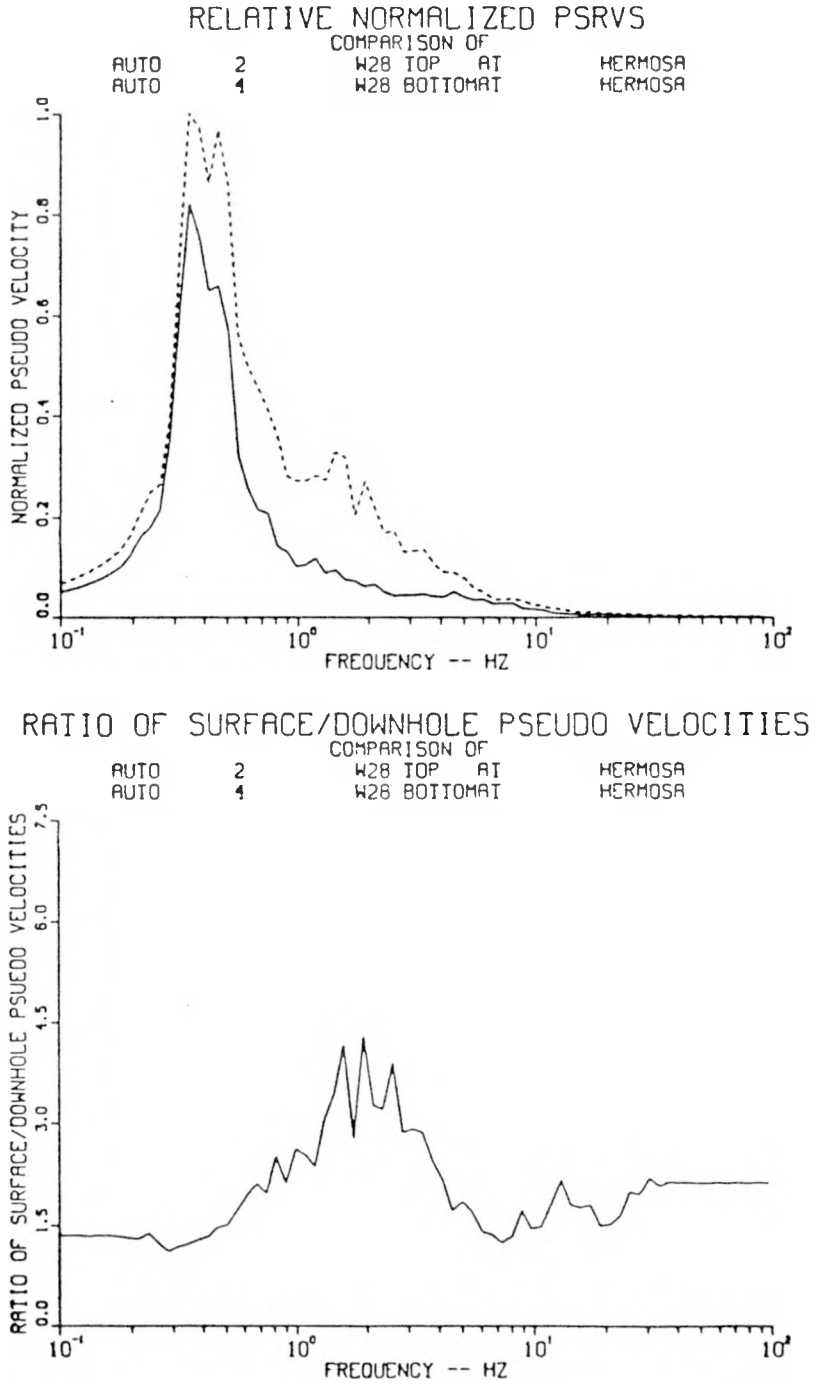

Figure B.4. Relative Normalized PSRVs and Ratios of Surface/Downhole PSRVs for Vertical Motions, Station W28, Event Cottage

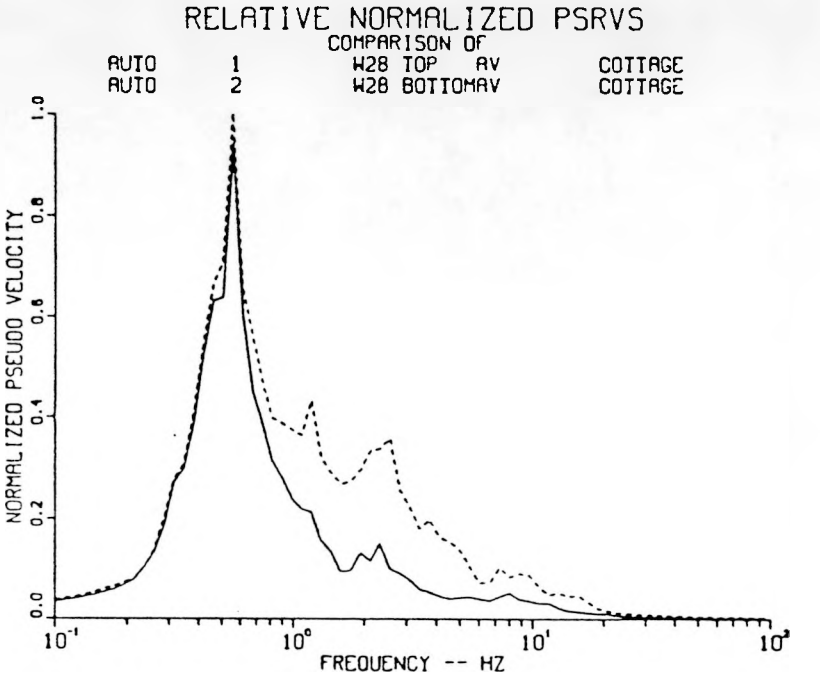

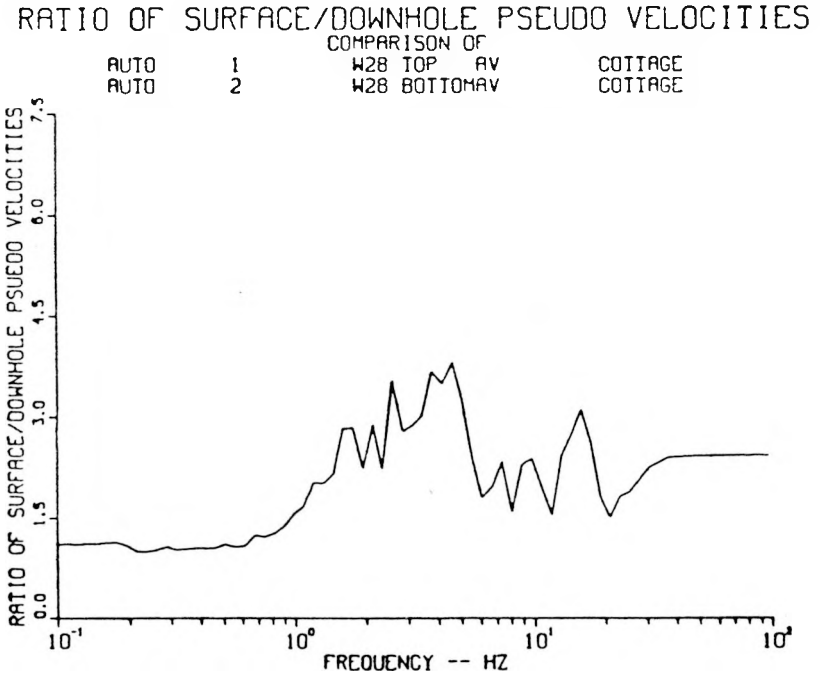

Figure B.5. Relative Normalized PSRVs and Ratios of Surface/Downhole PSRVs for Radial Motions, Station W28, Event Cottage

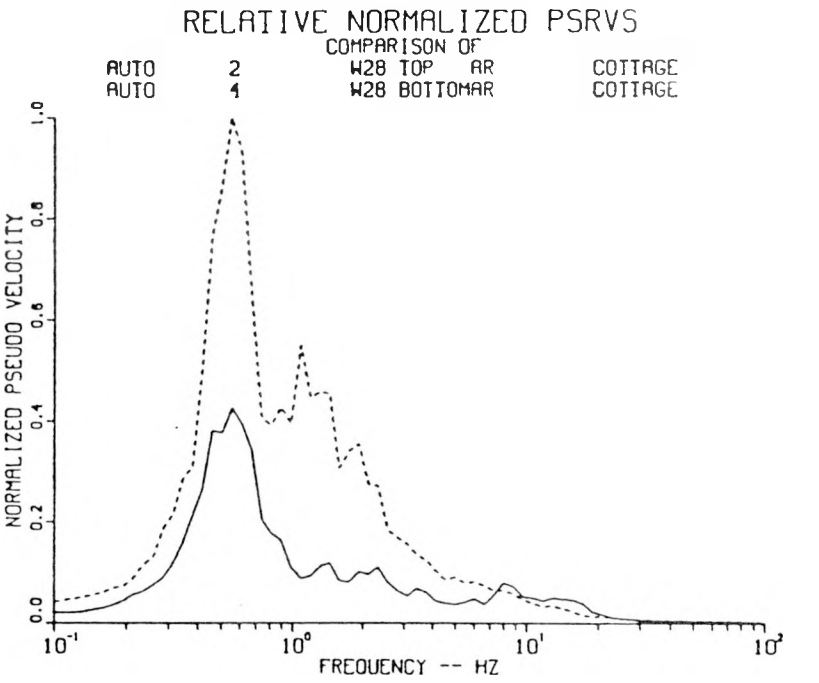

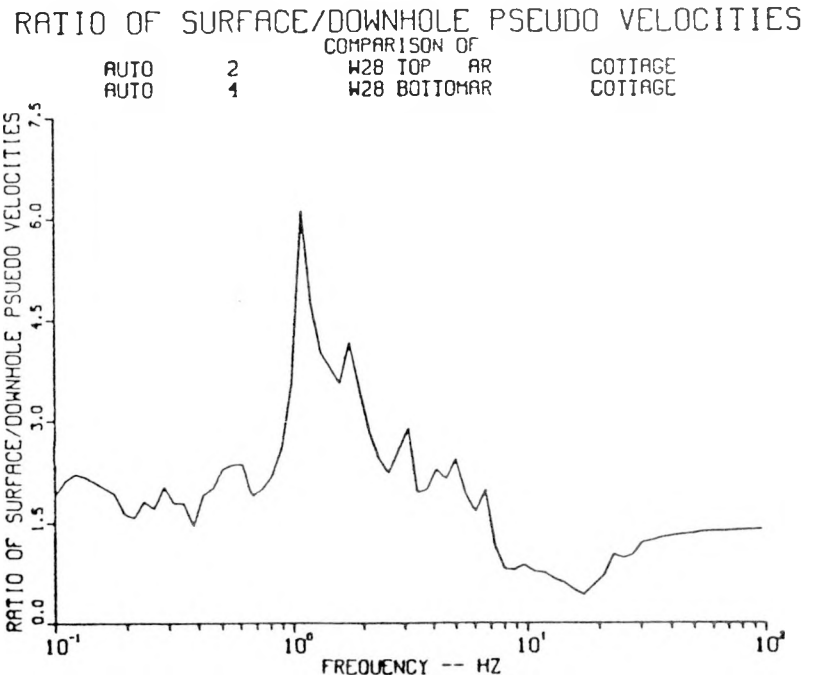

Figure B.6. Relative Normalized PSRVs and Ratios of Surface/Downhole PSRVs for Transverse Motions, Station W28, Event Cottage

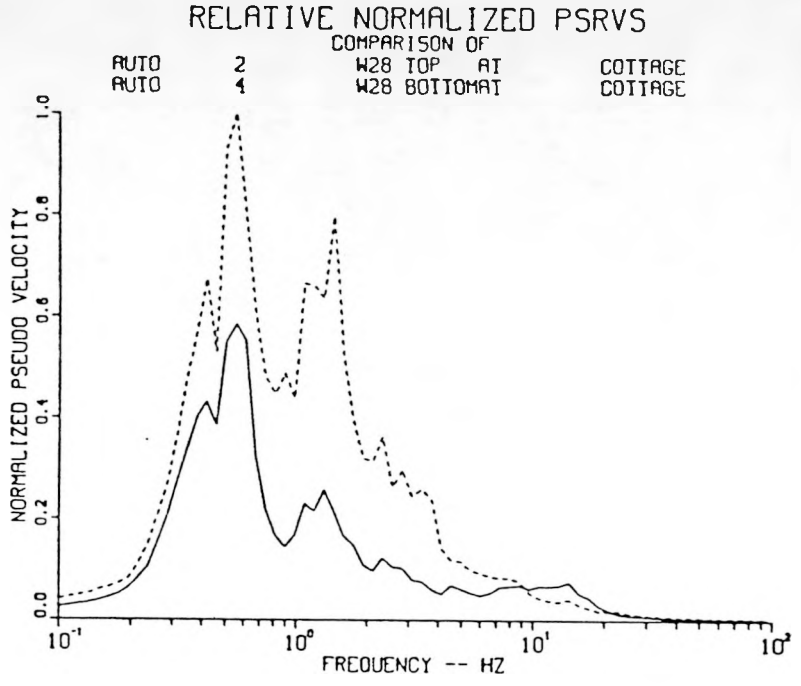

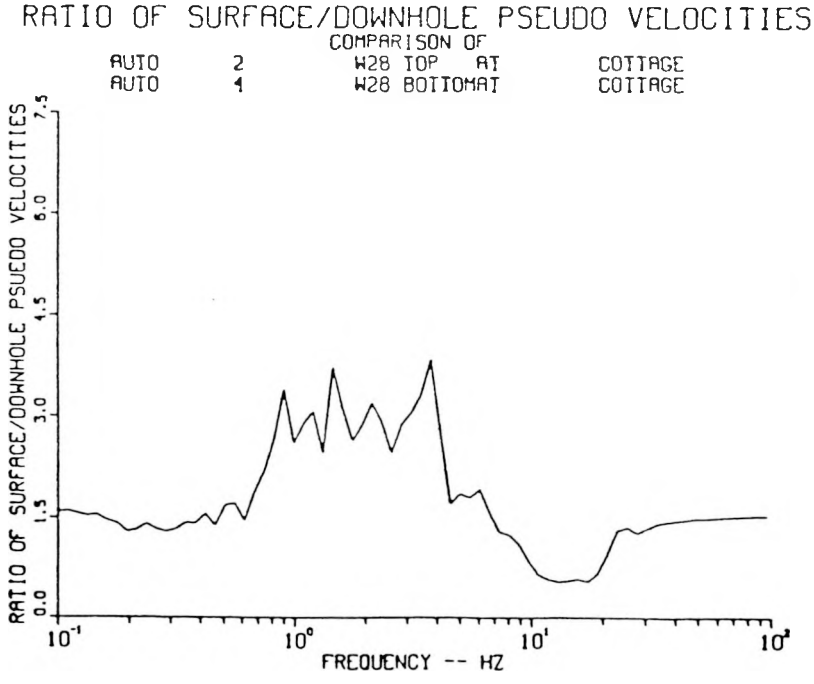

APPENDIX C

A Discussion of PSRVs

Many engineering systems may be represented as a single-degree-of-freedom (SDOF) system or a combination of SDOF systems such as that shown in Figure C.1. This figure shows a schematic representation of a SDOF system subjected to a base motion. The parameters of this system are mass (m), spring stiffness (k), damping (c), base displacement (y), mass displacement (x) and relative displacement (u). A convenient representation of the response of such a system to the amplitude and frequency content of input ground motion is the response spectrum. The response spectrum may be expressed in terms of the relative displacement between the mass and the base, the relative velocity between the mass and the base or the absolute acceleration of the mass. The following discussion will provide some background on the concept of the pseudo relative velocity response spectrum or PSRV. Much of this information was condensed from Crawford et. al., 1974, Higgins et. al., 1978 and Newmark and Rosenbluth, 1971.

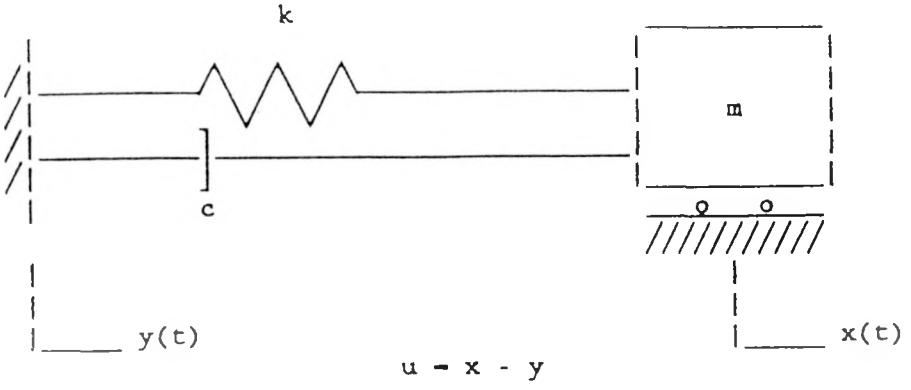

Figure C.1. Single-degree-of-freedom system subjected to base motion.

The equation of motion for the mass in Figure C.1 is

$$\ddot{u}(t) + 2\beta\omega_n\dot{u}(t) + \omega_n^2 u(t) = -y(t) \qquad (1)$$

x,y and u are as described above;
the dot indicates differentiation with respect to time;

β is the damping ratio ($c/2\sqrt{km}$)

ω_n is the undamped natural frequency ($\sqrt{km}$)

Assuming zero initial conditions, this equation can be solved to yield an expression for relative displacement (Higgins et. al., 1978). This expression is

$$u = \frac{-1}{\omega_n\sqrt{1-\beta^2}} \int_o^t y(\tau) e^{-\beta\omega_n(t-\tau)} \sin \omega_n\sqrt{1-\beta^2}\,(t-\tau)\,d\tau \qquad (2)$$

Through manipulation (differentiation with respect to time, the use of the relationship between relative displacement and absolute acceleration and simplification) expressions for relative velocity and absolute acceleration may be derived. The maximum values from equation 2, and the derived expressions for absolute acceleration and relative velocity can be computed as a function of natural frequency and damping of the system for any base motion and plotted as a function of frequency. The resulting curves are the response spectra for the system. Each one of these parameters is important in describing the response of the system. The maximum relative velocity spectrum is a direct measure of the maximum energy per unit mass in the system; the relative displacement spectrum is related to system strain; and absolute acceleration spectrum is related to the lateral force coefficient frequently used in building codes.

These spectra are usually simplified by making the assumption of small damping (i.e., $\beta < 0.2$, such that $\sqrt{1-\beta^2} \sim 1$). This simplifies equation 2 to

$$u = \frac{-1}{\omega_n} \int_o^t y(\tau) e^{-\beta\omega_n(t-\tau)} \sin \omega_n(t-\tau)\; d\tau \qquad (3)$$

Performing the same manipulations discussed above and dropping the separate terms with β and β^2 yields simplified expressions for absolute acceleration and relative velocity. The maximum values of pseudo acceleration (so called because of the simplifications, but whose amplitude is generally close to the absolute acceleration--Newmark and Rosenbluth, 1971) and relative displacement are related in the following manner

$$A = \omega_n^2 D \qquad (4)$$

where: A is the pseudo acceleration;
D is the relative displacement.

The derived expression for the relative velocity differs from the other two parameters by a factor of the natural frequency and the fact that it contains a cosine function rather than a sine function. If the cosine is replaced by the sine in the expression for the relative velocity, the three parameters are related in the following manner

$$\frac{1}{\omega_n} A = V = \omega_n D \qquad (5)$$

where: V is the psuedo velocity.

Relative velocity and pseudo velocity will be significantly different when the system period is much longer than the duration of the input ground motion (Higgins et. al., 1978) For many instances, however, the pseudo velocity and relative velocity will be roughly equal.

The A, V and D parameters are generally plotted in log space on tripartite graph paper. The horizontal axis is frequency and the vertical axis is pseudo velocity. Any point on this plot for a given frequency describes the system strain, energy absorbed by the system and the maximum force in the system. The discussions presented in this report deal entirely with the pseudo velocity parameter.

References:

Crawford, R. E., Higgins, C. J. and Bultmann, E. H., The Air Force Manual for Design and Analysis of Hardened Structures, AFWL-TR-74-102, Air Force Weapons Laboratory, Kirtland Air Force Base, N.M., October 1974 (NNA.891208.0047).

Higgins, C. J., Johnson, R. L. and Triandafilidis, G. E., The Simulation of Earthquake-Like Ground Motions with High Explosives, CE-48(78)NSF-507-1, Vol. 1, University of New Mexico Department of Civil Engineering and Bureau of Engineering Research, Albuquerque, N.M., July 1978 (NNA.891107.0100).

Newmark, N. M. and Rosenbluth, E., Fundamentals of Earthquake Engineering, Prentice-Hall, Inc., Englewood Cliffs, N.J., 1971 (NNA.891106.0212).

APPENDIX D

TYPICAL SURFACE/DOWNHOLE WAVEFORMS FOR YUCCA MOUNTAIN STATIONS

This appendix contains acceleration time histories recorded during the Serena event. Data were collected at all surface/downhole stations located in the vicinity of Yucca Mountain. This was a low yield (<150 kt) event. (NOTE: In the figures that follow, the surface time history is placed on the top half of the page. The downhole time history is on the bottom half of the page.)

Figure D.1. Vertical Surface and Downhole Accelerations Recorded at Station W25

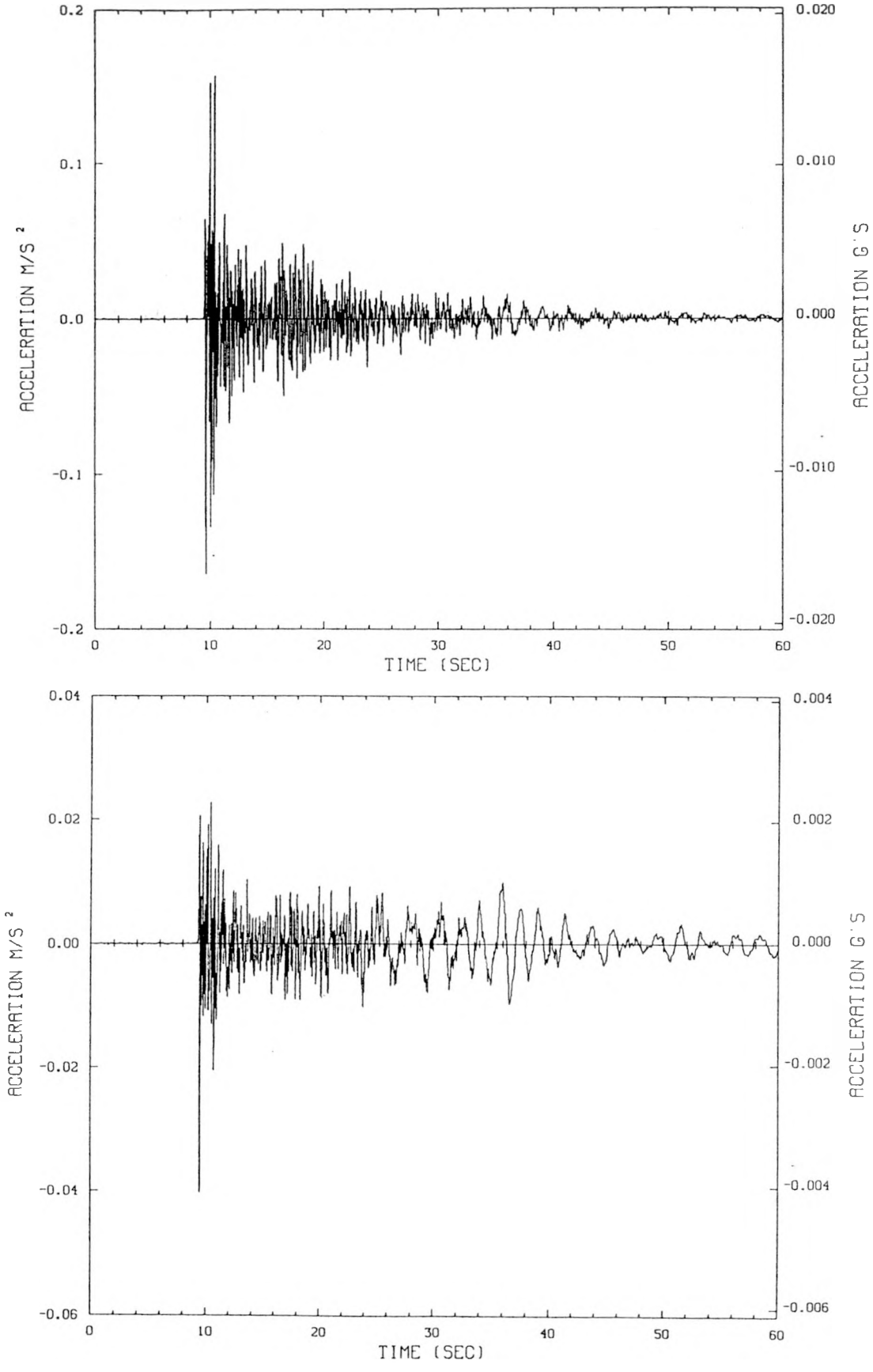

Figure D.2. Radial Surface and Downhole Accelerations Recorded at Station W25

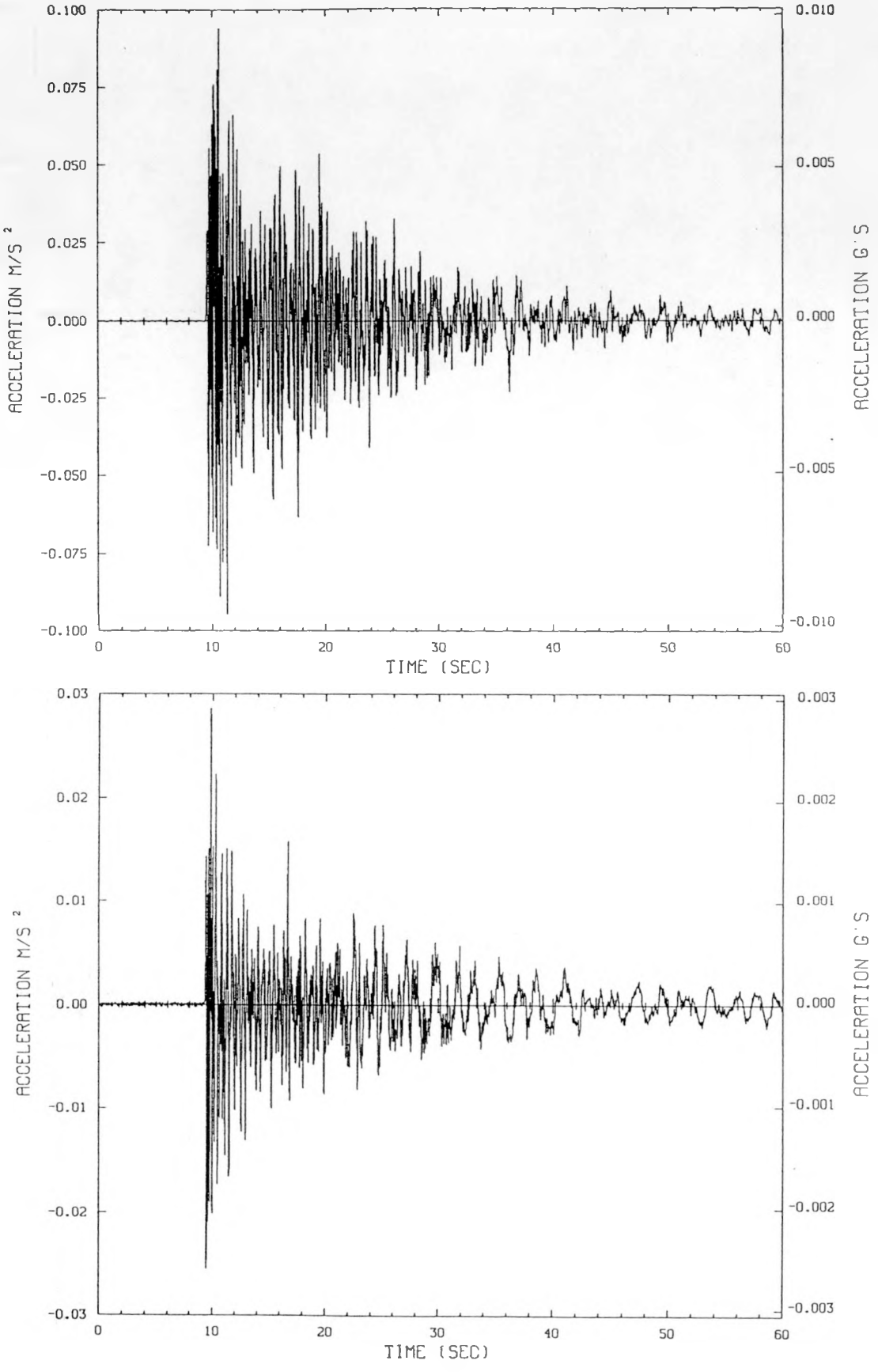

Figure D.3. Transverse Surface and Downhole Accelerations Recorded at Station W25

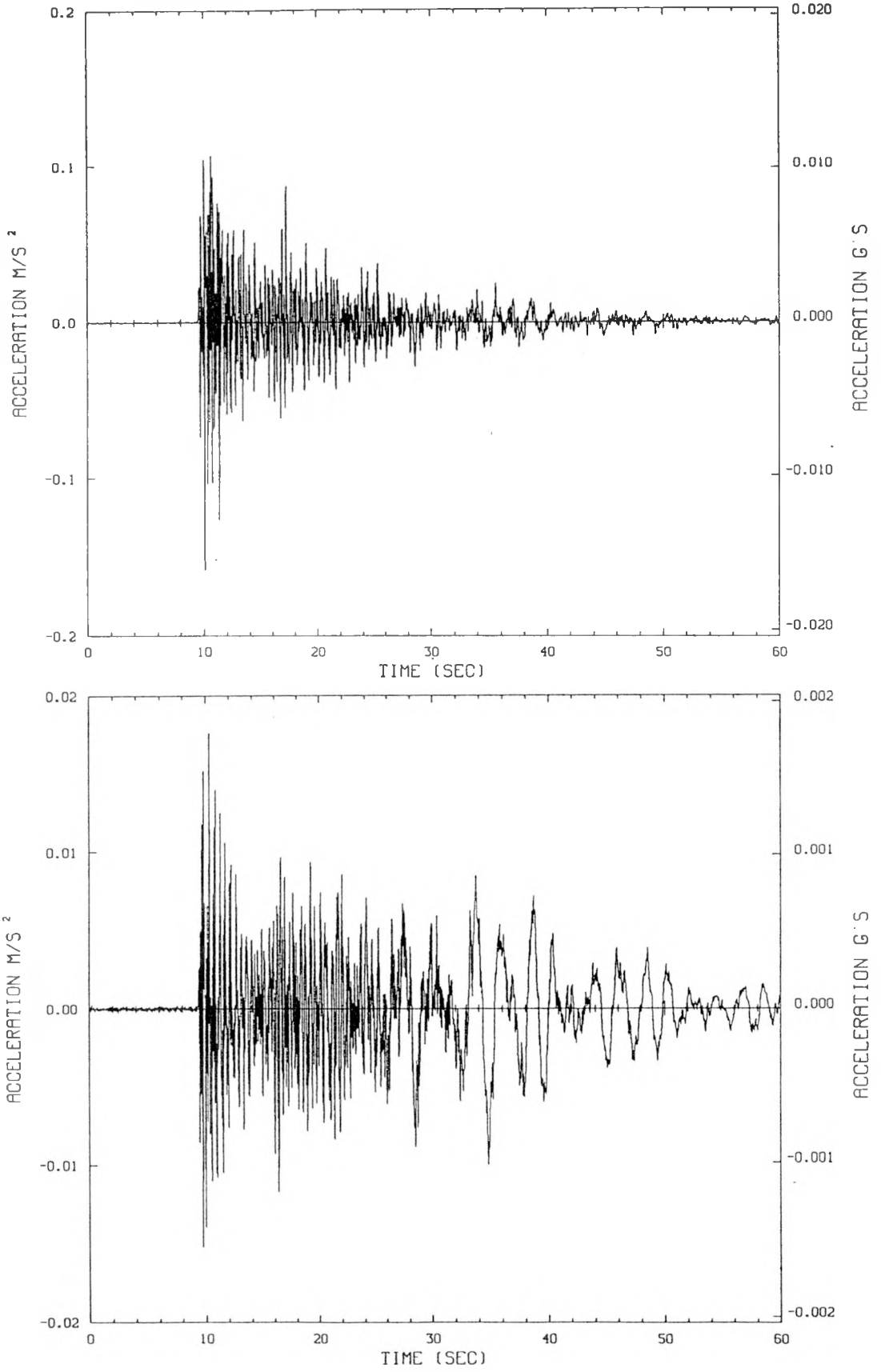

Figure D.4. Vertical Surface and Downhole Accelerations Recorded at Station W28

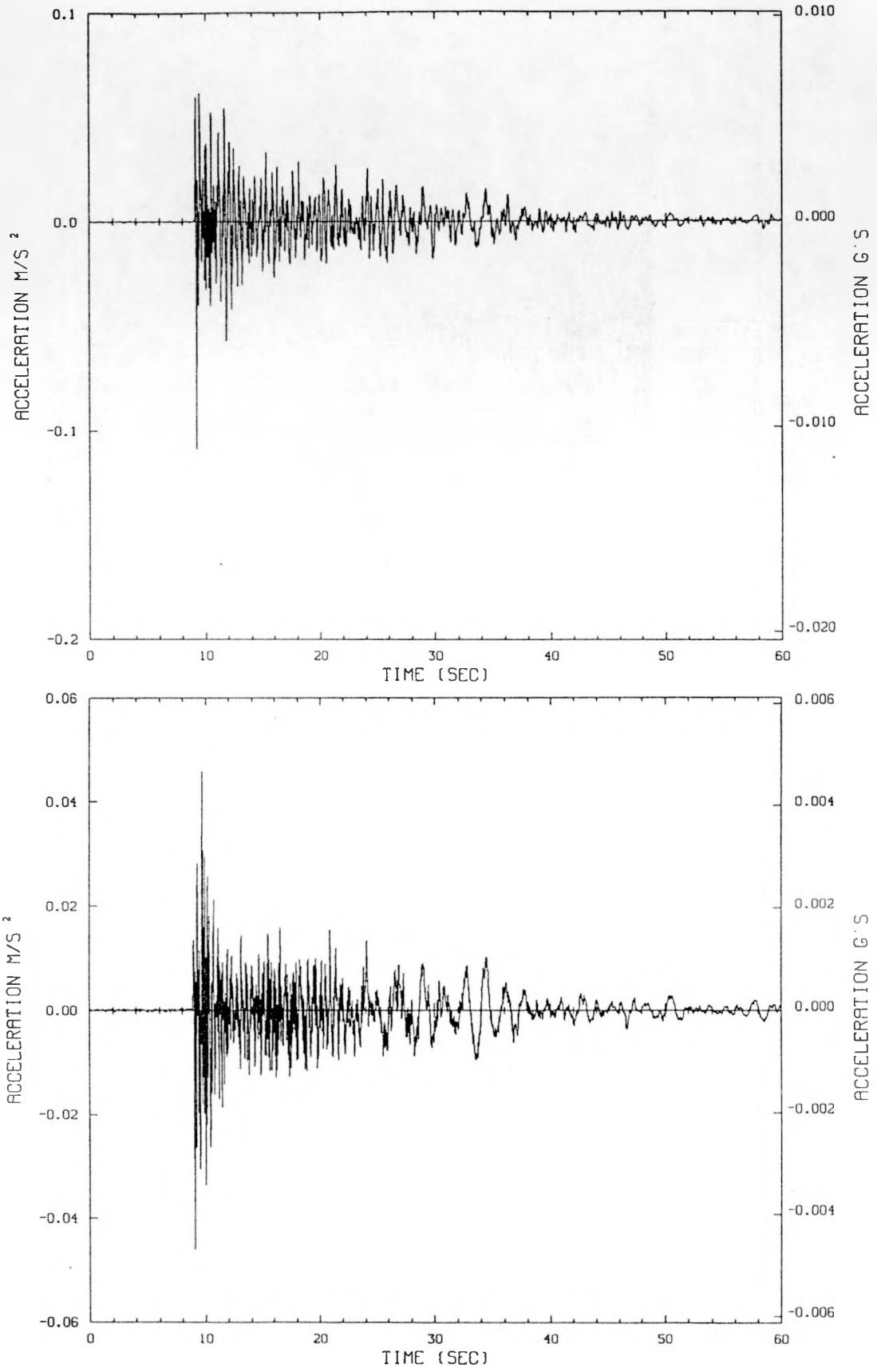

Figure D.5. Radial Surface and Downhole Accelerations Recorded at Station W28

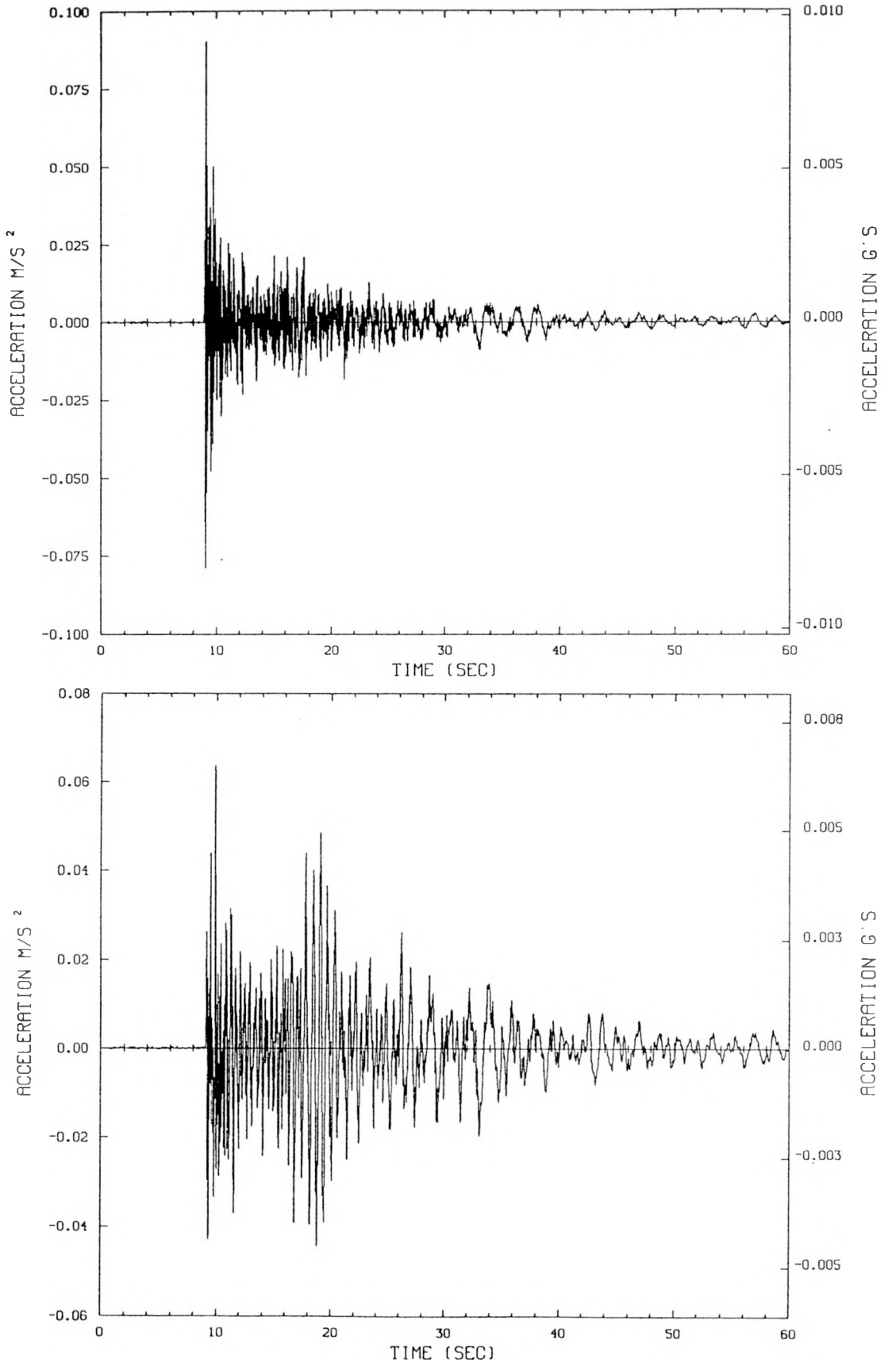

Figure D.6. Transverse Surface and Downhole Accelerations Recorded at Station W28

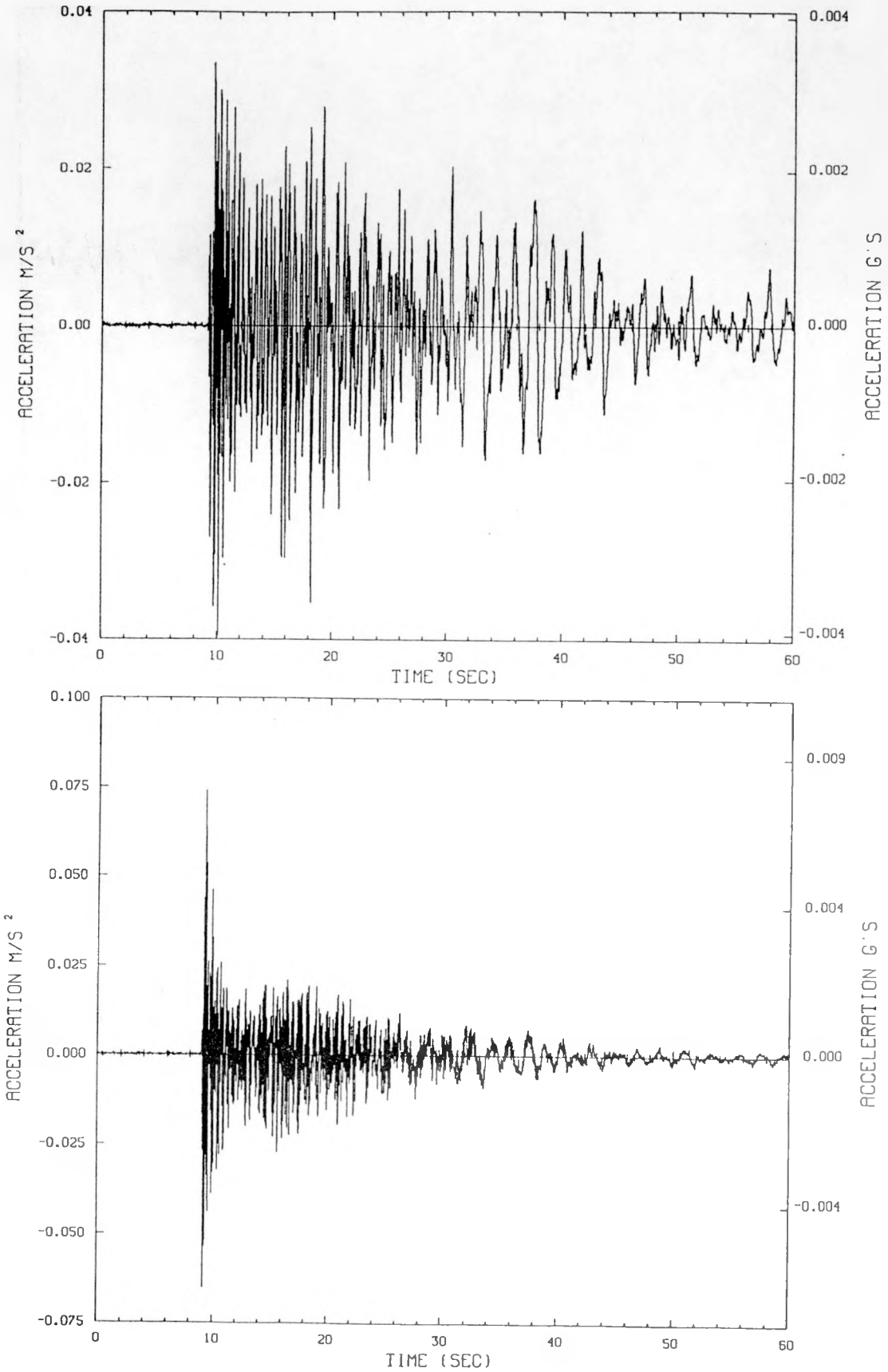

Figure D.7. Vertical Surface and Downhole Accelerations Recorded at Station W29

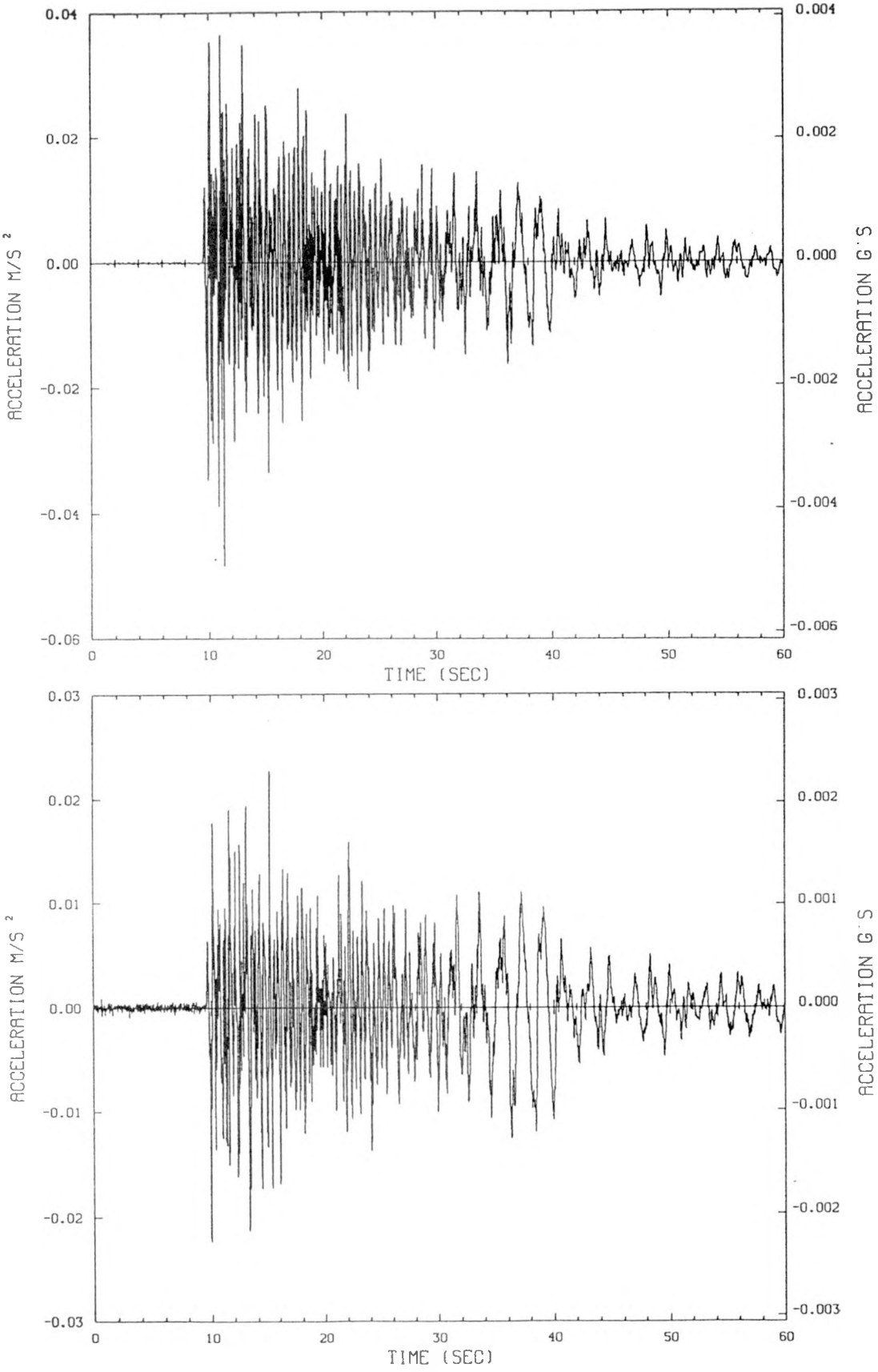

Figure D.8. Radial Surface and Downhole Accelerations Recorded at Station W29

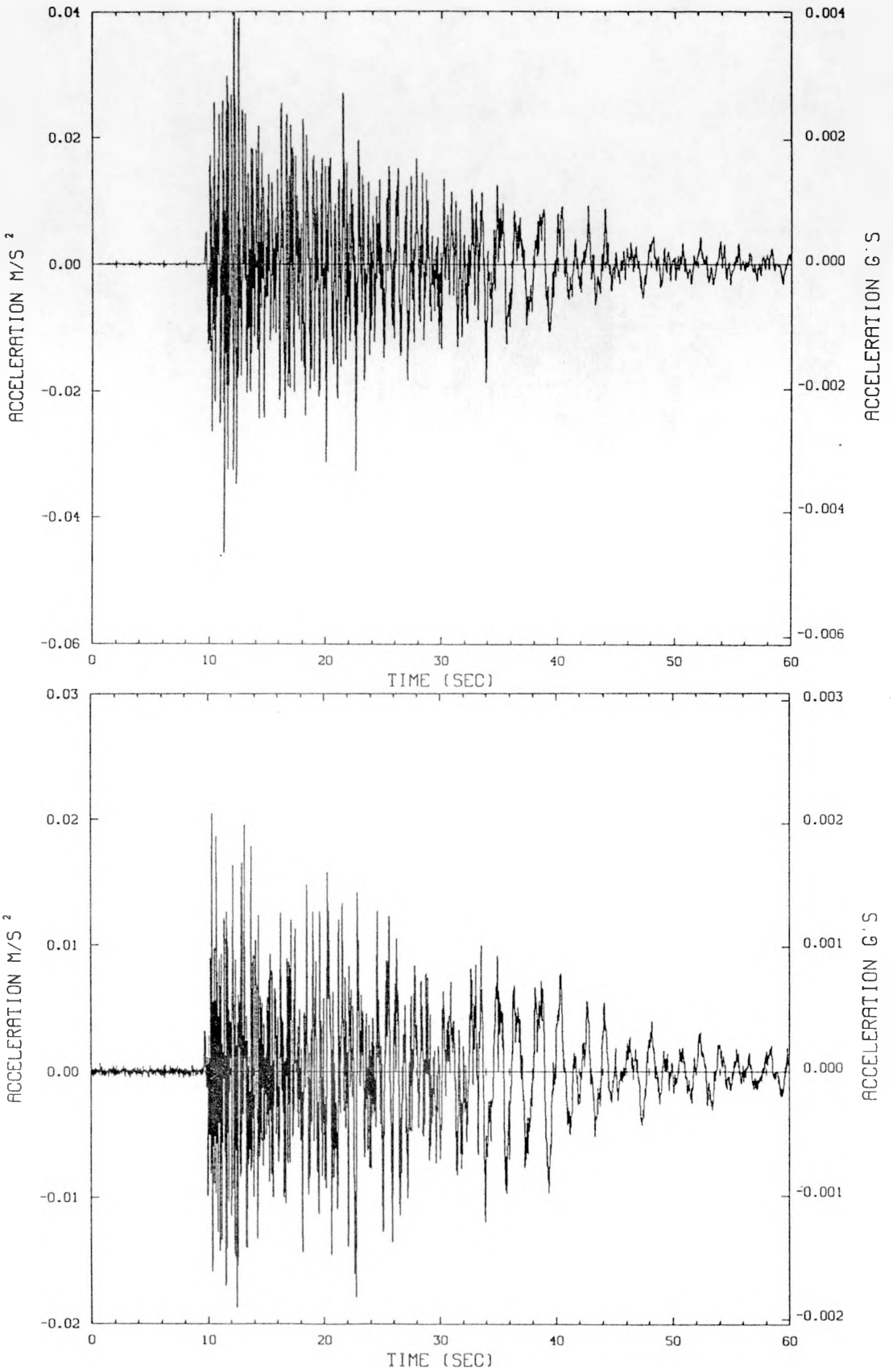

Figure D.9. Transverse Surface and Downhole Accelerations Recorded at Station W29

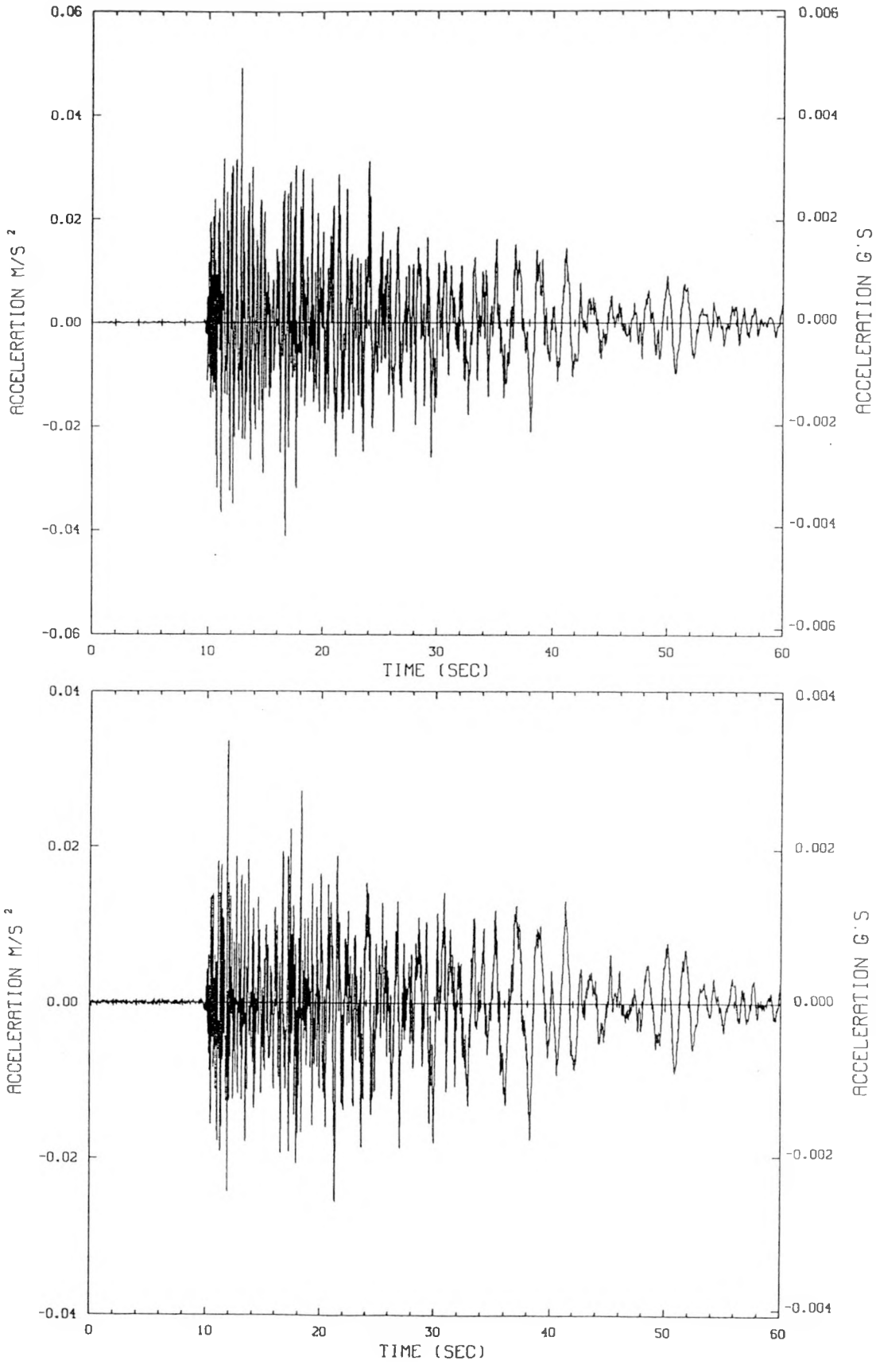

Figure D.10. Vertical Surface and Downhole Accelerations Recorded at Station W30

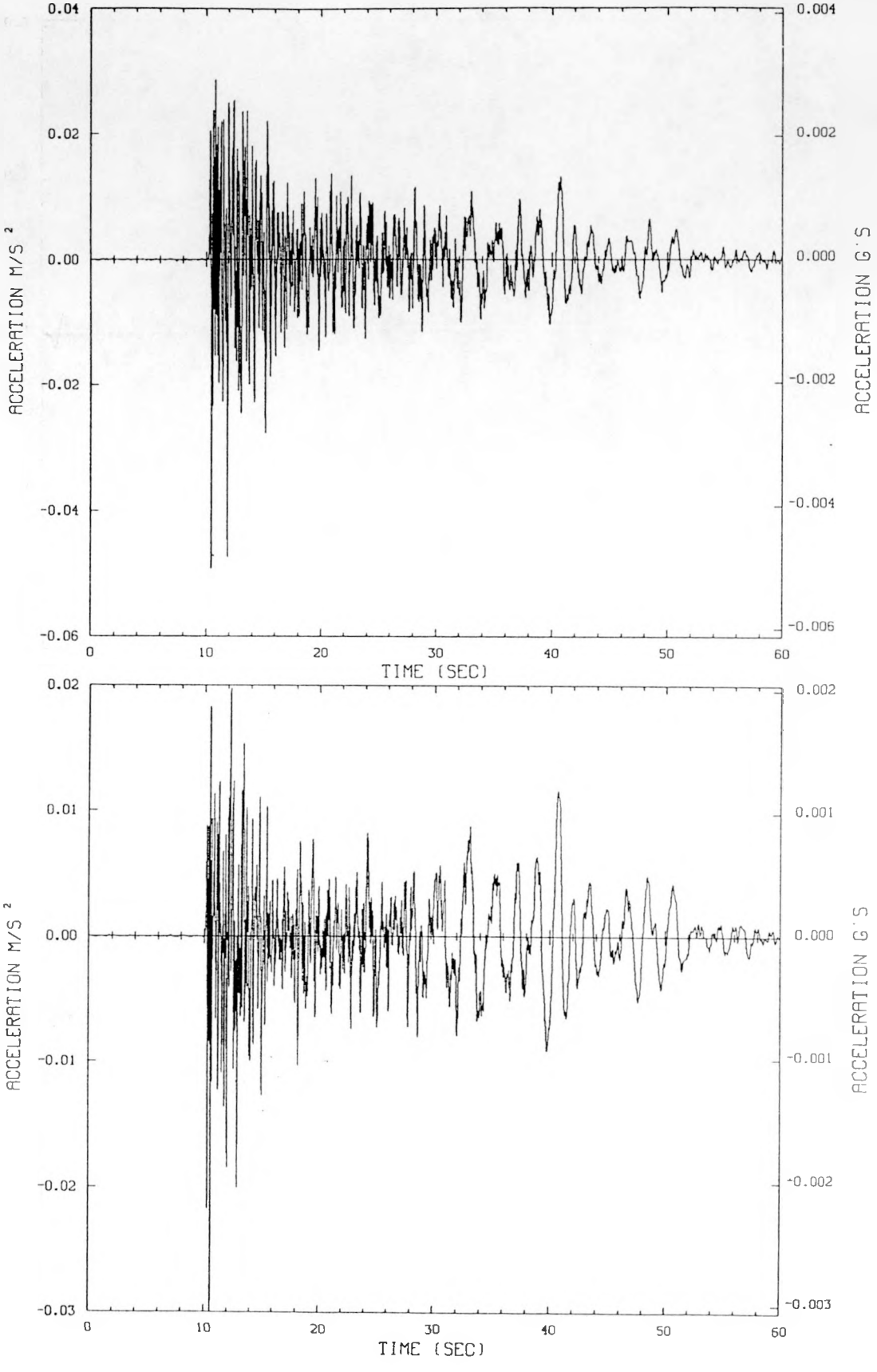

Figure D.11. Radial Surface and Downhole Accelerations Recorded at Station W30

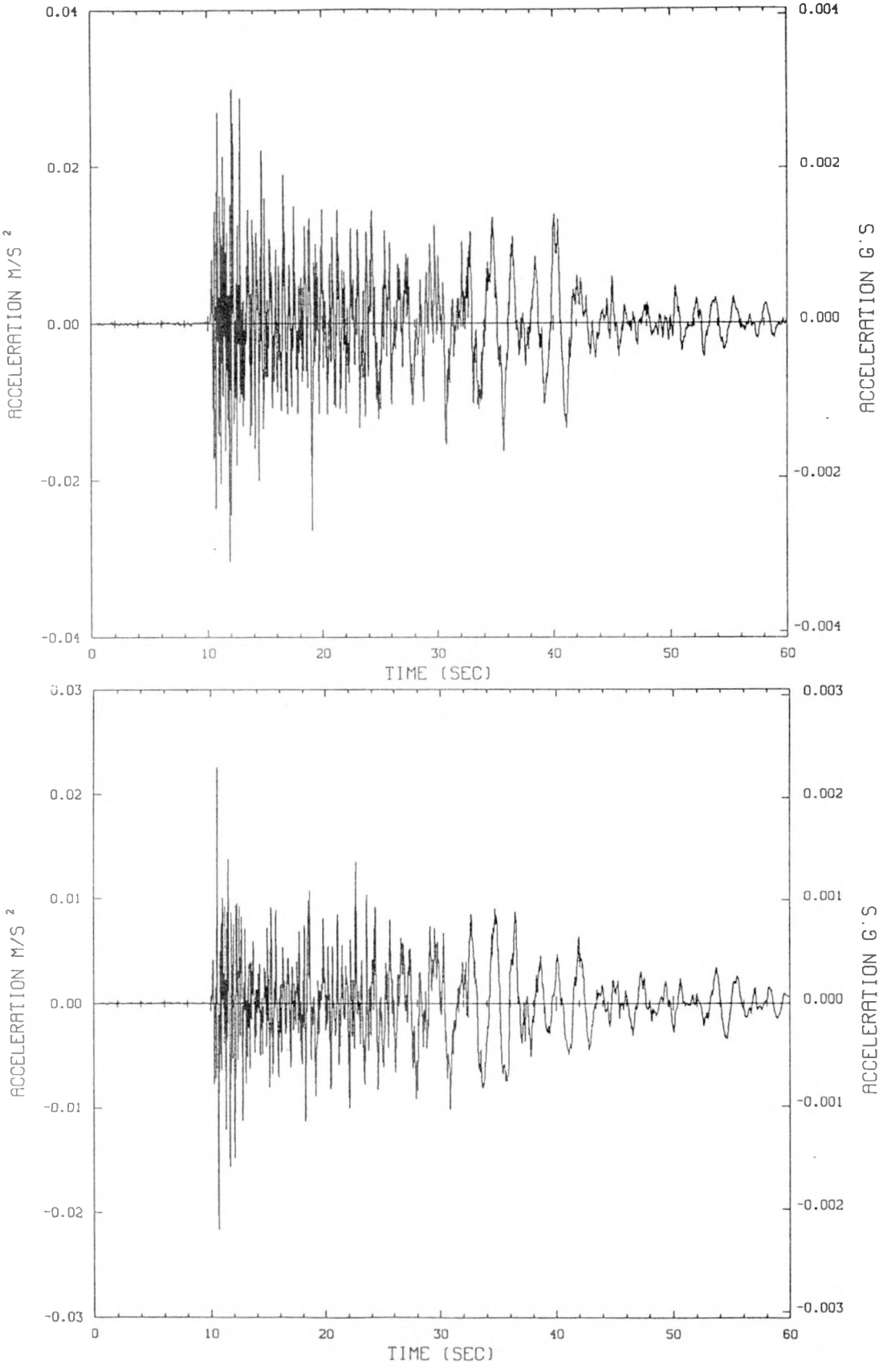

Figure D.12. Transverse Surface and Downhole Accelerations Recorded at Station W30

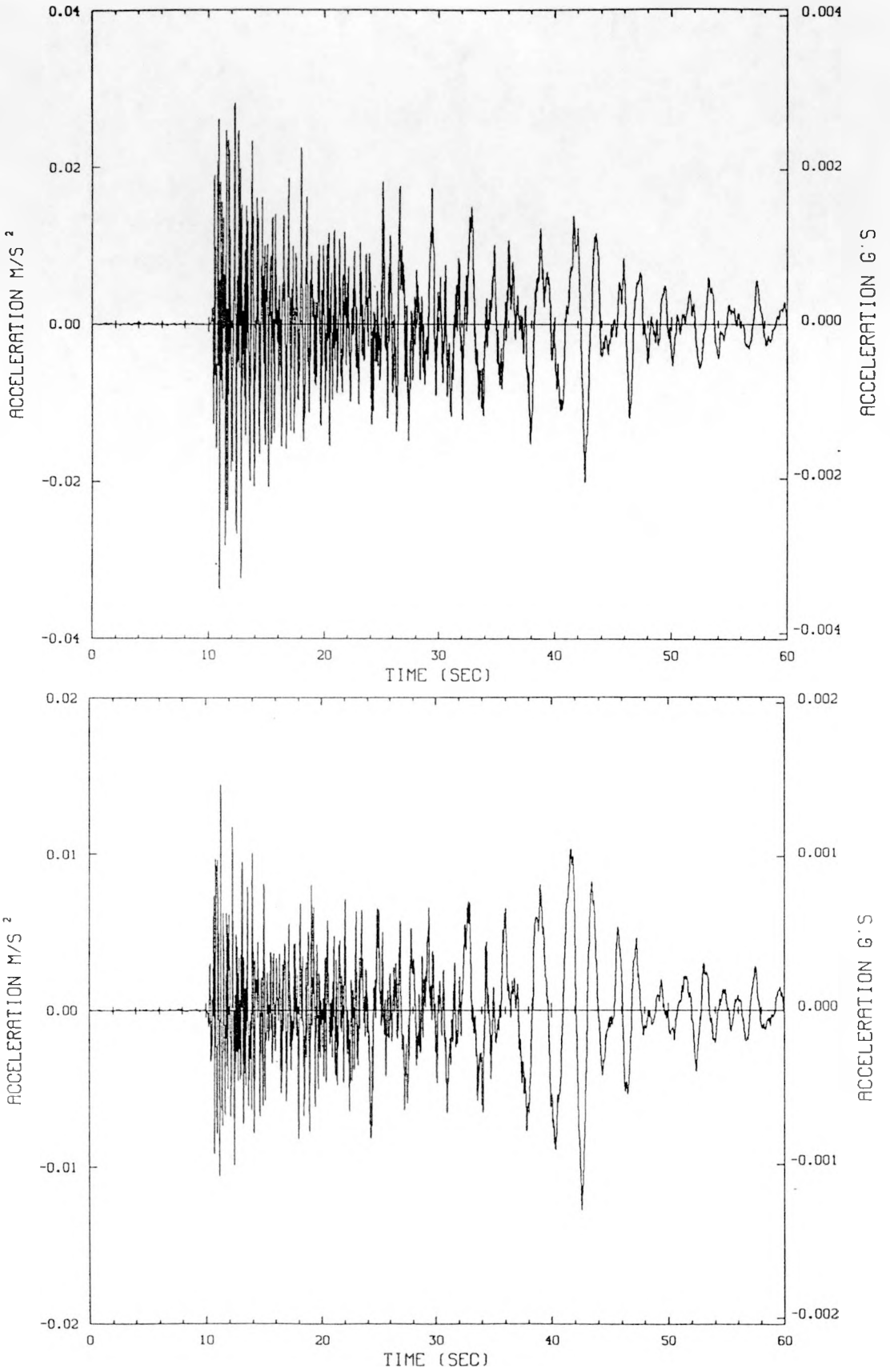

APPENDIX E

RIB/SEPDB Data

This report contains no data from, or for inclusion in, the RIB and/or SEPDB.

DISTRIBUTION LIST

1 John W. Bartlett, Director (RW-1)
Office of Civilian Radioactive
Waste Management
U.S. Department of Energy
Forrestal Bldg.
Washington, D.C. 20585

1 F. G. Peters, Deputy Director (RW-2)
Office of Civilian Radioactive
Waste Management
U.S. Department of Energy
Forrestal Bldg.
Washington, D.C. 20585

1 Ralph Stein (RW-30)
Office of Civilian Radioactive
Waste Management
U.S. Department of Energy
Forrestal Bldg.
Washington, D.C. 20585

1 M. W. Frei (RW-22)
Office of Civilian Radioactive
Waste Management
U.S. Department of Energy
Forrestal Bldg.
Washington, D.C. 20585

1 B. G. Gale (RW-23)
Office of Civilian Radioactive
Waste Management
U.S. Department of Energy
Forrestal Bldg.
Washington, D.C. 20585

1 J. D. Saltzman (RW-5)
Office of External Relations
Office of Civilian Radioactive
Waste Management
U.S. Department of Energy
Forrestal Bldg.
Washington, D.C. 20585

1 S. J. Brocoum (RW-20)
Office of Civilian Radioactive
Waste Management
U.S. Department of Energy
Forrestal Building
Washington, D.C. 20585

1 T. H. Isaacs (RW-4)
Office of Stratigic Planning
and International Programs
Office of Civilian Radioactive
Waste Management
U.S. Department of Energy
Forrestal Bldg.
Washington, D.C. 20585

1 D. H. Alexander (RW-332)
Office of Civilian Radioactive
Waste Management
U.S. Department of Energy
Forrestal Bldg.
Washington, D.C. 20585

1 J. C. Bresee (RW-10)
Office of Civilian Radioactive
Waste Management
U.S. Department of Energy
Forrestal Bldg.
Washington, D.C. 20585

1 Samuel Rousso (RW-10)
Office of Program and Resources
Management
Office of Civilian Radioactive
Waste Management
U.S. Department of Energy
Forrestal Bldg.
Washington, D.C. 20585

1 Gerald Parker (RW-30)
Office of Civilian Radioactive
Waste Management
U.S. Department of Energy
Forrestal Bldg.
Washington, D.C. 20585

1 D. G. Horton (RW-3)
Office of Quality Assurance
Office of Civilian Radioactive
Waste Management
U.S. Department of Energy
Forrestal Bldg.
Washington, D.C. 20585

February 7, 1991

1 D. E. Shelor (RW-30)
Office of Systems and Compliance
Office of Civilian Radioactive
Waste Management
U.S. Department of Energy
Forrestal Bldg.
Washington, D.C. 20585

1 L. H. Barrett (RW-40)
Office of Storage and Transportation
Office of Civilian Radioactive
Waste Management
U.S. Department of Energy
Forrestal Bldg.
Washington, D.C. 20585

1 F. G. Peters (RW-50)
Office of Contractor Business
Management
Office of Civilian Radioactive
Waste Management
U.S. Department of Energy
Forrestal Bldg.
Washington, D.C. 20585

1 Senior Project Manager for Yucca
Mountain Repository Project Branch
Division of Waste Management
U.S. Nuclear Regulatory Commission
Washington, D.C. 20555

1 NTS Section Leader
Repository Project Branch
Division of Waste Management
U.S. Nuclear Regulatory Commission
Washington, D.C. 20555

1 Repository Licensing & Quality
Assurance Project Directorate
Division of Waste Management
U.S. Nuclear Regulatory Commission
Washington, DC 20555

1 NRC Document Control Clerk
Division of Waste Management
U.S. Nuclear Regulatory Commission
Washington, D.C. 20555

1 Carl P. Gertz (RW-20)
Office of Geologic Disposal
Office of Civilian Radioactive
Waste Management
U.S. Department of Energy
Forrestal Bldg.
Washington, D.C. 20585

1 D. U. Deere, Chairman
Nuclear Waste Technical
Review Board
1100 Wilson Blvd. #910
Arlington, VA 22209-2297

1 NRC Document Control Desk
Division of Waste Management
U.S. Nuclear Regulatory Commission
Washington, D.C. 20555

5 Carl P. Gertz, Project Manager
Yucca Mountain Project Office
Nevada Operations Office
U.S. Department of Energy
Mail Stop 523
P.O. Box 98518
Las Vegas, NV 89193-8518

12 Technical Information Office
Nevada Operations Office
U. S. Department of Energy
P.O. Box 98518
Las Vegas, NV 89193-8518

1 C. L. West, Director
Office of External Affairs
Nevada Operations Office
U.S. Department of Energy
P.O. Box 98518
Las Vegas, NV 89193-8518

1 W. M. Hewitt, Program Manager
Roy F. Weston, Inc.
955 L'Enfant Plaza, Southwest
Suite 800
Washington, D.C. 20024

1 Technical Information Center
Roy F. Weston, Inc.
955 L'Enfant Plaza, Southwest
Suite 800
Washington, D.C. 20024

3 L. J. Jardine
Technical Project Officer for YMP
Lawrence Livermore National Laboratory
Mail Stop L-204
P.O. Box 808
Livermore, CA 94550

1 J. H. Nelson
Technical Project Officer for YMP
Science Applications International Corp.
101 Convention Center Dr.
Suite 407
Las Vegas, NV 89109

1 H. N. Kalia
Exploratory Shaft Test Manager
Los Alamos National Laboratory
Mail Stop 527
101 Convention Center Dr.
Suite 820
Las Vegas, NV 89109

1 Arend Meijer
Los Alamos National Laboratory
Mail Stop J514
P.O. Box 1663
Los Alamos, NM 87545

4 R. J. Herbst
Technical Project Officer for YMP
Los Alamos National Laboratory
N-5, Mail Stop J521
P.O. Box 1663
Los Alamos, NM 87545

6 L. R. Hayes
Technical Project Officer for YMP
U.S. Geological Survey
P.O. Box 25046
421 Federal Center
Denver, CO 80225

1 K. W. Causseaux
NHP Reports Chief
U.S. Geological Survey
P.O. Box 25046
421 Federal Center
Denver, CO 80225

1 R. V. Watkins, Chief
Project Planning and Management
U.S. Geological Survey
P.O. Box 25046
421 Federal Center
Denver, CO 80225

1 Center for Nuclear Waste Regulatory Analyses
6220 Culebra Road
Drawer 28510
San Antonio, TX 78284

1 D. L. Lockwood, General Manager
Raytheon Services, Inc.
Mail Stop 514
P.O. Box 93265
Las Vegas, NV 89193-3265

1 Richard L. Bullock
Technical Project Officer for YMP
Raytheon Services, Inc.
101 Convention Center Dr.
Suite P250
Las Vegas, NV 89109

1 James C. Calovini
Raytheon Services, Inc.
101 Convention Center Dr.
Suite P-280
Las Vegas, NV 89109

1 Dr. David W. Harris
YMP Technical Project Officer
Bureau of Reclamation
P.O. Box 25007 Bldg. 67
Denver Federal Center
Denver, CO 80225-0007

1 A. E. Gurrola
General Manager
Raytheon, Inc.
Mail Stop 580
P.O. Box 93838
Las Vegas, NV 89193-3838

1 M. D. Voegele
Science Applications International Corp.
101 Convention Center Dr.
Suite 407
Las Vegas, NV 89109

1 P. T. Prestholt
NRC Site Representative
1050 East Flamingo Road
Suite 319
Las Vegas, NV 89119

1 R. E. Lowder
Technical Project Officer for YMP
MAC Technical Services
Valley Bank Center
101 Convention Center Drive
Suite 1100
Las Vegas, NV 89109

1 D. L. Fraser, General Manager
Reynolds Electrical & Engineering Co.
P.O. Box 98521
Mail Stop 555
Las Vegas, NV 89193-8521

1 P. K. Fitzsimmons, Director
Health Physics & Environmental Division
Nevada Operations Office
U.S. Department of Energy
P.O. Box 98518
Las Vegas, NV 89193-8518

1 Robert F. Pritchett
Technical Project Officer for YMP
Reynolds Electrical & Engineering Co.
Mail Stop 615
P.O. Box 98521
Las Vegas, NV 89193-8521

1 D. Zesiger
U.S. Geological Survey
101 Convention Center Dr.
Suite 860 - MS509
Las Vegas, NV 89109

1 Elaine Ezra
YMP GIS Project Manager
EG&G Energy Measurements, Inc.
P.O. Box 1912
Mail Stop H-02
Las Vegas, NV 89125

2 SAIC-T&MSS Library
Science Applications International Corp.
101 Convention Center Dr.
Suite 407
Las Vegas, NV 89109

1 Dr. Martin Mifflin
Desert Research Institute
Water Resources Center
2505 Chandler Avenue
Suite 1
Las Vegas, NV 89120

1 E. P. Binnall
Field Systems Group Leader
Building 50B/4235
Lawrence Berkeley Laboratory
Berkeley, CA 94720

1 J. F. Divine
Assistant Director for Engineering Geology
U.S. Geological Survey
106 National Center
12201 Sunrise Valley Dr.
Reston, VA 22092

1 V. M. Glanzman
U.S. Geological Survey
P.O. Box 25046
913 Federal Center
Denver, CO 80225

1 C. H. Johnson
Technical Program Manager
Nuclear Waste Project Office
State of Nevada
Evergreen Center, Suite 252
1802 North Carson Street
Carson City, NV 89710

1 T. Hay, Executive Assistant
Office of the Governor
State of Nevada
Capitol Complex
Carson City, NV 89710

3 R. R. Loux, Jr.
Executive Director
Nuclear Waste Project Office
State of Nevada
Evergreen Center, Suite 252
1802 North Carson Street
Carson City, NV 89710

1 John Fordham
Water Resources Center
Desert Research Institute
P.O. Box 60220
Reno, NV 89506

1 Prof. S. W. Dickson
Department of Geological Sciences
Mackay School of Mines
University of Nevada
Reno, NV 89557

1 J. R. Rollo
Deputy Assistant Director for
Engineering Geology
U.S. Geological Survey
106 National Center
12201 Sunrise Valley Dr.
Reston, VA 22092

1 Eric Anderson
Mountain West Research-Southwest
Inc.
2901 N. Central Ave. #1000
Phoenix, AZ 85012-2730

5 Judy Foremaster
City of Caliente
P.O. Box 158
Caliente, NV 89008

1 D. J. Bales
Science and Technology Division
Office of Scientific and Technical
Information
U.S. Department of Energy
P.O. Box 62
Oak Ridge, TN 37831

1 Carlos G. Bell, Jr.
Professor of Civil Engineering
Civil and Mechanical Engineering
Department
University of Nevada, Las Vegas
4505 South Maryland Parkway
Las Vegas, NV 89154

1 C. F. Costa, Director
Nuclear Radiation Assessment
Division
U.S. Environmental Protection
Agency
Environmental Monitoring Systems
Laboratory
P.O. Box 93478
Las Vegas, NV 89193-3478

1 J. Z. Bem
Project Manager
Bechtel National Inc.
P.O. Box 3965
San Francisco, CA 94119

1 R. Harig
Parsons Brinckerhoff Quade &
Douglas
303 Second Street
Suite 700 North
San Francisco, CA 94107-1317

1 Dr. Roger Kasperson
CENTED
Clark University
950 Main Street
Worcester, MA 01610

1 Robert E. Cummings
Engineers International, Inc.
P.O. Box 43817
Tucson, AZ 85733-3817

1 Dr. Jaak J. K. Daemen
University of Nevada
Mackay School of Mines
Reno, NV 89557-0139

1 Department of Comprehensive Planning
Clark County
225 Bridger Avenue, 7th Floor
Las Vegas, NV 89155

1 Economic Development Department
City of Las Vegas
400 East Stewart Avenue
Las Vegas, NV 89109

1 Planning Department
Nye County
P.O. Box 153
Tonopah, NV 89049

1 Director of Community Planning
City of Boulder City
P.O. Box 367
Boulder City, NV 89005

1 Commission of the European
Communities
200 Rue de la Loi
B-1049 Brussels
Belgium

1 Lincoln County Commission
Lincoln County
P.O. Box 90
Pioche, NV 89043

1 Community Planning & Development
City of North Las Vegas
P.O. Box 4086
North Las Vegas, NV 89030

1 City Manager
City of Henderson
Henderson, NV 89015

1 ONWI Library
Battelle Columbus Laboratory
Office of Nuclear Waste Isolation
505 King Avenue
Columbus, OH 43201

1 Librarian
Los Alamos Technical
Associates, Inc.
P.O. Box 410
Los Alamos, NM 87544

1 Loren Lorig
Itasca Consulting Group, Inc.
1313 5th Street SE, Suite 210
Minneapolis, MN 55414

1 James K. Lein
Department of Geography
122 Clippinger Laboratories
Ohio University
Athens, OH 45701-2979

1 6300 T. O. Hunter, Actg.
1 6310 T. E. Blejwas, Actg.
1 6310A F. W. Bingham
1 6310 YMP CRF
1 6310 100/1232833/SAND87-2381/QA
1 6311 A. L. Stevens
1 6312 F. W. Bingham, Actg.
1 6313 L. E. Shephard, Actg.
1 6314 L. S. Costin
1 6315 F. B. Nimick, Actg.
1 6316 R. P. Sandoval
1 6317 S. Sinnock
2 6318 L. J. Erickson
1 6318 C. Crawford
for Accession No. Data Base
1 6319 R. R. Richards
20 6341 WMT Library
1 6410 D. J. McCloskey, Actg.
5 3141 S. A. Landenberger
3 3151 G. L. Esch
1 8524 J. A. Wackerly
8 3145 Document Processing
for DOE/OSTI
1 9300 J. E. Powell
1 9310 J. D. Plimpton
10 9311 J. S. Phillips

The number in the lower right-hand corner is an accession number used for Office of Civilian Radioactive Waste Management purposes only. It should not be used when ordering this publication.

Org.	Bldg.	Name	Rec'd by	Org.	Bldg.	Name	Rec'd by